UNIVERSIDAD AUTONOMA DE MADRID

The mathematical models of rotating droplets with charge or subject to electric fields

Analysis and Numerical Simulation

A thesis submitted in partial fulfillment of the requirements for the degree of Doctor of Philosophy in Mathematics

Author

Víctor José García Garrido

Advisors

Dr. Marco Antonio Fontelos López

Dr. Ultano Kindelán Bustelo

October 31, 2013

ICMAT Instituto de Ciencias Matemáticas

CSIC Consejo Superior de Investigaciones Científicas

"Philosophy is written in this grand book, the universe, which stands continually open to our gaze. But the book cannot be understood unless one first learns to comprehend the language and read the letters in which it is composed. It is written in the language of mathematics, and its characters are triangles, circles, and other geometric figures without which it is humanly impossible to understand a single word of it; without these, one wanders about in a dark labyrinth."

Galileo Galilei (1564-1642)

"A smile is the shortest distance between two people."

Victor Borge (1909-2000)

"When you have eliminated all that is impossible,
whatever remains must be the truth,
no matter how improbable."

Sherlock Holmes

"Only a few find the way, some don't recognize it
when they do - some... don't ever want to."

The Cheshire Cat

Abstract

The main goal of this thesis is to give an answer to the question: **How does rotation influence the evolution of a charged or neutral droplet that could also be subject to an external electric field along its axis of rotation?** It is well known from experiments that a drop can develop singularities in the form of Taylor cones when it holds an amount of charge larger than Rayleigh's limit on its surface [58] and/or it is immersed in a sufficiently strong electric field [68]. From the cone tips, a thin jet of microdroplets is eventually emitted [20], which is of crucial importance and has many applications in industrial processes such as electrospraying, elecronic printing, Field Induced Droplet Ionization mass spectrometry and Field Emission Electric Propulsion thrusters among others. An intriguing and yet not completely understood problem is the discrepancy existent between the results given for the opening semiangle of these cones by theoretical calculations, experiments and numerical simulations [27]. This thesis tries to give an insight into this problem by a complete description on how the stability of a conducting and viscous drop changes when rotation is considered as a force acting on the system.

When dealing with rotating bodies, there are two possible situations: one where the angular speed ω remains fixed, i.e. imagine a constant force turning the system at a constant rate, or another where the system is initally set into rotation and is left to evolve without further interaction with it, so its angular momentum $\mathcal{L}$ is conserved. This work discusses both cases. The free boundary problem arising from the modeling of rotating droplets is described, in the limit of large Ekman number and small Reynolds number, by Stokes equation [56] and simulated with a Boundary Element Method (BEM) that has the capability of mesh adaption [17]. With this approach, we can analyze with precision the regions of the drop's interface where singularities (Taylor cones or drop breakup) develop and their formation process.

We begin by studying the evolution of a viscous drop, contained in another viscous fluid, that rotates about a fixed axis at constant angular speed or angular momentum. The analysis is carried out by combining asymptotic analysis and full numerical simulation, focusing on the stability/instability of equilibrium shapes and the formation of singularities that change the topology of the fluid domain. When evolution is at constant ω, unstable drops can take the form of a flat film whose thickness goes to zero in finite time or an elongated filament that extends indefinitely in finite time. On the other hand, if evolution takes place at constant $\mathcal{L}$, and axial symmetry is imposed, thin films surrounded by a toroidal rim can develop, but the film thickness does not vanish in finite time. In the absence of axial symmetry, and for sufficiently large $\mathcal{L}$, drops break axial symmetry and reach an equilibrium configuration with a 2-fold symmetry or break up into several drops with a 2 or 3-fold symmetry. The mechanism of breakup is also described.

After describing the evolution of rotating drops, this thesis analyzes the effects that rotation has on the evolution of a conducting and viscous drop, contained in another viscous and insulating fluid, when it holds an amount of charge Q on its surface or is immersed in an external electric field of magnitude $\mathcal{E}_\infty$ parallel to the rotation axis. We pay special attention to the case where rotation is at constant angular momentum because of its physical relevance. Numerical simulations and stability analysis show that the Rayleigh fissibility ratio χ at which charged drops become unstable decreases with angular momentum, whereas for neutral drops subject to an electric field the critical value of the field at which the droplet destabilizes increases with rotation. Concerning equilibrium shapes, approximate spheroids and ellipsoids are obtained and the transition between these two families of solutions is established with an energy minimization argument. When drops become unstable, two-lobed structures form, where a pinch-off occurs in finite time, or dynamic Taylor cones in the sense of [7] develop. An interesting feature about these cones is that for small $\mathcal{L}$, their seamiangle remains the same as if there was no rotation in the system.

Finally, and as part of the work I developed during a research stay at the University of Cambridge, the evolution problem is solved with the Finite Element Method (FEM). This approach, which validates the axisymmetric results obtained in this thesis for rotating drops using BEM, will allow us in the future to study the influence that the inertial terms present in Navier-Stokes equations have on the stability of the system.

Resumen

El objetivo principal de esta tesis es dar respuesta a la pregunta: **¿Cómo influye la rotación en la evolución de una gota cargada o neutra que también puede estar sometida a un campo eléctrico aplicado en la dirección de su eje de giro?** Experimentalmente es bien conocido que una gota puede desarrollar singularidades en la forma de conos de Taylor cuando almacena en su superficie una cantidad de carga superior al límite de Rayleigh [58] y/ó está inmersa en un campo eléctrico suficientemente intenso [68]. Desde la punta del cono, se emite un delgado jet de microgotas [20], que resulta de crucial importancia y tiene multitud de aplicaciones en procesos industriales como el electrospraying, la impresión electrónica, el método para espectrometría de masas denominado Field Induced Droplet Ionization y los propulsores del tipo Field Emission Electric Propulsion entre otros. Un problema interesante y que aún no se ha podido resolver es la discrepancia existente entre los resultados teóricos obtenidos para el semiángulo de apertura de los conos y los determinados experimentalmente y mediante simulaciones numéricas [27]. La tesis aborda este problema presentando una completa descripción de cómo la estabilidad de una gota cambia cuando uno considera la rotación como una fuerza que actúa sobre el sistema.

Cuando se estudian objetos en rotación, tenemos dos posibles situaciones: una donde la velocidad angular ω permanece constante (imaginemos una fuerza que hace girar el sistema a un ritmo constante), y otra en la que el sistema es puesto inicialmente en rotación y se le deja evolucionar sin ninguna interacción posterior con él, luego el momento angular $\mathcal{L}$ se conserva. Este trabajo discute ambos casos. El problema de frontera libre que surge de la modelización de gotas en rotación viene descrito, en el límite de número de Ekman grande y de Reynolds pequeño, por la ecuación de Stokes [56] y se resuelve mediante la implementación de un Método de Elementos de Cotorno (BEM) que contiene un módulo de adaptación de mallado [17]. Este acercamiento nos permite analizar con precisión las regiones de la interfase de la gota donde se pueden desarrollar singularidades (conos de Taylor ó la ruptura en gotas pequeñas) y estudiar en detalle su proceso de formación.

Comenzaremos estudiando la evolución de una gota viscosa, contenida en otro fluido viscoso, que rota alrededor de un eje a velocidad ó momento angular constante. El análisis se lleva a cabo combinando análisis asintótico y simulaciones numéricas, prestando especial atención a la estabilidad/inestabilidad de las soluciones de equilibrio y la posible formación de singularidades que representan un cambio en la topología de la gota. Cuando la evolución es a ω constante, las gotas inestables toman la forma de una capa delgada cuyo espesor tiende a cero en tiempo finito ó de un filamento delgado que se extiende indefinidamente en tiempo finito. Por otro lado, si la rotación tiene lugar a $\mathcal{L}$ constante, e imponemos simetría axial, se desarrollan capas delgadas rodeadas de un anillo toroidal, pero el espesor de la capa no se anula en tiempo finito. Si no suponemos simetría axial del problema, y para $\mathcal{L}$ suficientemente grande, la gota deja de ser axisimétrica y alcanza una configuración de equilibrio con una simetría de dos lóbulos ó desarrolla simetrías de dos ó tres lóbulos que se acaban rompiendo en varias gotas. También describimos el mecanismo de ruptura.

Después de estudiar la evolución de gotas en rotación, esta tesis describe los efectos que la rotación tiene sobre la evolución de una gota de fluido viscoso y conductor, contenida en otro fluido viscoso y aislante, cuando ésta almacena una carga Q en su superficie ó está inmersa en un campo eléctrico de intensidad $\mathcal{E}_\infty$ paralelo al eje de giro. Describiremos en detalle el caso de rotación a $\mathcal{L}$ constante por su relevancia física. Los resultados numéricos y un análisis de estabilidad muestran que el límite de Rayleigh para el cual las gotas cargadas se vuelven inestables decrece con el momento angular, mientras que para gotas neutras sometidas a un campo eléctrico, el valor crítico del campo para el cual la gota se desestabiliza aumenta con la rotación. Encontramos también que los esferoides y elipsoides son soluciones de equilibrio aproximadas y calculamos la transición entre estas dos familias mediante un argumento energético. Con respecto a las singularidades, la gota puede desarrollar una estructura de dos lóbulos que da lugar a un pinch-off en tiempo finito ó a la aparición de conos de Taylor dinámicos [7]. Una característica interesante de estos conos es que para pequeños valores de $\mathcal{L}$, su semiángulo es el mismo que si el sistema no estuviera rotando.

Finalmente, y como parte del trabajo realizado durante mi estancia de investigación en la Universidad de Cambridge, abordamos el problema de evolución mediante el Método de Elementos Finitos (FEM). Este enfoque, con el que validamos los resultados axisimétricos obtenidos en esta tesis con BEM para gotas que únicamente están sometidas a rotación, nos permitirá en trabajos futuros estudiar la influencia que los términos de inercia de las ecuaciones de Navier-Stokes tienen sobre la estabilidad del sistema.

Agradecimientos

Me gustaría expresar de corazón mi más sincera gratitud hacia todas las personas que me han acompañado de la mano durante estos últimos años y han contribuido a la culminación de esta tesis. Primero, a los profesores Marco Fontelos y Ultano Kindelán por proponerme un problema tan interesante sobre el que trabajar. Ellos me han proporcionado, con pacencia y dedicación, una fuente incalculable de conocimiento y oportunidades para formarme como científico. No quiero olvidar en esta faceta al profesor Jie Li, que tan amablemente me acogió durante mi estancia en la Universidad de Cambridge. Gracias también a todos mis amigos y familiares por todo el cariño y ánimo que me han dado siempre, a mis amigos de Cambridge por su hospitalidad y compañía durante mis cinco meses en el extranjero, y a mis compañeros de despacho del ICMAT y de la UPM por esos agradables momentos y animadas charlas que hemos compartido juntos en la comida y que tanto echo de menos ahora. Por encima de todo, gracias a mis padres y mi hermano por creen en mí en todo momento y por inculcarme día a día, con todo su amor, un espíritu de sacrificio y superación que me permite afrontar cualquier reto. Gracias a ellos soy una persona humilde, curiosa, responsable y feliz en este viaje de descubrimiento, realizacón personal y profesional que todos afrontamos, la vida. Por último, quisiera darle las gracias a Julia por estar a mi lado con todo su apoyo y cariño en los momentos finales de esta tesis. Ella es la luz de mi vida, que se iluminó durante un congreso que siempre guardaré en mi memoria. Gracias a ti, el camino a recorrer que se abre ahora ante mis ojos es mucho más claro. Necesitaría un libro más grande que esta tesis para relatar los momentos tan especiales que hemos compartido juntos desde entonces y todos los que están aún por llegar.

Contents

List of Figures

List of Tables

Symbols

Symbol	Units	Denotation
ω	T^{-1}	Drop's angular speed
$\mathcal{L}$	$\mathrm{ML}^2\mathrm{T}^{-1}$	Drop's angular momentum
$\mathcal{I}$	ML^2	Drop's moment of inertia
V	L^3	Drop's volume
$\mathcal{A}_d$	L^2	Drop's surface area
$\mathcal{H}$	L^{-1}	Mean curvature at the interface
ϱ_1	ML^{-3}	Drop's density
μ_1	$\mathrm{ML}^{-1}\mathrm{T}^{-1}$	Drop's viscosity
ϱ_2	ML^{-3}	Density of the surrounding fluid
μ_2	$\mathrm{ML}^{-1}\mathrm{T}^{-1}$	Viscosity of the surrounding fluid
γ	MT^{-2}	Surface tension
$\mathbf{E}$	$\mathrm{MLT}^{-3}\mathrm{I}^{-1}$	Electric field
$\mathcal{E}_\infty$	$\mathrm{MLT}^{-3}\mathrm{I}^{-1}$	Electric field intensity
Q	TI	Electric charge
σ	TIL^{-2}	Surface charge density
$\mathcal{V}$	$\mathrm{ML}^2\mathrm{T}^{-3}\mathrm{I}^{-1}$	Electrostatic potential
ε_0	$\mathrm{M}^{-1}\mathrm{L}^{-3}\mathrm{T}^4\mathrm{I}^2$	Permittivity of free space
$\mathbf{B}$	$\mathrm{MT}^{-2}\mathrm{I}^{-1}$	Magnetic field
μ_0	$\mathrm{MLT}^{-2}\mathrm{I}^2$	Permeability of free space
Ω		Dimensionless angular speed
L		Dimensionless angular momentum
χ		Rayleigh fissibility ratio
E_∞		Dimensionless electric field intensity
λ		Viscosity ratio
ζ		Density ratio
Re		Reynolds number
Ek		Ekman number
Bo		Bond number
Fr		Froudé number

Chapter 1

Introduction

1.1. Brief history and state of the art

The problem of describing the evolution, stability and equilibrium shapes of a fluid droplet immersed in another viscous fluid and subject to different forces has provided the scientific community, for more than three centuries, with an endless source of inspiration and challenges. One of the first pioneers in this subject, Sir Isaac Newton, dedicated part of his life trying to explain the Earth's shape as a self-gravitating mass of fluid rotating in space. But surely, the most influential figure associated with the birth of this problem is that of the belgian physicist Joseph-Antoine Ferdinand Plateau (1801-1883), whose interest in validating the theory put forward by Newton, led him to conduct some experiments between 1843 and 1869. To make his research possible, he designed and built a neutral buoyancy tank filled with a combination of water and methanol and, within this mixture, a silicone oil drop pierced by a vertical shaft was placed. By turning the shaft, Plateau induced rotation on the droplet and studied its evolution and equilibriums for different values of the angular speed. In this experimental setting, surface tension forces would play the role that self-gravitation had in Newton's model. Interestingly, all his results [51, 52] were consistent with the existing theory of planetary bodies [46, 39] except for one detail: he observed toroidal equilibrium shapes, which were thought to be impossible solutions for self-gravitating masses of fluid. This discovery became the key motivation to find all possible equilibrium solutions for rotating drops.

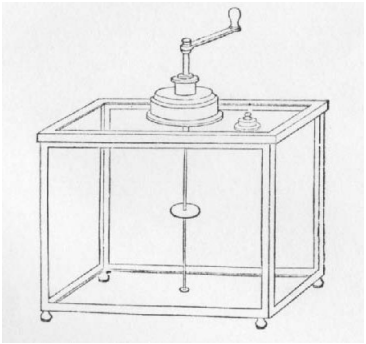

Figure 1.1: Neutral bouyancy tank designed by Plateau.

The first theoretical approach to calculate equilibrium configurations for rotating drops was undertaken in 1869, when Beer determined a one-parameter family of axially symmetric solutions with the topology of the sphere [6], i.e. spheroidal-like shapes. These results were extended later by Poincaré in 1885, showing the existence of a two-lobed family of solutions [53], and in 1984 by Gulliver, confirming the existence of the toroidal solutions experimentally observed by Plateau. From the numerical point of view, the study of the stationary problem started around 1980 with Brown & Scriven [11]. Using a Galerkin method based on FEM, they determined branches of solutions with a 2-fold, 3-fold or in general n-fold symmetry together with their stability, which bifurcate from the spheroidal family (see figures 1.5 and 1.6). For example, the 2-fold symmetry can be observed when a drop rolling over a tilted plane leaves the incline, undergoes free

falling and evolves into a *peanut* shape [2]. Remarkably, the branches of solutions with n-fold symmetry contain also solutions such that each lobe consists of a chain of small droplets connected by thin filaments as demonstrated by Heine [35]. In recent years, and with the purpose of validating all the theoretical results and numerical data available to date, experiments aimed in the same direction as those originally devised by Plateau were conducted under zero gravity conditions during the flight of Spacelab 3 and at JPL (*Jet Propulsion Laboratory*). At that time, going out to space was a necessary requirement to avoid earthbound issues concerning gravity. Nowadays, these complications have been resolved in the laboratory with the development of diamagnetic levitation techniques [36]. A fully detailed description of all space experiments performed by NASA can be obtained from reports [72, 73] and all references included therein.

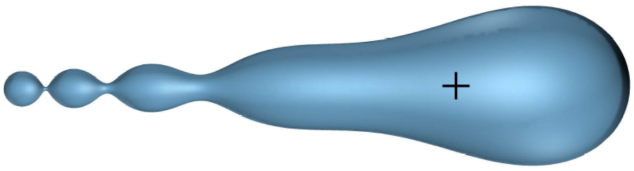

Figure 1.2: Equilibrium shape for a rotating drop with a 2-fold symmetry presenting a cascade of necks [35].

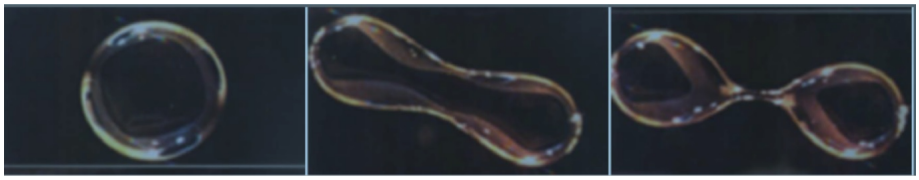

Figure 1.3: Equilibrium shapes obtained for a rotating drop during Spacelab experiments [72].

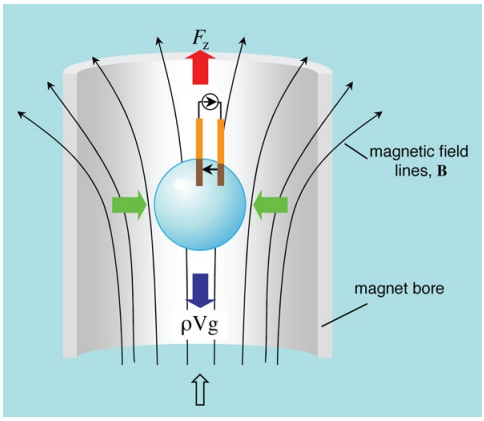

(a) Rotating a drop with diamagnetic levitation.

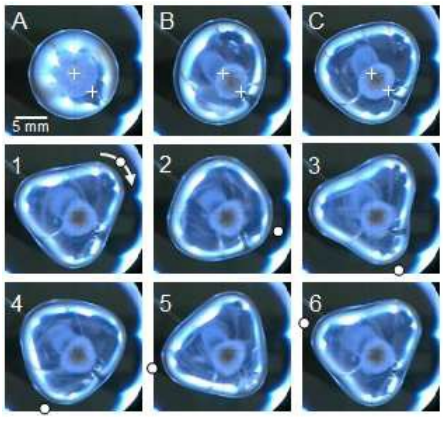

(b) Evolution of a levitated rotating drop.

Figure 1.4: On the left, the mechanism that rotates a drop using diamagnetic levitation is sketched. On the right, we show an ordered sequence of frames taken from the evolution of a levitated and rotating droplet. Observe that the drop develops a 3-fold structure during this process. These pictures appear in [36].

Even though rotating drops present a huge wealth of equilibrium shapes, one cannot expect all of them to be stable. Once a rotating droplet in equilibrium destabilizes, there are essentially two possibilities: the drop undergoes a transition towards another equilibrium shape, or evolves in such a way that its surface becomes non-smooth at some time and a singularity, wether representing a surface cusp or a topological change in the drop's domain (breakup into smaller droplets), develops. The fact that singularities may take place in free-surface hydrodynamic flows is well known and has been the subject of intensive research in different

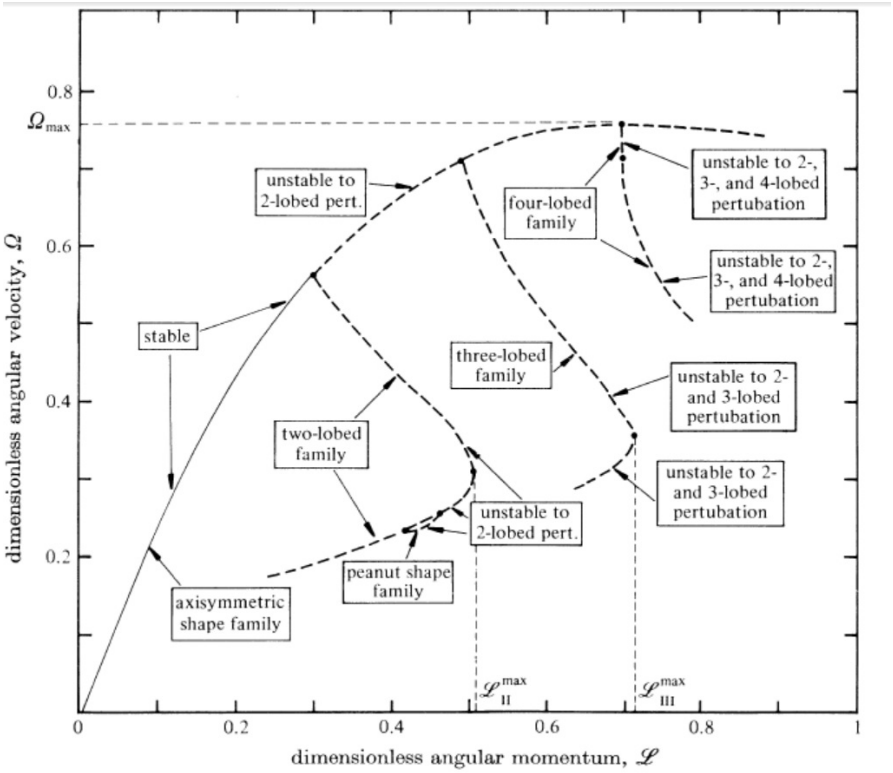

Figure 1.5: Bifurcation diagram obtained in [11] for rotating drops at constant angular speed.

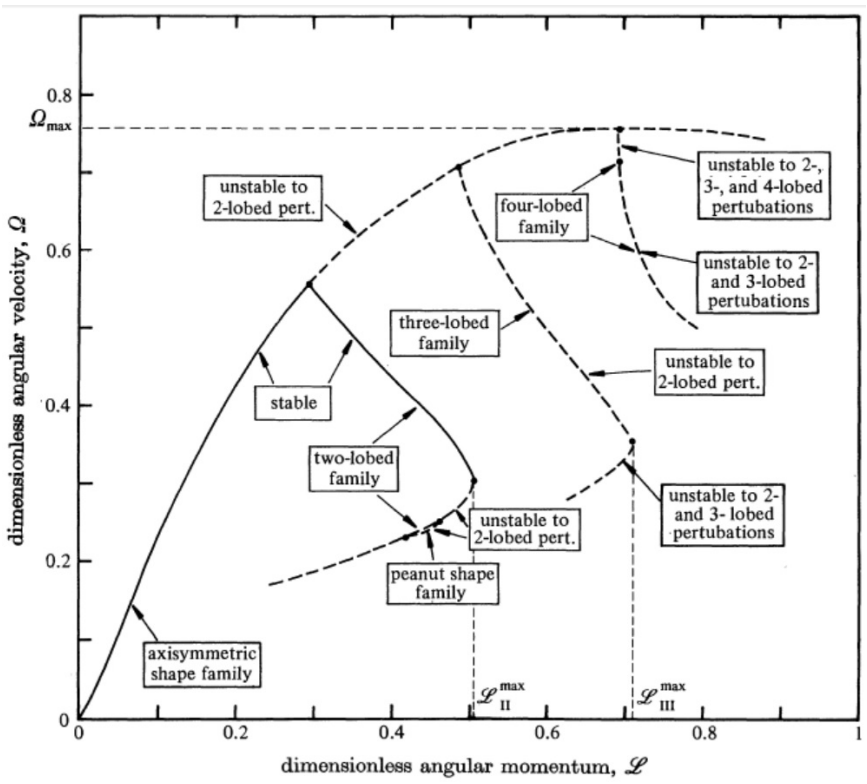

Figure 1.6: Bifurcation diagram obtained in [11] for rotating drops at constant angular momentum.

contexts such as capillary drop breakup or air entrainment. For an updated general review on free-surface flows see [23] and [22] for a review on singularities.

During the last decades, rotating masses of fluid have been applied to industrial processes such as polymer manufacturing [50] and spinning drop tensiometry techniques used to measure interfacial tension in the laboratory [57]. Also, the rotating drop problem has been applied at the atomic level, as a model proposed in 1939 by Bohr & Wheele [8] for nuclear fission that concerns the breakup of a charged rotating liquid drop, where nuclear forces play the role of surface tension. On astronomical scales, shapes and stability of self-gravitating masses rotating freely in space were studied in detail by Chandrasekhar [12].

Besides rotation, one can consider electromagnetic forces acting on a drop. In this direction, Lord Rayleigh investigated in 1882 the effects that charge has on a conducting droplet [58]. Using an energy stability analysis, he showed that a conducting spherical drop of radius R and surface tension γ surrounded by an insulating medium with permittivity ε_0 looses stability at critical values of the charge:

$$Q_c^n = 4\pi\sqrt{\varepsilon_0 \gamma R^3 \,(n+2)} \quad , \quad n \geqslant 2 \,,$$

to shape perturbations given by the n-th order Legendre polynomial (number of lobes on the perturbed shape). At each critical value Q_c^n, the sphere is neutrally stable and a family of n-lobed shapes branch. For example, if $n = 2$, a two-lobed family bifurcates transcritically from the spherical family, with one of its arms consisting of stable shapes (supercritical branch) that can be approximated by oblate spheroids [5], and the other is unstable (subcritical branch) and corresponds to prolate-like solutions [68]. In particular, when a droplet holds an amount of charge on its surface larger than Q_c^2, it becomes unstable and evolves into a prolate spheroid that eventually develops cone tips at the poles (known in the literature as Taylor cones [68]). From these tips, thin jets of microdroplets are ejected, carrying about 30% of the total charge from the mother drop but only 1% of its mass [20]. The study of a neutral conducting drop under the influence of an electric field dates back to the works by Taylor in 1964. In his works, he obtained a family of approximate prolate solutions and identified a critical value of the electric field for which these configurations become unstable and develop the same Taylor cone structures discussed earlier [68]. Taylor also predicted theoretically an opening semiangle for the cones of 49.3°, which has turned out to be very different from the average value of about 30° obtained from simulations [27] and laboratory experiments [20]. Moreover, this angle seems to depend slightly on the viscosity ratio for the two fluids involved and interestingly it develops in a self-similar way [27]. Numerically, the search for stationary solutions for charged conducting drops started in 1989, when Basaran & Scriven used FEM to study the families of n-lobed shapes predicted by Rayleigh. Later, this work was extended to deal with charged drops that are also immersed in an external electric field [4]. Below, we present a bifurcation diagram that summarizes these results:

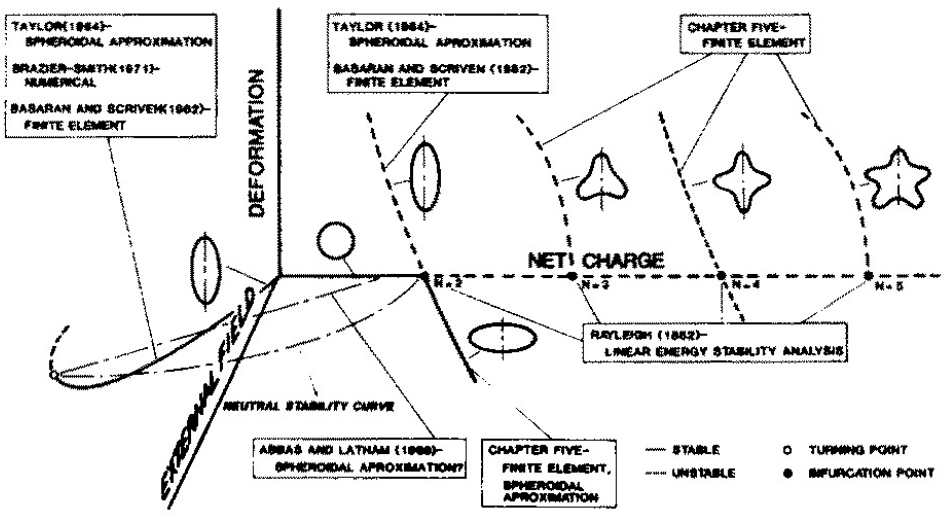

Figure 1.7: Bifurcation diagram for charged drops subject to an electric field [4].

Many industrial and technological applications arise when one considers electromagnetic forces acting on a fluid, as is the case for conducting drops holding an amount of charge on its surface, neutral drops subject to an external electric field or a combination of both effects. The development of techniques such as electrospinning, electrospraying, Field Induced Droplet Ionization (FIDI) mass spectrometry [32] and the design of Field Emission Electric Propulsion (FEEP) colloid thrusters for space vehicles [69] is clear evidence of its importance. We should also mention its contributions to electrowetting and electronic paper [34] and the promising microfluidic chips, where electric fields are used to control chemicals inside a small device with very thin channels [15, 66]. Concerning physical applications, the understanding of coalescence and fission processes for charged droplets is crucial to study how thunderstorm clouds are formed [20].

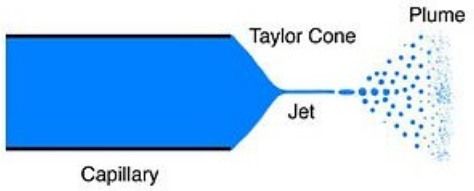

Figure 1.8: Taylor cone mechanism involved in FIDI spectrometry and FEEP thrusters.

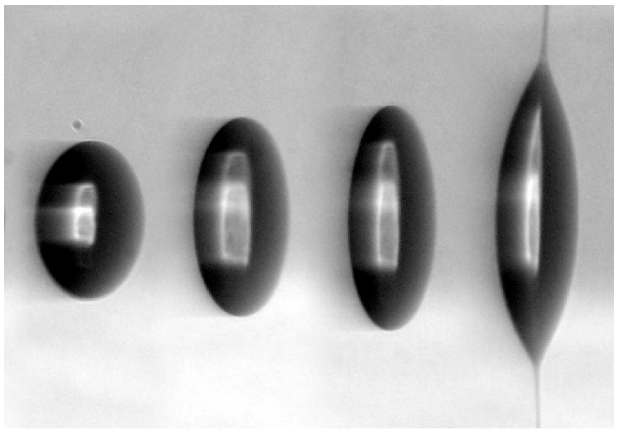

Figure 1.9: Evolution of a droplet subject to a strong electric field, resulting in Taylor cone formation [32]. Observe that in the last picture one can clearly see that from the tips, a thin jet of microdroplets is emitted.

Finally, some interesting research has been carried out recently to simulate numerically the evolution of drops subject to different forces. Notice that all research explained above only solves the equilibrium problem, so in order to be able to describe in detail the behaviour and stability of drops, a deeper understanting of the evolution process is required. Many authors solve this free-surface problem using numerical methods such as BEM, which is perfectly suited to deal with fluids subject to Stokes regimes. Concerning drop evolution, we can point to [70, 27], where the effects of charge and/or electric fields on viscous and conducting drops is addressed together with the formation of Taylor cone singularities. The main goal of this thesis is to combine previous works together with rotational effects, allowing us to build a more general theory that describes droplet evolution.

1.2. Thesis outline

The contents of this thesis are organized as follows: in Chapter 2 we introduce Navier-Stokes equations in a rotating frame of reference and obtain from them the equations that rotating drops satisfy under Stokes approximation. Chapter 3 is devoted to deriving the boundary integral equation that governs the velocity field at the drop's interface, and lays the foundations for the BEM algorithms implemented in Chapter 4 to solve the evolution problem. Chapters 5 and 6 present the main contributions of this thesis, where we first

study the problem of rotating drops and then move to analyze the effects that rotation has on charged drops or neutral drops immersed in an electric field. All results included in these two chapters have been published in [25] and [28]. Finally, in Chapter 7, and following my research stay at the BP Institute for Multiphase Flow at Cambridge University, the Finite Element Method (FEM) is applied to simulate rotating drops under Stokes regime, serving as a validation for the data obtained with BEM. The advantage of FEM is that it can be used to determine how the nonlinear terms appearing in Navier-Stokes equations influence droplet evolution. This is work in progress and future research to come.

Chapter 2

The mathematical model

The aim of this chapter is to describe in detail the mathematical model that governs the evolution of a rotating fluid droplet immersed in another fluid of infinite extension. The fundamental PDEs involved are the classical Navier-Stokes equations, which one has to conveniently modify to include rotation effects. In the figure below, a representation of the rotating droplet problem is given including all possible electrostatic effects acting on it (charge and an external electric field).

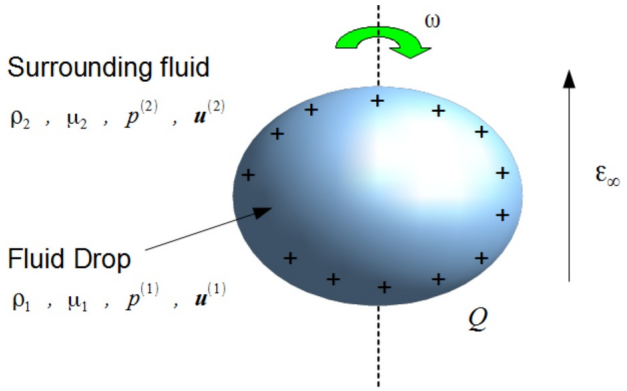

Figure 2.1: Rotating drop model.

Throughout this work, we make use of *Einstein's summation convention* to abbreviate formulas. This notation states that, if a subscript appears twice in an expression involving products, then summation over that subscript is implied in its range.

2.1. Navier-Stokes in rotating frames

In order to describe the dynamics of a rotating fluid, sometimes it is interesting to rewrite its equations of motion in a frame of reference that rotates with the fluid [31]. As a result of the change of coordinates, ficticious forces appear, namely the Coriolis, Euler and centrifugal forces. In this section we will derive Navier-Stokes equations in a rotating frame.

Suppose that a fluid rotates about an axis in the counter-clockwise direction with angular velocity $\boldsymbol{\omega}(t)$ and take two reference frames, $\mathcal{R} = \{\mathbf{O}; \mathbf{e}_1, \mathbf{e}_2, \mathbf{e}_3\}$ which is inertial (stationary), and $\tilde{\mathcal{R}} = \{\mathbf{O}; \tilde{\mathbf{e}}_1(t), \tilde{\mathbf{e}}_2(t), \tilde{\mathbf{e}}_3(t)\}$ that rotates with the fluid. Any point in the fluid can be described as:

$$\mathbf{x}(t) = x_i(t)\,\mathbf{e}_i \equiv \mathbf{x}_{\mathcal{R}} \quad , \quad \mathbf{x}(t) = \tilde{x}_i(t)\,\tilde{\mathbf{e}}_i(t) \equiv \mathbf{x}_{\tilde{\mathcal{R}}} \, .$$

Taking the time derivative of these expressions:

$$\frac{d\mathbf{x}}{dt} = \frac{dx_i}{dt}\mathbf{e}_i \equiv \left(\frac{d\mathbf{x}}{dt}\right)_{\mathcal{R}} \equiv \mathbf{u}_{\mathcal{R}} \quad , \quad \frac{d\mathbf{x}}{dt} = \frac{d\tilde{x}_i}{dt}\tilde{\mathbf{e}}_i + \tilde{x}_i\frac{d\tilde{\mathbf{e}}_i}{dt} = \left(\frac{d\mathbf{x}}{dt}\right)_{\tilde{\mathcal{R}}} + \tilde{x}_i\frac{d\tilde{\mathbf{e}}_i}{dt} = \mathbf{u}_{\tilde{\mathcal{R}}} + \tilde{x}_i\frac{d\tilde{\mathbf{e}}_i}{dt} \, , \tag{2.1}$$

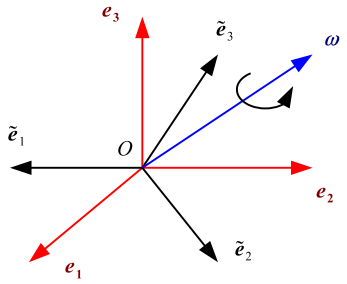

Figure 2.2: Inertial and rotating reference frames.

where $\mathbf{u}_{\mathcal{R}}$ and $\mathbf{u}_{\tilde{\mathcal{R}}}$ are the velocities in the inertial and rotating frames respectively. Since both expressions in (2.1) represent the same vector:

$$\left(\frac{d\mathbf{x}}{dt}\right)_{\mathcal{R}} = \left(\frac{d\mathbf{x}}{dt}\right)_{\tilde{\mathcal{R}}} + \tilde{x}_i \frac{d\tilde{\mathbf{e}}_i}{dt} \ . \tag{2.2}$$

Now, the following results [29] prove to be very useful:

Proposition 2.1 (Rodrigues rotation formula)**.** *Given a vector* $\mathbf{v}$*, if we apply a rotation of angle* ϕ *about an axis defined by the unit vector* $\mathbf{h}$*, the rotated vector has the form:*

$$\mathbf{v}_{rot} = \mathbf{v}\cos\phi + (\mathbf{h}\times\mathbf{v})\sin\phi + \mathbf{h}\,(\mathbf{h}\cdot\mathbf{v})\,(1-\cos\phi) \ .$$

Proposition 2.2. *Consider a rotation about an axis with angular velocity* $\boldsymbol{\omega}(t)$*. The rate of change of a vector* $\mathbf{A}(t)$ *can be obtained from:*

$$\frac{d\mathbf{A}}{dt} = \boldsymbol{\omega}(t)\times\mathbf{A}(t) \ ,$$

Proof. Take as rotation axis $\mathbf{h} = \frac{\boldsymbol{\omega}}{\|\boldsymbol{\omega}\|}$ and a rotation of angle $\delta\phi = \|\boldsymbol{\omega}\|\,\delta t$ about it. By Rodrigues formula:

$$\delta\mathbf{A} = \mathbf{A}_{rot} - \mathbf{A} = (\mathbf{A} + \mathbf{h}\,(\mathbf{h}\cdot\mathbf{A}))\,(1-\cos\delta\phi) + (\mathbf{h}\times\mathbf{A})\sin\delta\phi \ .$$

Since $\delta\phi \ll 1$ we have:

$$\cos\delta\phi = 1 + O\left(\delta\phi^2\right) \quad , \quad \sin\delta\phi = \delta\phi + O\left(\delta\phi^2\right) \ ,$$

and consequently:

$$\delta\mathbf{A} = \mathbf{h}\times\mathbf{A}\delta\phi + O\left(\delta\phi^2\right) \ .$$

Dividing by δt:

$$\frac{\delta\mathbf{A}}{\delta t} = \boldsymbol{\omega}\times\mathbf{A} + O(\delta t) \ ,$$

and taking the limit when $\delta t \to 0$ we obtain the desired result. ■

Applying the previous result to $\tilde{\mathbf{e}}_i$ one gets:

$$\frac{d\tilde{\mathbf{e}}_i}{dt} = \boldsymbol{\omega}(t)\times\tilde{\mathbf{e}}_i(t) \ ,$$

and thus (2.2) becomes:

$$\left(\frac{d\mathbf{x}}{dt}\right)_{\mathcal{R}} = \left(\frac{d\mathbf{x}}{dt}\right)_{\tilde{\mathcal{R}}} + \boldsymbol{\omega}(t)\times\mathbf{x}(t) \ ,$$

or equivalently:

$$\mathbf{u}_{\mathcal{R}} = \mathbf{u}_{\tilde{\mathcal{R}}} + \boldsymbol{\omega}(t)\times\mathbf{x}(t) \ . \tag{2.3}$$

Taking another derivative of (2.3) gives:

$$\begin{aligned}\left(\frac{d^2\mathbf{x}}{dt^2}\right)_{\mathcal{R}} &= \frac{d}{dt}\left(\left(\frac{d\mathbf{x}}{dt}\right)_{\tilde{\mathcal{R}}} + \boldsymbol{\omega}(t)\times\mathbf{x}(t)\right)_{\tilde{\mathcal{R}}} + \boldsymbol{\omega}(t)\times\left(\left(\frac{d\mathbf{x}}{dt}\right)_{\tilde{\mathcal{R}}} + \boldsymbol{\omega}(t)\times\mathbf{x}(t)\right) \\ &= \left(\frac{d^2\mathbf{x}}{dt^2}\right)_{\tilde{\mathcal{R}}} + \underbrace{2\,\boldsymbol{\omega}(t)\times\mathbf{u}_{\tilde{\mathcal{R}}}}_{\text{Coriolis force}} + \underbrace{\boldsymbol{\omega}(t)\times(\boldsymbol{\omega}(t)\times\mathbf{x}(t))}_{\text{Centrifugal force}} + \underbrace{\frac{d\boldsymbol{\omega}}{dt}\times\mathbf{x}(t)}_{\text{Euler force}} \ ,\end{aligned}$$

where:

$$a_{\mathcal{R}} \equiv \left(\frac{d^2\mathbf{x}}{dt^2}\right)_{\mathcal{R}} \quad , \quad a_{\widetilde{\mathcal{R}}} \equiv \left(\frac{d^2\mathbf{x}}{dt^2}\right)_{\widetilde{\mathcal{R}}} ,$$

are the accelerations in the inertial and rotating frames respectively. Applying Newton's second law to the inertial frame yields:

$$\varrho\, a_{\mathcal{R}} = \mathbf{F}_b \quad \Leftrightarrow \quad \varrho\, a_{\widetilde{\mathcal{R}}} = \mathbf{F}_b - \mathbf{F}_{Coriolis} - \mathbf{F}_{Centrifugal} - \mathbf{F}_{Euler} ,$$

where ϱ is the density of the fluid, $\mathbf{F}_b = \varrho\, \mathbf{f}_b$ are the body forces (per unit volume) acting on the fluid and:

$$\mathbf{F}_{Coriolis} = 2\varrho\, \boldsymbol{\omega} \times \mathbf{u}_{\widetilde{\mathcal{R}}} \quad , \quad \mathbf{F}_{Centrifugal} = \varrho\, \boldsymbol{\omega} \times (\boldsymbol{\omega} \times \mathbf{x}) \quad , \quad \mathbf{F}_{Euler} = \varrho\, \frac{d\boldsymbol{\omega}}{dt} \times \mathbf{x} .$$

Consequently, for an incompressible and viscous newtonian fluid rotating about an axis with angular velocity $\boldsymbol{\omega}(t)$, Navier-Stokes equations in the rotating frame become:

$$\begin{cases} \varrho \left(\dfrac{\partial \mathbf{u}}{\partial t} + (\mathbf{u} \cdot \nabla)\, \mathbf{u} \right) = \mathbf{F}_b + \nabla \cdot \widetilde{T} - 2\varrho\, \boldsymbol{\omega} \times \mathbf{u} - \varrho\, \boldsymbol{\omega} \times (\boldsymbol{\omega} \times \mathbf{x}) - \varrho\, \dfrac{d\boldsymbol{\omega}}{dt} \times \mathbf{x} \\ \nabla \cdot \mathbf{u} = 0 \end{cases} . \tag{2.4}$$

where $\mathbf{u}$ and $\mathbf{x}$ are respectively the velocity and position vectors with respect to the rotating frame (we have dropped the $\widetilde{\mathcal{R}}$ notation for simplicity) and $\widetilde{T}$ is the stress tensor:

$$\widetilde{T} = -p\, \mathbb{I} + \mu \left(\nabla \mathbf{u} + (\nabla \mathbf{u})^T \right) \quad , \quad \mathbb{I} \equiv \text{Identity matrix} . \tag{2.5}$$

where μ is the viscosity of the fluid and p its pressure. Observe that we can include in the pressure the centrifugal force and conservative body forces, $\mathbf{F}_b = -\nabla h$. Indeed, using Binet-Cauchy identity:

$$(\mathbf{a} \times \mathbf{b}) \cdot (\mathbf{c} \times \mathbf{d}) = (\mathbf{a} \cdot \mathbf{c})\, (\mathbf{b} \cdot \mathbf{d}) - (\mathbf{a} \cdot \mathbf{d})\, (\mathbf{b} \cdot \mathbf{c}) \quad , \quad \mathbf{a}, \mathbf{b}, \mathbf{c}, \mathbf{d} \in \mathbb{R}^n ,$$

one can write:

$$\|\boldsymbol{\omega} \times \mathbf{x}\|^2 = (\boldsymbol{\omega} \times \mathbf{x}) \cdot (\boldsymbol{\omega} \times \mathbf{x}) = \|\boldsymbol{\omega}\|^2 \|\mathbf{x}\|^2 - (\mathbf{x} \cdot \boldsymbol{\omega})^2 .$$

Now, if we take the gradient and apply the vector identity:

$$\mathbf{a} \times (\mathbf{b} \times \mathbf{c}) = \mathbf{b}\, (\mathbf{a} \cdot \mathbf{c}) - \mathbf{c}\, (\mathbf{a} \cdot \mathbf{b}) \quad , \quad \mathbf{a}, \mathbf{b}, \mathbf{c} \in \mathbb{R}^n ,$$

we get:

$$\frac{1}{2} \nabla \left(\|\boldsymbol{\omega} \times \mathbf{x}\|^2 \right) = \|\boldsymbol{\omega}\|^2 \mathbf{x} - (\mathbf{x} \cdot \boldsymbol{\omega})\, \boldsymbol{\omega} = -\boldsymbol{\omega} \times (\boldsymbol{\omega} \times \mathbf{x}) .$$

Defining a reduced pressure Π and a modified stress tensor T in the form:

$$\Pi = p + h - \frac{\varrho}{2} \|\boldsymbol{\omega} \times \mathbf{x}\|^2 \quad , \quad T = -\Pi\, \mathbb{I} + \mu \left(\nabla \mathbf{u} + (\nabla \mathbf{u})^T \right) , \tag{2.6}$$

Navier-Stokes equations reduce to:

$$\begin{cases} \varrho \left(\dfrac{\partial \mathbf{u}}{\partial t} + (\mathbf{u} \cdot \nabla)\, \mathbf{u} \right) = \nabla \cdot T - 2\varrho\, \boldsymbol{\omega} \times \mathbf{u} - \varrho\, \dfrac{d\boldsymbol{\omega}}{dt} \times \mathbf{x} \\ \nabla \cdot \mathbf{u} = 0 \end{cases} . \tag{2.7}$$

Our model supposes that the rate of change in angular velocity is negligible, so Euler force can be left out of Navier-Stokes equations. Indeed, since we will be working in regimes where the Reynolds number is small, there will be time for diffusion of vorticity to occur provided that deformation is sufficiently slow, leading to an almost solid-body rotation. This allows us to neglect the ficticious force arising from the variable rate of rotation of the frame of reference:

$$\begin{cases} \varrho \left(\dfrac{\partial \mathbf{u}}{\partial t} + (\mathbf{u} \cdot \nabla)\, \mathbf{u} \right) = \mathbf{F}_b - \nabla p + \mu \Delta \mathbf{u} - 2\varrho\, \boldsymbol{\omega} \times \mathbf{u} - \varrho\, \boldsymbol{\omega} \times (\boldsymbol{\omega} \times \mathbf{x}) \\ \nabla \cdot \mathbf{u} = 0 \end{cases} . \tag{2.8}$$

To study the relative importance of the different terms in (2.8), we write the equations in dimensionless form by choosing appropriate length l, velocity U and time τ scales. The dimensionless variables are:

$$\mathbf{u}^* = \frac{\mathbf{u}}{U} \quad , \quad \mathbf{x}^* = \frac{\mathbf{x}}{l} \quad , \quad t^* = \frac{t}{\tau} \quad , \quad p^* = \frac{l}{\mu U} p \quad , \quad \boldsymbol{\omega} = \omega \mathbf{k} \quad , \quad \tau = \frac{l}{U} \, , \tag{2.9}$$

which yield, omitting asterisks:

$$\begin{cases} Re \left(\dfrac{\partial \mathbf{u}}{\partial t} + (\mathbf{u} \cdot \nabla) \, \mathbf{u} \right) = \dfrac{Re}{Fr} \dfrac{\mathbf{f}_b}{\|\mathbf{f}_b\|} - \nabla p + \Delta \mathbf{u} - \dfrac{2}{Ek} \mathbf{k} \times \mathbf{u} - Bo \, \mathbf{k} \times (\mathbf{k} \times \mathbf{x}) \\ \nabla \cdot \mathbf{u} = 0 \end{cases} \quad , \tag{2.10}$$

where:

- Re is the Reynolds number (measures the relative importance between inertial and viscous forces).
- Ek is the Ekman number (characterizing the relation between Coriolis and viscous forces).
- Fr is the Froudé number (gives the relation between inertial convective forces and body forces).
- Bo is the Bond number (measures the relative importance between centrifugal and viscous forces).
- $\mathbf{k}$ is a unit vector describing the droplet's axis of rotation.

and the dimensionless numbers are defined as follows:

$$Re = \frac{\rho U l}{\mu} \quad , \quad Ek = \frac{\mu}{\rho \omega l^2} \quad , \quad Fr = \frac{U^2}{\|\mathbf{f}_b\| \, l} \quad , \quad Bo = \frac{\varrho l^3 \omega^2}{\mu U} \, . \tag{2.11}$$

Since the model will be used to describe small droplets ($l \ll 1$) rotating with a not too large angular speed, viscous, body and centrifugal forces dominate inertial and Coriolis forces, i.e. $Re, Fr \ll 1$ and $Ek \gg 1$, so Navier-Stokes equations (2.10) reduce to Stokes system:

$$\begin{cases} \nabla \cdot T = \mathbf{0} \\ \nabla \cdot \mathbf{u} = 0 \end{cases} \quad \Leftrightarrow \quad \begin{cases} \mu \Delta \mathbf{u} - \nabla \Pi = \mathbf{0} \\ \nabla \cdot \mathbf{u} = 0 \end{cases} \quad , \tag{2.12}$$

which has to be applied to both the drop and the fluid surrounding it and complemented with the appropriate boundary conditions: the balance of forces at the interface and a kinematic boundary condition that determines how the interface evolves with time. These ingredients will be added later in this chapter.

2.2. Conductors and insulators

In nature, the behaviour of matter immersed in an electric field depends on its internal structure and the mobility of the electrons that constitute it. We can distinguish two main classes of materials attending to how they react. For insulating (or dielectric) materials such as paper or glass, electrons are not allowed to move freely and are toghtly bound to their orbits around atoms. For this reason, insulators become polarized and resist electric charge fluxes, giving weak interactions with electrostatic fields. On the other hand, for conducting materials, electrons can move freely from one atom to another, creating electric currents that tend to reach an electrostatic equilibrium. Typical conductors are of metallic origin (copper and silver among others), but one can also find many non-metallic conductors such as graphite and saline solutions. The basic properties of a conducting object are:

1. The electric field inside a conductor vanishes ($\mathbf{E}_{inside} = \mathbf{0}$) and thus all the charge accumulates on its surface. This is a consequence of *Gauss' law*.

2. The tangential component of the electric field at the surface of a conductor is zero ($E_t = 0$). Indeed, taking a closed path Γ enclosing a patch of the surface:

   and decomposing the field into its tangential and normal components:

$$\mathbf{E} = E_t \widehat{\mathbf{t}} + E_n \widehat{\mathbf{n}} \, ,$$

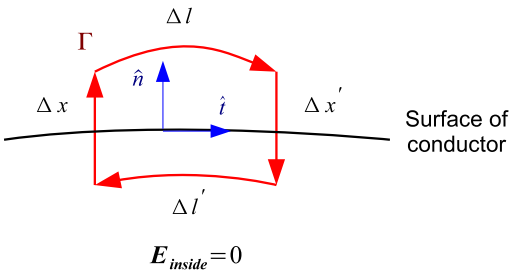

Figure 2.3: Path of integration for the electric field of a conductor.

we get:

$$\int_\Gamma \mathbf{E}\cdot d\mathbf{l} = E_t\Delta l + E_n\Delta x - 0\Delta l' - E_n\Delta x' \ .$$

Now, take the limit $\Delta x, \Delta x' \to 0$, and since $\mathbf{E}$ is conservative:

$$\int_\Gamma \mathbf{E}\cdot \ d\mathbf{l} = 0 \ ,$$

we obtain $E_t = 0$. In the case where the tangential component of $\mathbf{E}$ at the surface is initially non-zero (there is no electrostatic equilibrium) then the charges will move until they reach the equilibrium state corresponding to $\mathbf{E}_{inside} = \mathbf{0}$.

3. The surface of a conductor is an equipotential surface, i.e., the electrostatic potential on it is constant. As a consequence, the electric field outside the conductor is normal to the surface in a vicinity of it.

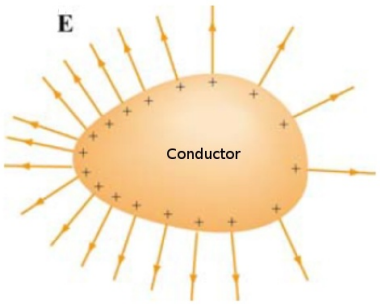

Figure 2.4: Electric field lines near the surface of a conductor.

Suppose that we introduce a conductor inside an external electric field $\mathbf{E}_0$ generated by a capacitor (for example in the middle of two parallel plates subject to a potential difference). Then the charge distributes over the surface so that the electric field that they generate cancels the effect of $\mathbf{E}_0$ inside the conductor. If $\mathbf{E}'$ is the field generated by the surface charge density on the conductor then, by the superposition principle, the total electric field is:

$$\mathbf{E} = \mathbf{E}_0 + \mathbf{E}' \ .$$

We know that:

$$\mathbf{E}_{inside} = \mathbf{0} \quad \Rightarrow \quad \mathbf{E}_{0,inside} = -\mathbf{E}'_{inside} \ .$$

What is the electric field, $\mathbf{E}_{outside}$, just outside the conductor? Consider a surface patch with area dA and take a symmetric cylinder $\mathcal{P}$ with respect to this patch of infinitesimal height that traverses the surface of the conductor and whose cross section coincides with that of the patch (this cylinder is called a *gaussian pillbox*). Using Gauss' law over that cylinder one gets:

$$\frac{Q_{\ inside\ \mathcal{P}}}{\varepsilon_0} \equiv \frac{\sigma dA}{\varepsilon_0} = \int_{\mathcal{P}} \mathbf{E}\cdot d\mathbf{S} = E_{n,outside}\ dA = \quad \Rightarrow \quad E_{n,outside} = \frac{\sigma}{\varepsilon_0} \quad \Rightarrow \quad \mathbf{E}_{outside} = \frac{\sigma}{\varepsilon_0}\hat{\mathbf{n}} \ ,$$

where σ is the surface charge density, ε_0 the permittivity of free space and $\hat{\mathbf{n}}$ the outward unit normal to the surface. Observe that the normal component of $\mathbf{E}$ exhibits a discontinuity at the surface of the conductor, and that the discontinuity jump is:

$$[E_n] = E_{n,outside} - E_{n,inside} = \frac{\sigma}{\varepsilon_0} - 0 = \frac{\sigma}{\varepsilon_0} \, .$$

2.2.1. Relating curvature and charge density

One of the singularity formation processes studied in this thesis are Taylor cones, where interface curvature and surface charge density values are both very high. The purpose of this section is to show with an example how this two quantities are intrinsically related. The best way to illustrate this at the surface of a conductor is to analyze the case where one has two conducting spheres of radii R_1 and R_2 joined by a conducting wire. Since they are connected, both spheres have the same electrostatic potential. Using the formula for the potential of a sphere we get:

$$\mathcal{V}_1 = \frac{Q_1}{4\pi\varepsilon_0 R_1} = \mathcal{V}_2 = \frac{Q_2}{4\pi\varepsilon_0 R_2} \, ,$$

where Q_1 and Q_2 are the charge values for the spheres respectively. Then:

$$\frac{Q_1}{R_1} = \frac{Q_2}{R_2} \, .$$

We also know that the electric field generated by the spheres on their surface is given by:

$$E_1 = \frac{Q_1}{4\pi R_1^2 \varepsilon_0} = \frac{\sigma_1}{\varepsilon_0} \quad , \quad E_2 = \frac{Q_2}{4\pi R_2^2 \varepsilon_0} = \frac{\sigma_2}{\varepsilon_0} \, .$$

So the relation yields:

$$\frac{\sigma_1}{\sigma_2} = \frac{Q_1 R_2^2}{Q_2 R_1^2} = \frac{R_2}{R_1} \, ,$$

from which we can conclude that the regions with small radii of curvature (high curvature values) have high surface charge density values, making the electric field stronger there.

2.2.2. Electrostatic force on a conductor

In this subsection we derive the electrostatic force experienced by a conducting object due to the charge stored on its surface. Consider a surface patch of charge, the total electric field can be written as:

$$\mathbf{E} = \mathbf{E}_{patch} + \mathbf{E}' \, ,$$

where $\mathbf{E}_{patch}$ is the electric field generated by the surface patch of charge and $\mathbf{E}'$ is the one created by the other charges located on the surface. The question is: What is the force experienced by the patch due to these other charges? Since by Newton's third law the patch cannot exert a force over itself, then:

$$\mathbf{F}_{patch} = Q_{patch}\mathbf{E}' = \sigma_{patch} A_{patch} \mathbf{E}' \, .$$

Now, the force per unit area acting on the patch is:

$$\mathbf{F} \equiv \frac{\mathbf{F}_{patch}}{A_{patch}} = \sigma_{patch}\mathbf{E}'$$

To compute $\mathbf{E}'$, given that the outward unit normal to the patch is $\mathbf{n}$, consider again a gaussian pillbox $\mathcal{P}$ centered at the patch. Using Gauss' law in that region:

$$\frac{Q_{patch}}{\varepsilon_0} \equiv \frac{A_{patch}\sigma_{patch}}{\varepsilon_0} = \int_{\mathcal{P}} \mathbf{E}_{patch} \cdot d\mathbf{S} = A_{patch}\mathbf{E}_{patch,above} \cdot \mathbf{n} - A_{patch}\mathbf{E}_{patch,below} \cdot \mathbf{n} \, .$$

By a symmetry argument, the electric field created by the patch has to be the same with a sign change at a fixed distance above and below it:

$$\mathbf{E}_{patch,above} = -\mathbf{E}_{patch,below} \, .$$

Therefore, we have:

$$\frac{A_{patch}\sigma_{patch}}{\varepsilon_0} = 2A_{patch}\mathbf{E}_{patch,above}\cdot\mathbf{n} \quad \Rightarrow \quad \mathbf{E}_{patch,above} = \frac{\sigma_{patch}}{2\varepsilon_0}\mathbf{n}\,,$$

and the electric field created by the patch is discontinuous on its surface since:

$$[\mathbf{E}_{patch}] = \mathbf{E}_{patch,above} - \mathbf{E}_{patch,below} = \frac{\sigma_{patch}}{\varepsilon_0}\mathbf{n}\,.$$

Using the expressions:

$$\mathbf{E}_{patch,below} = -\frac{\sigma_{patch}}{2\varepsilon_0}\mathbf{n} \quad , \quad \mathbf{E}_{patch,above} = \frac{\sigma_{patch}}{2\varepsilon_0}\mathbf{n}\,,$$

we get:

$$\mathbf{E}_{above} = \frac{\sigma_{patch}}{2\varepsilon_0}\mathbf{n} + \mathbf{E}' \quad , \quad \mathbf{E}_{below} = -\frac{\sigma_{patch}}{2\varepsilon_0}\mathbf{n} + \mathbf{E}' \quad , \quad \mathbf{E}' = \frac{\mathbf{E}_{above} + \mathbf{E}_{below}}{2}\,.$$

and since we are working with a conducting object:

$$\mathbf{E}_{above} = \frac{\sigma_{patch}}{\varepsilon_0}\mathbf{n} \quad , \quad \mathbf{E}_{below} = \mathbf{0} \quad \Rightarrow \quad \mathbf{E}' = \frac{\sigma_{patch}}{2\varepsilon_0}\mathbf{n}\,.$$

Consequently, the electrostatic force per unit area (or electrostatic pressure) is:

$$\mathbf{F} = \frac{\sigma_{patch}^2}{2\varepsilon_0}\mathbf{n}\,. \tag{2.13}$$

2.2.3. Electrostatic potential energy of a conductor

Later in this thesis, we will use an energy minimization argument that requires the expression for the amount of energy stored by a conductor. In what follows, a derivation of this energy is given in detail. Consider a volume charge density ρ and a conservative electric field ($\mathbf{E} = -\nabla\mathcal{V}$). The electric potential over a region $\Omega \subset \mathbb{R}^3$ is described by the integral equation:

$$\mathcal{V}(\mathbf{x}') = \frac{1}{4\pi\varepsilon_0}\int_\Omega \frac{\rho(\mathbf{x})}{\|\mathbf{x}-\mathbf{x}'\|}\,d\mathbf{x}\,. \tag{2.14}$$

The electrostatic potential energy is given by:

$$\mathcal{W} = \frac{1}{2}\int_\Omega \rho(\mathbf{x})\,\mathcal{V}(\mathbf{x})\;d\mathbf{x} = \frac{\varepsilon_0}{2}\int_\Omega \nabla\cdot(\mathbf{E}(\mathbf{x}))\,\mathcal{V}(\mathbf{x})\;d\mathbf{x} = \frac{\varepsilon_0}{2}\left(\int_{\partial\Omega}\mathcal{V}(\mathbf{x})\,\mathbf{E}(\mathbf{x})\cdot d\mathbf{S} + \int_\Omega \|\mathbf{E}\|^2\;d\mathbf{x}\right)\,.$$

Now, take $\Omega = B_r(\mathbf{0})$ and make its radius tend to infinity. We know that in general, the electric field far from a bounded charge distribution behaves like the field generated by a point charge, decaying like r^{-2}. Similarly, the electric potential decays like r^{-1} and the surface area of a sphere grows like r^2. Then:

$$\int_{\partial B_r(\mathbf{0})}\mathcal{V}(\mathbf{x})\,\mathbf{E}(\mathbf{x})\cdot d\mathbf{S} \sim \frac{1}{r}\;\to 0 \quad \text{when } r\to\infty\,,$$

so the electrostatic energy is:

$$\mathcal{W} = \frac{\varepsilon_0}{2}\int_{\mathbb{R}^3}\|\mathbf{E}\|^2\;d\mathbf{x}\,, \tag{2.15}$$

which tells us that the electrostatic energy for a charge distribution is stored in the electric field it creates. Now, given a conductor that occupies a region $\mathcal{D} \subset \mathbb{R}^3$ with surface charge density σ, consider its electrostatic energy. Since $\mathbf{E} = \mathbf{0}$ inside $\mathcal{D}$ we have that, using the first Green identity, taking the outward unit normal vector $\mathbf{n}$ to $\mathcal{D}$ and that:

$$\sigma = -\varepsilon_0\frac{\partial\mathcal{V}}{\partial\mathbf{n}}\,, \tag{2.16}$$

one gets:

$$\mathcal{W} = \frac{\varepsilon_0}{2}\int_{\mathbb{R}^3\setminus\mathcal{D}}\|\mathbf{E}\|^2\;d\mathbf{x} = -\frac{\varepsilon_0}{2}\left(\int_{\mathbb{R}^3\setminus\mathcal{D}}\mathcal{V}\Delta\mathcal{V}\,d\mathbf{x} + \int_{\partial\mathcal{D}}\mathcal{V}\frac{\partial\mathcal{V}}{\partial\mathbf{n}}\,dS\right) = \frac{1}{2}\int_{\partial\mathcal{D}}\mathcal{V}_0\,\sigma\,d\mathbf{x} = \frac{1}{2}Q\mathcal{V}_0 = \frac{Q^2}{2\mathcal{C}}\,,$$

where we have used that $\mathcal{V}$ is harmonic outside $\mathcal{D}$, the total charge stored on the surface of the conductor is Q, $\mathcal{V}_0$ is the value for the electric potential on the surface and $\mathcal{C}$ is the capacitance, defined as follows:

$$\mathcal{C} = -\frac{\epsilon_0}{\mathcal{V}_0}\int_{\partial\mathcal{D}}\frac{\partial\mathcal{V}}{\partial\mathbf{n}}\,dS = \frac{1}{\mathcal{V}_0}\int_{\partial\mathcal{D}}\sigma\,dS = \frac{Q}{\mathcal{V}_0}\,. \tag{2.17}$$

2.3. Capillary forces

This section is devoted to introducing capillary forces (originated due to surface tension) present at the interface of two fluids. Surface tension is a phenomenon by which the interface between two immiscible fluids behaves like a thin elastic film. Although similar situations arise in systems of the liquid-gas type (for example, the free surface between the atmosphere and seawater) out interest lies in the liquid-liquid case. This analogy was introduced by Young in 1805 and has since become a cornerstone to the theory of capillary phenomena. Surface tension forces have units of force per unit length or energy per unit area and their main purpose is to minimize the contact surface area between the fluids involved. These capillary forces come from cohesive and repulsive intermolecular forces and act only on the interface for the following reason: if we choose a molecule from the bulk of a fluid, the net force acting on it is zero, as all neighboring molecules exert forces which cancel by symmetry. However, for an interface molecule, such molecule is subject to a net force inwards as it is not completely surrounded by other molecules of the same fluid. An interesting result related to surface tension is the spherical shape that fluid droplets take in the absence of external forces such as gravity. The system assumes this form because the sphere encloses a given volume with the smallest surface area. Also, capillary forces are used by many insects to their benefit in order to stand on top of liquids.

Given an interface between two fluids, its surface energy is defined as:

$$E_{area} = \gamma \mathcal{A} \, ,$$

where $\mathcal{A}$ is the interfacial area and $\gamma > 0$ is the surface tension coefficient for the interaction of both fluids, whose magnitude depends fundamentally on the temperature and physical properties of the fluids in contact. For gas-liquid systems, the highest values of surface tension correspond to liquid metals, such as mercury with $\gamma_{_{Hg}} \sim 500$ dynes/cm. For non-metallic fluids, water has one of the highest surface tension coefficients, $\gamma_{_{H_2O}} \sim 70$ dynes/cm.

To derive the tangential and normal boundary conditions for the capillary surface between two fluids, characterized by a surface tension coefficient γ, consider a patch of interface denoted by $\mathcal{S}$ and delimited by the closed curve Γ. Suppose that for each point in the curve there exists a force acting in the binormal direction $\mathbf{b} = \mathbf{t} \times \mathbf{n}$ that tends to flatten $\mathcal{S}$, where $\mathbf{t}$ is the unit tangent vector to the curve and $\mathbf{n}$ the unit normal vector to the interface pointing from fluid 1 into fluid 2. Then, the following balance of forces must hold over $\mathcal{S}$:

$$\int_{\mathcal{S}} \left(\widetilde{T}^{(1)} \hat{\mathbf{n}} + \widetilde{T}^{(2)} \mathbf{n} \right) \, dS + \int_{\Gamma} \gamma \mathbf{b} \, dl = 0 \, ,$$

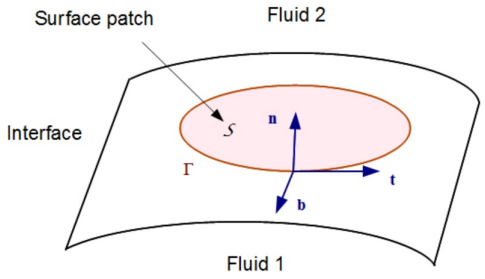

Figure 2.5: Surface tension acting on a patch of interface between two fluids.

where $\hat{\mathbf{n}} = -\mathbf{n}$ and the stress tensors satisfy:

$$\int_{\mathcal{S}} \widetilde{T}^{(1)} \hat{\mathbf{n}} \, dS \equiv \text{ hydrodynamic force exerted by fluid 1 on the interface} \, ,$$

$$\int_{\mathcal{S}} \widetilde{T}^{(2)} \mathbf{n} \, dS \equiv \text{ hydrodynamic force exerted by fluid 2 on the interface} \, .$$

Then:

$$\int_{\mathcal{S}} \left(\widetilde{T}^{(2)} - \widetilde{T}^{(1)} \right) \mathbf{n} \, dS + \int_{\Gamma} \gamma \mathbf{b} \, dl = 0 \, .$$

Now, Stokes theorem says that:

$$\int_\Gamma \mathbf{F} \cdot \ d\mathbf{l} \equiv \int_\Gamma \mathbf{F} \cdot \mathbf{t} \ dl = \int_\mathcal{S} \mathbf{n} \cdot (\nabla \times \mathbf{F}) \ dS \ .$$

If we take $\mathbf{F} = \mathbf{f} \times \mathbf{d}$ where $\mathbf{d}$ is an arbitrary constant vector:

$$\mathbf{d} \cdot \int_\Gamma (\mathbf{f} \times \mathbf{t}) \ dl = \mathbf{d} \cdot \int_\mathcal{S} (\mathbf{n}\nabla \cdot \mathbf{f} - \nabla \mathbf{f} \cdot \mathbf{n}) \ dS \ .$$

Since $\mathbf{d}$ is arbitrary:

$$\int_\Gamma (\mathbf{f} \times \mathbf{t}) \ dl = \int_\mathcal{S} (\mathbf{n}\nabla \cdot \mathbf{f} - \nabla \mathbf{f} \cdot \mathbf{n}) \ dS \ .$$

Taking $\mathbf{f} = \gamma \mathbf{n}$ and using:

$$(\nabla \mathbf{n}) \, \mathbf{n} = \frac{1}{2} \nabla \left(\mathbf{n} \cdot \mathbf{n} \right) = \frac{1}{2} \nabla \left(1 \right) = 0 \ ,$$

yields:

$$\int_\Gamma \gamma \mathbf{b} \ dl = \int_\mathcal{S} \left(\left(\mathbb{I} - \mathbf{n} \otimes \mathbf{n} \right) \nabla \gamma - \gamma \mathbf{n} \nabla \cdot \mathbf{n} \right) \ dS \ .$$

Therefore, the balance of stresses can be written as:

$$\int_\mathcal{S} \left(\widetilde{T}^{(2)} - \widetilde{T}^{(1)} \right) \mathbf{n} \ dS = \int_\mathcal{S} \left(\gamma \mathbf{n} \nabla \cdot \mathbf{n} - \left(\mathbb{I} - \mathbf{n} \otimes \mathbf{n} \right) \nabla \gamma \right) \ dS \ ,$$

or equivalently:

$$\left(\widetilde{T}^{(2)} - \widetilde{T}^{(1)} \right) \mathbf{n} = \gamma \mathbf{n} \nabla \cdot \mathbf{n} - \left(\mathbb{I} - \mathbf{n} \otimes \mathbf{n} \right) \nabla \gamma \ .$$

The projection matrix $\mathbb{I} - \mathbf{n} \otimes \mathbf{n}$ extracts the tangential component of any vector, giving:

$$\left(\widetilde{T}^{(2)} - \widetilde{T}^{(1)} \right) \mathbf{n} = \gamma \mathbf{n} \nabla \cdot \mathbf{n} - \nabla_s \gamma \ ,$$

where ∇_s is the surface gradient:

$$\nabla_s \gamma \equiv \left(\mathbb{I} - \mathbf{n} \otimes \mathbf{n} \right) \nabla \gamma = \nabla \gamma - \frac{\partial \gamma}{\partial \mathbf{n}} \mathbf{n} \ .$$

The normal component of the stress balance is:

$$\mathbf{n} \cdot \left(\widetilde{T}^{(2)} - \widetilde{T}^{(1)} \right) \mathbf{n} = \gamma \nabla \cdot \mathbf{n} \ ,$$

and since $\nabla \cdot \mathbf{n} = 2\mathcal{H}$ (see [19] and [48]), one can write:

$$\mathbf{n} \cdot \left(\widetilde{T}^{(2)} - \widetilde{T}^{(1)} \right) \mathbf{n} = 2\gamma \mathcal{H} \ , \tag{2.18}$$

where $\mathcal{H}$ is the mean curvature of the interface[1]. Now, the tangential component of the stress balance is:

$$\mathbf{t} \cdot \left(\widetilde{T}^{(2)} - \widetilde{T}^{(1)} \right) \mathbf{n} = -\nabla_s \gamma \cdot \mathbf{t} \ ,$$

representing the Marangoni forces produced by the surface tension gradients at the interface of the drop. In our model the surface tension is considered to be constant and thus Marangoni forces are not present:

$$\mathbf{t} \cdot \left(\widetilde{T}^{(2)} - \widetilde{T}^{(1)} \right) \mathbf{n} = 0 \ .$$

Observe that decomposing the gradient into its tangential and normal components:

$$\nabla = \nabla_s + \nabla_n \quad , \quad \nabla_n = \mathbf{n} \left(\mathbf{n} \cdot \nabla \right) \quad , \quad \nabla_s = \nabla - \nabla_n = \left(\mathbb{I} - \mathbf{n} \otimes \mathbf{n} \right) \nabla \ ,$$

[1]The mean curvature is a geometric measure of how much a surface deviates from being flat. The criterion that we have established for its sign is that the mean curvature is positive in those points where the surface curves away from the unit normal.

then:

$$\nabla \cdot \mathbf{n} = (\nabla_s + \nabla_n) \cdot \mathbf{n} = \nabla_s \cdot \mathbf{n} + \nabla_n \cdot \mathbf{n} = \nabla_s \cdot \mathbf{n} \, ,$$

since $\nabla_n \cdot \mathbf{n} = 0$ and consequently we can substitute the gradient with the surface gradient when computing the divergence of the normal vector. Associated to surface tension, one has Young-Laplace equation establishing the pressure difference sustained across the interface between two stationary fluids. It is used in the study of capillary equilibrium surfaces and is the stationary version of (2.18):

$$\delta p \equiv p^{(1)} - p^{(2)} = 2\gamma H = \gamma \left(\frac{1}{R_1} + \frac{1}{R_2} \right) \, , \tag{2.19}$$

where δp is the pressure difference and R_1 and R_2 are the principal radii of curvature of the interface.

2.4. The drop model

We are interested in the evolution, stability and equilibrium configurations of a viscous and conducting drop surrounded by another viscous and insulating fluid when both fluids rotate about a common axis (i.e. the z axis) with angular velocity $\boldsymbol{\omega}(t) = \omega(t)\mathbf{k}$. Working in a rotating frame, Navier-Stokes equations for an incompressible fluid with viscosity μ_i, density ϱ_i, reduced pressure $\Pi^{(i)}$ and velocity field $\mathbf{u}^{(i)}$ are:

$$\begin{cases} \varrho_i \left(\dfrac{\partial \mathbf{u}^{(i)}}{\partial t} + \mathbf{u}^{(i)} \cdot \nabla \mathbf{u}^{(i)} \right) = -\nabla \Pi^{(i)} + \mu_i \Delta \mathbf{u}^{(i)} - 2\varrho_i \, \boldsymbol{\omega} \times \mathbf{u}^{(i)} \quad , \quad \text{in } \mathcal{D}_i(t) \\ \nabla \cdot \mathbf{u}^{(i)} = 0 \quad , \quad \text{in } \mathcal{D}_i(t) \end{cases} \, , \tag{2.20}$$

where $\mathcal{D}_1(t)$ is the region enclosed by the droplet and $\mathcal{D}_2(t)$ that of the surrounding fluid.

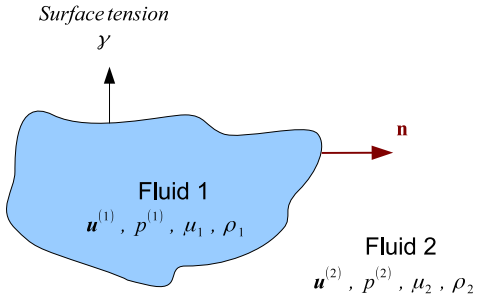

Figure 2.6: Physical properties for the drop and the surrounding fluid.

In the absence of body forces, $\mathbf{F}_b \equiv \mathbf{0}$, the reduced pressure (2.6) in cylindrical coordinates is:

$$\Pi^{(i)} = p^{(i)} - \frac{\varrho_i}{2} \left\| \boldsymbol{\omega} \times \mathbf{x} \right\|^2 = p^{(i)} - \frac{\varrho_i}{2} \left\| \boldsymbol{\omega} \right\|^2 \left\| \mathbf{x} \right\|^2 \sin^2 \theta = p^{(i)} - \frac{\varrho_i}{2} \omega^2 r_{axis}^2 \quad , \quad i \in \{1, 2\} \, , \tag{2.21}$$

where $p^{(i)}$ is the pressure and r_{axis} the distance from point $\mathbf{x}$ to the axis of rotation. Introducing the droplet's angular momentum $\mathcal{L}$ one gets:

$$\Pi^{(i)} = p^{(i)} - \varrho_i \frac{\mathcal{L}^2}{2\mathcal{I}^2} r_{axis}^2 \quad , \quad i \in \{1, 2\} \, . \tag{2.22}$$

where $\mathcal{I}$ is the moment of inertia of the drop:

$$\mathcal{I} = \varrho_1 \int_{\mathcal{D}_1(t)} r_{axis}^2 \, d\mathbf{x} \, . \tag{2.23}$$

and the relation between the angular velocity and angular momentum is given by:

$$\mathcal{L} = \mathcal{I} \boldsymbol{\omega} \, . \tag{2.24}$$

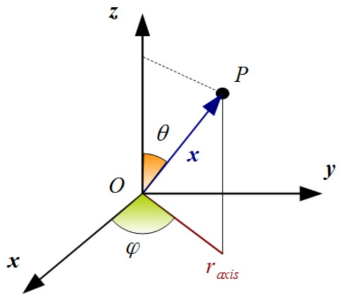

Figure 2.7: Cylindrical coordinate system.

To non-dimensionalize (2.20), take a characteristic length l, velocity U and time scale $\tau = l/U$ so that:

$$\overline{\mathbf{u}}^{(i)} = \frac{\mathbf{u}^{(i)}}{U} \quad , \quad \overline{\mathbf{x}} = \frac{\mathbf{x}}{l} \quad , \quad \overline{t} = \frac{t}{\tau} \quad , \quad \overline{\Pi}^{(i)} = \frac{l}{\mu_1 U}\Pi^{(i)} \quad , \quad \boldsymbol{\omega} = \omega\mathbf{k} \quad , \quad \lambda = \frac{\mu_2}{\mu_1} \quad , \quad \zeta = \frac{\rho_2}{\rho_1} \, . \tag{2.25}$$

Omitting overbars to simplify notation, the non-dimensional problem is:

$$\begin{cases} \zeta^{i-1} Re \left(\dfrac{\partial \mathbf{u}^{(i)}}{\partial t} + \mathbf{u}^{(i)} \cdot \nabla \mathbf{u}^{(i)} \right) = -\nabla \Pi^{(i)} + \lambda^{i-1} \Delta \mathbf{u}^{(i)} - 2\dfrac{\zeta^{i-1}}{Ek} \mathbf{k} \times \mathbf{u}^{(i)} \quad , \quad \text{in } \mathcal{D}_i(t) \\ \nabla \cdot \mathbf{u}^{(i)} = 0 \quad , \quad \text{in } \mathcal{D}_i(t) \end{cases} , \tag{2.26}$$

where the Reynolds and Ekman numbers appear:

$$Re = \frac{\varrho_1 U l}{\mu_1} \quad , \quad Ek = \frac{\mu_1}{\varrho_1 \omega l^2} \, , \tag{2.27}$$

We will study regimes where viscous forces dominate inertial and Coriolis forces, known in the literature as Stokes or creeping flows. They occur when $Re \ll 1$ and $Ek \gg 1$, giving:

$$\begin{cases} -\nabla \Pi^{(i)} + \lambda^{i-1} \Delta \mathbf{u}^{(i)} = \mathbf{0} \quad , \quad \text{in } \mathcal{D}_i(t) \\ \nabla \cdot \mathbf{u}^{(i)} = 0 \quad , \quad \text{in } \mathcal{D}_i(t) \end{cases} , \tag{2.28}$$

to which we impose that the normal component of the velocity is continuous across the boundary:

$$\mathbf{u}^{(1)} \cdot \mathbf{n} = \mathbf{u}^{(2)} \cdot \mathbf{n} \quad , \quad \text{on} \quad \partial\mathcal{D}(t) \, , \tag{2.29}$$

and the kinematic condition:

$$u_n = \mathbf{u} \cdot \mathbf{n} \quad , \quad \text{on} \quad \partial\mathcal{D}(t) \, , \tag{2.30}$$

with u_n being the normal velocity of the free boundary and $\mathbf{n}$ the outward unit normal to the drop.

Now, since the drop is considered an ideal conductor, the electric potential $\mathcal{V}$ must be constant inside the drop and on its surface, and all the charge Q distributes over the boundary. Considering an external electric field of magnitude $\mathcal{E}_\infty$ applied to the drop in the direction of its rotation acis, the electric potential satisfies the following Laplace problem:

$$\begin{cases} \Delta \mathcal{V} = 0 \quad , \quad \text{in } \mathcal{D}_2(t) \\ \mathcal{V} = \mathcal{V}_0 \quad , \quad \text{on } \partial\mathcal{D}(t) \\ \mathcal{V} \to -\mathcal{E}_\infty z + O\left(r^{-1}\right) \quad , \quad \text{as } r \to \infty \end{cases} , \tag{2.31}$$

where $r = \|\mathbf{x}\|$ and $\mathcal{V}_0$ has to be chosen so that the total charge is Q. At the drop's interface, the surface charge density σ is proportional to the normal derivative of the potential:

$$\sigma = -\varepsilon_0 \frac{\partial \mathcal{V}}{\partial \mathbf{n}} \, , \tag{2.32}$$

with ε_0 the permittivity of the surrounding fluid. To solve (2.28) we need to impose a boundary condition, which is a balance of stresses between viscous, capillary, electrostatic and centrifugal forces at the interface of both fluids. Since at the surface of a conductor the repulsive electrostatic force per unit area is given by:

$$\mathbf{F}_e = \frac{\varepsilon_0}{2}\left(\frac{\partial \mathcal{V}}{\partial \mathbf{n}}\right)^2 \mathbf{n} = \frac{\sigma^2}{2\varepsilon_0}\mathbf{n}\,,$$

the balance is:

$$\left(T^{(2)} - T^{(1)}\right)\mathbf{n} = \left(2\gamma\mathcal{H} - \Delta\varrho\frac{\mathcal{L}^2}{2\mathcal{I}^2}r_{axis}^2 - \frac{\sigma^2}{2\varepsilon_0}\right)\mathbf{n} \quad , \quad \text{on } \partial\mathcal{D}\,(t)\ , \tag{2.33}$$

or written in terms of the angular speed:

$$\left(T^{(2)} - T^{(1)}\right)\mathbf{n} = \left(2\gamma\mathcal{H} - \Delta\varrho\frac{\omega^2}{2}r_{axis}^2 - \frac{\sigma^2}{2\varepsilon_0}\right)\mathbf{n} \quad , \quad \text{on } \partial\mathcal{D}\,(t)\ , \tag{2.34}$$

where $\Delta\varrho = \varrho_1 - \varrho_2$ is the density difference, γ the surface tension and $\mathcal{H}$ the mean curvature. The stress tensor has the form:

$$T_{ij}^{(k)} = -\Pi^{(k)}\delta_{ij} + \mu_k\left(\frac{\partial u_i^{(k)}}{\partial x_j} + \frac{\partial u_j^{(k)}}{\partial x_i}\right) \quad , \quad k \in \{1,2\}\ . \tag{2.35}$$

To make the boundary conditions (2.33) and (2.34) dimensionless, introduce the characteristic scales:

$$l = \sqrt[3]{V_0} \quad , \quad U = \frac{\gamma}{\mu_1} \quad , \quad \tau = \frac{l}{U}\,, \tag{2.36}$$

and the quantities:

$$\overline{T}^{\,(i)} = \frac{l}{\gamma}T^{(i)} \quad , \quad \overline{r}_{axis} = \frac{r_{axis}}{l} \quad , \quad \overline{\mathcal{H}} = l\mathcal{H} \quad , \quad \overline{\mathcal{I}} = \frac{\mathcal{I}}{l^5\varrho_1} \quad , \quad \overline{\sigma} = \sqrt{\frac{l}{\gamma\varepsilon_0}}\sigma\,, \tag{2.37}$$

where V_0 is the drop's volume. By defining the dimensionless physical quantities:

$$L = \sqrt{\frac{\psi}{\varrho_1 l^7\gamma}}\mathcal{L} \quad , \quad \chi = \frac{\overline{Q}^2}{48\pi} = \frac{Q^2}{48\pi\gamma\varepsilon_0 l^3} \quad , \quad E_\infty = \sqrt{\frac{\varepsilon_0 l}{\gamma}}\mathcal{E}_\infty \quad , \quad \Omega = \sqrt{\frac{\Delta\varrho l^3}{\gamma}}\omega\,, \tag{2.38}$$

with $\psi = 1 - \zeta$, one obtains, omitting overbars, the boundary condition:

$$\left(T^{(2)} - T^{(1)}\right)\mathbf{n} = \left(2\mathcal{H} - \frac{L^2}{2\mathcal{I}^2}r_{axis}^2 - \frac{\sigma^2}{2}\right)\mathbf{n} \quad , \quad \text{on } \partial\mathcal{D}\,(t)\ , \tag{2.39}$$

or in terms of the dimensionless angular speed:

$$\left(T^{(2)} - T^{(1)}\right)\mathbf{n} = \left(2\mathcal{H} - \frac{\Omega^2}{2}r_{axis}^2 - \frac{\sigma^2}{2}\right)\mathbf{n} \quad , \quad \text{on } \partial\mathcal{D}\,(t)\ , \tag{2.40}$$

where χ is known as Rayleigh's fissibility ratio. In this thesis we will describe the results in terms of the parameters in (2.38). Notice that one can easily recover the physical values by solving for $\mathcal{L}$, ω, Q, and $\mathcal{E}_\infty$. Observe also that the process of making the equations nondimensional is not unique, and, in order to compare our results to those by Brown & Scriven [11], the relation between the rotation parameters is:

$$\Omega = 4\sqrt{\frac{2\pi}{3}}\Omega_{BS} \quad , \quad L = 8\sqrt{2}\left(\frac{3}{4\pi}\right)^{\frac{7}{6}}L_{BS}\ .$$

Concerning the stationary problem (i.e. $\mathbf{u}^{(i)}$ is constant), all equilibrium solutions can be calculated by solving the modified Young-Laplace equation:

$$\delta\Pi = 2\gamma\mathcal{H} - \Delta\varrho\frac{\mathcal{L}^2}{2\mathcal{I}^2}r_{axis}^2 - \frac{\sigma^2}{2\varepsilon_0} \quad , \quad \text{on } \partial\mathcal{D}\,, \tag{2.41}$$

or in terms of the angular speed:

$$\delta\Pi = 2\gamma\mathcal{H} - \Delta\varrho\frac{\omega^2}{2}r_{axis}^2 - \frac{\sigma^2}{2\varepsilon_0} \quad , \quad \text{on } \partial\mathcal{D} \, , \tag{2.42}$$

where $\mathcal{D}$ is the region enclosed by the drop and $\delta\Pi = \Pi^{(1)} - \Pi^{(2)}$ is the reduced pressure difference across the drop's surface. Notice that this equation is the Euler-Lagrange equation of a particular energy functional. In a variational framework, our problem reduces to the minimization of the total energy for the closed system:

$$E_{total} = E_{area} \pm E_{kinetic} + \mathcal{W} - \delta\Pi\left(V - V_0\right) \, , \tag{2.43}$$

where $\delta\Pi\left(V - V_0\right)$ is the constraint ($\delta\Pi$ plays the role of a Lagrange multiplier) so the volume of the drop is V_0, E_{area} is the energy due to surface area, $E_{kinetic}$ is the rotational kinetic energy (plus or minus sign applied for constant angular momentum or constant angular speed rotation respectively) and $\mathcal{W}$ is the electrostatic energy. These energies can be obtained from:

$$E_{area} = \gamma\mathcal{A}_d \quad , \quad E_{kinetic} = \psi\frac{\mathcal{L}^2}{2\mathcal{I}} = \psi\frac{\omega^2}{2}\mathcal{I} \quad , \quad \mathcal{W} = \frac{\varepsilon_0}{2}\int_{\mathbb{R}^3\setminus\mathcal{D}} \|\mathbf{E}\|^2 \, d\mathbf{x} \, , \tag{2.44}$$

where $\mathcal{A}_d$ is the droplet's surface area. Since the electric field is conservative, $\mathbf{E} = -\nabla\mathcal{V}$, integrating by parts one can write the electrostatic energy as:

$$\mathcal{W} = \frac{\varepsilon_0}{2}\int_{\mathbb{R}^3\setminus\mathcal{D}} \|\mathbf{E}\|^2 \, d\mathbf{x} = -\frac{\varepsilon_0}{2}\int_{\partial\mathcal{D}} \mathcal{V}\frac{\partial\mathcal{V}}{\partial\mathbf{n}} \, dS = \frac{1}{2}\int_{\partial\mathcal{D}} \mathcal{V}_0\sigma \, d\mathbf{x} = \frac{1}{2}Q\mathcal{V}_0 = \frac{Q^2}{2\mathcal{C}} \, , \tag{2.45}$$

where $\mathcal{C}$ is the capacitance of the drop:

$$\mathcal{C} = -\frac{\epsilon_0}{\mathcal{V}_0}\int_{\partial\mathcal{D}} \frac{\partial\mathcal{V}}{\partial\mathbf{n}} \, dS = \frac{1}{\mathcal{V}_0}\int_{\partial\mathcal{D}} \sigma \, dS = \frac{Q}{\mathcal{V}_0} \, . \tag{2.46}$$

Chapter 3

The boundary integral formulation

Once we have introduced the equations governing the evolution of a rotating drop, this chapter focuses on the derivation of a boundary integral representation formula for the velocity field at the droplet's interface. This integral equation will be approximated numerically by means of the BEM later in this thesis to study the evolution and stability of rotating drops and the effects of rotation on charged droplets or neutral drops subject to an external electric field.

3.1. Green's functions for Stokes flow

In this section we derive the fundamental solutions for Stokes equation using the Fourier transform method explained in the appendix of this thesis. These solutions are the building blocks needed in the next sections to obtain the boundary integral formulation. Recall the system of PDEs:

$$(\mathcal{P}_{\mathcal{S}}) \quad \begin{cases} \mu\Delta\mathbf{u} - \nabla\Pi = \mathbf{f} \\ \nabla\cdot\mathbf{u} = 0 \end{cases} \quad , \quad \text{in } \mathbb{R}^3 \, . \tag{3.1}$$

To calculate the Green's functions for (3.1) consider the following fundamental problem:

$$\left(\mathcal{P}_{\mathcal{S}}^{\mathcal{F}}\right) \quad \begin{cases} \mu\Delta\mathbf{u} - \nabla\Pi = -\mathbf{b}\,\delta_{\mathbf{x}_0} \\ \nabla\cdot\mathbf{u} = 0 \end{cases} \quad , \quad \text{in } \mathbb{R}^3 \, . \tag{3.2}$$

Physically, the solution to this problem represents the flow in an infinite region obtained by applying a point force at $\mathbf{x}_0$ with direction $\mathbf{b}$ (represented by a Dirac's delta function). We can decompose this problem into three subproblems in the form:

$$\left(\mathcal{P}_{\mathcal{S}}^{\mathcal{F}}\right)_k \quad \begin{cases} \mu\Delta\mathbb{G}_k - \nabla\mathbb{P}_k = -\delta_{\mathbf{x}_0}\mathbf{e}_k \\ \nabla\cdot\mathbb{G}_k = \mathbf{0} \end{cases} \quad , \quad \text{in } \mathbb{R}^3 \quad , \quad k \in \{1,2,3\} \, ,$$

allowing us to write the solution of $\left(\mathcal{P}_{\mathcal{S}}^{\mathcal{F}}\right)$ as:

$$\mathbf{u} = \mathbb{G}\mathbf{b} \quad (\Leftrightarrow \quad u_j = \mathbb{G}_{jk}b_k) \quad , \quad \Pi = \mathbb{P}\cdot\mathbf{b} \quad (\Leftrightarrow \quad \Pi = \mathbb{P}_k b_k) \, .$$

Taking Fourier transforms in $\left(\mathcal{P}_{\mathcal{S}}^{\mathcal{F}}\right)_k$ one gets:

$$\begin{cases} -\mu\left\|\boldsymbol{\xi}\right\|^2 \mathcal{F}\left(\mathbb{G}_{jk}\right) - i\xi_j \mathcal{F}\left(\mathbb{P}_k\right) = -\delta_{jk}\dfrac{e^{\,-i\,\boldsymbol{\xi}\cdot\mathbf{x}_0}}{(2\pi)^{\frac{3}{2}}} \\ \xi_j \mathcal{F}\left(\mathbb{G}_{jk}\right) = 0 \end{cases} \quad , \quad k,j \in \{1,2,3\} \, .$$

Solving the first equation:

$$\mathcal{F}\left(\mathbb{G}_{jk}\right) = \frac{1}{\mu\left\|\boldsymbol{\xi}\right\|^2}\left(\delta_{jk}\frac{e^{\,-i\,\boldsymbol{\xi}\cdot\mathbf{x}_0}}{(2\pi)^{\frac{3}{2}}} - i\xi_j\mathcal{F}\left(\mathbb{P}_k\right)\right) \, ,$$

and substituting it in the second gives:

$$0 = \frac{\xi_j}{\mu \left\|\boldsymbol{\xi}\right\|^2}\left(\delta_{jk}\frac{e^{\,-i\,\boldsymbol{\xi}\cdot\mathbf{x}_0}}{(2\pi)^{\frac{3}{2}}} - i\xi_j \mathcal{F}\left(\mathbb{P}_k\right)\right) = \frac{1}{\mu \left\|\boldsymbol{\xi}\right\|^2}\left(\xi_k\frac{e^{\,-i\,\boldsymbol{\xi}\cdot\mathbf{x}_0}}{(2\pi)^{\frac{3}{2}}} - i\left\|\boldsymbol{\xi}\right\|^2 \mathcal{F}\left(\mathbb{P}_k\right)\right) .$$

Then:

$$\mathcal{F}\left(\mathbb{P}_k\right) = -\frac{i\xi_k\, e^{\,-i\,\boldsymbol{\xi}\cdot\mathbf{x}_0}}{(2\pi)^{\frac{3}{2}}\left\|\boldsymbol{\xi}\right\|^2} \quad , \quad \mathcal{F}\left(\mathbb{G}_{jk}\right) = \frac{1}{\mu\left\|\boldsymbol{\xi}\right\|^2(2\pi)^{\frac{3}{2}}}\left(\delta_{jk} - \frac{\xi_j\xi_k}{\left\|\boldsymbol{\xi}\right\|^2}\right)e^{\,-i\,\boldsymbol{\xi}\cdot\mathbf{x}_0} .$$

If we define $\widehat{\mathbf{x}} = \mathbf{x} - \mathbf{x}_0$ and take inverse transforms:

$$\begin{aligned}
\mathbb{G}_{jk} &= \frac{1}{\mu\,(2\pi)^3}\left(\int_{\mathbb{R}^n}\left(\frac{\delta_{jk}}{\left\|\boldsymbol{\xi}\right\|^2} - \frac{\xi_j\xi_k}{\left\|\boldsymbol{\xi}\right\|^4}\right)e^{\,i\,\boldsymbol{\xi}\cdot\widehat{\mathbf{x}}}\,d\boldsymbol{\xi}\right) = \\
&= \frac{1}{\mu}\left(\delta_{jk}\{\text{Sol. of } -\Delta u = \delta_{\mathbf{x}_0}\} - \frac{\partial^2}{\partial x_j\partial x_k}\left(\{\text{Sol. of } -\Delta^2 u = \delta_{\mathbf{x}_0}\}\right)\right) , \\
\mathbb{P}_k &= -\frac{i}{(2\pi)^3}\int_{\mathbb{R}^n}\frac{\xi_k}{\left\|\boldsymbol{\xi}\right\|^2}\,e^{\,i\,\boldsymbol{\xi}\cdot\widehat{\mathbf{x}}}\,d\boldsymbol{\xi} = -\frac{\partial}{\partial x_k}\left(\{\text{Sol. of } -\Delta u = \delta_{\mathbf{x}_0}\}\right) .
\end{aligned}$$

Using the fundamental solutions for the laplace and biharmonic operators in $\mathbb{R}^3$ one gets:

$$\begin{aligned}
\mathbb{G}_{jk} &= \frac{1}{\mu}\left(\delta_{jk}\frac{1}{4\pi\left\|\widehat{\mathbf{x}}\right\|} - \frac{\partial^2}{\partial x_j\partial x_k}\left(\frac{\left\|\widehat{\mathbf{x}}\right\|}{8\pi}\right)\right) = \frac{1}{8\pi\mu}\left(\frac{\delta_{jk}}{\left\|\widehat{\mathbf{x}}\right\|} + \frac{\widehat{x}_j\widehat{x}_k}{\left\|\widehat{\mathbf{x}}\right\|^3}\right) , \\
\mathbb{P}_k &= -\frac{\partial}{\partial x_k}\left(\frac{1}{4\pi\left\|\widehat{\mathbf{x}}\right\|}\right) = \frac{1}{8\pi}\frac{2\widehat{x}_k}{\left\|\widehat{\mathbf{x}}\right\|^3} .
\end{aligned}$$

To avoid the numerical factors rewrite the solution of (3.2) as:

$$\begin{aligned}
u_j\left(\mathbf{x}\right) &= \frac{1}{8\pi\mu}\mathbb{G}_{jk}\left(\mathbf{x},\mathbf{x}_0\right)b_k \\
\Pi\left(\mathbf{x}\right) &= \frac{1}{8\pi}\mathbb{P}_k\left(\mathbf{x},\mathbf{x}_0\right)b_k
\end{aligned} \quad , \quad j,k\in\{1,2,3\} , \tag{3.3}$$

so the fundamental solutions are:

$$\begin{aligned}
\mathbb{G}_{jk}\left(\mathbf{x},\mathbf{x}_0\right) &= \frac{\delta_{jk}}{\left\|\widehat{\mathbf{x}}\right\|} + \frac{\widehat{x}_j\widehat{x}_k}{\left\|\widehat{\mathbf{x}}\right\|^3} \\
\mathbb{P}_k\left(\mathbf{x},\mathbf{x}_0\right) &= \frac{2\widehat{x}_k}{\left\|\widehat{\mathbf{x}}\right\|^3}
\end{aligned} \quad , \quad j,k\in\{1,2,3\} , \tag{3.4}$$

and satisfy:

$$\Delta\mathbb{G}_{ij}\left(\mathbf{x},\mathbf{x}_0\right) - \frac{\partial\mathbb{P}_j}{\partial x_i}\left(\mathbf{x},\mathbf{x}_0\right) = -8\pi\delta_{ij}\delta_{\mathbf{x}_0}\left(\mathbf{x}\right) . \tag{3.5}$$

The $\mathbb{G}$ kernel is known as Stokeslet (or Oseen-Burger's tensor) and has the symmetry property:

$$\mathbb{G}_{jk}\left(\mathbf{x},\mathbf{x}_0\right) = \mathbb{G}_{kj}\left(\mathbf{x}_0,\mathbf{x}\right) . \tag{3.6}$$

Observe that as a consequence of the incompressibility condition we have:

$$\nabla\cdot\mathbf{u} = 0 \quad \Leftrightarrow \quad \frac{\partial\mathbb{G}_{ij}}{\partial x_i} = 0 \quad \Leftrightarrow \quad \nabla\cdot\mathbb{G} = 0 . \tag{3.7}$$

To finish, the fundamental stress tensor (or Stresslet) in $\mathbb{R}^3$ of a viscous fluid, $\mathbb{T}_{ijk}$, is given by:

$$\mathbb{T}_{ijk}\left(\mathbf{x},\mathbf{x}_0\right) = -\delta_{ik}\mathbb{P}_j + \left(\frac{\partial\mathbb{G}_{ij}}{\partial x_k} + \frac{\partial\mathbb{G}_{kj}}{\partial x_i}\right) = -6\frac{\widehat{x}_i\widehat{x}_j\widehat{x}_k}{\left\|\widehat{\mathbf{x}}\right\|^5} \quad , \quad i,j,k\in\{1,2,3\} , \tag{3.8}$$

allowing us to write:

$$T_{ik}\left(\mathbf{x}\right) = -\delta_{ik}\Pi + \mu\left(\frac{\partial u_i}{\partial x_k} + \frac{\partial u_k}{\partial x_i}\right) = \frac{1}{8\pi}\mathbb{T}_{ijk}\left(\mathbf{x},\mathbf{x}_0\right)b_j .$$

3.2. The integral equation

Our mathematical model establishes that the droplet and the fluid surrounding it are both incompressible and satisfy Stokes equations:

$$\begin{cases} \mu_i \Delta \mathbf{u}^{(i)} - \nabla \Pi^{(i)} = \mathbf{0} & , \quad \text{in } \mathcal{D}_i(t) \\ \nabla \cdot \mathbf{u}^{(i)} = 0 & , \quad \text{in } \mathcal{D}_i(t) \end{cases} \quad , \quad i \in \{1,2\} \ . \tag{3.9}$$

Since the boundary integral formulation is used as a fundamental tool in this work, we have decided to include here, for the sake of clarity and as a reference to the reader, some relevant results necessary to derive it, which are well known in the literature [56].

Theorem 3.1 (Lorentz reciprocal relation)**.** *Consider two incompressible newtonian fluids with velocities* $\mathbf{u}$ *and* $\mathbf{u}'$*, pressures* Π *and* Π'*, viscosities* μ *and* μ' *and stress tensors* Σ *and* Σ'*. Then:*

$$\mu' \left(\mathbf{u}' \cdot (\nabla \cdot \Sigma) \right) - \mu \left(\mathbf{u} \cdot \left(\nabla \cdot \Sigma' \right) \right) = \nabla \cdot \left(\mu' \Sigma \mathbf{u}' - \mu \Sigma' \mathbf{u} \right) \ .$$

Proof. We have:

$$\begin{aligned} \mathbf{u}' \cdot (\nabla \cdot \Sigma) = u_j' \frac{\partial \Sigma_{ij}}{\partial x_i} &= \frac{\partial}{\partial x_i} \left(u_j' \Sigma_{ij} \right) - \Sigma_{ij} \frac{\partial u_j'}{\partial x_i} = \frac{\partial}{\partial x_i} \left(u_j' \Sigma_{ij} \right) - \left(-\Pi \delta_{ij} + \mu \left(\frac{\partial u_i}{\partial x_j} + \frac{\partial u_j}{\partial x_i} \right) \right) \frac{\partial u_j'}{\partial x_i} = \\ &= \frac{\partial}{\partial x_i} \left(u_j' \Sigma_{ij} \right) + \Pi \frac{\partial u_i'}{\partial x_i} - \mu \left(\frac{\partial u_i}{\partial x_j} + \frac{\partial u_j}{\partial x_i} \right) \frac{\partial u_j'}{\partial x_i} \underbrace{=}_{\substack{\text{Incompresible:} \\ \frac{\partial u_i'}{\partial x_i} = 0}} \frac{\partial}{\partial x_i} \left(u_j' \Sigma_{ij} \right) - \mu \left(\frac{\partial u_i}{\partial x_j} + \frac{\partial u_j}{\partial x_i} \right) \frac{\partial u_j'}{\partial x_i} \ . \end{aligned}$$

Similarly:

$$\mathbf{u} \cdot \left(\nabla \cdot \Sigma' \right) = \frac{\partial \left(u_j \Sigma_{ij}' \right)}{\partial x_i} - \mu' \left(\frac{\partial u_i'}{\partial x_j} + \frac{\partial u_j'}{\partial x_i} \right) \frac{\partial u_j}{\partial x_i} \ .$$

Multiplying the first relation by μ' and the second by μ and subtracting we obtain the desired result. ■

Proposition 3.1. *Given a domain* $D \subset \mathbb{R}^3$ *and a fluid with stress tensor* Σ*, we have:*

$$\int_D \Sigma_{ij} \, d\mathbf{x} = \int_{\partial D} x_j \left(\Sigma \mathbf{n} \right)_i \, dS - \int_D x_j \left(\nabla \cdot \Sigma \right)_i \, d\mathbf{x} \ ,$$

where $\mathbf{n}$ *is the outward unit normal to* ∂D*. In the case where the fluid satisfies Stokes equation:*

$$\int_D \Sigma_{ij} \, d\mathbf{x} = \int_{\partial D} x_j \left(\Sigma \mathbf{n} \right)_i \, dS \ .$$

Proof. Using the divergence theorem and the symmetry of Σ:

$$\begin{aligned} \int_{\partial D} x_j \Sigma_{ik} n_k \, dS &= \int_D \frac{\partial}{\partial x_k} \left(x_j \Sigma_{ik} \right) \, d\mathbf{x} = \int_D \delta_{jk} \Sigma_{ik} \, d\mathbf{x} + \int_D x_j \frac{\partial \Sigma_{ik}}{\partial x_k} \, d\mathbf{x} \\ &= \int_D \delta_{jk} \Sigma_{ik} \, d\mathbf{x} + \int_D x_j \frac{\partial \Sigma_{ki}}{\partial x_k} \, d\mathbf{x} = \int_D \Sigma_{ij} \, d\mathbf{x} + \int_D x_j \left(\nabla \cdot \Sigma \right)_i \, d\mathbf{x} \ . \end{aligned}$$

When the fluid satisfies Stokes equation, $\nabla \cdot \Sigma = \mathbf{0}$, proving the last statement of this proposition. ■

Proposition 3.2. *Given a domain* $D \subset \mathbb{R}^3$ *and two incompressible fluids, the following property holds:*

$$\int_{\partial D} \left(u_i' \frac{\partial u_k}{\partial x_i} - u_i \frac{\partial u_k'}{\partial x_i} \right) n_k \, dS = 0 \ .$$

Proof. Using the divergence theorem:

$$\begin{aligned} \int_{\partial D} \left(u_i' \frac{\partial u_k}{\partial x_i} - u_i \frac{\partial u_k'}{\partial x_i} \right) n_k \, dS &= \int_D \frac{\partial}{\partial x_k} \left(u_i' \frac{\partial u_k}{\partial x_i} - u_i \frac{\partial u_k'}{\partial x_i} \right) \, d\mathbf{x} = \\ &= \int_D \frac{\partial u_i'}{\partial x_k} \frac{\partial u_k}{\partial x_i} + u_i' \frac{\partial^2 u_k}{\partial x_k \partial x_i} - u_i \frac{\partial^2 u_k'}{\partial x_k \partial x_i} - \frac{\partial u_i}{\partial x_k} \frac{\partial u_k'}{\partial x_i} \, d\mathbf{x} \underbrace{=}_{\substack{\frac{\partial u_i'}{\partial x_k} \frac{\partial u_k}{\partial x_i} = \frac{\partial u_i}{\partial x_k} \frac{\partial u_k'}{\partial x_i}}} \\ &= \int_D u_i' \frac{\partial^2 u_k}{\partial x_k \partial x_i} - u_i \frac{\partial^2 u_k'}{\partial x_k \partial x_i} \, d\mathbf{x} \ . \end{aligned}$$

Since $\mathbf{u}$ and $\mathbf{u}'$ are solenoidal:

$$\frac{\partial u_k}{\partial x_k} = 0 \quad , \quad \frac{\partial u'_k}{\partial x_k} = 0 \, ,$$

yielding:

$$\int_D u'_i \frac{\partial^2 u_k}{\partial x_k \partial x_i} - u_i \frac{\partial^2 u'_k}{\partial x_k \partial x_i} \, d\mathbf{x} = 0 \, .$$

■

Proposition 3.3. *Given a regular domain $D \subset \mathbb{R}^3$ the Stokeslet satisfies:*

$$\int_{\partial D} \mathbb{G}_{ij} \left(\mathbf{x}, \mathbf{x}_0 \right) n_i \left(\mathbf{x} \right) \, dS = 0 \, .$$

Proof. Since the Stokeslet is divergenceless (3.7):

$$\nabla \cdot \mathbb{G} = \mathbf{0} \quad \left(\Leftrightarrow \quad \frac{\partial \mathbb{G}_{ij}}{\partial x_i} = 0 \right) \, ,$$

using the divergence theorem gives:

$$0 = \int_D \frac{\partial \mathbb{G}_{ij}}{\partial x_i} \left(\mathbf{x}, \mathbf{x}_0 \right) \, d\mathbf{x} = \int_{\partial D} \mathbb{G}_{ij} \left(\mathbf{x}, \mathbf{x}_0 \right) n_i \left(\mathbf{x} \right) \, dS \, .$$

■

Proposition 3.4. *The Stresslet satisfies the relation:*

$$\frac{\partial \mathbb{T}_{ijk}}{\partial x_k} = -8\pi \delta_{ij} \delta_{\mathbf{x}_0} \left(\mathbf{x} \right) \quad , \quad \textit{in } \mathbb{R}^3 \, .$$

Then, if $D \subset \mathbb{R}^3$ with regular boundary ∂D we have:

$$-\frac{1}{8\pi} \int_{\partial D} \mathbb{T}_{ijk} \left(\mathbf{x}, \mathbf{x}_0 \right) n_k \left(\mathbf{x} \right) \, dS = \begin{cases} \delta_{ij} & , \, \mathbf{x}_0 \textit{ inside } D \\ \dfrac{\delta_{ij}}{2} & , \, \mathbf{x}_0 \in \partial D \\ 0 & , \, \mathbf{x}_0 \textit{ outside } D \end{cases} \, .$$

where $\mathbf{n}$ is the outward unit normal to ∂D.

Proof.

$$\frac{\partial \mathbb{T}_{ijk}}{\partial x_k} = \frac{\partial}{\partial x_k} \left(-\delta_{ik} \mathbb{P}_j + \left(\frac{\partial \mathbb{G}_{ij}}{\partial x_k} + \frac{\partial \mathbb{G}_{kj}}{\partial x_i} \right) \right) = -\frac{\partial \mathbb{P}_j}{\partial x_i} + \Delta \mathbb{G}_{ij} = -8\pi \delta_{ij} \delta_{\mathbf{x}_0} \left(\mathbf{x} \right) \, ,$$

by virtue of last proposition and (3.5). To complete the proof, it suffices to take integrals and use the divergence theorem together with the following property of the Dirac delta function:

$$\int_D \delta_{\mathbf{x}_0} \left(\mathbf{x} \right) \, d\mathbf{x} = \begin{cases} 1 & , \quad \mathbf{x}_0 \text{ inside } D \\ \frac{1}{2} & , \quad \mathbf{x}_0 \in \partial D \\ 0 & , \quad \mathbf{x}_0 \text{ outside } D \end{cases} \, .$$

■

Using the previous propositon one has the important identity:

$$\lim_{\mathbf{x}_0 \to \partial D} \int_{\partial D} \mathbb{T}_{ijk} \left(\mathbf{x}, \mathbf{x}_0 \right) n_k \left(\mathbf{x} \right) \, dS = \int_{\partial D}^{PV} \mathbb{T}_{ijk} \left(\mathbf{x}, \mathbf{x}_0 \right) n_k \left(\mathbf{x} \right) \, dS \mp 4\pi \delta_{ij} \, , \tag{3.10}$$

where the minus sign applies when $\mathbf{x}_0$ tends to ∂D from the inside the domain and the plus sign when the convergence is from the outside. All these results are the necessary ingredients to obtain the boundary integral formulation sought.

Consider a fluid satisfying Stokes equation with viscosity μ, velocity $\mathbf{u}$ and stress tensor Σ and let $\mathbf{u}'$ and Σ' be the velocity and stress tensor respectively of that fluid when subject to a constant point force $\mathbf{b}$ at $\mathbf{x}_0$. One can write:

$$\mathbf{u}'_i(\mathbf{x}) = \frac{1}{8\pi\mu}\mathbb{G}_{ij}(\mathbf{x},\mathbf{x}_0)\,b_j \quad , \quad \Sigma'_{ki}(\mathbf{x}) = \frac{1}{8\pi}\mathbb{T}_{kji}(\mathbf{x},\mathbf{x}_0)\,b_j \ ,$$

where:

$$\nabla\cdot\Sigma' = -\delta_{\mathbf{x}_0}\mathbf{b} \ . \tag{3.11}$$

Using the Lorentz reciprocal relation for this fluid, i.e. $\mu = \mu'$, we get:

$$\mathbf{u}'\cdot(\nabla\cdot\Sigma) - \mathbf{u}\cdot\left(\nabla\cdot\Sigma'\right) = \nabla\cdot\left(\Sigma\mathbf{u}' - \Sigma'\mathbf{u}\right) \ .$$

Since $\mathbf{u}$ and Σ satisfy Stokes equation, we have that $\nabla\cdot\Sigma = \mathbf{0}$, and using (3.11), the above identity becomes:

$$\mathbf{u}\cdot\mathbf{b}\,\delta_{\mathbf{x}_0} = \nabla\cdot\left(\Sigma\mathbf{u}' - \Sigma'\mathbf{u}\right) \ .$$

Taking into account the symmetry of $\mathbb{T}$, $\mathbb{G}$ and Σ:

$$\mathbf{u}\cdot\mathbf{b}\,\delta_{\mathbf{x}_0} = \frac{1}{8\pi\mu}\nabla\cdot(\mathbb{G}\Sigma\mathbf{b}) - \frac{1}{8\pi}\nabla\cdot(\mathbf{u}\cdot\mathbb{T}\mathbf{b}) = \frac{1}{8\pi\mu}\nabla\cdot(\mathbb{G}\Sigma)\cdot\mathbf{b} - \frac{1}{8\pi}\nabla\cdot(\mathbf{u}\cdot\mathbb{T})\cdot\mathbf{b} \ .$$

Simplifying the constant vector $\mathbf{b}$:

$$\mathbf{u}\,\delta_{\mathbf{x}_0} = \frac{1}{8\pi\mu}\nabla\cdot(\mathbb{G}\Sigma) - \frac{1}{8\pi}\nabla\cdot(\mathbf{u}\cdot\mathbb{T}) \ ,$$

and integrating over a control volume D to use the divergence theorem:

$$\int_D u_j(\mathbf{x})\,\delta_{\mathbf{x}_0}(\mathbf{x})\ d\mathbf{x} = \frac{1}{8\pi\mu}\int_{\partial D}\mathbb{G}_{ij}(\mathbf{x},\mathbf{x}_0)\,\Sigma_{ik}(\mathbf{x})\,n_k(\mathbf{x})\ dS - \frac{1}{8\pi}\int_{\partial D}u_i(\mathbf{x})\,\mathbb{T}_{ijk}(\mathbf{x},\mathbf{x}_0)\,n_k(\mathbf{x})\ dS \ .$$

If the traction at the boundary is defined as:

$$\mathbf{f}(\mathbf{x}) = \Sigma(\mathbf{x})\,\mathbf{n}(\mathbf{x}) \quad , \quad \mathbf{x}\in\partial D \ ,$$

then we can write:

$$\int_D u_j(\mathbf{x})\,\delta_{\mathbf{x}_0}(\mathbf{x})\ d\mathbf{x} = \frac{1}{8\pi\mu}\int_{\partial D}\mathbb{G}_{ij}(\mathbf{x},\mathbf{x}_0)\,f_i(\mathbf{x})\ dS - \frac{1}{8\pi}\int_{\partial D}u_i(\mathbf{x})\,\mathbb{T}_{ijk}(\mathbf{x},\mathbf{x}_0)\,n_k(\mathbf{x})\ dS \ . \tag{3.12}$$

Suppose now that $\mathbf{x}_0$ is inside D, then the equation (3.12) transforms into:

$$u_j(\mathbf{x}_0) = \frac{1}{8\pi\mu}\int_{\partial D}\mathbb{G}_{ij}(\mathbf{x},\mathbf{x}_0)\,f_i(\mathbf{x})\ dS - \frac{1}{8\pi}\int_{\partial D}u_i(\mathbf{x})\,\mathbb{T}_{ijk}(\mathbf{x},\mathbf{x}_0)\,n_k(\mathbf{x})\ dS \ . \tag{3.13}$$

Furthermore, if $\mathbf{x}_0$ is outside D we have:

$$0 = \frac{1}{8\pi\mu}\int_{\partial D}\mathbb{G}_{ij}(\mathbf{x},\mathbf{x}_0)\,f_i(\mathbf{x})\ dS - \frac{1}{8\pi}\int_{\partial D}u_i(\mathbf{x})\,\mathbb{T}_{ijk}(\mathbf{x},\mathbf{x}_0)\,n_k(\mathbf{x})\ dS \ . \tag{3.14}$$

Finally, if $\mathbf{x}_0\in\partial D$, it is enough to take the limit in (3.12) when $\mathbf{x}_0$ approaches ∂D from the inside of D:

$$u_j(\mathbf{x}_0) = \frac{1}{8\pi\mu}\lim_{\mathbf{x}_0\to\partial D}\int_{\partial D}\mathbb{G}_{ij}(\mathbf{x},\mathbf{x}_0)\,f_i(\mathbf{x})\ dS - \frac{1}{8\pi}\lim_{\mathbf{x}_0\to\partial D}\int_{\partial D}u_i(\mathbf{x})\,\mathbb{T}_{ijk}(\mathbf{x},\mathbf{x}_0)\,n_k(\mathbf{x})\ dS \ . \tag{3.15}$$

Now:

$$\lim_{\mathbf{x}_0\to\partial D}\int_{\partial D}\mathbb{G}_{ij}(\mathbf{x},\mathbf{x}_0)\,f_i(\mathbf{x})\ dS = \int_{\partial D}\mathbb{G}_{ij}(\mathbf{x},\mathbf{x}_0)\,h_i(\mathbf{x})\ dS \ , \tag{3.16}$$

as the integrand is continuous across the boundary. Moreover, using (3.10) we get:

$$\lim_{\mathbf{x}_0\to\partial D}\int_{\partial D}u_i(\mathbf{x})\,\mathbb{T}_{ijk}(\mathbf{x},\mathbf{x}_0)\,n_k(\mathbf{x})\ dS = \int^{PV}_{\partial D}u_i(\mathbf{x})\,\mathbb{T}_{ijk}(\mathbf{x},\mathbf{x}_0)\,n_k(\mathbf{x})\ dS - 4\pi u_j(\mathbf{x}_0) \tag{3.17}$$

In this way (3.15) yields:

$$u_j(\mathbf{x}_0) = \frac{1}{4\pi\mu}\int_{\partial D}\mathbb{G}_{ij}(\mathbf{x},\mathbf{x}_0)\, f_i(\mathbf{x})\ dS - \frac{1}{4\pi}\int_{\partial D}^{PV} u_i(\mathbf{x})\,\mathbb{T}_{ijk}(\mathbf{x},\mathbf{x}_0)\, n_k(\mathbf{x})\ dS \quad , \quad \mathbf{x}_0 \in \partial D\ , \tag{3.18}$$

where the first and second integrals are known respectively as the single layer potential (SLP) and the double layer potential (DLP). If we specify a value for the traction force $\mathbf{f}$, our problem (3.18) reduces to a Fredholm integral equation of the second kind for the velocity $\mathbf{u}$ on ∂D.

To obtain the integral equation for the velocity at the droplet's interface, use the description (3.9) together with the traction forces:

$$\mathbf{f}^{(k)} = T^{(k)}\mathbf{n}^{(k)} \quad , \quad k \in \{1,2\}\ , \tag{3.19}$$

where $T^{(k)}$ is the stress tensor for each fluid, determined by (2.35). At the interface we have:

$$\mathbf{u}(\mathbf{x}) \equiv \mathbf{u}^{(1)}(\mathbf{x}) = \mathbf{u}^{(2)}(\mathbf{x}) \quad , \quad \mathbf{n}(\mathbf{x}) \equiv \mathbf{n}^{(1)}(\mathbf{x}) = -\mathbf{n}^{(2)}(\mathbf{x}) \quad , \quad \mathbf{x} \in \partial\mathcal{D}(t)\ , \tag{3.20}$$

where $\mathbf{n}^{(1)}$ and $\mathbf{n}^{(2)}$ are the unit outward normals to the drop and the surrounding fluid respectively. Taking $\mathbf{x}_0 \in \mathcal{D}_1(t)$, one can write for the drop:

$$u_j^{(1)}(\mathbf{x}_0) = \frac{1}{8\pi\mu_1}\int_{\partial\mathcal{D}(t)}\mathbb{G}_{ij}(\mathbf{x},\mathbf{x}_0)\, f_i^{(1)}(\mathbf{x})\ dS - \frac{1}{8\pi}\int_{\partial\mathcal{D}(t)} u_i^{(1)}(\mathbf{x})\,\mathbb{T}_{ijk}(\mathbf{x},\mathbf{x}_0)\, n_k^{(1)}(\mathbf{x})\ dS\ , \tag{3.21}$$

and for the outer fluid:

$$0 = \frac{1}{8\pi\mu_2}\int_{\partial\mathcal{D}(t)}\mathbb{G}_{ij}(\mathbf{x},\mathbf{x}_0)\, f_i^{(2)}(\mathbf{x})\ dS - \frac{1}{8\pi}\int_{\partial\mathcal{D}(t)} u_i^{(2)}(\mathbf{x})\,\mathbb{T}_{ijk}(\mathbf{x},\mathbf{x}_0)\, n_k^{(2)}(\mathbf{x})\ dS\ .$$

Now, multiplying the last equation by $\dfrac{\mu_2}{\mu_1}$ we get:

$$0 = \frac{1}{8\pi\mu_1}\int_{\partial\mathcal{D}(t)}\mathbb{G}_{ij}(\mathbf{x},\mathbf{x}_0)\, f_i^{(2)}(\mathbf{x})\ dS - \frac{\mu_2}{8\pi\mu_1}\int_{\partial\mathcal{D}(t)} u_i^{(2)}(\mathbf{x})\,\mathbb{T}_{ijk}(\mathbf{x},\mathbf{x}_0)\, n_k^{(2)}(\mathbf{x})\ dS\ . \tag{3.22}$$

Adding (3.21) to (3.22) and using the relations (3.19) and (3.20) this yields:

$$\begin{aligned} u_j^{(1)}(\mathbf{x}_0) = {} & \frac{1}{8\pi\mu_1}\int_{\partial\mathcal{D}(t)}\mathbb{G}_{ij}(\mathbf{x},\mathbf{x}_0)\left(T_{ik}^{(1)}(\mathbf{x}) - T_{ik}^{(2)}(\mathbf{x})\right) n_k(\mathbf{x})\ dS + \\ & + \frac{1}{8\pi}\left(\frac{\mu_2}{\mu_1} - 1\right)\int_{\partial\mathcal{D}(t)} u_i(\mathbf{x})\,\mathbb{T}_{ijk}(\mathbf{x},\mathbf{x}_0)\, n_k(\mathbf{x})\ dS\ . \end{aligned}$$

Taking the limit when $\mathbf{x}_0$ approaches $\partial\mathcal{D}(t)$ from the inside:

$$\begin{aligned} u_j(\mathbf{x}_0) = {} & \frac{1}{8\pi\mu_1}\int_{\partial\mathcal{D}(t)}\mathbb{G}_{ij}(\mathbf{x},\mathbf{x}_0)\left(T_{ik}^{(1)}(\mathbf{x}) - T_{ik}^{(2)}(\mathbf{x})\right) n_k(\mathbf{x})\ dS + \\ & + \frac{1}{8\pi}\left(\frac{\mu_2}{\mu_1} - 1\right)\left(\int_{\partial\mathcal{D}(t)}^{PV} u_i(\mathbf{x})\,\mathbb{T}_{ijk}(\mathbf{x},\mathbf{x}_0)\, n_k(\mathbf{x})\ dS - 4\pi u_j(\mathbf{x}_0)\right)\ , \end{aligned}$$

and rearranging the equation:

$$\begin{aligned} u_j(\mathbf{x}_0) = {} & -\frac{1}{4\pi(\mu_1+\mu_2)}\int_{\partial\mathcal{D}(t)}\mathbb{G}_{ij}(\mathbf{x},\mathbf{x}_0)\left(T_{ik}^{(2)}(\mathbf{x}) - T_{ik}^{(1)}(\mathbf{x})\right) n_k(\mathbf{x})\ dS - \\ & - \frac{\mu_1-\mu_2}{4\pi(\mu_1+\mu_2)}\int_{\partial\mathcal{D}(t)}^{PV} u_i(\mathbf{x})\,\mathbb{T}_{ijk}(\mathbf{x},\mathbf{x}_0)\, n_k(\mathbf{x})\ dS\ . \end{aligned}$$

If we define the balance of stresses (traction junp) as:

$$\mathbf{f} = \left(T^{(2)} - T^{(1)}\right)\mathbf{n}\ ,$$

one can write:

$$\begin{aligned} u_j(\mathbf{x}_0) = &-\frac{1}{4\pi(\mu_1+\mu_2)}\int_{\partial\mathcal{D}(t)}\mathbb{G}_{ij}(\mathbf{x},\mathbf{x}_0)\,f_i(\mathbf{x})\;dS- \\ &-\frac{\mu_1-\mu_2}{4\pi(\mu_1+\mu_2)}\int^{PV}_{\partial\mathcal{D}(t)}u_i(\mathbf{x})\,\mathbb{T}_{ijk}(\mathbf{x},\mathbf{x}_0)\,n_k(\mathbf{x})\;dS \quad,\quad i,j,k\in\{1,2,3\} \quad,\quad \mathbf{x}_0\in\partial\mathcal{D}(t)\;, \end{aligned} \tag{3.23}$$

which is the equation describing the evolution of the velocity field at the interface between the droplet and the surrounding fluid. Observe that this integral equation is complemented in a natural way by the condition (2.33) or (2.34) depending on whether rotation takes place at constant angular momentum or constant angular speed respectively. Equation (3.23) can be made non-dimensional by scaling the variables as follows:

$$\mathbf{u}^* = \frac{\mathbf{u}}{U} \quad,\quad dS^* = \frac{dS}{l^2} \quad,\quad \mathbf{f}^* = \frac{l}{\gamma}\mathbf{f} \quad,\quad \mathbb{G}^* = l\mathbb{G} \quad,\quad \mathbb{T}^* = l^2\mathbb{T}\;,$$

resulting in:

$$4\pi(1+\lambda)\,u_j(\mathbf{x}_0) = -\int_{\partial\mathcal{D}(t)}\mathbb{G}_{ij}(\mathbf{x},\mathbf{x}_0)\,f_i(\mathbf{x})\;dS-(1-\lambda)\int^{PV}_{\partial\mathcal{D}(t)}u_i(\mathbf{x})\,\mathbb{T}_{ijk}(\mathbf{x},\mathbf{x}_0)\,n_k(\mathbf{x})\;dS\;. \tag{3.24}$$

and the traction jump variables:

$$\mathcal{H}^* = l\mathcal{H} \quad,\quad r^*_{axis} = \frac{r_{axis}}{l} \quad,\quad \sigma^* = \sqrt{\frac{l}{\gamma\varepsilon_0}}\sigma$$

giving:

$$\mathbf{f} = \left(2\mathcal{H} - \frac{Bo}{2}r^2_{axis} - \frac{\sigma^2}{2}\right)\mathbf{n} \quad,\quad Bo = \frac{\Delta\varrho\,\omega^2 l^3}{\gamma}\;, \tag{3.25}$$

where we have dropped asterisks for clarity. A dimensionless number arises at this point, the Bond number Bo, which measures the relative importance between centrifugal and capillary forces. Notice that a Bond number was already obtained in chapter 2 when relating centrifugal to viscous forces:

$$Bo = \frac{\varrho_1\omega^2 l^3}{\mu_1 U}\;.$$

Comparing both Bond numbers we can reach the conclusion that the characteristic velocity behaves as:

$$U = \frac{\gamma}{\mu_1\psi}\;,$$

and since $U = \dfrac{l}{\tau}$, the characteristic time τ is:

$$\tau = \frac{\mu_1\psi l}{\gamma}\;.$$

3.3. Continuity properties of SLP and DLP

We finish this chapter proving the properties (3.16) and (3.17) used in the previous section. Given $\mathbf{x}_0$ inside D, consider the limit where the point approaches the boundary from the inside. To compute this limit, focus on a small region of the smooth boundary, which can be approximated by a flat surface. Take the modified boundary as the one that includes a half-sphere of radius ε centered at $\mathbf{x}_0$, $\mathcal{S}_\varepsilon$, and where the disk D_ε has been removed (see figure 3.1).

For the SLP we have:

$$\begin{aligned} \lim_{\mathbf{x}_0\to\partial D}\int_{\partial D}\mathbb{G}_{ij}(\mathbf{x},\mathbf{x}_0)\,f_i(\mathbf{x})\;dS &= \lim_{\varepsilon\to0}\int_{\partial D\setminus D_\varepsilon}\mathbb{G}_{ij}(\mathbf{x},\mathbf{x}_0)\,f_i(\mathbf{x})\;dS+\lim_{\varepsilon\to0}\int_{\mathcal{S}_\varepsilon}\mathbb{G}_{ij}(\mathbf{x},\mathbf{x}_0)\,f_i(\mathbf{x})\;dS = \\ &= \int^{PV}_{\partial D}\mathbb{G}_{ij}(\mathbf{x},\mathbf{x}_0)\,f_i(\mathbf{x})\;dS+\lim_{\varepsilon\to0}\int_{\mathcal{S}_\varepsilon}\mathbb{G}_{ij}(\mathbf{x},\mathbf{x}_0)\,f_i(\mathbf{x})\;dS\;. \end{aligned}$$

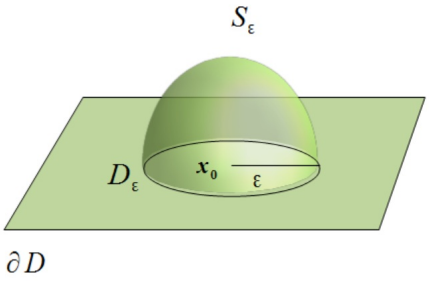

Figure 3.1: Modified boundary to integrate the single and double layer potentials.

In spherical coordinates, the outward unit normal to the spherical cap $\mathcal{S}_\varepsilon$ is:

$$\mathbf{n}\left(\mathbf{x}\right)=\frac{\mathbf{x}-\mathbf{x}_0}{\left\|\mathbf{x}-\mathbf{x}_0\right\|}=\frac{\widehat{\mathbf{x}}}{\varepsilon}=\boldsymbol{\tau}\quad,\quad\mathbf{x}=\mathbf{x}_0+\varepsilon\left(\cos\varphi\sin\theta,\sin\varphi\sin\theta,\cos\theta\right)=\mathbf{x}_0+\varepsilon\boldsymbol{\tau}\quad,\quad\left\|\boldsymbol{\tau}\right\|=1\,,$$

so:

$$\lim_{\varepsilon\to0}\int_{\mathcal{S}_\varepsilon}\mathbb{G}_{ij}\left(\mathbf{x},\mathbf{x}_0\right)f_i\left(\mathbf{x}\right)\,dS=\lim_{\varepsilon\to0}\int_0^{2\pi}\int_0^{\frac{\pi}{2}}\varepsilon\left(\delta_{ij}+\tau_i\tau_j\right)\left(T_{ik}^{(2)}\left(\mathbf{x}\right)-T_{ik}^{(1)}\left(\mathbf{x}\right)\right)\tau_k\sin\theta\,d\theta\,d\varphi=0\,.$$

As a result:

$$\lim_{\mathbf{x}_0\to\partial D}\int_{\partial D}\mathbb{G}_{ij}\left(\mathbf{x},\mathbf{x}_0\right)f_i\left(\mathbf{x}\right)\,dS=\int_{\partial D}^{PV}\mathbb{G}_{ij}\left(\mathbf{x},\mathbf{x}_0\right)f_i\left(\mathbf{x}\right)\,dS\,,$$

proving that the SLP is continuous across the boundary. A similar and straightforward approach could be used to prove the same result when the point tends to the boundary from outside the domain.

To finish we will prove that the DLP is discountiuous across the boundary:

$$\begin{aligned}\lim_{\mathbf{x}_0\to\partial D}\int_{\partial D}u_i\left(\mathbf{x}\right)\mathbb{T}_{ijk}\left(\mathbf{x},\mathbf{x}_0\right)n_k\left(\mathbf{x}\right)\,dS&=\lim_{\varepsilon\to0}\int_{\partial D\setminus D_\varepsilon}u_i\left(\mathbf{x}\right)\mathbb{T}_{ijk}\left(\mathbf{x},\mathbf{x}_0\right)n_k\left(\mathbf{x}\right)\,dS+\\&+\lim_{\varepsilon\to0}\int_{\mathcal{S}_\varepsilon}u_i\left(\mathbf{x}\right)\mathbb{T}_{ijk}\left(\mathbf{x},\mathbf{x}_0\right)n_k\left(\mathbf{x}\right)\,dS=\\&=\int_{\partial D}^{PV}u_i\left(\mathbf{x}\right)\mathbb{T}_{ijk}\left(\mathbf{x},\mathbf{x}_0\right)n_k\left(\mathbf{x}\right)\,dS+\\&+\lim_{\varepsilon\to0}\int_{\mathcal{S}_\varepsilon}u_i\left(\mathbf{x}\right)\mathbb{T}_{ijk}\left(\mathbf{x},\mathbf{x}_0\right)n_k\left(\mathbf{x}\right)\,dS\,.\end{aligned}$$

Working in spherical coordinates as before:

$$\begin{aligned}\lim_{\varepsilon\to0}\int_{\mathcal{S}_\varepsilon}u_i\left(\mathbf{x}\right)\mathbb{T}_{ijk}\left(\mathbf{x},\mathbf{x}_0\right)n_k\left(\mathbf{x}\right)\,dS&=-6u_i\left(\mathbf{x}_0\right)\int_0^{2\pi}\int_0^{\frac{\pi}{2}}\tau_i\tau_j\tau_k^2\sin\theta\,d\theta\,d\varphi=\\&=-6u_i\left(\mathbf{x}_0\right)\int_0^{2\pi}\int_0^{\frac{\pi}{2}}\tau_i\tau_j\sin\theta\,d\theta\,d\varphi=-4\pi u_j\left(\mathbf{x}_0\right)\,,\end{aligned}$$

yielding:

$$\lim_{\mathbf{x}_0\to\partial D}\int_{\partial D}u_i\left(\mathbf{x}\right)\mathbb{T}_{ijk}\left(\mathbf{x},\mathbf{x}_0\right)n_k\left(\mathbf{x}\right)\,dS=\int_{\partial D}^{PV}u_i\left(\mathbf{x}\right)\mathbb{T}_{ijk}\left(\mathbf{x},\mathbf{x}_0\right)n_k\left(\mathbf{x}\right)\,dS-4\pi u_j\left(\mathbf{x}_0\right)\,,$$

proving that the DLP has a discontinuity across the interface. Observe that with a similar argument one can show that, when $\mathbf{x}_0$ tends to the boundary from outside D, then:

$$\lim_{\mathbf{x}_0\to\partial D}\int_{\partial D}u_i\left(\mathbf{x}\right)\mathbb{T}_{ijk}\left(\mathbf{x},\mathbf{x}_0\right)n_k\left(\mathbf{x}\right)\,dS=\int_{\partial D}^{PV}u_i\left(\mathbf{x}\right)\mathbb{T}_{ijk}\left(\mathbf{x},\mathbf{x}_0\right)n_k\left(\mathbf{x}\right)\,dS+4\pi u_j\left(\mathbf{x}_0\right)\,.$$

Chapter 4

The BEM

The advantage of recasting the rotating drop problem into an integral equation over the drop's interface is what makes the BEM a suitable choice to simulate free boundary problems. Since we have to solve for the velocity field on a surface, this technique simplifies the work by lowering the dimensionality of the problem and decreasing the degrees of freedom. It also facilitates the discretization task, considering that it is always easier to mesh a surface with triangles rather than filling a region of space with tetrahedra, as is the case when using the Finite Element Method (FEM). The main drawback of boundary elements is that all the nodes influence each other, giving rise to large and complex linear systems with dense matrices in comparison to the sparse matrices obtained with finite elements, where nodes only affect their neighbours. These issues penalize the performance with large processing times, which we speed up by making use of iterative methods, such as the Generalized Minimal Residual Method (GMRES) developed by Yousef Saad and Martin H. Schultz [62] in 1986, to solve the algebraic equations involved.

For this thesis two computer codes have been developed to study the evolution and stability of rotating droplets. One imposes axial symmetry of the model with respect to the rotation axis and the other is capaple of performing full 3D simulations. The axisymmetric version of the problem reduces velocity field calculation to the approximation of elliptic integrals, since the azimuthal component of the integrals involved in the boundary formulation can be explicitly expressed in those terms. Before giving any further details on the numerical implementation, we move to introduce the steps followed to approximate the free surface problem.

4.1. The simulation algorithm

Given a time $t > 0$, we start by discretising the free boundary $\partial\mathcal{D}(t)$ into a mesh. Then, we calculate on each node the centrifugal force, mean curvature, surface charge density and interface velocity together with the drop's moment of inertia and volume. Finally, we evolve the surface with the velocity field and adapt the mesh to gain precision and avoid its degeneration. The steps of the algorithm to evolve the drop are:

1. Compute the drop's volume and moment of inertia about the z-axis.
2. Calculate the mean curvature, centrifugal force and surface charge density on each node of the mesh.
3. Obtain the traction $\mathbf{f}$ and solve the interface velocity equation (3.23) with BEM.
4. Move the surface using an explicit Euler scheme:

$$\mathbf{x}^{i+1} = \mathbf{x}^i + \Delta t \ \left(\mathbf{u}^i \cdot \mathbf{n}\right) \quad , \quad \Delta t = t_{i+1} - t_i \ .$$

   Observe that we use the normal component of the velocity field at time t_i, since the tangential component only redistributes the nodes over the surface and thus can be removed.
5. Regularize the mesh if necessary. This step is crucial since the mesh may deteriorate as the drop evolves with time. One needs to apply several techniques to maintain its good quality throughout simulation:
   - Delaunay remeshing.
   - Mesh relaxation.
   - Mesh refinement.

Notice how crucial the moment of inertia computation becomes, as it plays a key role when the evolution of the system takes place at constant angular momentum. Observe also that in order to calculate the surface charge density one has to solve another boundary integral equation with BEM. Indeed, since the electric potential satisfies (2.31), it can be written as:

$$\mathcal{E}_\infty z\left(\mathbf{x}\right)+\mathcal{V}\left(\mathbf{x}\right)=\frac{1}{4\pi\varepsilon_0}\int_{\partial\mathcal{D}(t)}\frac{\sigma\left(\mathbf{x}'\right)}{\left\|\mathbf{x}-\mathbf{x}'\right\|}\,dS\quad,\quad\mathbf{x}\in\partial\mathcal{D}\left(t\right)\,, \tag{4.1}$$

and this holds because the auxiliary potential $\widetilde{\mathcal{V}}=\mathcal{V}+\mathcal{E}_\infty z$ solves:

$$\begin{cases}\Delta\widetilde{\mathcal{V}}=0 & , \quad \text{in } \mathbb{R}^3\backslash\mathcal{D}_1\left(t\right)\\ \widetilde{\mathcal{V}}=\mathcal{V}_0+\mathcal{E}_\infty z & , \quad \text{on } \partial\mathcal{D}\left(t\right)\\ \widetilde{\mathcal{V}}\to O(\left\|\mathbf{x}\right\|^{-1}) & , \quad \text{when } \left\|\mathbf{x}\right\|\to\infty\end{cases},$$

with the condition that $\mathcal{V}_0$ has to be chosen so that:

$$Q=\int_{\partial\mathcal{D}(t)}\sigma\left(\mathbf{x}\right)\,dS\,. \tag{4.2}$$

Since the value for the potential is $\mathcal{V}_0$ at the drop's surface then:

$$\mathcal{E}_\infty z\left(\mathbf{x}\right)+\mathcal{V}_0=\frac{1}{4\pi\varepsilon_0}\int_{\partial\mathcal{D}(t)}\frac{\sigma\left(\mathbf{x}'\right)}{\left\|\mathbf{x}-\mathbf{x}'\right\|}\,dS\quad,\quad\mathbf{x}\in\partial\mathcal{D}\left(t\right)\,. \tag{4.3}$$

Consequently, one has to account for two different contributions to the surface charge density: the charge density created by the amount of charge Q that the drop holds on its surface, and the ficticious density induced by the action of a uniform external electric field of magnitude $\mathcal{E}_\infty$ in the z direction. To obtain the surface charge density σ that solves (4.3) we use the superposition principle to write:

$$\sigma=\sigma_0\mathcal{V}_0+\sigma_{ind}\,, \tag{4.4}$$

where σ_{ind} is the surface charge density induced by the external electric field and σ_0 the one corresponding to a potential of $\mathcal{V}=1$. The values for σ_0 and σ_{ind} can be computed by solving the following integral equations:

$$\mathcal{E}_\infty z\left(\mathbf{x}\right)=\frac{1}{4\pi\varepsilon_0}\int_{\partial\mathcal{D}(t)}\frac{\sigma_{ind}\left(\mathbf{x}'\right)}{\left\|\mathbf{x}-\mathbf{x}'\right\|}\,dS\quad,\quad\mathbf{x}\in\partial\mathcal{D}\left(t\right)\,, \tag{4.5}$$

$$1=\frac{1}{4\pi\varepsilon_0}\int_{\partial\mathcal{D}(t)}\frac{\sigma_0\left(\mathbf{x}'\right)}{\left\|\mathbf{x}-\mathbf{x}'\right\|}\,dS\quad,\quad\mathbf{x}\in\partial\mathcal{D}\left(t\right)\,. \tag{4.6}$$

Integrating (4.4), the potential on the surface satisfies:

$$\mathcal{V}_0\int_{\partial\mathcal{D}(t)}\sigma_0\left(\mathbf{x}\right)\,dS=Q\,.$$

Observe that we have used Gauss's law to get:

$$\int_{\partial\mathcal{D}(t)}\sigma_{ind}\left(\mathbf{x}\right)\,dS=\frac{\text{charge generating }\mathcal{E}_\infty\text{ enclosed by }\partial\mathcal{D}\left(t\right)}{\varepsilon_0}=0\,,$$

since the external electric field is not generated by charges inside the droplet.

In the next sections we will describe in detail how to discretize the velocity and surface charge density integral equations to use BEM, the algorithms implemented to calculate the mean curvature and surface charge density together with the ones for the drop's moment of inertia and volume. We also explain the techniques employed to regularize the mesh. For our simulations we have used two codes based on the general principles sketched above. In the simplest one, axial symmetry is assumed and explicit integration of the boundary integrals in the azimuthal coordinate θ is performed. The other code does not assume any kind of symmetry and deals with the full 3D problem.

4.2. The axisymmetric problem

In this section we will describe how the numerical algorithm is implemented when axial symmetry with respect to the rotation axis is imposed on the problem. To discretise the boundary in the counter-clockwise direction, we use a family of segments $\{\mathcal{S}_j\}_{j=1}^{N-1}$ and nodes $\{(r_j, z_j)\}_{j=1}^{N}$ as shown below:

$$\mathcal{S}_i = \{(r,z) \ : \ r\,(z) = \frac{r_{i+1}-r_i}{z_{i+1}-z_i}\,(z-z_i)+r_i \ , \ z \in [z_i, z_{i+1}]\} \quad , \quad i \in \{1,\ldots,N-1\} \ .$$

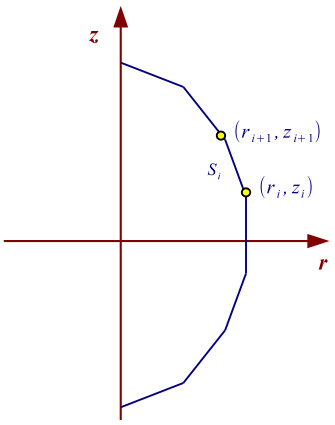

Figure 4.1: Axisymmetric mesh.

4.2.1. Volume and moment of inertia

We deal here with the formulas to approximate numerically the volume and moment of inertia with respect the z axis of an axisymmetric drop. We have that:

$$V \approx \sum_{i=1}^{N-1} V\,(\mathcal{S}_i) \quad , \quad \mathcal{I} \approx \sum_{i=1}^{N-1} \mathcal{I}\,(\mathcal{S}_i) \ ,$$

where:

$$V\,(\mathcal{S}_i) = 2\pi \int_{z_i}^{z_{i+1}} \int_0^{r(z)} \rho \, d\rho \, dz = \pi \int_{z_i}^{z_{i+1}} (r\,(z))^2 \ dz = \frac{\pi}{3}\,(z_{i+1}-z_i)\left(r_i^2 + r_i r_{i+1} + r_{i+1}^2\right) \ , \tag{4.7}$$

$$\mathcal{I}\,(\mathcal{S}_i) = 2\pi\varrho_1 \int_{z_i}^{z_{i+1}} \int_0^{r(z)} \rho^3 \, d\rho \, dz = \frac{\pi\varrho_1}{10}\,(z_{i+1}-z_i)\left(r_i^4 + r_i^3 r_{i+1} + r_i^2 r_{i+1}^2 + r_i r_{i+1}^3 + r_{i+1}^4\right) \ . \tag{4.8}$$

Observe that if the boundary is discretised in the clockwise direction, the final values for the volume and moment of inertia change sign. This method of approximation is known as the trapezoidal method, which considers the truncated cones that result from revolving the segments $\mathcal{S}_i$ about the z axis.

An alternative approach is to use the method of cylinders, based on the approximation by the cylinders obtained with the midpoints of the segments, when revolved about the z axis:

$$V = \int_{\mathcal{D}_1(t)} d\mathbf{x} = 2\pi \int_{\mathcal{D}_1(t)} rz \ dr \approx 2\pi \sum_{i=1}^{N-1} r_i^m \left|(r_{i+1}-r_i)\, z_i^m\right| \ , \tag{4.9}$$

$$\mathcal{I} = \varrho_1 \int_{\mathcal{D}_1(t)} r^2 \ d\mathbf{x} = 2\pi\varrho_1 \int_{\mathcal{D}_1(t)} r^3 z \ dr \approx 2\pi\varrho_1 \sum_{i=1}^{N-1} \left(r_i^m\right)^3 \left|(r_{i+1}-r_i)\, z_i^m\right| \ , \tag{4.10}$$

where the midpoints are defined in the usual way:

$$r_i^m = \frac{r_{i+1}+r_i}{2} \quad , \quad z_i^m = \frac{z_{i+1}+z_i}{2} \quad , \quad i \in \{1,\ldots,N-1\} \ .$$

As a validation, we have compared the results obtained with these approximations and the known values for the volume and moment of inertia of a sphere with unit radius and density to show in figure 4.2 that the relative error is inversely proportional to the number of nodes in the mesh squared:

$$e_{rel} \quad \propto \quad \frac{1}{N^2} \ ,$$

resulting in a quadratic convergence.

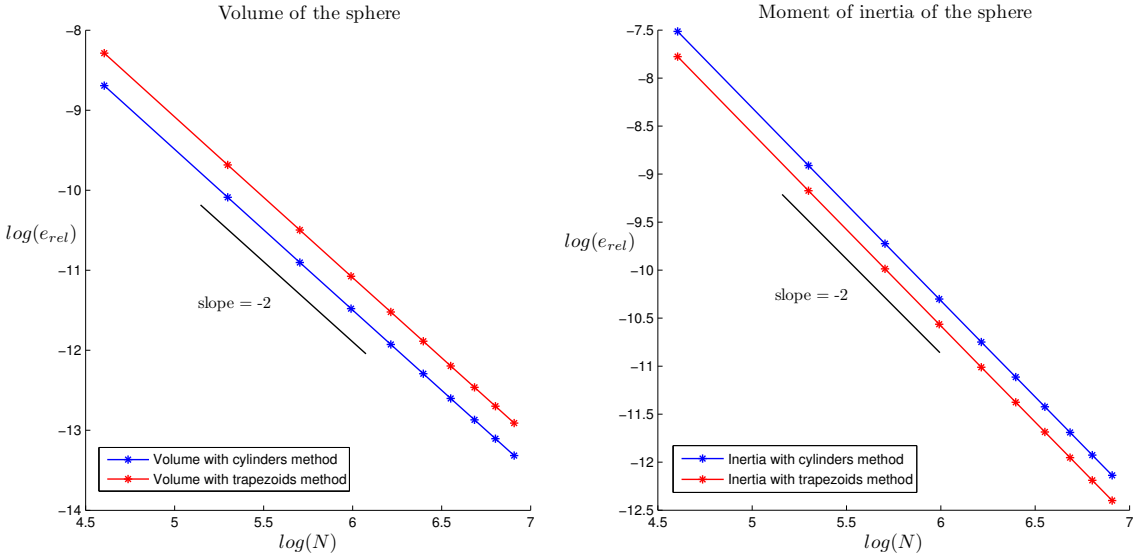

Figure 4.2: Volume and moment of inertia computation with different methods.

4.2.2. Mean curvature

To compute the mean curvature $\mathcal{H}$ on each node, we introduce two standard procedures. The first algorithm uses Frenet-Serret formulas for the profile curve. We know that:

$$2\mathcal{H} = -\frac{1}{r}\frac{\partial}{\partial r}\left(\frac{rz'(r)}{\sqrt{1+(z'(r))^2}}\right) = -\left(\frac{z'(r)}{r\sqrt{1+(z'(r))^2}} + \frac{z''(r)}{\left(1+(z'(r))^2\right)^{\frac{3}{2}}}\right)$$

and by Frenet-Serret:

$$\mathbf{t}\cdot\frac{d\mathbf{n}}{dl} = \kappa = -\frac{z''(r)}{\left(1+(z'(r))^2\right)^{\frac{3}{2}}} \ ,$$

where $\mathbf{t}$ is the unit tangent to the curve, $\mathbf{n}$ is the outward unit normal, κ is the usual curvature of the profile curve and l is the arclength. The curvature due to axisymmetry is:

$$\kappa_{axi} = \frac{n_r}{r} = -\frac{z'(r)}{r\sqrt{1+(z'(r))^2}} \ ,$$

where n_r is the radial component of the normal. One can write:

$$2\mathcal{H} = \frac{n_r}{r} + \kappa = \kappa_{axi} + \kappa \ , \tag{4.11}$$

The second technique consists in approximating the curvature of the profile curve at each node with the inverse of the radius of the circumcircle that contains the current node and its neighbors. From figure 4.3 the radius of the circumcircle satisfies:

$$\frac{1}{R} = \frac{4Area(\widehat{ABC})}{abc} \approx \kappa(\mathbf{x}_i) \ .$$

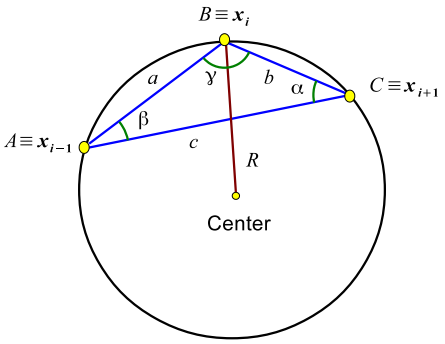

Figure 4.3: Circumcircle passing through node $\mathbf{x}_i$ and its neighbors.

Now, to compute κ_{axi} take the displacement vector:

$$\mathbf{v} = \mathbf{x}_{i+1} - \mathbf{x}_{i-1} \ ,$$

as shown in figure 4.4 to get:

$$\kappa_{axi}\left(\mathbf{x}_i\right) \approx -\frac{dz}{r_i\sqrt{dr^2+dz^2}} \quad , \quad \mathbf{v} = (dr, dz) \quad , \quad \mathbf{x}_i = (r_i, z_i) \ .$$

Observe that for the initial and final nodes $\mathbf{x}_1$ and $\mathbf{x}_N$, since they are located on the axis of rotation, symmetric and virtual nodes must be considered:

$$\mathbf{x}_0 = (-r_1, z_1) \quad , \quad \mathbf{x}_{N+1} = (-r_N, z_N) \ .$$

Moreover, at these nodes we have:

$$\lim_{r\to 0} \frac{z''(r)}{\left(1+\left(z'(r)\right)^2\right)^{\frac{3}{2}}} = \lim_{z'\to 0} \frac{z''(r)}{\left(1+\left(z'(r)\right)^2\right)^{\frac{3}{2}}} = z''(0) \ ,$$

$$\lim_{r\to 0} \frac{z'(r)}{r\sqrt{1+\left(z'(r)\right)^2}} = \lim_{z'\to 0} \frac{z'(r)}{r\sqrt{1+\left(z'(r)\right)^2}} = \lim_{r\to 0} \frac{z'(r)}{r} = z''(0) \ ,$$

where we have used that $z'(0) = 0$. Thus:

$$\kappa\left(x_i\right) = \kappa_{axi}\left(x_i\right) \quad , \quad i \in \{1, N\} \ .$$

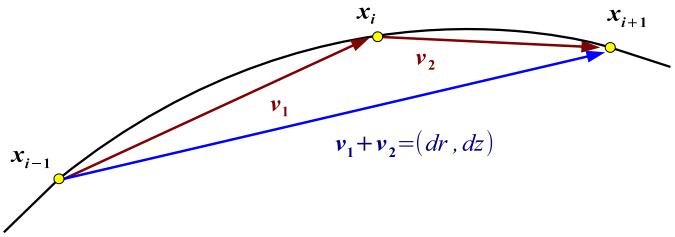

Figure 4.4: Approximate tangent vector at point $\mathbf{x}_i$.

4.2.3. The surface charge density

Consider an axisymmetric drop of conducting fluid that holds an amount of charge Q on its surface. In order to calculate the surface charge density σ, one needs to solve (4.5) and (4.6), which are integral equations in the form:

$$4\pi\varepsilon_0 g\left(\mathbf{x}_0\right) = \int_{\partial\mathcal{D}(t)} \frac{h\left(\mathbf{x}\right)}{\left\|\mathbf{x}-\mathbf{x}_0\right\|}\, dS \quad , \quad \mathbf{x}_0 \in \partial\mathcal{D}\left(t\right) \ ,$$

with $h \equiv \sigma_0$ if $g \equiv 1$ and $h \equiv \sigma_{ind}$ for $g\left(\mathbf{x}\right) = \mathcal{E}_\infty z$. Take a profile curve Γ in the OXZ plane and two points:

$$\mathbf{x} = \left(r\cos\phi, r\sin\phi, z\right) \quad , \quad \mathbf{x}_0 = \left(r_0, 0, z_0\right) \in \Gamma \ ,$$

where $\hat{\mathbf{x}} = \mathbf{x} - \mathbf{x}_0$. One can write:

$$\int_{\partial\mathcal{D}(t)} \frac{1}{\left\|\mathbf{x}-\mathbf{x}_0\right\|}\, dS = \int_\Gamma r\left(\int_0^{2\pi} \frac{d\phi}{\sqrt{\hat{z}^2 + r^2 + r_0^2 - 2rr_0\cos\phi}}\right) dl = \int_\Gamma \frac{4rF\left(k\right)}{\sqrt{\hat{z}^2 + \left(r+r_0\right)^2}}\, dl \ ,$$

where F is the complete elliptic integral of the first kind:

$$F\left(k\right) = \int_0^{\frac{\pi}{2}} \frac{d\phi}{\sqrt{1-k^2\cos^2\phi}} \quad , \quad k^2 = \frac{4rr_0}{\hat{z}^2 + \left(r+r_0\right)^2} \quad , \quad 0 < k^2 < 1 \ . \tag{4.12}$$

Discretize Γ into a collection of nodes $\{\mathbf{x}_i \equiv (r_i, z_i)\}_{i=1}^N$ where the segment have arclengths and midpoints:

$$l_i = \sqrt{\left(r_{i+1}-r_i\right)^2 + \left(z_{i+1}-z_i\right)^2} \quad , \quad \mathbf{x}_i^m \equiv \left(r_i^m, z_i^m\right) = \frac{\mathbf{x}_i + \mathbf{x}_{i+1}}{2} \quad , \quad i \in \{1, \ldots, N-1\} \ .$$

By symmetry, h is constant along a given parallel, and supposing that it is also constant over each segment:

$$\int_{\partial\mathcal{D}(t)} \frac{h\left(\mathbf{x}\right)}{\left\|\mathbf{x}-\mathbf{x}_0\right\|}\, dS = \int_\Gamma rh\left(\mathbf{x}\right)\left(\int_0^{2\pi} \frac{d\phi}{\left\|\mathbf{x}-\mathbf{x}_0\right\|}\right) dl \approx r_j^m h_j \left(\int_0^{2\pi} \frac{d\phi}{\left\|\mathbf{x}_i^m - \mathbf{x}_j^m\right\|}\right) l_j = \mathcal{A}_{ij} h_j \ ,$$

with:

$$h_j \approx h\left(\mathbf{x}_j^m\right) \quad , \quad \mathcal{A}_{ij} = l_j r_j^m \int_0^{2\pi} \frac{d\phi}{\left\|\mathbf{x}_i^m - \mathbf{x}_j^m\right\|} \ , \tag{4.13}$$

our problem reduces to the linear system:

$$\mathbf{g} = \mathcal{A}\mathbf{h} \quad , \quad g_i = 4\pi\varepsilon_0 g\left(\mathbf{x}_i^m\right) \ . \tag{4.14}$$

4.2.4. The velocity field

In this subsection we will obtain the axisymmetric version of (3.23). Considering axial symmetry of the problem about the z axis, which is actually the rotation axis, the boundary integral equation for the velocity field simplifies, as the integrals that involve the azimuthal angle can be calculated explicitly in terms of elliptic functions [56].

Fix a cylindrical coordinate system whose z axis coincides with the rotation axis, and the radial r axis with the cartesian x axis. By a symmetry argument, all variables and physical properties of the system are independent of the azimuthal coordinate ϕ and, since the inertial terms of Navier-Stokes equations are negligible (remeber that we are working with Stokes flow), one can impose without loss of generality that the azimuthal component of all vectors is zero (or constant), in particular the ones corrsponding to the velocity, the normal vector and the traction force over the boundary:

$$u_\phi = n_\phi = f_\phi = 0 \ .$$

Observe that this is possible due to the fact that the equations for the velocity components are decoupled, allowing us to choose any possible solution for the azimuthal velocity without affecting the dynamics of the system. This last hypothesis is not true when Coriolis force is included in Stokes system (in this case the corrsponding equation for the radial velocity is coupled with the one for azimuthal velocity). Now, the differential of area in cylindrical coordinates is:

$$dS = r\, d\phi\, dl \ ,$$

where dl is the arclength differential over the profile curve. In components, the vectors are:

$$\mathbf{f} \equiv \begin{cases} f_x = f_r \cos\phi \\ f_y = f_r \sin\phi \\ f_z = f_z \end{cases} \quad , \quad \mathbf{u} \equiv \begin{cases} u_x = u_r \cos\phi \\ u_y = u_r \sin\phi \\ u_z = u_z \end{cases} \quad , \quad \mathbf{n} \equiv \begin{cases} n_x = n_r \cos\phi \\ n_y = n_r \sin\phi \\ n_z = n_z \end{cases} \quad , \tag{4.15}$$

with $x\,(\equiv r)$, y and z corresponding respectively to the index values 1, 2 and 3 in (3.23). Write:

$$\Theta\left(\phi\right) = \begin{pmatrix} \cos\phi & \sin\phi & 0 \\ 0 & 0 & 1 \end{pmatrix} , \tag{4.16}$$

and introduce (4.15) into the single layer potential integral to yield:

$$\int_{\partial\mathcal{D}(t)} \mathbb{G}_{ij} f_i \; dS = \int_\Gamma \left(f_r, f_z\right) r \left(\int_0^{2\pi} \Theta\left(\phi\right) \begin{pmatrix} \mathbb{G}_{xx} & \mathbb{G}_{xy} & \mathbb{G}_{xz} \\ \mathbb{G}_{yx} & \mathbb{G}_{yy} & \mathbb{G}_{yz} \\ \mathbb{G}_{zx} & \mathbb{G}_{zy} & \mathbb{G}_{zz} \end{pmatrix} d\phi \right) dl \; .$$

The j-th component of the double layer potential is:

$$\int_{\partial\mathcal{D}(t)}^{PV} u_i \mathbb{T}_{ijk} n_k \; dS = \int_\Gamma \left(u_r, u_z\right) r \left(\int_0^{2\pi} \Theta\left(\phi\right) \begin{pmatrix} \mathbb{T}_{xjx} & \mathbb{T}_{xjy} & \mathbb{T}_{xjz} \\ \mathbb{T}_{yjx} & \mathbb{T}_{yjy} & \mathbb{T}_{yjz} \\ \mathbb{T}_{zjx} & \mathbb{T}_{zjy} & \mathbb{T}_{zjz} \end{pmatrix} \Theta\left(\phi\right)^T d\phi \right) \begin{pmatrix} n_r \\ n_z \end{pmatrix} dl \; .$$

Defining:

$$\mathbb{T}^j_\Theta = \Theta \begin{pmatrix} \mathbb{T}_{xjx} & \mathbb{T}_{xjy} & \mathbb{T}_{xjz} \\ \mathbb{T}_{yjx} & \mathbb{T}_{yjy} & \mathbb{T}_{yjz} \\ \mathbb{T}_{zjx} & \mathbb{T}_{zjy} & \mathbb{T}_{zjz} \end{pmatrix} \Theta^T \; , \tag{4.17}$$

we can use the symmetry property, $\mathbb{T}_{ijk} = \mathbb{T}_{kji}$, to write:

$$\mathbb{T}^j_\Theta = \begin{pmatrix} \mathbb{T}_{xjx}\cos^2\phi + \mathbb{T}_{yjy}\sin^2\phi + \mathbb{T}_{xjy}\sin\left(2\phi\right) & \mathbb{T}_{xjz}\cos\phi + \mathbb{T}_{yjz}\sin\phi \\ \mathbb{T}_{zjx}\cos\phi + \mathbb{T}_{zjy}\sin\phi & \mathbb{T}_{zjz} \end{pmatrix} .$$

The equation (3.23) becomes:

$$4\pi\left(\mu_1+\mu_2\right)\mathbf{u} = -\int_\Gamma \int_0^{2\pi} r\left(f_r, f_z\right)\Theta\left(\phi\right)\mathbb{G}\; d\phi\; dl - \left(\mu_1-\mu_2\right)\int_\Gamma \int_0^{2\pi} r\left(u_r, u_z\right)\mathbb{T}_\Theta \begin{pmatrix} n_r \\ n_z \end{pmatrix} \; d\phi\; dl \; .$$

Now, take the profile curve Γ in the OXZ $(\equiv \phi_0 = 0)$ plane and the points:

$$\mathbf{x} = \left(r\cos\phi, r\sin\phi, z\right) \quad , \quad \mathbf{x}_0 = \left(r_0, 0, z_0\right) \in \Gamma \; ,$$

with:

$$\hat{\mathbf{x}} = \mathbf{x} - \mathbf{x}_0 \quad , \quad \left\|\hat{\mathbf{x}}\right\|^2 = \hat{z}^2 + r^2 + r_0^2 - 2rr_0\cos\phi \equiv \Delta \; .$$

In compact form:

$$4\pi\left(\mu_1+\mu_2\right)u_\beta\left(\mathbf{x}_0\right) = -\int_\Gamma f_\alpha\left(\mathbf{x}\right)\mathcal{M}_{\alpha\beta}\left(\mathbf{x},\mathbf{x}_0\right)\; dl - \left(\mu_1-\mu_2\right)\int_\Gamma u_\alpha\left(\mathbf{x}\right)q_{\alpha\beta\gamma}\left(\mathbf{x},\mathbf{x}_0\right)n_\gamma\left(\mathbf{x}\right)\; dl \; ,$$

where $\alpha, \beta, \gamma \in \{x \equiv r, z\}$ and:

$$\mathcal{M} \equiv \begin{pmatrix} \mathcal{M}_{rr} & \mathcal{M}_{rz} \\ \mathcal{M}_{zr} & \mathcal{M}_{zz} \end{pmatrix} = r\int_0^{2\pi} \begin{pmatrix} \mathbb{G}_{xx}\cos\phi + \mathbb{G}_{yx}\sin\phi & \mathbb{G}_{xz}\cos\phi + \mathbb{G}_{yz}\sin\phi \\ \mathbb{G}_{zx} & \mathbb{G}_{zz} \end{pmatrix} \; d\phi \; , \tag{4.18}$$

$$\begin{aligned} q_{\alpha r\gamma} &\equiv \begin{pmatrix} q_{rrr} & q_{rrz} \\ q_{zrr} & q_{zrz} \end{pmatrix} = r\int_0^{2\pi} \mathbb{T}^r_\Theta \; d\phi \; , \\ q_{\alpha z\gamma} &\equiv \begin{pmatrix} q_{rzr} & q_{rzz} \\ q_{zzr} & q_{zzz} \end{pmatrix} = r\int_0^{2\pi} \mathbb{T}^z_\Theta \; d\phi \; . \end{aligned} \tag{4.19}$$

Define the integral:

$$I_{mn}\left(\hat{z},r,r_0\right)=\int_0^{2\pi}\frac{\cos^n\phi}{\Delta^{\frac{m}{2}}}\,d\phi=\frac{4k^m}{\left(4rr_0\right)^{\frac{m}{2}}}\int_0^{\frac{\pi}{2}}\frac{\left(2\cos^2\phi-1\right)^n}{\left(1-k^2\cos^2\phi\right)^{\frac{m}{2}}}\,d\phi\quad,\quad k^2=\frac{4rr_0}{\hat{z}^2+\left(r+r_0\right)^2}\,,\tag{4.20}$$

Indeed:

$$\begin{aligned}\int_0^{2\pi}\frac{\cos^n\phi}{\left(\hat{z}^2+r^2+r_0^2-2rr_0\cos\phi\right)^{\frac{m}{2}}}\,d\phi&=\int_0^{2\pi}\frac{\cos^n\phi}{\left(\hat{z}^2+\left(r+r_0\right)^2-2rr_0\left(\cos\phi+1\right)\right)^{\frac{m}{2}}}\,d\phi=\\&=\frac{k^m}{\left(4rr_0\right)^{\frac{m}{2}}}\int_0^{2\pi}\frac{\left(2\cos^2\left(\frac{\phi}{2}\right)-1\right)^n}{\left(1-k^2\cos^2\left(\frac{\phi}{2}\right)\right)^{\frac{m}{2}}}\,d\phi=\\&=\frac{4k^m}{\left(4rr_0\right)^{\frac{m}{2}}}\int_0^{\frac{\pi}{2}}\frac{\left(2\cos^2\alpha-1\right)^n}{\left(1-k^2\cos^2\alpha\right)^{\frac{m}{2}}}\,d\alpha\,.\end{aligned}$$

Given $0<k^2<1$, the complete elliptic integral of the second kind is:

$$E\left(k\right)=\int_0^{\frac{\pi}{2}}\sqrt{1-k^2\cos^2\phi}\,d\phi\,.\tag{4.21}$$

To calculate $\mathcal{M}$ recall that:

$$\mathbb{G}_{ij}\left(\mathbf{x},\mathbf{x}_0\right)=\frac{\delta_{ij}}{\left\|\mathbf{x}-\mathbf{x}_0\right\|}+\frac{\left(x_i-x_{0,i}\right)\left(x_j-x_{0,j}\right)}{\left\|\mathbf{x}-\mathbf{x}_0\right\|^3}\,.$$

Then:

$$\begin{aligned}\mathcal{M}_{rr}&=r\int_0^{2\pi}\mathbb{G}_{xx}\cos\phi+\mathbb{G}_{yx}\sin\phi\,d\phi=r\int_0^{2\pi}\left(\frac{1}{\sqrt{\Delta}}+\frac{\left(r\cos\phi-r_0\right)^2}{\Delta^{\frac{3}{2}}}\right)\cos\phi+\frac{r\left(r\cos\phi-r_0\right)}{\Delta^{\frac{3}{2}}}\sin^2\phi\,d\phi=\\&=r\left(I_{11}+\left(r^2+r_0^2\right)I_{31}-rr_0\left(I_{30}+I_{32}\right)\right)\,,\\\mathcal{M}_{rz}&=r\int_0^{2\pi}\mathbb{G}_{xz}\cos\phi+\mathbb{G}_{yz}\sin\phi\,d\phi=r\int_0^{2\pi}\frac{\hat{z}\left(r\cos\phi-r_0\right)}{\Delta^{\frac{3}{2}}}\cos\phi+\frac{r\hat{z}}{\Delta^{\frac{3}{2}}}\sin^2\phi\,d\phi=r\hat{z}\left(rI_{30}-r_0I_{31}\right)\,,\\\mathcal{M}_{zr}&=r\int_0^{2\pi}\mathbb{G}_{zx}\,d\phi=r\int_0^{2\pi}\frac{\hat{z}\left(r\cos\phi-r_0\right)}{\Delta^{\frac{3}{2}}}=r\hat{z}\left(rI_{31}-r_0I_{30}\right)\,,\\\mathcal{M}_{zz}&=r\int_0^{2\pi}\mathbb{G}_{zz}\,d\phi=r\int_0^{2\pi}\frac{1}{\sqrt{\Delta}}+\frac{\hat{z}^2}{\Delta^{\frac{3}{2}}}\,d\phi=r\left(I_{10}+\hat{z}^2I_{30}\right)\,.\end{aligned}$$

In order to express $\mathcal{M}$ and q in terms of elliptic integrals use the properties (see [30]):

1. $\displaystyle\int_0^{\frac{\pi}{2}}\frac{d\phi}{\left(1-k^2\cos^2\phi\right)^{\frac{3}{2}}}=\frac{1}{k'^2}E\left(k\right)\,.$
2. $\displaystyle\int_0^{\frac{\pi}{2}}\frac{\cos^2\phi}{\left(1-k^2\cos^2\phi\right)^{\frac{3}{2}}}\,d\phi=\frac{1}{k^2}\left(\frac{1}{k'^2}E\left(k\right)-F\left(k\right)\right)\,.$
3. $\displaystyle\int_0^{\frac{\pi}{2}}\frac{\cos^2\phi}{\sqrt{1-k^2\cos^2\phi}}\,d\phi=\frac{1}{k^2}\left(F\left(k\right)-E\left(k\right)\right)\,.$
4. $\displaystyle\int_0^{\frac{\pi}{2}}\frac{\cos^4\phi}{\left(1-k^2\cos^2\phi\right)^{\frac{3}{2}}}\,d\phi=\frac{1}{k^4}\left(\left(1+\frac{1}{k'^2}\right)E\left(k\right)-2F\left(k\right)\right)\,.$
5. $\displaystyle\int_0^{\frac{\pi}{2}}\frac{d\phi}{\left(1-k^2\cos^2\phi\right)^{\frac{5}{2}}}=\frac{1}{3k'^2}\left(\left(2+\frac{2}{k'^2}\right)E\left(k\right)-F\left(k\right)\right)\,.$

where:

$$k'^2 = 1 - k^2 = \frac{\widehat{x}^2 k^2}{4rr_0} \quad , \quad \widehat{x} = \widehat{z} + (r - r_0)^2 \ .$$

We have that:

$$\begin{aligned}
\mathcal{M}_{zz} &= 2k\sqrt{\frac{r}{r_0}}\left(F\left(k\right) + \frac{\widehat{z}^2}{\widehat{x}^2}E\left(k\right)\right) \ , \\
\mathcal{M}_{rz} &= k\frac{\widehat{z}}{\sqrt{rr_0}}\left(F\left(k\right) + \frac{r^2 - r_0^2 - \widehat{z}^2}{\widehat{x}^2}E\left(k\right)\right) \ , \\
\mathcal{M}_{zr} &= -k\frac{\widehat{z}}{r_0}\sqrt{\frac{r}{r_0}}\left(F\left(k\right) + \frac{r_0^2 - r^2 - \widehat{z}^2}{\widehat{x}^2}E\left(k\right)\right) \ , \\
\mathcal{M}_{rr} &= \frac{k}{rr_0}\sqrt{\frac{r}{r_0}}\left(\left(2\widehat{z}^2 + r^2 + r_0^2\right)F\left(k\right) - \frac{2\widehat{z}^4 + 3\widehat{z}^2\left(r^2 + r_0^2\right) + \left(r^2 - r_0^2\right)^2}{\widehat{x}^2}E\left(k\right)\right) \ .
\end{aligned}$$

Consider now the coefficients of tensor q. Recall that:

$$\mathbb{T}_{ijk}\left(\mathbf{x}, \mathbf{x}_0\right) = -6\frac{\left(x_i - x_{0,i}\right)\left(x_j - x_{0,j}\right)\left(x_k - x_{0,k}\right)}{\left\|\mathbf{x} - \mathbf{x}_0\right\|^5} \ ,$$

so one can write:

$$\begin{aligned}
q_{zzz} &= r\int_0^{2\pi} \mathbb{T}_{zzz}\, d\phi = -6r\widehat{z}^3 I_{50} = 4k\frac{\widehat{z}^3}{\widehat{x}^4}\sqrt{\frac{r}{r_0}}\left(\left(1 - k^2\right)F\left(k\right) - 2\left(2 - k^2\right)E\left(k\right)\right) \ , \\
q_{rzr} &= r\int_0^{2\pi} \mathbb{T}_{xzx}\cos^2\phi + \mathbb{T}_{yzy}\sin^2\phi + \mathbb{T}_{xzy}\sin\left(2\phi\right)\, d\phi = -6r\widehat{z}\left(r^2 I_{50} + r_0^2 I_{52} - 2rr_0 I_{51}\right) \ , \\
q_{zzr} &= q_{rzz} = r\int_0^{2\pi} \mathbb{T}_{zzx}\cos\phi + \mathbb{T}_{zzy}\sin\phi\, d\phi = -6r\widehat{z}^2\left(rI_{50} - r_0 I_{51}\right) \ , \\
q_{zrz} &= r\int_0^{2\pi} \mathbb{T}_{zxz}\, d\phi = -6r\widehat{z}^2\left(rI_{51} - r_0 I_{50}\right) \ , \\
q_{zrr} &= q_{rrz} = r\int_0^{2\pi} \mathbb{T}_{zxx}\cos\phi + \mathbb{T}_{zxy}\sin\phi\, d\phi = -6r\widehat{z}\left(\left(r^2 + r_0^2\right)I_{51} - rr_0\left(I_{50} + I_{52}\right)\right) \ , \\
q_{rrr} &= r\int_0^{2\pi} \mathbb{T}_{xxx}\cos^2\phi + \mathbb{T}_{yxy}\sin^2\phi + \mathbb{T}_{xxy}\sin\left(2\phi\right)\, d\phi = \\
&= -6r\left(r^3 I_{51} + rr_0^2\left(2I_{51} + I_{53}\right) - r_0^3 I_{52} - r_0 r^2\left(I_{50} + 2I_{52}\right)\right) \ .
\end{aligned}$$

When approximating elliptic functions, one can use the following recursive relations [18]:

$$F\left(k\right) = \frac{\pi}{2}\prod_{i=1}^{\infty}(1 + k_i) \quad , \quad E\left(k\right) = F\left(k\right)\left(1 - \frac{k^2}{2}p\right) \ ,$$

where:

$$\begin{cases} k_0 = k \\ k_i = \dfrac{1 - c}{1 + c} \end{cases} \quad , \quad c = \sqrt{1 - k_{i-1}^2} \quad , \quad p = 1 + \frac{k_1}{2}\left(1 + \frac{k_2}{2}\left(\cdots\right)\right) \ .$$

A different way is to employ the polynomial approximations in [1]. Notice that, when $\mathbf{x}$ is close to $\mathbf{x}_0$, k tends to 1 and F gets an infinite value. To study the behaviour of $\mathcal{M}$ use the asymptotic expansions:

$$F\left(k\right) \approx \ln\left(\frac{4}{\sqrt{1 - k^2}}\right) + \cdots \approx -\ln\widehat{x} + \cdots \quad , \quad E\left(k\right) \approx 1 + \cdots \ ,$$

obtaining that the off-diagonal coefficients of $\mathcal{M}$ take finite values, whereas those on the diagonal present logarithmic singularities $\mathcal{M}_{rr} \approx -2\ln\widehat{x} + \cdots$ and $\mathcal{M}_{zz} \approx -2\ln\widehat{x} + \cdots$.

4.3. The 3D problem

This section presents in detail all the steps necessary to implement the numerical method that simulates drop evolution in 3D. We start by discretising the surface of the drop with a triangle mesh $\mathcal{M} = (\mathbb{V}, \mathcal{F})$, formed by a family of vertices $\mathbb{V} = \{V_1, \ldots, V_N\}$ and faces $\mathcal{F} = \{F_1, \ldots, F_M\}$ so that:

$$\partial\mathcal{D}(t) \approx \mathcal{P}(t) \quad , \quad \mathcal{P}(t) = \bigcup_{i=1}^{M} F_i \ . \tag{4.22}$$

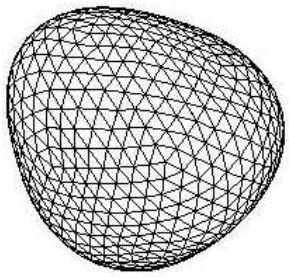

Figure 4.5: Triangle mesh.

A triangle facet $F_m \in \mathcal{F}$ is defined by three vertices:

$$\mathcal{V}_m = \{V_m^1, V_m^2, V_m^3\} \ ,$$

and any point $\mathbf{x}^m$ inside that triangle can be described with barycentric coordinates:

$$\mathbf{x}^m \equiv \mathbf{x}^m(\boldsymbol{\tau}) = \tau_i \mathbf{x}_m^i \quad , \quad \sum_{i=1}^{3} \tau_i = 1 \quad , \quad \boldsymbol{\tau} = (\tau_1, \tau_2, \tau_3)^T \ ,$$

where $\mathbf{x}_m^i$ are the coordinates of V_m^i. Given a vertex $V_n \in \mathbb{V}$, the set of triangles sharing that vertex is:

$$\mathcal{F}_n = \{F_n^1, \ldots, F_n^{N_n}\} = \{F_m \in \mathcal{F} \mid V_n \in \mathcal{V}_m\} \ ,$$

and its degree:

$$deg(V_n) = \#(\mathcal{F}_n) = N_n \ .$$

For any vertex $V_n \in \mathbb{V}$ and triangle $F_m \in \mathcal{F}$ with $V_n \in \mathcal{V}_m$, define $I(m,n)$ as the unique integer satisfying:

$$V_m^{I(m,n)} = V_n \ .$$

Another important concept is the adjacency function $\mathcal{A}$ which is defined as follows:

$$\mathcal{A} : \mathbb{V} \times \mathbb{V} \to \{0,1\} \quad , \quad \alpha_{ij} \equiv \mathcal{A}(V_i, V_j) = \begin{cases} 1 \ , & \text{if } V_i \text{ and } V_j \text{ are connected by an edge} \\ 0 \ , & \text{otherwise} \end{cases} \ .$$

Now, any scalar property $f : \partial\mathcal{D}(t) \to \mathbb{R}$ can be approximated by a function $\tilde{f} : \mathcal{P}(t) \to \mathbb{R}$ which is linear over each triangle of the mesh. With this assumption, one can calculate the value of the function at any point inside a triangle $F_m \in \mathcal{F}$ just by knowing the barycentric coordinates of that point and the values of the function at the triangle vertices:

$$\tilde{f}(\mathbf{x}^m) \equiv \tilde{f}(\mathbf{x}^m(\boldsymbol{\tau})) = \tau_i f\left(\mathbf{x}_m^i\right) \ .$$

Using a gaussian quadrature formula with G points, the integral of a scalar function over the interface is:

$$\int_{\partial\mathcal{D}(t)} f(\mathbf{x}) \ dS \approx \int_{\mathcal{P}(t)} \tilde{f}(\mathbf{x}) \ dS = \sum_{F_m \in \mathcal{F}} \int_{F_m} \tilde{f}(\mathbf{x}) \ dS \approx \tau_i^p f\left(\mathbf{x}_m^i\right) w_p A_m \ ,$$

where w_p are the weights, A_m is the area of triangle F_m and $(\tau_1^p, \tau_2^p, \tau_3^p)$ are the barycentric coordinates of the gaussian point p. The area of the triangles is:

$$A_m = \frac{\left\| \left(\mathbf{x}_m^2 - \mathbf{x}_m^1\right) \times \left(\mathbf{x}_m^3 - \mathbf{x}_m^1\right) \right\|}{2} \,. \tag{4.23}$$

In matrix form:

$$\int_{\mathcal{P}(t)} \tilde{f}\left(\mathbf{x}\right)\, dS \approx A_m \mathbf{f}_m^T \mathcal{T} \mathbf{w} \quad , \quad \mathbf{f}_m = \begin{pmatrix} f\left(\mathbf{x}_m^1\right) \\ f\left(\mathbf{x}_m^2\right) \\ f\left(\mathbf{x}_m^3\right) \end{pmatrix} \quad , \quad \mathbf{w} = \begin{pmatrix} w_1 \\ \vdots \\ w_G \end{pmatrix} \quad , \quad \mathcal{T}_{ip} = \tau_i^p \,. \tag{4.24}$$

n	W_i	ζ_1^i	ζ_2^i, ζ_3^i	M	p
1	1.000000000000000	0.333333333333333	0.333333333333333		1
			0.333333333333333	1	
3	0.333333333333333	0.666666666666667	0.166666666666667		2
			0.166666666666667	3	
4	-0.562500000000000	0.333333333333333	0.333333333333333		3
			0.333333333333333	1	
	0.520833333333333	0.600000000000000	0.200000000000000		
			0.200000000000000	3	
6	0.109951743655322	0.816847572980459	0.091576213509771		4
			0.091576213509771	3	
	0.223381589678011	0.108103018168070	0.445948490915965		
			0.445948490915965	3	
7	0.225000000000000	0.333333333333333	0.333333333333333		5
			0.333333333333333	1	
	0.125939180544827	0.797426985353087	0.101286507323456		
			0.101286507323456	3	
	0.132394152788506	0.059715871789770	0.470142064105115		
			0.470142064105115	3	

Figure 4.6: Gaussian quadrature points to interpolate a function over a flat triangle.

4.3.1. Volume and moment of inertia

To deal with the evolution of rotating droplets at constant angular momentum, one needs to compute their moment of inertia when the boundary is approximated by a triangle mesh. A simple and efficient numerical algorithm, which is described in detail in [40], is briefly introduced here for this purpose. The moment of inertia about the z axis of a drop with constant density ϱ_1 is given by the formula:

$$\mathcal{I} = \varrho_1 \int_{\mathcal{D}_1(t)} (x^2 + y^2)\, d\mathbf{x} \,,$$

where $\mathcal{D}_1(t)$ is the region occupied by the droplet. To calculate this integral, consider $\mathcal{P}(t)$ as the polyhedral solid approximation of $\mathcal{D}_1(t)$ whose facets $\mathcal{F}$ are triangles. Thus, $\mathcal{P}(t)$ can be conceived as a signed sum of tetrahedra, $\mathcal{C}_{\mathcal{P}}(t)$, where its elements are constructed from the origin to the vertices of each of the triangle

facets $F \in \mathcal{F}$. The sign of the contribution for each tetrahedron $\mathcal{T}$, $\epsilon(\mathcal{T})$, is determined by the dot product between the barycenter of the facet and the outward unit normal vector to that triangle, namely:

$$\epsilon(\mathcal{T}) = \text{sign}\left(\mathbf{b}_F \cdot \mathbf{n}_F\right) \ .$$

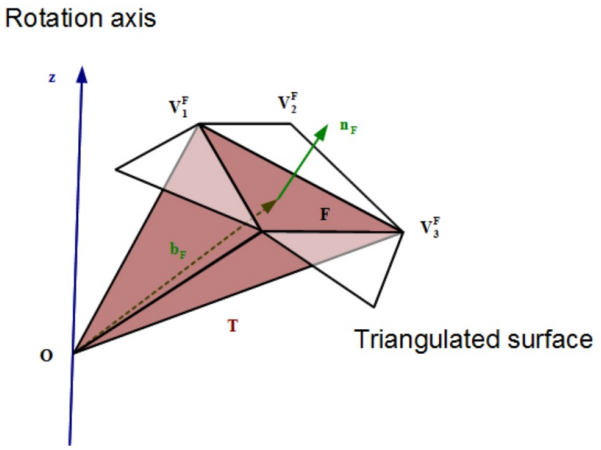

Figure 4.7: Tetrahedron defined to compute the moment of inertia.

This yields the following approximation:

$$\mathcal{I} = \varrho_1 \int_{\mathcal{D}_1(t)} (x^2 + y^2)\, d\mathbf{x} \approx \varrho_1 \sum_{\mathcal{T} \in \mathcal{C}_\mathcal{P}(t)} \int_{\mathcal{T}} (x^2 + y^2)\, d\mathbf{x} \ ,$$

which can be precisely computed as the integral of an homogeneous quadratic polynomial $f(x, y, z)$ (in our case $f(x, y, z) = x^2 + y^2$) over a tetrahedron $\mathcal{T} \in \mathcal{C}_\mathcal{P}(t)$ whose surface triangle vertices $\left(V_1^F, V_2^F, V_3^F\right)$ satisfy:

$$\int_{\mathcal{T}} f(x, y, z)\, d\mathbf{x} = \frac{\nu\left(\mathcal{T}\right)}{20} \left(f\left(V_1^F\right) + f\left(V_2^F\right) + f\left(V_3^F\right) + f\left(V_1^F + V_2^F + V_3^F\right)\right) \ ,$$

where $\nu(\mathcal{T})$ is the signed volume of the tetrahedron $\mathcal{T}$:

$$\nu\left(\mathcal{T}\right) = \epsilon\left(\mathcal{T}\right) \frac{\left|\det\left(V_1^F, V_2^F, V_3^F\right)\right|}{6} \ .$$

Note that with this method, one can easily calculate the drop's volume by applying:

$$V = \varrho_1 \int_{\mathcal{D}_1(t)} d\mathbf{x} \approx \varrho_1 \sum_{\mathcal{T} \in \mathcal{C}_\mathcal{P}(t)} \nu(\mathcal{T}) \ .$$

The accuracy of this method has been tested to measure its convergence for spheroids and ellipsoids, and results show that the relative error follows the laws:

$$e_{rel} \ \propto \ \frac{1}{N} \quad , \quad e_{rel} \ \propto \ \sqrt{h} \ ,$$

where N is the number of vertices and h is a measure of the mesh size, which has been calculated as:

$$h = \frac{2}{\sqrt[4]{3}} \max_{F \in \mathcal{F}} \sqrt{Area\left(F\right)} \ ,$$

with h the maximum edge length, regarding each triangle as being equilateral.

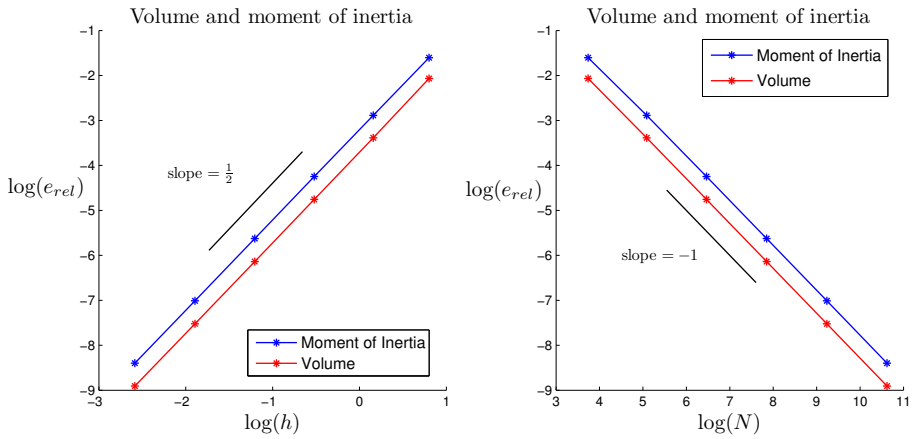

Figure 4.8: Volume and moment of inertia computation for an oblate spheroid with semiaxes $a = 4$ and $c = 1$.

4.3.2. Mean curvature

Throughout the literature, one can find many different techniques to compute the mean curvature of a surface described by a triangle mesh [67]. The method that we will use here is called the *iterative paraboloid fitting method* and is described in detail in [75]. The basic idea is to calculate the mean curvature at each node of the mesh by approximating the surface locally, with the least-squares method, by a paraboloid, and taking for the mean curvature at that vertex the one for the paraboloid.

Suppose that we want to calculate the mean curvature at point P. Set local coordinates at that point (make P the origin) and take the z-axis in that frame to be the normal vector. Then we look for:

$$z = f(x, y) = Ax^2 + Bxy + Cy^2 + Dx + Ey \,, \tag{4.25}$$

containing P and its neighbor nodes which minimizes:

$$F = \sum_{i=1}^{N_P} \frac{\left(Ax_i^2 + Bx_iy_i + Cy_i^2 + Dx_i + Ey_i - z_i\right)^2}{x_i^2 + y_i^2 + z_i^2} \quad , \quad N_P \equiv \text{number of neighbors of } P \,, \tag{4.26}$$

where $\bar{\mathbf{r}}_i = (x_i, y_i, z_i)$ are the local coordinates of the neighbor point P_i. The weights $w_i = \left(x_i^2 + y_i^2 + z_i^2\right)^{-1}$ in F are taken so that the closest neighbors contribute the most. However, the normal vector at P is not known *a priori*, so the method should be implemented to be iterative. To start the method, take as an approximation to the normal vector at vertex P the one corresponding to the previous evolution time step, $\mathbf{n}_P^{t-\Delta t}$. For the initial time $t = 0$, since we start our simulations from nearly spherical droplets, the approximation to the normal can be chosen to be the normalized position vector of vertex P. Now, set a coordinate frame centered at P, with that approximate normal as its z-axis, and find the paraboloid which passes through P and best fits its neighbors. The new normal to this paraboloid is then used as the new z-axis and this process is repeated until convergence is reached. Then, the mean curvvature and the normal vector at point P are given by the resulting paraboloid.

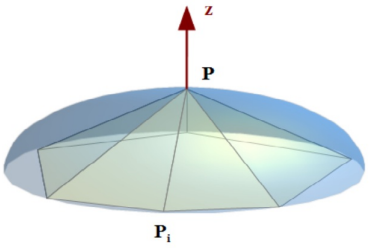

Figure 4.9: Paraboloid that best fits P and its neighbors.

Given a surface in the form $z = f(x,y)$, where (x,y,z) are the relative coordinates to P in the frame where the approximate normal is the z-axis, the mean and gaussian curvatures can be written as [19]:

$$\mathcal{H} = \frac{2\,\frac{\partial f}{\partial x}\frac{\partial f}{\partial y}\frac{\partial^2 f}{\partial x \partial y} - \left(1+\left(\frac{\partial f}{\partial x}\right)^2\right)\frac{\partial^2 f}{\partial y^2} - \left(1+\left(\frac{\partial f}{\partial y}\right)^2\right)\frac{\partial^2 f}{\partial x^2}}{2\left(1+\left(\frac{\partial f}{\partial x}\right)^2+\left(\frac{\partial f}{\partial y}\right)^2\right)^{\frac{3}{2}}} \quad , \quad \mathcal{K} = \frac{\frac{\partial^2 f}{\partial x^2}\frac{\partial^2 f}{\partial y^2} - \left(\frac{\partial^2 f}{\partial x \partial y}\right)^2}{\left(1+\left(\frac{\partial f}{\partial x}\right)^2+\left(\frac{\partial f}{\partial y}\right)^2\right)^2} \,.$$

At point P, $\bar{\mathbf{r}}_P = (0,0,0)$, and thus:

$$\mathcal{H}_P = \frac{DEB - \left(1+D^2\right)C - \left(1+E^2\right)A}{\left(1+D^2+E^2\right)^{\frac{3}{2}}} \quad , \quad \mathcal{K}_P = \frac{4AC - B^2}{\left(1+D^2+E^2\right)^2} \,. \tag{4.27}$$

The unit normal vector $\mathbf{n}_P$ at P is the cross product of the tangent vectors $\mathbf{t}_x^P$ and $\mathbf{t}_y^P$:

$$\mathbf{n}_P = \frac{\mathbf{t}_x^P \times \mathbf{t}_y^P}{\left\|\mathbf{t}_x^P \times \mathbf{t}_y^P\right\|} = \frac{(-D,-E,1)}{\sqrt{1+D^2+E^2}} \,, \tag{4.28}$$

where:

$$\mathbf{t}_x^P = \left(1,0,\frac{\partial f}{\partial x}(0,0)\right) = (1,0,D) \quad , \quad \mathbf{t}_y^P = \left(0,1,\frac{\partial f}{\partial y}(0,0)\right) = (0,1,E) \,.$$

To set $\mathbf{n}_P^{t-\Delta t}$ as the z-axis of the local frame, perform a rotation in space of angle $\phi = 180°$ about the axis:

$$\mathbf{h} = \frac{\hat{\mathbf{z}} + \mathbf{n}_P^{t-\Delta t}}{\left\|\hat{\mathbf{z}} + \mathbf{n}_P^{t-\Delta t}\right\|} \quad , \quad \hat{\mathbf{z}} = (0,0,1) \,, \tag{4.29}$$

by applying Rodrigues' rotation formula [74]:

$$\mathbf{v}_{rot} = \mathbf{v}\cos\phi + (\mathbf{h}\times\mathbf{v})\sin\phi + \mathbf{h}\,(\mathbf{h}\cdot\mathbf{v})\,(1-\cos\phi) \,,$$

where $\mathbf{v}_{rot}$ is the rotated vector.

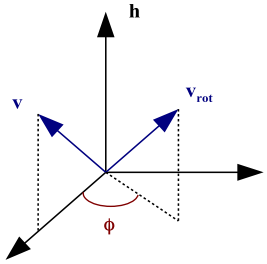

Figure 4.10: Rotation of vector $\mathbf{v}$ and angle ϕ about the h axis.

Observe that to avoid $\left\|\hat{\mathbf{z}} + \mathbf{n}_P^{t-\Delta t}\right\| = 0$ one could set:

$$\mathbf{h} = (1,0,0) \quad \text{whenever} \quad \left\|\hat{\mathbf{z}} + \mathbf{n}_P^{t-\Delta t}\right\| \ll 1 \,.$$

Now, all neighbor nodes must be expressed in the local frame:

$$\begin{aligned} \bar{\mathbf{r}}_i &= \mathbf{r}_P - \mathbf{r}_i \\ \bar{\mathbf{r}}_{i,rot} &= 2\mathbf{h}\,(\mathbf{h}\cdot\bar{\mathbf{r}}_i) - \bar{\mathbf{r}}_i \end{aligned} \quad , \tag{4.30}$$

and to minimize F we proceed in the usual way:

$$F \equiv F(A,B,C,D,E) \quad \text{minimum} \quad \Leftrightarrow \quad \nabla F = \mathbf{0} \,. \tag{4.31}$$

Consequently:

$$\begin{aligned}
\frac{\partial F}{\partial A} &= \sum_{i=1}^{N_P} \frac{\left(Ax_i^2 + Bx_iy_i + Cy_i^2 + Dx_i + Ey_i - z_i\right)}{w_i} x_i^2 = 0 \\
\frac{\partial F}{\partial B} &= \sum_{i=1}^{N_P} \frac{\left(Ax_i^2 + Bx_iy_i + Cy_i^2 + Dx_i + Ey_i - z_i\right)}{w_i} x_iy_i = 0 \\
\frac{\partial F}{\partial C} &= \sum_{i=1}^{N_P} \frac{\left(Ax_i^2 + Bx_iy_i + Cy_i^2 + Dx_i + Ey_i - z_i\right)}{w_i} y_i^2 = 0 \\
\frac{\partial F}{\partial D} &= \sum_{i=1}^{N_P} \frac{\left(Ax_i^2 + Bx_iy_i + Cy_i^2 + Dx_i + Ey_i - z_i\right)}{w_i} x_i = 0 \\
\frac{\partial F}{\partial E} &= \sum_{i=1}^{N_P} \frac{\left(Ax_i^2 + Bx_iy_i + Cy_i^2 + Dx_i + Ey_i - z_i\right)}{w_i} y_i = 0
\end{aligned} \quad .$$

In matrix form:

$$M\mathbf{c} = \mathbf{s} \, ,$$

where:

$$M = \sum_{i=1}^{N_P} \frac{1}{w_i} \begin{pmatrix} x_i^4 & x_i^3y_i & x_i^2y_i^2 & x_i^3 & x_i^2y_i \\ x_i^3y_i & x_i^2y_i^2 & x_iy_i^3 & x_i^2y_i & x_iy_i^2 \\ x_i^2y_i^2 & x_iy_i^3 & y_i^4 & x_iy_i^2 & y_i^3 \\ x_i^3 & x_i^2y_i & x_iy_i^2 & x_i^2 & x_iy_i \\ x_i^2y_i & x_iy_i^2 & y_i^3 & x_iy_i & y_i^2 \end{pmatrix} \quad , \quad \mathbf{c} = \begin{pmatrix} A \\ B \\ C \\ D \\ E \end{pmatrix} \quad , \quad \mathbf{s} = \sum_{i=1}^{N_P} \frac{z_i}{w_i} \begin{pmatrix} x_i^2 \\ x_iy_i \\ y_i^2 \\ x_i \\ y_i \end{pmatrix} . \tag{4.32}$$

An important observation about this method is that it requires all the nodes of the mesh to have at least 5 neighbors in order for the paraboloid fit to work properly, since (4.25) has that number of free parameters.

Algorithm 1 Mean and gaussian curvatures computation

1: Let $\mathbf{n}_0 \equiv \mathbf{n}_P^{t-\Delta t}$ be an initial approximation to the outward unit normal at P.
2: $i \leftarrow 0$.
3: **repeat**
4: Choose local coordinates with origin at P and the z-axis along $\mathbf{n}_i$.
5: Find the coefficients A, B, C, D and E which minimize:

$$F = \sum_{i=1}^{N_P} \frac{\left(Ax_i^2 + Bx_iy_i + Cy_i^2 + Dx_i + Ey_i - z_i\right)^2}{x_i^2 + y_i^2 + z_i^2} \quad , \quad N_P \equiv \text{number of neighbors of } P \, .$$

6: Take the normal:

$$\mathbf{n}_{_P} = \frac{(-D, -E, 1)}{\sqrt{1 + D^2 + E^2}} \, ,$$

as a new approximation in the rotated frame.
7: Return the normal to the original frame:

$$\mathbf{n}_{i+1} = 2\mathbf{h}\left(\mathbf{h} \cdot \mathbf{n}_{_P}\right) - \mathbf{n}_{_P} \, .$$

8: $i \leftarrow i + 1$.
9: **until** $\|\mathbf{n}_{i+1} - \mathbf{n}_i\| < \varepsilon$.
10:

$$\mathcal{H}_P \leftarrow \frac{DEB - \left(1 + D^2\right)C - \left(1 + E^2\right)A}{\left(1 + D^2 + E^2\right)^{\frac{3}{2}}} \quad , \quad \mathcal{K}_P \leftarrow \frac{4AC - B^2}{\left(1 + D^2 + E^2\right)^2} \, .$$

The accuracy of this method has been tested for spheroids and ellipsoid to find that the mean relative error, $[e_{rel}]$, follows the laws:

$$[e_{rel}] \quad \propto \quad N^{-0.937} \quad , \quad [e_{rel}] \quad \propto \quad [h]^{1.875} \, , \tag{4.33}$$

where N is the number of vertices and $[h]$ is a measure of the mean mesh size:

$$[h] = \frac{2}{\sqrt[4]{3}} \frac{1}{N_{\mathcal{F}}} \sum_{F \in \mathcal{F}} \sqrt{Area\,(F)} \quad ,$$

with $N_{\mathcal{F}}$ the number of triangles. The maximum mesh size, h, has been calculated as:

$$h = \frac{2}{\sqrt[4]{3}} \max_{F \in \mathcal{F}} \sqrt{Area\,(F)} \, ,$$

with h the maximum edge length, regarding each triangle as being equilateral.

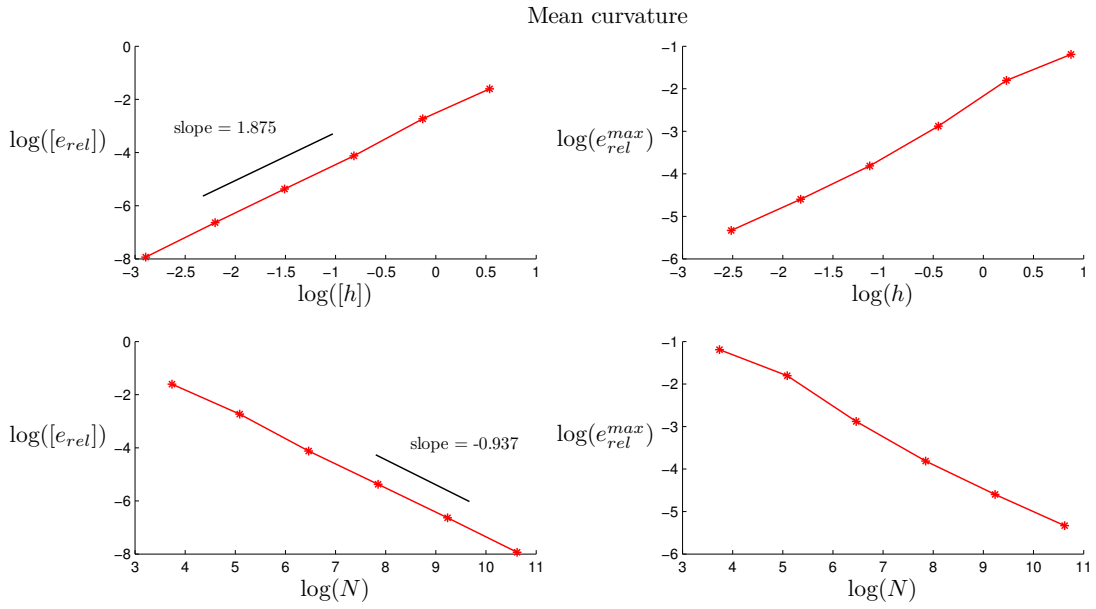

Figure 4.11: Mean curvature for an oblate spheroid with semiaxes $a = 4$ and $c = 1$.

Finally, it is important to introduce the concept of radius of curvature, which plays a key role in the local refinement and smoothing techniques implemented to regularize the triangle mesh as it evolves with time. This property can be derived from the mean and gaussian curvatures in the following way: it is well known [19] that the principal curvatures at a point P, κ_1^P and κ_2^P, satisfy:

$$\mathcal{H}_P = \frac{\kappa_1^P + \kappa_2^P}{2} \quad , \quad \mathcal{K}_P = \kappa_1^P \kappa_2^P \, ,$$

and thus can be computed by solving the quadratic polynomial:

$$x^2 - 2\mathcal{H}_p x + \mathcal{K}_P = 0 \, .$$

Then, the radius of curvature at P, r_c^P, is defined as the inverse of the maximum principal curvature $\kappa_{\max}^P$:

$$r_c^P = \frac{1}{\kappa_{\max}^P} \quad , \quad \kappa_{\max}^P = \max\{|\kappa_1^P| \, , |\kappa_2^P|\} \, . \tag{4.34}$$

4.3.3. The surface charge density

Before calculating the velocity field at the drop's interface (3.23), one has to determine the surface charge density by solving 4.5 and 4.6, which are two integral equations in the general form:

$$4\pi\varepsilon_0 g\,(\mathbf{x}) = \int_{\partial\mathcal{D}(t)} h\,(\mathbf{x}')\, K\,(\mathbf{x}, \mathbf{x}')\; dS \quad , \quad K\,(\mathbf{x}, \mathbf{x}') = \frac{1}{\|\mathbf{x} - \mathbf{x}'\|} \, , \tag{4.35}$$

where $h \equiv \sigma_0$ when $g \equiv 1$ and $h \equiv \sigma_{ind}$ for $g(\mathbf{x}) = \mathcal{E}_{\mathscr{O}} z$. We have implemented two different algorithms to invert numerically (4.35):

1. Using linear interpolation and gaussian quadrature formulas with 16 points:

$$\begin{aligned} 4\pi\varepsilon_0 g(\mathbf{x}) &= \int_{\partial\mathcal{D}(t)} h\left(\mathbf{x}'\right) K\left(\mathbf{x},\mathbf{x}'\right)\, dS \approx \sum_{F_m\in\mathcal{F}} \int_{F_m} h\left(\mathbf{x}'\right) K\left(\mathbf{x},\mathbf{x}'\right)\, dS \approx \\ &\approx \sum_{F_m\in\mathcal{F}} h\left(\mathbf{x}^m\left(\boldsymbol{\tau}_p\right)\right) K\left(\mathbf{x},\mathbf{x}^m\left(\boldsymbol{\tau}_p\right)\right) A_m w_p \approx \sum_{F_m\in\mathcal{F}} \tau_i^p h_m^i K\left(\mathbf{x},\mathbf{x}^m\left(\boldsymbol{\tau}_p\right)\right) A_m w_p \ , \end{aligned} \tag{4.36}$$

where A_m the area of triangle F_m and:

$$h_m^i \approx h\left(\mathbf{x}_m^i\right) \quad , \quad \mathbf{x}^m\left(\boldsymbol{\tau}_p\right) = \sum_{i=1}^{3} \tau_i^p \mathbf{x}_m^i \ .$$

We know that for each $i \in \{1,2,3\}$ and $F_m \in \mathcal{F}$ there exists an unique $V_n \in \mathbb{V}$ such that:

$$h_m^i = h_m^{I(m,n)} \equiv h_n \approx h\left(\mathbf{x}_n\right) \ ,$$

where $\mathbf{x}_n$ are the coordinates of vertex V_n. We can then rearrange (4.36) to yield:

$$4\pi\varepsilon_0 g(\mathbf{x}) \approx \sum_{V_n\in\mathbb{V}} \sum_{F_m\in\mathcal{F}_n} \tau_{I(m,n)}^p K\left(\mathbf{x},\mathbf{x}^m\left(\boldsymbol{\tau}_p\right)\right) A_m w_p h_n \ .$$

Evaluating this expression at the collocation points (vertices of the mesh) we obtain the linear system:

$$4\pi\varepsilon_0 g_t = \sum_{V_n\in\mathbb{V}} \left(\sum_{F_m\in\mathcal{F}_n} \tau_{I(m,n)}^p K\left(\mathbf{x}_t,\mathbf{x}^m\left(\boldsymbol{\tau}_p\right)\right) A_m w_p \right) h_n = \mathbb{A}_{tn} h_n \quad , \quad g_t = g\left(\mathbf{x}_t\right) \ . \tag{4.37}$$

Observe that, whenever we compute $\mathbb{A}_{tn}$ such that $\mathcal{F}_t \bigcap \mathcal{F}_n \neq \varnothing$ (in particular, if $t = n$), we need to be very careful because K may diverge. Indeed, since $\mathbf{x}_t$ and $\mathbf{x}^m\left(\boldsymbol{\tau}_p\right)$ both belong to the same triangle facet, their dstance may become zero. This results in an important source of numerical error if not handled appropriately. To avoid it, we use a singularity removal technique. Take $F_m \in \mathcal{F}$ and set the collocation point $\mathbf{x} = \mathbf{x}_m^i \in \mathcal{V}_m$ (the collocation point is a vertex of F_m). Adding and subtracting the value of h at $\mathbf{x}_m^i$ one gets:

$$\int_{F_m} h\left(\mathbf{x}'\right) K\left(\mathbf{x}_m^i,\mathbf{x}'\right)\, dS = \int_{F_m} \left(h\left(\mathbf{x}'\right) - h_m^i\right) K\left(\mathbf{x}_m^i,\mathbf{x}'\right)\, dS + h_m^i \int_{F_m} K\left(\mathbf{x}_m^i,\mathbf{x}'\right)\, dS \ . \tag{4.38}$$

If we suppose that h is lipschitz continuous:

$$\left|h\left(\mathbf{x}'\right) - h_m^i\right| \leqslant C K\left(\mathbf{x}_m^i,\mathbf{x}'\right) \ ,$$

the first integral on the RHS of (4.38) can be computed accurately with a gaussian quadrature formula:

$$\int_{F_m} \left(h\left(\mathbf{x}'\right) - h_m^i\right) K\left(\mathbf{x}_m^i,\mathbf{x}'\right)\, dS \approx \left(\tau_i^p - 1\right) K\left(\mathbf{x}_m^i,\mathbf{x}^m\left(\boldsymbol{\tau}_p\right)\right) w_p A_m h_m^i \ .$$

Now, we can easily derive an analytical expression for the second integral on the RHS of (4.38). Indeed, taking the vertex V_m^i as the origin of a polar coordinate frame over the triangle (see figure 4.12):

$$S_m^i = \int_{F_m} K\left(\mathbf{x}_m^i,\mathbf{x}'\right)\, dS = \int_{-\theta_1}^{\theta_2} \int_0^{\frac{h}{\cos\varphi}} dr d\varphi = h \int_{-\theta_1}^{\theta_2} \frac{d\varphi}{\cos\varphi} = h\left(\operatorname{arctanh}\left(\cos\varphi_1\right) + \operatorname{arctanh}\left(\cos\varphi_2\right)\right) \ ,$$

where:

$$h = \left\|\mathbf{x}_m^i - \mathbf{x}_B\right\| \sin\varphi_1 \quad , \quad \cos\varphi_1 = \frac{\left(\mathbf{x}_m^i - \mathbf{x}_B\right)\cdot\left(\mathbf{x}_C - \mathbf{x}_B\right)}{\left\|\mathbf{x}_m^i - \mathbf{x}_B\right\|\left\|\mathbf{x}_C - \mathbf{x}_B\right\|} \ .$$

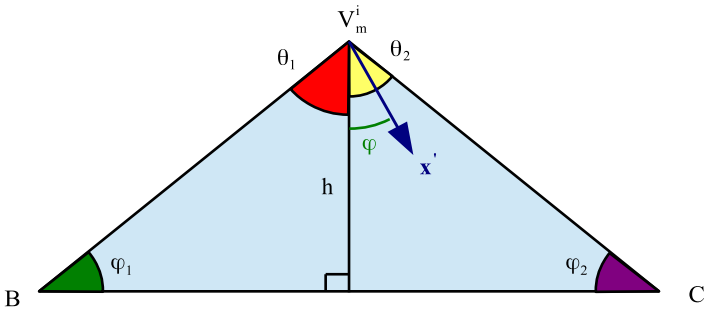

Figure 4.12: Polar coordinates over a triangle element.

Putting everything together:

$$\int_{F_m} \left(h\left(\mathbf{x}'\right) - h_m^i\right) K\left(\mathbf{x}_m^i, \mathbf{x}'\right)\, dS \approx \left(\left(\tau_i^p - 1\right) K\left(\mathbf{x}_m^i, \mathbf{x}^m\left(\boldsymbol{\tau}_p\right)\right) w_p A_m + S_m^i\right) h_m^i \ ,$$

where the matrix of the linear system (4.37), accounting for the singularity removal, is:

$$\mathbb{A}_{tn} = \sum_{F_m \in \mathcal{F}_n} \left(\tau^p_{I(m,n)} - \delta_{tn}\right) K\left(\mathbf{x}_t, \mathbf{x}^m\left(\boldsymbol{\tau}_p\right)\right) w_p A_m + \delta_{tn} S_m^{I(m,n)} \ . \tag{4.39}$$

2. An alternative method is to use piecewise constant functions, i.e. consider the surface charge density constant over each triangle element. In this way, one can write:

$$4\pi\varepsilon_0 g\left(\mathbf{b}_i\right) = \int_{\partial\mathcal{D}(t)} \frac{h\left(\mathbf{x}'\right)}{\left\|\mathbf{b}_i - \mathbf{x}'\right\|}\, dS \approx \sum_{F_j \in \mathcal{F}} \int_{F_j} \frac{h\left(\mathbf{x}'\right)}{\left\|\mathbf{b}_i - \mathbf{x}'\right\|}\, dS \approx \sum_{F_j \in \mathcal{F}} \mathbb{A}_{ij} h\left(\mathbf{b}_j\right) \quad , \quad \mathbb{A}_{ij} = \int_{F_j} \frac{dS}{\left\|\mathbf{b}_i - \mathbf{x}'\right\|} \ ,$$

where $\mathbf{b}_k$ is the barycenter of triangle F_k. When $i = j$, the integral in $\mathbb{A}_{ii}$ is singular but can be calculated analytically by subdividing the triangle into six subtriangles as shown in figure 4.13 to yield:

$$\mathbb{A}_{ii} = \sum_{k=1}^{6} \int_{T_{ik}} \frac{dS}{\left\|\mathbf{b}_i - \mathbf{x}'\right\|} = \sum_{k=1}^{6} a_k \log\left(\sec\alpha_k + \tan\alpha_k\right) \ . \tag{4.40}$$

For the case $i \neq j$, we subdivide the triangle F_j into subelements T_{jk} with barycenters $\mathbf{b}_{jk}$ so that:

$$\mathbb{A}_{ij} = \sum_{k=1}^{N_s} \mathbb{A}_{ij}^k \quad , \quad \mathbb{A}_{ij}^k = \frac{Area\left(T_{jk}\right)}{\left\|\mathbf{b}_{jk} - \mathbf{b}_i\right\|} \ . \tag{4.41}$$

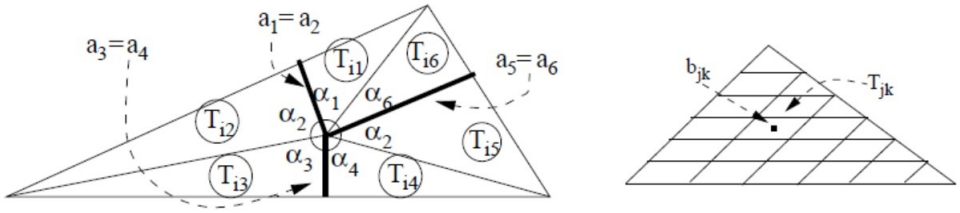

Figure 4.13: Triangle subdivsion to compute surface charge density.

Once the surface charge density is known at the barycenters, its value at any vertex of the mesh can be obtained by weighting over all the triangles sharing that vertex:

$$h_i \equiv h\left(\mathbf{x}_i\right) = \frac{1}{\mathcal{A}} \sum_{F_k \in \mathcal{F}_i} h\left(\mathbf{b}_k\right) Area\left(F_k\right) \quad , \quad \mathcal{A} = \sum_{F_k \in \mathcal{F}_i} Area\left(F_k\right) \ .$$

In terms of accuracy there are not significative differences between these two methods. The first one needs less memory while the second is faster. For that reason, we have mainly used the latter, except on those occasions where memory usage becomes critical.

4.3.4. The velocity field

In this section we derive the linear system governing the velocity field at the drop's surface. We know that the integral equation at the interface is:

$$u_j(\mathbf{x}_p) = -\frac{1}{4\pi(\mu_1+\mu_2)}\int_{\partial\mathcal{D}(t)} \mathbb{G}_{ij}(\mathbf{x},\mathbf{x}_p)\, f_i(\mathbf{x})\ dS - \frac{\mu_1-\mu_2}{4\pi(\mu_1+\mu_2)}\int_{\partial\mathcal{D}(t)}^{PV} u_i(\mathbf{x})\,\mathbb{T}_{ijk}(\mathbf{x},\mathbf{x}_p)\, n_k(\mathbf{x})\ dS \quad ,$$

where:

$$\mathbf{f}(\mathbf{x}) = \left(2\gamma\mathcal{H} - \Delta\varrho\frac{\omega^2}{2}r_{axis}^2 - \frac{\sigma^2}{2\varepsilon_0}\right)\mathbf{n}(\mathbf{x}) = \left(2\gamma\mathcal{H} - \Delta\varrho\frac{\mathcal{L}^2}{2\mathcal{I}}r_{axis}^2 - \frac{\sigma^2}{2\varepsilon_0}\right)\mathbf{n}(\mathbf{x}) \ ,$$

and the kernels have the form:

$$\mathbb{T}_{ijk}(\hat{\mathbf{x}}) \equiv \mathbb{T}_{ijk}(\mathbf{x},\mathbf{x}_p) = -6\frac{\hat{x}_i\hat{x}_j\hat{x}_k}{\|\hat{\mathbf{x}}\|^5} \quad , \quad \mathbb{G}_{ij}(\hat{\mathbf{x}}) \equiv \mathbb{G}_{ij}(\mathbf{x},\mathbf{x}_p) = \frac{\delta_{ij}}{\|\hat{\mathbf{x}}\|} + \frac{\hat{x}_i\hat{x}_j}{\|\hat{\mathbf{x}}\|^3} \quad , \quad \hat{\mathbf{x}} = \mathbf{x}-\mathbf{x}_p \ .$$

For fluids with the same viscosity, $\mu_1 = \mu_2 \equiv \mu$, the velocity can be calculated without solving any system:

$$u_j(\mathbf{x}_p) = -\frac{1}{8\pi\mu}\int_{\partial\mathcal{D}(t)} \mathbb{G}_{ij}(\mathbf{x},\mathbf{x}_p)\, f_i(\mathbf{x})\ dS \ . \tag{4.42}$$

Now, setting the constants:

$$\lambda_S = -\frac{1}{4\pi(\mu_1+\mu_2)} \quad , \quad \lambda_D = \frac{\mu_1-\mu_2}{4\pi(\mu_1+\mu_2)} \quad , \quad \beta = 1-4\pi\lambda_D \ ,$$

and using Propositions 3.3 and 3.4 to remove the singularities of both kernels at $\mathbf{x}=\mathbf{x}_p$, we have:

$$\int_{\partial\mathcal{D}(t)} \mathbb{G}_{ij}(\mathbf{x},\mathbf{x}_p)\, n_i(\mathbf{x})\ dS = 0 \quad , \quad \int_{\partial\mathcal{D}(t)}^{PV} \mathbb{T}_{ijk}(\mathbf{x},\mathbf{x}_p)\, n_k(\mathbf{x})\ dS = -4\pi\delta_{ij} \ ,$$

so one can add and subtract $u_i(\mathbf{x}_p)$ and $f_i(\mathbf{x}_p)$ in (3.23) to yield:

$$\beta u_j(\mathbf{x}_p) + \lambda_D\int_{\partial\mathcal{D}(t)}^{PV}(u_i(\mathbf{x})-u_i(\mathbf{x}_p))\,\mathbb{T}_{ijk}(\hat{\mathbf{x}})\, n_k(\mathbf{x})\ dS = \lambda_S\int_{\partial\mathcal{D}(t)} \mathbb{G}_{ij}(\hat{\mathbf{x}})\,(f_i(\mathbf{x})-f_i(\mathbf{x}_p))\ dS \ .$$

Equivalently, we can drop principal values:

$$\beta u_j(\mathbf{x}_p) + \lambda_D\int_{\partial\mathcal{D}(t)}(u_i(\mathbf{x})-u_i(\mathbf{x}_p))\,\mathbb{T}_{ijk}(\hat{\mathbf{x}})\, n_k(\mathbf{x})\ dS = \lambda_S\int_{\partial\mathcal{D}(t)} \mathbb{G}_{ij}(\hat{\mathbf{x}})\,(f_i(\mathbf{x})-f_i(\mathbf{x}_p))\ dS \ . \tag{4.43}$$

because when $\mathbf{x}_p$ approaches ∂D from the inside:

$$\lim_{\mathbf{x}_p\to\partial D}\int_{\partial D} u_i(\mathbf{x})\,\mathbb{T}_{ijk}(\hat{\mathbf{x}})\, n_k(\mathbf{x})\ dS = \int_{\partial D}^{PV} u_i(\mathbf{x})\,\mathbb{T}_{ijk}(\hat{\mathbf{x}})\, n_k(\mathbf{x})\ dS - 4\pi u_j(\mathbf{x}_p) \ ,$$

$$u_i(\mathbf{x}_p)\lim_{\mathbf{x}_p\to\partial D}\int_{\partial D} \mathbb{T}_{ijk}(\hat{\mathbf{x}})\, n_k(\mathbf{x})\ dS = u_i(\mathbf{x}_p)\left(\int_{\partial D}^{PV} \mathbb{T}_{ijk}(\hat{\mathbf{x}})\, n_k(\mathbf{x})\ dS - 4\pi\delta_{ij}\right) \ ,$$

and subtracting both equations:

$$\lim_{\mathbf{x}_p\to\partial D}\int_{\partial D}(u_i(\mathbf{x})-u_i(\mathbf{x}_p))\,\mathbb{T}_{ijk}(\hat{\mathbf{x}})\, n_k(\mathbf{x})\ dS = \int_{\partial D}^{PV}(u_i(\mathbf{x})-u_i(\mathbf{x}_p))\,\mathbb{T}_{ijk}(\hat{\mathbf{x}})\, n_k(\mathbf{x})\ dS \ .$$

Given a surface mesh with vertices and triangle faces, we will follow [75] to discretize (4.43). One can approximate the surface integrals with virtual area elements $\mathcal{S}_i$ by applying the trapezoidal rule:

$$\int_{\partial\mathcal{D}(t)} \phi(\mathbf{x})\ dS \approx \sum_{V_i\in\mathbb{V}} \phi(\mathbf{x}_i)\,\mathcal{S}_i \quad , \quad \mathcal{S}_i = \frac{1}{3}\sum_{F_m\in\mathcal{F}_i} Area(F_m) \ , \tag{4.44}$$

where $\mathbf{x}_i$ are the coordinates of vertex V_i. Define $\widehat{\mathbf{x}}^{lp} = \mathbf{x}_l - \mathbf{x}_p$ and use the approximation rule to get:

$$\beta u_j(\mathbf{x}_p) + \lambda_D \sum_{l \neq p} (u_i(\mathbf{x}_l) - u_i(\mathbf{x}_p)) \mathbb{T}_{ijk}\left(\widehat{\mathbf{x}}^{lp}\right) n_k(\mathbf{x}_l) \mathcal{S}_l = \lambda_S \sum_{l \neq p} \mathbb{G}_{ij}\left(\widehat{\mathbf{x}}^{lp}\right) (f_i(\mathbf{x}_l) - f_i(\mathbf{x}_p)) \mathcal{S}_l \ ,$$

with $i, j \in \{1,2,3\}$ and $p \in \{1, \ldots, N\}$. Now:

$$\begin{aligned} &\beta u_j(\mathbf{x}_p) + \lambda_D \sum_{l \neq p} (u_i(\mathbf{x}_l) - u_i(\mathbf{x}_p)) \mathbb{T}_{ijk}\left(\widehat{\mathbf{x}}^{lp}\right) n_k(\mathbf{x}_l) \mathcal{S}_l = \\ &\quad = \left(\beta \delta_{ij} \delta_{mp} + \lambda_D \sum_{l \neq p} \mathcal{S}_l (\delta_{ml} - \delta_{mp}) \mathbb{T}_{ijk}\left(\widehat{\mathbf{x}}^{lp}\right) n_k(\mathbf{x}_l) \right) u_i(\mathbf{x}_m) = \mathbb{A}^{im}_{jp} u_i(\mathbf{x}_m) \ , \end{aligned} \tag{4.45}$$

where $m \in \{1, \ldots, N\}$. Similarly, for the SLP:

$$\lambda_S \sum_{l \neq p} \mathbb{G}_{ij}\left(\widehat{\mathbf{x}}^{lp}\right) (f_i(\mathbf{x}_l) - f_i(\mathbf{x}_p)) \mathcal{S}_l = \lambda_S \sum_{l \neq p} \mathcal{S}_l \mathbb{G}_{ij}\left(\widehat{\mathbf{x}}^{lp}\right) (f_i(\mathbf{x}_l) - f_i(\mathbf{x}_p)) = b_{jp} \ , \tag{4.46}$$

obtaining the linear system of $3N$ equations in $3N$ unknowns:

$$\mathbb{A}^{im}_{jp} u_i(\mathbf{x}_m) = b_{jp} \quad , \quad i, j \in \{1,2,3\} \quad , \quad m, p \in \{1, \ldots, N\} \ . \tag{4.47}$$

We can write this system compactly in matrix form:

$$\mathbb{A}_{ts} \mathcal{U}_s = \mathcal{B}_t \quad , \quad s \in \{1, \ldots, 3N\} \quad \Leftrightarrow \quad \mathbb{A}\boldsymbol{\mathcal{U}} = \boldsymbol{\mathcal{B}} \ ,$$

where:

$$\boldsymbol{\mathcal{U}} = \begin{pmatrix} u_1(\mathbf{x}_1) \\ u_2(\mathbf{x}_1) \\ u_3(\mathbf{x}_1) \\ \vdots \\ u_1(\mathbf{x}_i) \\ u_2(\mathbf{x}_i) \\ u_3(\mathbf{x}_i) \\ \vdots \\ u_1(\mathbf{x}_N) \\ u_2(\mathbf{x}_N) \\ u_3(\mathbf{x}_N) \end{pmatrix} \quad , \quad \boldsymbol{\mathcal{B}} = \begin{pmatrix} b_{11} \\ b_{21} \\ b_{31} \\ \vdots \\ b_{1i} \\ b_{2i} \\ b_{3i} \\ \vdots \\ b_{1N} \\ b_{2N} \\ b_{3N} \end{pmatrix} \ .$$

Equivalently:

$$\mathcal{U}_{i+3(m-1)} = u_i(\mathbf{x}_m) \quad , \quad \mathcal{B}_{j+3(p-1)} = b_{jp} \quad , \quad i, j \in \{1,2,3\} \quad , \quad p, m \in \{1, \ldots, N\} \ ,$$

$$\mathbb{A}^{im}_{jp} \equiv \mathbb{A}_{ts} \quad , \quad s = i + 3(m-1) \quad , \quad t = j + 3(p-1) \ .$$

To finish this section we will analyze the structure of $\mathbb{A}$. Since the matrix has dimensions $3N \times 3N$, we can see it as composed of block matrices of size 3×3 organized in N rows and N columns. The indices p and m indicate the row and column location respectively of a 3×3 block matrix. Given p and m, the indices j and i are the row and column respectively inside the 3×3 matrix. Schematically:

$$\mathbb{A}^{im}_{jp} \equiv B_{pm} \in \mathcal{M}_{3\times 3} \quad , \quad \mathbb{A} = \begin{pmatrix} B_{11} & \cdots & B_{1N} \\ \vdots & \ddots & \vdots \\ B_{N1} & \cdots & B_{NN} \end{pmatrix} \ .$$

The diagonal elements of $\mathbb{A}$ are given by:

$$t = s \quad \Leftrightarrow \quad (i-j) + 3(m-p) = 0 \quad \Leftrightarrow \quad i = j \quad , \quad m = p \ ,$$

$$\mathbb{A}_{tt} \equiv \mathbb{A}^{im}_{im} = \beta - \lambda_D \sum_{l \neq p} \mathcal{S}_l \mathbb{T}_{iik}\left(\widehat{\mathbf{x}}^{lp}\right) n_k(\mathbf{x}_l) \quad , \quad \mathbb{T}_{iik}\left(\widehat{\mathbf{x}}^{lp}\right) = -6 \frac{\left(\widehat{x}_i^{\,lp}\right)^2 \widehat{x}_k^{\,lp}}{\left\|\widehat{\mathbf{x}}^{lp}\right\|^5} \ ,$$

For the elements where $i \neq j$ and $m = p$ we have:

$$\mathbb{A}_{ts} \equiv \mathbb{A}_{jm}^{im} = -\lambda_D \sum_{l \neq p} \mathcal{S}_l \mathbb{T}_{ijk} \left(\widehat{\mathbf{x}}^{lp} \right) n_k \left(\mathbf{x}_l \right) \quad , \quad \mathbb{T}_{ijk} \left(\widehat{\mathbf{x}}^{lp} \right) = -6 \frac{\widehat{x}_i^{\,lp} \, \widehat{x}_j^{\,lp} \, \widehat{x}_k^{\,lp}}{\left\| \widehat{\mathbf{x}}^{lp} \right\|^5} \, .$$

Finally, for the case $m \neq p$ we get:

$$\mathbb{A}_{ts} \equiv \mathbb{A}_{jp}^{im} = \lambda_D \mathcal{S}_m \mathbb{T}_{ijk} \left(\widehat{\mathbf{x}}^{mp} \right) n_k \left(\mathbf{x}_m \right) \quad , \quad \mathbb{T}_{ijk} \left(\widehat{\mathbf{x}}^{mp} \right) = -6 \frac{\widehat{x}_i^{\,mp} \, \widehat{x}_j^{\,mp} \, \widehat{x}_k^{\,mp}}{\left\| \widehat{\mathbf{x}}^{mp} \right\|^5} \, .$$

4.4. Mesh adaption

Once the velocity field at the interface is known, the next step is to move the nodes with the normal velocity. The tangential component of the velocity field is not considered because its only contribution is to redistribute the vertices throughout the surface of the drop. The mesh vertices are thus updated with an Euler explicit scheme:

$$\mathbf{x}_i^{t+\Delta t} = \mathbf{x}_i^t + \Delta t \, u_{i,n} \, \mathbf{n}_i \quad , \quad u_{i,n} = \mathbf{u}_i \cdot \mathbf{n}_i \, , \tag{4.48}$$

where $\mathbf{n}_i$ and $\mathbf{u}_i$ are respectively the unit normal and velocity at vertex V_i. It is crucial to choose the time step adaptively in order to obtain a valid mesh, so that the resulting numerical method is accurate and stable. A natural bound for the time step is:

$$\Delta t \leqslant \min_{V_i \in \mathbb{V}} \frac{d_i}{\left\| \mathbf{u_i} \right\|} \quad , \quad d_i = \min_{\substack{V_j \in \mathbb{V} \\ \alpha_{ij} = 1}} d_{ij} \quad , \quad d_{ij} = \left\| \mathbf{x}_i - \mathbf{x}_j \right\| \, .$$

When evolving the free surface, the capability of the mesh to approximate the interface may deteriorate rapidly with time, especially in the cases where the geometry of the interface changes radically, for instance when singularities such as cones or necks form. For this reason, the code must implement a number of mesh regularization techniques based on previous works by Cristini, Blawzdziewicz, and Loewenberg [17] and Vantzos [70] that allow the mesh to adapt to the evolving geometry of the interface. The aim of this section is to describe these algorithms in detail.

4.4.1. Relaxing the mesh

Since one of the main interests of this thesis lies in the accurate description of singularity formation, one requires high concentration of nodes in regions where necks or cone tips develop. This is achieved in two different ways: first, we need to relax the mesh by moving the vertices to areas of the interface with high curvature values, and second, a refinement algorithm has to be implemented to locally subdivide triangles in critical regions. Here we will explain how the mesh is relaxed, leaving the description of the refinement algorithm for a later subsection.

Given a surface mesh, the idea behind relaxation is to consider the edges as massless springs which can move freely over the drop's surface. The most basic operation in this sense is known in the literature as laplacian smoothing, which is widely used in computational geometry and ensures uniform node distribution:

$$\mathbf{x}_i^{(n+1)} = \mathbf{x}_i^{(n)} + h \Delta \mathbf{x}_{ij} \quad , \quad \Delta \mathbf{x}_{ij} = \sum_{\substack{V_j \in \mathbb{V} \\ \alpha_{ij} = 1}} \left(\mathbf{x}_j^{(n)} - \mathbf{x}_i^{(n)} \right) \, .$$

Since this operator has to be shape-preserving when applied to the mesh, the normal component of the displacement must be subtracted from the equation. Additionally, we need to move the nodes to high curvature regions, and to do so, the smoothing operator has to be modified:

$$\mathbf{x}_i^{(n+1)} = \mathbf{x}_i^{(n)} + h \left(\Delta_m \mathbf{x}_{ij} - \left(\Delta_m \mathbf{x}_{ij} \cdot \mathbf{n}_i \right) \mathbf{n}_i \right) \, , \tag{4.49}$$

where:

$$\Delta_m \mathbf{x}_{ij} = \sum_{\substack{V_j \in \mathbb{V} \\ \alpha_{ij} = 1}} w_{ij} \left(\mathbf{x}_j^{(n)} - \mathbf{x}_i^{(n)} \right) \quad , \quad w_{ij} = 1 - C \frac{\rho_{ij}}{d_{ij}} \quad , \quad \rho_{ij} = \frac{\rho_i + \rho_j}{2} \quad , \quad d_{ij} = \left\| \mathbf{x}_i - \mathbf{x}_j \right\| \, , \tag{4.50}$$

and ρ_i, ρ_j are the radius of curvature at vertices V_i and V_j respectively. The displacement factor h has to be taken small enough so that the mesh does not deteriorate:

$$h = \min_{V_i \in \mathbb{V}} \{\min \{C_1 \frac{d_i}{\|\Delta_m \mathbf{x}_{ij}\|}, C_2 \rho_i\}\} \quad , \quad d_i = \min_{\substack{V_j \in \mathbb{V} \\ \alpha_{ij}=1}} d_{ij} \quad , \quad C_1, C_2 \in (0,1) \ , \tag{4.51}$$

and the selection of the weights w_{ij} for our smoothing operator is done so that the qantity:

$$\frac{1}{2N_{edges}} \sum_{\substack{V_i, V_j \in \mathbb{V} \\ \alpha_{ij}=1}} |1 - C\frac{\rho_{ij}}{d_{ij}}| \quad , \quad N_{edges} = \#\mathbb{V} + \#\mathcal{F} - 2 \ ,$$

is minimized. In this case, all the edges must have their lengths approximately equal to $C\rho_{ij}$. This smoothing process is applied iteratively until a desired node configuration is reached.

4.4.2. Delaunay triangulation

When solving problems over a triangulated surface, it is important to avoid skinny triangles (those for which the ratio of two of its edges is very small). These triangles can appear as the mesh evolves in time and give rise to a source of error and instability for the numerical simulation. This issue can be tackled by remeshing with a Delaunay algorithm, which maximizes the minimum angle of the triangles that approximate the surface, provided that no vertex of the mesh lies inside the circumcircle of any mesh triangle. In particular, for a plane meshed region, this maximization condition to obtain a Delanay triangulation can be expressed in terms of the angles of the quadrilateral formed by two adjacent mesh triangles:

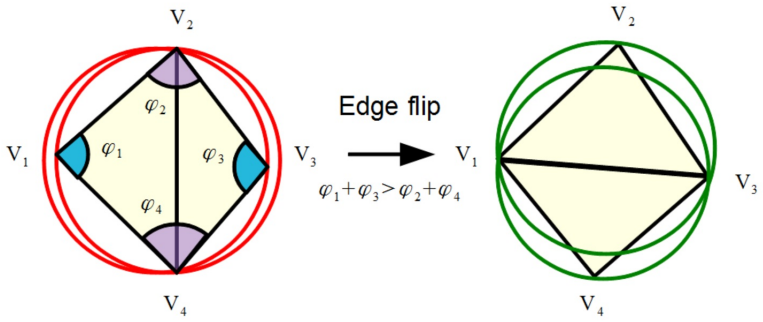

Figure 4.14: Delaunay condition.

Since we want to apply Delaunay algorithm to a surface mesh, we need to take into account dihedral angles between the triangles, because they do not lie on the same plane. The dihedral angle ϕ between two planes with unit normal vectors $\mathbf{n}_1$ and $\mathbf{n}_2$ is defined as follows:

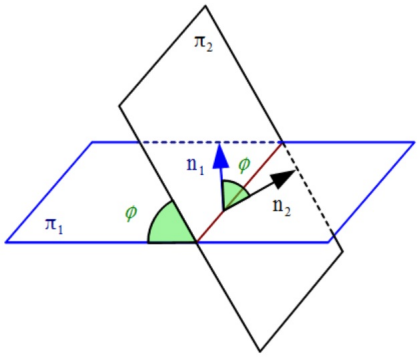

Figure 4.15: Dihedral angle ϕ between planes.

and given by the formula:

$$\cos\phi = \mathbf{n}_1 \cdot \mathbf{n}_2 \ .$$

So we have to modify Delaunay condition with:

$$\varphi_1 + \varphi_3 + |\pi - \omega_1| > \varphi_2 + \varphi_4 + |\pi - \omega_2| \quad , \quad \cos\omega_1 = \frac{\mathbf{n}_1 \cdot \mathbf{n}_3}{\|\mathbf{n}_1\| \, \|\mathbf{n}_3\|} \quad , \quad \cos\omega_2 = \frac{\mathbf{n}_2 \cdot \mathbf{n}_4}{\|\mathbf{n}_2\| \, \|\mathbf{n}_4\|} \ . \tag{4.52}$$

The remeshing algorithm loops over all the mesh edges, performing an edge flip whenever (4.52) is met, and is repeated until there are no more edge flips.

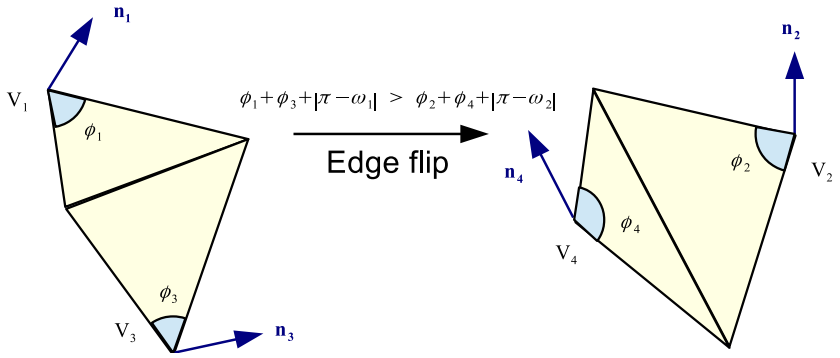

Figure 4.16: Edge flip condition for surface triangles.

4.4.3. Mesh refinement

As the droplet evolves with time, regions of high curvature develop on its surface. In order to obtain a detailed description of these new features, it is necessary to design an algorithm that allows us to refine the mesh locally in those areas of interest. Given a triangle $F_m \in \mathcal{F}$, we divide it into subtriangles if the following criterion is satisfied:

$$A_m \geqslant \frac{\sqrt{3}}{4} \left(C_r \rho_m\right)^2 \ , \tag{4.53}$$

where A_m is the area of the triangle, C_r is a refinement constant and ρ_m is the mean radius of curvature of the vertices forming the triangle. Observe that the right hand side is the area of an equilateral triangle of edges with length $C_r\rho_m$. The refinement process is repeated until no triangle satisfies (4.53). This algorithm is combined with mesh relaxation and Delaunay remeshing to obtain a good quality and smooth mesh:

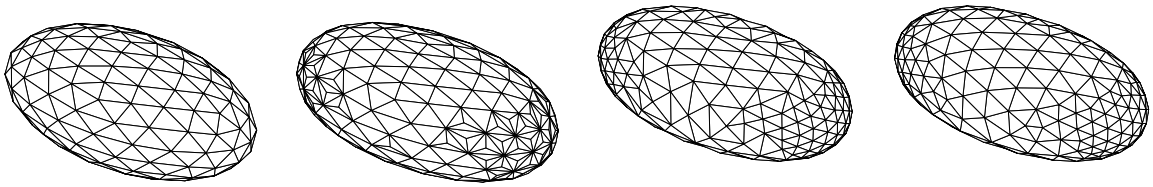

Figure 4.17: Example of mesh regularization. Starting from left to right, we begin with a given mesh, then we refine the areas of high curvature, we apply remeshing and finally relaxation.

When a mesh triangle is subdivided into three smaller triangles, a new vertex must be added to the surface of the droplet. This is done by considering the barycenter of the triangle as a starting point and calculating the normal projection of this point onto the three osculating paraboloids associated to the triangle vertices. The mean of these projection will be tbe new mesh vertex.

Given a triangle with vertices V_1, V_2 and V_3, its barycenter has the form:

$$\mathbf{b} = \frac{\mathbf{x}_1 + \mathbf{x}_2 + \mathbf{x}_3}{3} \ ,$$

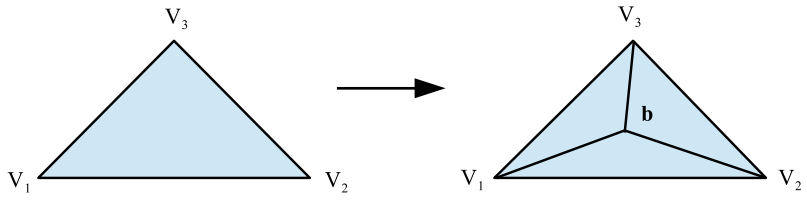

Figure 4.18: Surface triangle refinement.

where $\mathbf{x}_i$ are the coordinates of vertex V_i. The normal at the barycenter is approximated by the mean of the normals at the vertices of the triangle:

$$\mathbf{n} = \frac{\mathbf{n}_1 + \mathbf{n}_2 + \mathbf{n}_3}{3} \ .$$

Consider now the line that passes through $\mathbf{b}$ with direction $\mathbf{n}$, $r_{\mathbf{b},\mathbf{n}}$, and the paraboloid P:

$$r_{\mathbf{b},\mathbf{n}} \ : \ \begin{cases} x = b_1 + \lambda n_1 \\ y = b_2 + \lambda n_2 \\ z = b_3 + \lambda n_3 \end{cases} \quad , \quad P \ : \ z = ax^2 + bxy + cy^2 + dx + ey \ .$$

The intersection of the line with the paraboloid is a straightforward computation:

$$b_3 + \lambda n_3 = a\left(b_1 + \lambda n_1\right)^2 + b\left(b_1 + \lambda n_1\right)\left(b_2 + \lambda n_2\right) + c\left(b_2 + \lambda n_2\right)^2 + d\left(b_1 + \lambda n_1\right) + e\left(b_2 + \lambda n_2\right) \ ,$$

which reduces to a quadratic equation:

$$a_2\lambda^2 + a_1\lambda + a_0 = 0 \ , \tag{4.54}$$

with:

$$a_2 = an_1^2 + bn_1n_2 + cn_2^2 \ ,$$
$$a_1 = 2\left(ab_1n_1 + cb_2n_2\right) + b\left(b_1n_2 + b_2n_1\right) + dn_1 + en_2 - n_3 \ ,$$
$$a_0 = ab_1^2 + bb_1b_2 + cb_2^2 + db_1 + eb_2 - b_3 \ .$$

Taking:

$$\lambda^* = \min\{|\lambda_+|, |\lambda_-|\} \ , \tag{4.55}$$

where λ_+ and λ_- are the roots of (4.54), the projetion of $\mathbf{b}$ onto the paraboloid is:

$$\mathbf{p} = \mathbf{b} + \lambda^*\mathbf{n} \ . \tag{4.56}$$

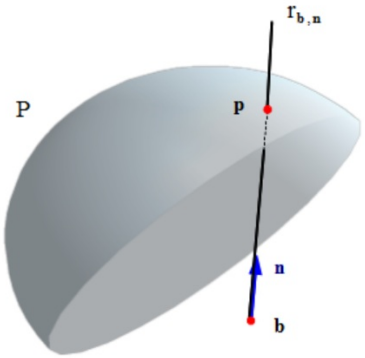

Figure 4.19: Paraboloid projection of point $\mathbf{b}$ in the direction $\mathbf{n}$.

Chapter 5

Evolution of rotating drops

In this chapter we will study the evolution and stability of rotating drops at constant angular speed or constant angular momentum and focus on the formation of singularities that lead to changes in the topology of the droplet. We start by introducing axisymmetric equilibrium configurations [6, 49, 2, 33] to validate the simulations performed with our computer codes, and then, we move to describing the evolution and behaviour of the system for different values of the rotation parameters (angular speed and angular momentum), firstly for the axially symmetric problem, and finally for the full 3D model. All results included below have been published in [25].

5.1. Axisymmetric equilibrium shapes

In order to obtain the equilibrium configurations for rotating drops, the velocity field has to be stationary in (2.28), (2.33) and (2.34), from which one can easily deduce:

$$\Pi^{(i)} = C_i \quad \text{is constant over } \mathcal{D}_i \quad , \quad i \in \{1,2\} \, .$$

This condition yields, in the absence of electrostatic forces, the modified Young-Laplace equation:

$$\delta\Pi = 2\gamma\mathcal{H} - \frac{\Delta\varrho}{2}\omega^2 r_{axis}^2 \quad , \quad \text{on } \partial\mathcal{D} \, , \tag{5.1}$$

which has been studied in detail throughout the literature. One can highlight the works by Beer [6] and Gulliver [33], where spheroidal and toroidal solutions were obtained respectively. To calculate axisymmetric solutions of (5.1) with respect to the rotation axis, i.e. the z axis, it is sufficient to solve the problem for the profile curve generating the surface, which can be described using cylindrical coordinates as:

$$\Gamma_{axi} : \mathbf{x}\,(r) = r\hat{\mathbf{r}} + z\,(r)\,\hat{\mathbf{k}} \, . \tag{5.2}$$

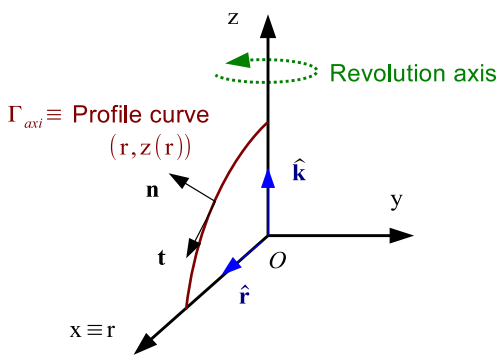

Figure 5.1: Profile curve generating the axisymmetric surface about the z-axis.

The tangent vector to this curve is:

$$\mathbf{t} \equiv \frac{d\mathbf{x}}{dr} = \widehat{\mathbf{r}} + z'(r)\,\widehat{\mathbf{k}}\,,$$

and its outward unit normal:

$$\mathbf{n} = \frac{-z'(r)\,\widehat{\mathbf{r}} + \widehat{\mathbf{k}}}{\sqrt{1+(z'(r))^2}} \equiv n_r\widehat{\mathbf{r}} + n_z\widehat{\mathbf{k}}\,.$$

We know that the mean curvature at the interface is given by:

$$2\mathcal{H} = \nabla\cdot\mathbf{n} = -\frac{1}{r}\frac{d}{dr}\left(\frac{rz'(r)}{\sqrt{1+(z'(r))^2}}\right),$$

so equation (5.1) becomes:

$$\frac{\gamma}{r}\frac{d}{dr}\left(\frac{rz'(r)}{\sqrt{1+(z'(r))^2}}\right) = -\delta\Pi - \frac{\Delta\varrho}{2}\omega^2 r^2\,. \tag{5.3}$$

Following the nondimensional form of (3.25) we can write:

$$Bo \equiv \Omega^2 = \frac{\Delta\varrho\,\omega^2\sqrt[3]{V_0}}{\gamma} \quad , \quad k \equiv -\delta\Pi^* = -\frac{\sqrt[3]{V_0}}{\gamma}\delta\Pi \quad , \quad r^* = \frac{r}{\sqrt[3]{V_0}} \quad , \quad z^* = \frac{z}{\sqrt[3]{V_0}}\,,$$

where V_0 is the drop's volume. Omitting asterisks:

$$\frac{1}{r}\frac{d}{dr}\left(\frac{rz'(r)}{\sqrt{1+(z'(r))^2}}\right) = k - \frac{\Omega^2}{2}r^2\,. \tag{5.4}$$

Observe that for the variables r^* and z^* the volume is $V_0 = 1$. Now, multiplying by r we get:

$$\frac{d}{dr}\left(\frac{rz'(r)}{\sqrt{1+(z'(r))^2}}\right) = kr - \frac{\Omega^2}{2}r^3\,.$$

We can scale this equation further to leave it in terms of a single parameter:

$$\widetilde{r} = \sqrt[3]{\frac{2}{\Omega^2}}\,r^* \quad , \quad \widetilde{z} = \sqrt[3]{\frac{2}{\Omega^2}}\,z^* \quad , \quad \kappa = \sqrt[3]{\frac{2}{\Omega^2}}\,k\,,$$

to yield, omitting the tilde notation:

$$\frac{d}{dr}\left(\frac{rz'(r)}{\sqrt{1+(z'(r))^2}}\right) = \kappa r - r^3\,. \tag{5.5}$$

Among the solutions to (5.5), we will explore first the ones that have the topology of the sphere. To obtain these solutions, which are attained for values of $\kappa \in (-\infty, 1.26]$, it is natural to impose the initial condtions $z(0) = z'(0) = 0$, which yield, after integrating (5.5) and manipulating:

$$z(r) = \int_0^r \frac{f_\kappa(\rho)}{\sqrt{1-(f_\kappa(\rho))^2}}\,d\rho \quad , \quad 0 \leqslant r \leqslant r_{max} \quad , \quad f_\kappa(\rho) = \frac{\kappa}{2}\rho - \frac{\rho^3}{4}\,.$$

This integral can be solved in terms of elliptic integrals [49]:

$$z(r) = r_{max}\sqrt{h}\left(\Delta E_{\psi_0,\psi(r),l} + \left(\frac{2}{r_{max}^3 h} - \frac{1}{2}\right)\Delta F_{\psi_0,\psi(r),l} - K_{\psi(r),l} + K_{\psi_0,l}\right)\,, \tag{5.6}$$

where:

$$\Delta E_{\psi_0,\psi(r),l} = \int_{\psi_0}^{\psi(r)}\sqrt{1-l^2\sin^2\varphi}\,d\varphi \quad , \quad \Delta F_{\psi_0,\psi(r),l} = \int_{\psi_0}^{\psi(r)}\frac{d\varphi}{\sqrt{1-l^2\sin^2\varphi}}\,,$$

$$K_{\varphi,l} = \tan\left(\frac{\varphi}{2}\right)\sqrt{1-l^2\sin^2\varphi} \quad , \quad l^2 = \frac{1}{2} + \frac{8+r_{max}^3}{8\sqrt{4+2r_{max}^3}} \quad , \quad h = \frac{4}{r_{max}^3}\sqrt{1+\frac{r_{max}^3}{2}} \, ,$$

$$\frac{\psi_0}{2} = \arctan\left(\frac{1}{\sqrt{h}}\right) \quad , \quad \frac{\psi(r)}{2} = \arctan\left(\sqrt{\frac{r_{max}^2-r^2}{hr_{max}^2}}\right) \, ,$$

and the maximum equatorial radius of the drop solves:

$$-1 = f_\kappa(r_{max}) \quad \Leftrightarrow \quad r_{max} = \sqrt[3]{2+\sqrt{4-\frac{8}{27}\kappa^3}} + \sqrt[3]{2-\sqrt{4-\frac{8}{27}\kappa^3}} \, .$$

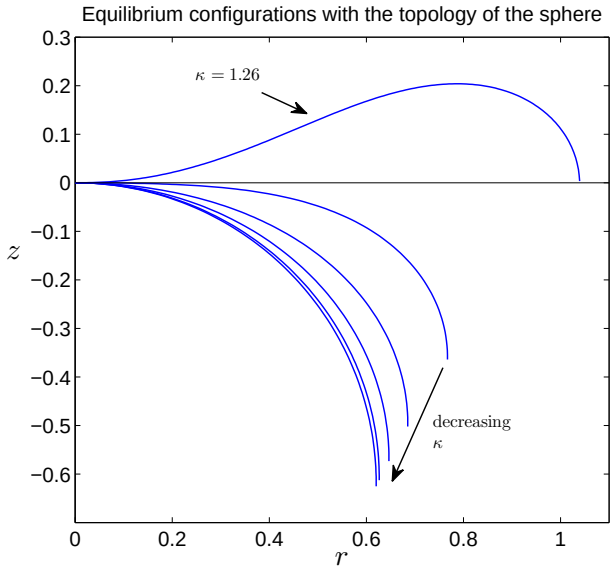

Figure 5.2: Solutions given by (5.6) for different values of $\kappa \in (-\infty, 1.26]$.

In order to compare the equilibrium shapes that result from the numerical simulation of the evolution problem with the solutions of (5.5), it is useful to use the volume constraint to express the angular momentum and angular speed of the drop as functions of κ:

$$1 = Vol(r^*, z^*) = 4\pi\int_0^{r^*_{max}} r^* z^*(r^*)\, dr^* = \frac{8\pi}{\Omega^2}\int_0^{\tilde{r}_{max}} \tilde{r}\tilde{z}(\tilde{r})\, d\tilde{r} = -\frac{4\pi}{\Omega^2}\int_0^{\tilde{r}_{max}} \tilde{r}^2\tilde{z}'(\tilde{r})\, d\tilde{r} \, .$$

This gives:

$$\Omega \equiv \Omega(\kappa) = \sqrt{-4\pi\int_0^{\tilde{r}_{max}} \frac{\tilde{r}^2 f_\kappa(\tilde{r})}{\sqrt{1-(f_\kappa(\tilde{r}))^2}}\, d\tilde{r}} \, , \tag{5.7}$$

and the angular momentum has the form:

$$\begin{aligned} L \equiv L(\kappa) = \Omega\mathcal{I}(r^*, z^*) = 4\pi\Omega\int_0^{r^*_{max}} (r^*)^3 z^*(r^*)\, dr^* = \\ = -\frac{2^{\frac{5}{3}}\pi}{\Omega^{\frac{7}{3}}}\int_0^{\tilde{r}_{max}} \tilde{r}^4\tilde{z}'(\tilde{r})\, d\tilde{r} = -\frac{2^{\frac{5}{3}}\pi}{\Omega^{\frac{7}{3}}}\int_0^{\tilde{r}_{max}} \frac{\tilde{r}^4 f_\kappa(\tilde{r})}{\sqrt{1-(f_\kappa(\tilde{r}))^2}}\, d\tilde{r} \, . \end{aligned} \tag{5.8}$$

A family of toroidal solutions for (5.5), which we label as toroidal type I, is obtained when one imposes the boundary conditions $z'(r_{min}) = +\infty$ and $z'(r_{max}) = -\infty$ as described in [33]. They bifurcate from the family of equilibrium configurations with the topology of the sphere in the limiting case where the boundary

conditions are $z'(0) = z''(0) = 0$ and $z'(r_{max}) = -\infty$. Under these assumptions, from (5.4) one easily gets that $k = 0$, and imposing that the volume is $V_0 = 1$, the bifurcation point occurs at $\Omega = 4\sqrt{\frac{\pi}{3}}$. To obtain the toroidal family, integrate (5.5) to yield:

$$\int_{r_{min}}^{r} \frac{d}{d\rho}\left(\frac{\rho z'(\rho)}{\sqrt{1+(z'(\rho))^2}}\right) d\rho = \int_{r_{min}}^{r} -\rho^3 + \kappa \, d\rho \quad , \quad r_{min} \leqslant r \leqslant r_{max} \, ,$$

or equivalently:

$$\frac{r z'(r)}{\sqrt{1+(z'(r))^2}} - \lim_{\rho \to r_{min}} \frac{\rho z'(\rho)}{\sqrt{1+(z'(\rho))^2}} = \frac{r_{min}^4}{4} - \frac{r_{min}^2 \kappa}{2} - \frac{r^4}{4} + \frac{r^2 \kappa}{2} \, .$$

From the initial condition $z'(r_{min}) = +\infty$ we know that:

$$\lim_{\rho \to r_{min}} \frac{\rho z'(\rho)}{\sqrt{1+(z'(\rho))^2}} = r_{min} \, ,$$

and rearranging:

$$z'(r) = \frac{f_{\kappa, r_{min}}(r)}{\sqrt{1-(f_{\kappa, r_{min}}(r))^2}} \quad , \quad f_{\kappa, r_{min}}(r) = \left(r_{min} + \frac{r_{min}^4}{4} - \frac{r_{min}^2 \kappa}{2}\right)\frac{1}{r} + \frac{\kappa r}{2} - \frac{r^3}{4} \, . \tag{5.9}$$

To compute r_{max}, the condition $z'(r_{max}) = -\infty$ implies:

$$-1 = f_{\kappa, r_{min}}(r_{max}) \, ,$$

which we can solve numerically with a Newton-Raphson algorithm. Once r_{max} is known, one can easily calculate the desired solution by applying a Runge-Kutta method to (5.9) in the interval $[r_{min}, r_{max}]$. Below we show some of the toroidal solutions calculated with this method.

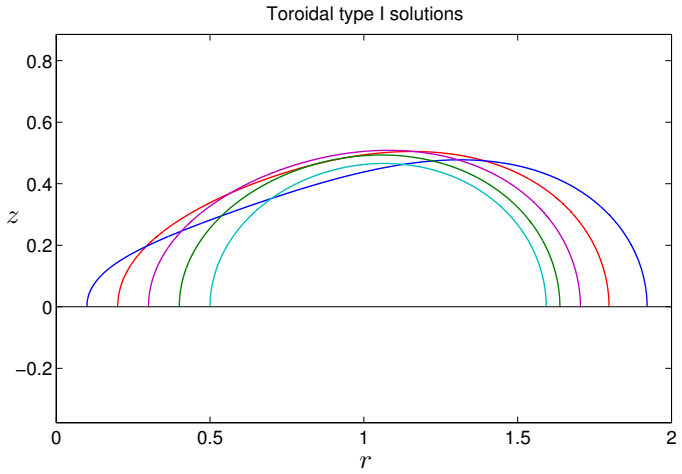

Figure 5.3: Toroidal type I solutions for different values of κ.

A third family of axisymmetric solutions to (5.5), that we name as toroidal type II, is discussed in detail in [2] and is characterized by a zero-thickness film of fluid in $0 \leqslant r \leqslant r_{min}$ with boundary conditions $z'(r_{min}) = 0$ and $z'(r_{max}) = -\infty$. These configurations, which also bifurcate from the family with the topology of the sphere at $\Omega = 4\sqrt{\frac{\pi}{3}}$, are obtained by integrating (5.5) to get:

$$\int_{r_{min}}^{r} \frac{d}{d\rho}\left(\frac{\rho z'(\rho)}{\sqrt{1+(z'(\rho))^2}}\right) d\rho = \int_{r_{min}}^{r} -\rho^3 + \kappa \, d\rho \quad , \quad r_{min} \leqslant r \leqslant r_{max} \, .$$

Equivalently:

$$\frac{rz'(r)}{\sqrt{1+(z'(r))^2}} = \frac{r_{min}^4}{4} - \frac{r_{min}^2\kappa}{2} - \frac{r^4}{4} + \frac{r^2\kappa}{2} ,$$

and rearranging one finds that:

$$z'(r) = \frac{h_{\kappa,r_{min}}(r)}{\sqrt{1-(h_{\kappa,r_{min}}(r))^2}} \quad , \quad h_{\kappa,r_{min}}(r) = \left(\frac{r_{min}^4}{4} - \frac{r_{min}^2\kappa}{2}\right)\frac{1}{r} + \frac{\kappa r}{2} - \frac{r^3}{4} , \tag{5.10}$$

where r_{max} is determined from $z'(r_{max}) = -\infty$ to yield:

$$-1 = h_{\kappa,r_{min}}(r_{max}) .$$

The solutions to (5.10) can be obtained with the same numerical method used for the toroidal type I family.

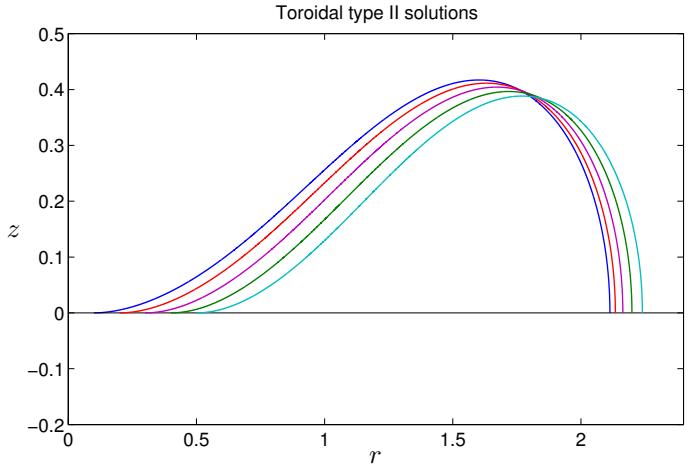

Figure 5.4: Toroidal type II solutions for different values of κ.

5.1.1. The variational formulation

Sometimes it is interesting to study the equilibrium configurations of a problem as the solutions that minimize a certain energy functional. In this subsection we show, using cylindrical coordinates and axial symmetry, how (5.1) is equivalent to the Euler-Lagrange equations of the energy functional describing the total energy of the rotating drop system.

When rotation takes place at constant angular momentum $\mathcal{L}$, an initial turn is given to the droplet about the z-axis and the system is let to evolve freely. In this case, the energies associated to the system are the rotational kinetic energy and the surface energy, together with the constraint that the volume is conserved:

$$E_{total}^{\mathcal{L}} = E_{surface} + E_{kinetic} - \delta\Pi\,(V - V_0) , \tag{5.11}$$

where $\delta\Pi$ is the lagrange multiplyer such that the volume V of the drop is equal to V_0. Alternatively, if rotation takes place at constant angular speed ω, the system needs an external force that continuously rotates the drop at that angular speed. The work done by an external force that generates a torque τ to rotate the drop an angle θ_1 about the z-axis is given by:

$$E_{external} = \int_0^{\theta_1} \tau\, d\theta = \int_0^{\theta_1} \frac{d\mathcal{L}}{dt}\, d\theta = \int_0^{t_1} \frac{d\mathcal{L}}{dt}\frac{d\theta}{dt}\, dt = \omega \int_0^{t_1} \frac{d\mathcal{L}}{dt}\, dt = \omega\mathcal{L}(t_1) .$$

Since $\mathcal{L} = \omega\mathcal{I}$, where $\mathcal{I}$ is the moment of inertia of the drop, the external energy is:

$$E_{external} = \omega^2\mathcal{I} ,$$

and the total energy of a rotating drop at constant ω is:

$$E^{\omega}_{total} = E_{surface} + E_{kinetic} - E_{external} - \delta\Pi\,(V - V_0)\ . \tag{5.12}$$

Now, the surface energy is:

$$E_{surface} = \gamma \mathcal{A}_d\ ,$$

where γ is the surface tension and $\mathcal{A}_d$ is the surface area of the droplet. The kinetic energy of the system is the sum of the kinetic energy for the drop and that of the surrounding fluid:

$$E_{kinetic} = E^{d}_{kinetic} + E^{o}_{kinetic} = \frac{1}{2}\omega^2\,(\mathcal{I} + \mathcal{I}_{outer}) \quad , \quad \mathcal{I} = \varrho_1 \int_{\mathcal{D}_1} r^2\, d\mathbf{x} \quad , \quad \mathcal{I}_{outer} = \varrho_2 \int_{\mathcal{D}_2} r^2\, d\mathbf{x}\ .$$

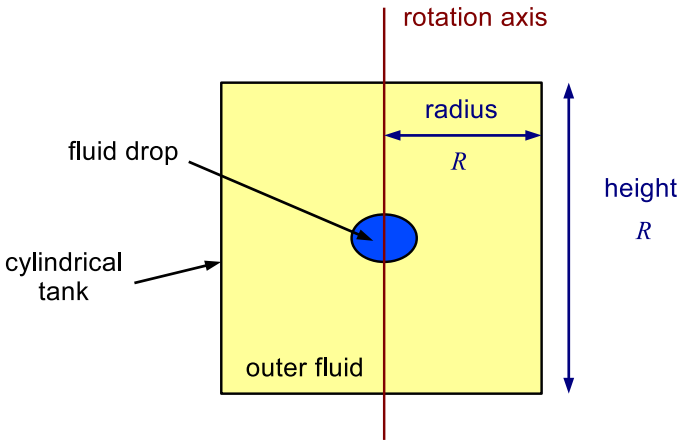

Figure 5.5: Cylindrical tank containing the drop.

Since the size of the drop is negligible with respect to the radius and height R of the cylindrical tank $\mathcal{T}$ containing both fluids, one can consider the tank radius to be large but finite, and thus the moment of inertia of the surrounding fluid can be expressed in terms of the drop's moment of inertia:

$$\mathcal{I}_{outer} = \varrho_2 \int_{\mathcal{D}_2} r^2\, d\mathbf{x} = \varrho_2 \left(\int_{\mathcal{T}} r^2\, d\mathbf{x} - \int_{\mathcal{D}_1} r^2\, d\mathbf{x} \right) = E_0 - \zeta\mathcal{I} \quad , \quad \zeta = \frac{\varrho_2}{\varrho_1}\ ,$$

with:

$$E_0 = \varrho_2 \int_{\mathcal{T}} r^2\, d\mathbf{x} = \frac{\varrho_2 \pi R^5}{2}\ .$$

Defining $\psi = 1 - \zeta$, one gets for the kinetic energy:

$$E_{kinetic} = \frac{1}{2}\psi\omega^2\mathcal{I} + E_0\ ,$$

and since E_0 is constant, it can be included in the total energy of the system with no further consequence.

Theorem 5.1. *Given the energies:*

$$E^{\mathcal{L}}_{total} = \gamma\mathcal{A}_d + \psi\frac{\mathcal{L}^2}{2\mathcal{I}} - \delta\Pi\,(V - V_0) \quad , \quad E^{\omega}_{total} = \gamma\mathcal{A}_d - \frac{1}{2}\psi\omega^2\mathcal{I} - \delta\Pi\,(V - V_0)\ ,$$

the Euler-Lagrange (EL) equation for these functionals is (5.3).

Proof. We will derive the EL equation for E^{ω}_{total}, since the first variation for both energies is the same:

$$\delta E^{\mathcal{L}}_{total} = \gamma\delta\mathcal{A}_d - \psi\frac{\mathcal{L}^2}{2\mathcal{I}^2}\delta\mathcal{I} - \delta\Pi\delta V = \gamma\delta\mathcal{A}_d - \psi\frac{1}{2}\omega^2\delta\mathcal{I} - \delta\Pi\delta V = \delta E^{\omega}_{total}\ ,$$

yielding the same stationary points. However, notice that the second variations of the energies differ, so there may be stationary solutions which are minima for $E^{\mathcal{L}}_{total}$ and not for E^{ω}_{total}:

$$\delta^2 E^{\omega}_{total} = \gamma\delta^2\mathcal{A}_d - \frac{1}{2}\psi\omega^2\delta^2\mathcal{I} - \delta\Pi\delta^2 V \ ,$$

$$\delta^2 E^{\mathcal{L}}_{total} = \gamma\delta^2\mathcal{A}_d - \psi\frac{\mathcal{L}^2}{2\mathcal{I}^2}\delta^2\mathcal{I} - \delta\Pi\delta^2 V + \psi\frac{\mathcal{L}^2}{\mathcal{I}^3}\left(\delta\mathcal{I}\right)^2 = \delta^2 E^{\omega}_{total} + \psi\frac{\mathcal{L}^2}{\mathcal{I}^3}\left(\delta\mathcal{I}\right)^2 \ .$$

The surface area, volume and moment of inertia of an axisymmetric surface have the form:

$$\mathcal{A}_d = 4\pi\int_0^{r_{max}} r\sqrt{1+\left(z'\left(r\right)\right)^2}\,dr \quad , \quad \mathcal{I} = 4\pi\varrho_1\int_0^{r_{max}} r^3 z\left(r\right)\,dr \quad , \quad V = 4\pi\int_0^{r_{max}} rz\left(r\right)\,dr \ .$$

Using these formulas, the total energy is:

$$E^{\omega}_{total} = 4\pi\gamma\int_0^{r_{max}} r\sqrt{1+\left(z'\left(r\right)\right)^2}\,dr - 2\pi\Delta\varrho\omega^2\int_0^{r_{max}} r^3 z\left(r\right)\,dr - \delta\Pi\left(4\pi\int_0^{r_{max}} rz\left(r\right)\,dr - V_0\right) \ .$$

Scaling the problem so that the volume of the drop is $V_0 = 1$ we have to define:

$$r^* = \frac{r}{\sqrt[3]{V_0}} \quad , \quad z^* = \frac{z}{\sqrt[3]{V_0}} \quad , \quad E^{\omega\,*}_{total} = \frac{E^{\omega}_{total}}{4\pi\gamma V_0^{\frac{2}{3}}} \quad , \quad \Omega^2 = \frac{\Delta\varrho\omega^2 V_0}{\gamma} \quad , \quad \delta\Pi^* = \frac{\sqrt[3]{V_0}}{\gamma}\delta\Pi \ ,$$

and the dimensionless functional becomes, omitting asterisks:

$$E^{\omega}_{total} = \int_0^{r_{max}} r\sqrt{1+\left(z'\left(r\right)\right)^2}\,dr - \frac{\Omega^2}{2}\int_0^{r_{max}} r^3 z\left(r\right)\,dr - \delta\Pi\left(\int_0^{r_{max}} rz\left(r\right)\,dr - \frac{1}{4\pi}\right) \ .$$

The Euler-Lagrange equations have the form:

$$\frac{d}{dr}\left(\frac{dE^{\omega}_{total}}{dz'}\right) = \frac{dE^{\omega}_{total}}{dz} \ ,$$

which gives (5.4) as desired. ■

5.2. Evolution & stability

In this section we carry out an analysis to discuss the evolution of rotating drops both at constant angular momentum or constant angular speed. For each situation, first the behaviour of axisymmetric drops is considered, and then, the general 3D evolution is described. We also validate the computer code implemented to solve the evolution problem by comparing in figure 5.2 the axisymmetric solutions to (5.1) with the equilibrium configurations resulting from axisymmetric simulations. It is clear from this comparison that there is an excellent agreement with results.

In what follows, all numerical experiments that impose axial symmetry start from a spherical drop of unit volume, viscosity ratio $\lambda = 0.1$ and surface tension $\gamma = 1$. For the 3D case, and starting also from a spherical drop of unit volume, the surface tension is left unchanged and the experiments deal with different values for the viscosity ratio.

5.2.1. Rotating drops at constant Ω

The mechanism of evolution for an axisymmetric rotating drop at constant Ω can be explained as follows:

- Starting from $\Omega = 0$ and increasing its value, the drop attains a spheroidal-like equilibrium solution for values of the angular speed $0 \leqslant \Omega \leqslant \Omega^*$, where $\Omega^* = 4.3648\ldots$, as shown in figure 5.2.
- When Ω is above the critical value Ω^*, there are no more equilibrium solutions and the drop becomes unstable, developing a hole and elongating to infinity in finite time. This singular behavior, discussed in detail in [37], consists in the formation of a toroidal rim of fluid with a thin film inside. According to [37], the radius of the toroidal rim grows as $r_{\max} \sim O((t_0 - t)^{-\frac{1}{2}})$, i.e. blows up in finite time. The minimum thickness $h_{\min}$ of the inner film vanishes at t_0 and its behaviour is characterized by a second

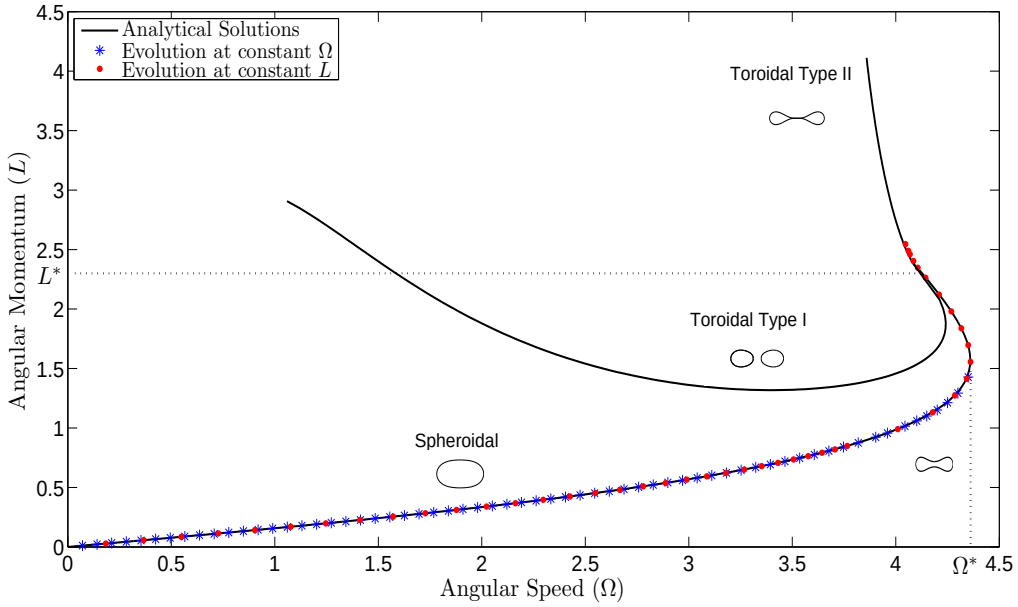

Figure 5.6: Bifurcation diagram of equilibrium shapes for axisymmetric rotating drops. Theoretical curves (continuous line) together with asymptotic values, for $t \to \infty$, of an initially spherical drop evolving at constant Ω (asterisks) or at constant L (dots).

kind self-similar solution. It follows the law $h_{\min}(t) \sim O((t_0 - t)^{p(\Omega)})$ with $p = 4.1236$ in the limit $\Omega \to \infty$ (or equivalently, when surface tension is neglected and $Bo \to \infty$). In fact, the divergence of r_{max} follows from the following argument in [37]: assume that the shape consists of a disc of radius $\beta(t)$ and thickness $h(r,t)$, surrounded by a toroidal rim with a tube radius $R(t)$. Then, the evolution can be described by the following thin film equations [37]:

$$\begin{cases} \dfrac{\partial h}{\partial t} + \dfrac{1}{r}\dfrac{\partial}{\partial r}\left(r h u_r\right) = 0 \\ \dfrac{4}{h}\dfrac{\partial}{\partial r}\left(\dfrac{h}{r}\dfrac{\partial}{\partial r}\left(r u_r\right)\right) - 2\dfrac{u_r}{hr}\dfrac{\partial h}{\partial r} = -\Omega^2 r + \dfrac{2}{R(t)}\delta\left(r - \beta(t)\right) \end{cases} , \tag{5.13}$$

where $u_r(r,t)$ is the radial velocity and δ is the Dirac delta function. The last term on the right-hand side of the second equation in (5.13) models the force that the toroidal rim exerts on the film. If we search for self-similar solutions to (5.13), from dimensional arguments one finds that they must have the form:

$$h(r,t) = (t_0 - t)^p f\left(r(t_0 - t)^{\frac{1}{2}}\right) \quad , \quad u_r(r,t) = (t_0 - t)^{-\frac{3}{2}} g\left(r(t_0 - t)^{\frac{1}{2}}\right) , \tag{5.14}$$

where p is a free parameter depending on Ω. The solution (5.14) implies that the radius of the disc $\beta(t)$ blows up at a rate $(t_0 - t)^{-\frac{1}{2}}$. Our numerical results for the growth of the drop's size r_{max}, blowing up at the same rate as $\beta(t)$, support the results in [37] for the lubrication system (5.13) (see figure 5.8) up to the maximum drop extension reachable with our method.

It is worth noting that the solutions representing a torus escaping to infinity in finite time cannot be a valid approximation to the real situation at all times. The reason is that velocity blows up at finite time and therefore inertial terms neglected under Stokes approximation will necessarily become dominant at some time. Then, the fluid particles will at most move with a centrifugal acceleration, so that their distance $r(t)$ to the axis will verify:

$$\frac{d^2 r(t)}{dt^2} \simeq \Omega^2 r(t) ,$$

yielding $r(t) \leqslant Ce^{\Omega t}$. Once a hole appears in the inner film, it will quickly retract and the resulting torus will be subject to Plateau-Rayleigh instabilities leading to breakup into smaller droplets. The breakup of a rotating torus will be discussed later in this section.

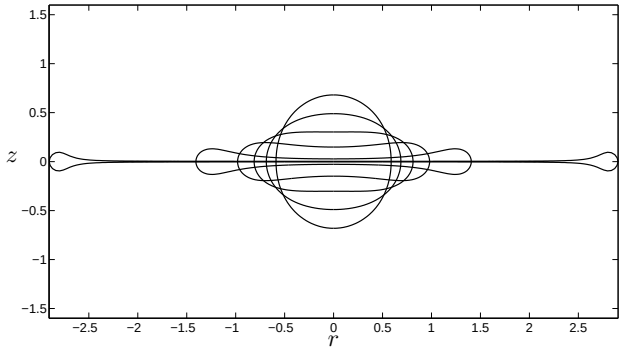

Figure 5.7: Evolution of a drop rotating at constant $\Omega = 10$ for times $t = 0, 0.1, 0.2, 0.3, 0.4, 0.5$.

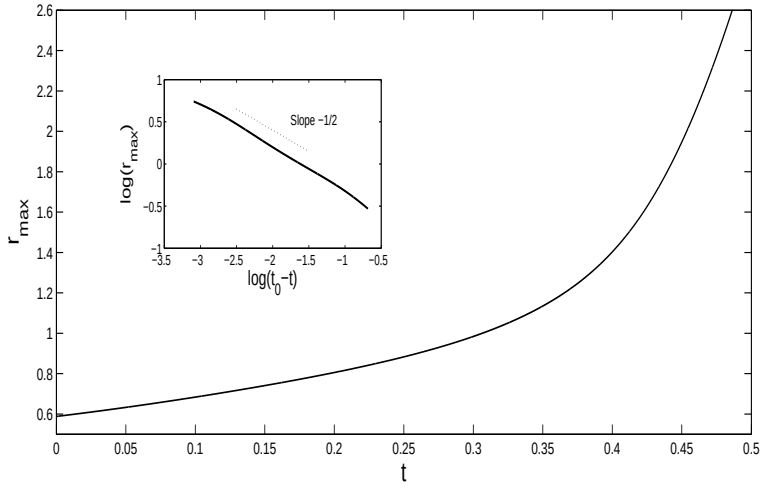

Figure 5.8: Evolution of the drop's equatorial radius at constant $\Omega = 10$ with $t_0 \simeq 0.51$.

We have seen that axisymmetric drops rotating at constant Ω, for $\Omega > \Omega^*$ evolve into the so-called (in the notation introduced by Howell et al. [37]) *pizza* shape. In this evolution process, the film at the center goes to zero in finite time as shown in [37]. Whether or not these axisymmetric shapes are stable or evolve towards a different configuration was mentioned as an open problem. With our 3D boundary elements code we have found that:

- When $\Omega < \Omega_2 \in (3.28, 3.31)$ the drop tends to an spheroidal-like axisymmetric equilibrium (the value of Ω_2 appearing in [11] corresponds, in our units to $\Omega_2 = 3.24$).
- For $\Omega_2 < \Omega < \Omega_{ap} \in (4.55, 4.59)$ an initially spherical drop evolves into an unstable *peanut* that elongates infinitely in finite time. The drop becomes approximately axisymmetric about the r axis and one can easily develop a thin jet model of the type described in [23], consisting in the following equations (we have simplified the situation by considering only one fluid with viscosity μ and density ϱ, although this can be easily generalized):

$$\begin{cases} \dfrac{3\mu}{h^2}\dfrac{\partial}{\partial r}\left(h^2\dfrac{\partial u_r}{\partial r}\right) = \dfrac{\partial \Pi}{\partial r} \\ \dfrac{\partial h}{\partial t} + \dfrac{h}{2}\dfrac{\partial u_r}{\partial r} + u_r\dfrac{\partial h}{\partial r} = 0 \end{cases}, \tag{5.15}$$

where u_r is the radial component of the velocity field, which is, at leading order, independent of z and dominant with respect to the vertical component of the velocity, and the pressure is given by:

$$\Pi(r,t) = 2\gamma\mathcal{H}(r,t) - \varrho\frac{\omega^2}{2}r^2 \simeq -\varrho\frac{\omega^2}{2}r^2 \ .$$

Observe that capillary forces are negligible with respect to centrifugal forces and only enter into play at the tips of the *peanut*, resulting in the formation of a small droplet whose size decreases with time.

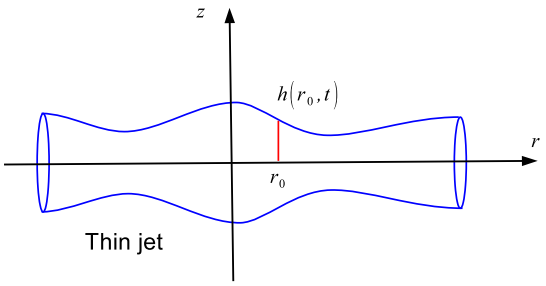

Figure 5.9: Thin jet model.

Theorem 5.2. *The system of equations (5.15) admits self-similar solutions in the form:*

$$h(r,t) = (t_0-t)^{\alpha} f(\xi) \quad , \quad u_r(r,t) = (t_0-t)^{\gamma} g(\xi) \quad , \quad \xi = (t_0-t)^{\beta} r \ ,$$

with exponents $\alpha = \frac{1}{4}$, $\beta = \frac{1}{2}$ *and* $\gamma = -\frac{3}{2}$.

Proof. Suppose that we can find similarity solutions to (5.15) in the form:

$$h(r,t) = (t_0-t)^{\alpha} f(\xi) \quad , \quad u_r(r,t) = (t_0-t)^{\gamma} g(\xi) \quad , \quad \xi = (t_0-t)^{\beta} r \ .$$

Introducing these expressions into the second equation of (5.15) one gets:

$$\gamma+\beta = -1 \quad , \quad 0 = -\alpha f - \beta\xi f' + gf' + \frac{1}{2}fg' \quad , \quad ' \equiv \frac{d}{d\xi} \ ,$$

and the first equation of (5.15) yields:

$$\gamma + 3\beta = 0 \quad , \quad -\varrho\frac{\omega^2}{3\mu}\xi f^2 = 2ff'g' + f^2g'' \ .$$

This requires in particular that $\beta = \frac{1}{2}$ and $\gamma = -\frac{3}{2}$. We end up with the system:

$$\begin{cases} 2ff'g' + f^2g'' = -\varrho\dfrac{\omega^2}{3\mu}\xi f^2 \\ -\alpha f - \dfrac{\xi}{2}f' + gf' + \dfrac{1}{2}fg' = 0 \end{cases} \ . \tag{5.16}$$

Now, observe that:

$$2ff'g' + f^2g'' = \left(f^2g'\right)' \ ,$$

and supposing $g(\xi) = \lambda\xi$ one gets:

$$\frac{\left(f^2\right)'}{f^2} = -\varrho\frac{\omega^2}{3\mu\lambda}\xi \ ,$$

which one can easily integrate to give:

$$f(\xi) = \sqrt{C}\exp\left(-\frac{\varrho\omega^2}{12\mu\lambda}\xi^2\right) \ .$$

Substituting f into the second equation of (5.16) one obtains that $\lambda = \frac{1}{2}$ and $\alpha = \frac{1}{4}$. Finally, the constant C must be chosen so that the drop has a fixed volume V_0, yielding:

$$V_0 = \pi \int_{-\infty}^{\infty} h^2 \, dr \quad \Leftrightarrow \quad \frac{V_0}{\pi C} = \int_{-\infty}^{\infty} \exp\left(-\frac{\varrho\omega^2}{3\mu}\xi^2\right) d\xi = \frac{1}{\omega}\sqrt{\frac{3\mu\pi}{\varrho}} \quad \Leftrightarrow \quad C = V_0\omega\sqrt{\frac{\varrho}{3\mu\pi^3}} \, .$$

This gives:

$$g\left(\xi\right) = \frac{\xi}{2} \quad , \quad f\left(\xi\right) = \sqrt[4]{\frac{V_0^2\omega^2\varrho}{3\mu\pi^3}} \exp\left(-\frac{\varrho\omega^2}{6\mu}\xi^2\right) \, .$$

■

As in the axisymmetric case, one cannot expect an infinite growth of the drop in finite time, since inertial terms in Navier-Stokes equations will necessarily become dominant before the drop spreads out to infinity. The result will be that the neck grows up to some sufficiently large length and then, Rayleigh-Plateau instabilities appear, breaking up the elongated drop in smaller droplets.

- If $\Omega_{ap} < \Omega < \Omega_{sp} \in (4.69, 4.73)$ the initial configuration evolves towards a non axisymmetric *pizza*-like shape (a torus with a thin film in the middle) that is also unstable.
- Finally, for $\Omega > \Omega_{sp}$ the drop turns into an axisymmetric *pizza* that evolves as described above.

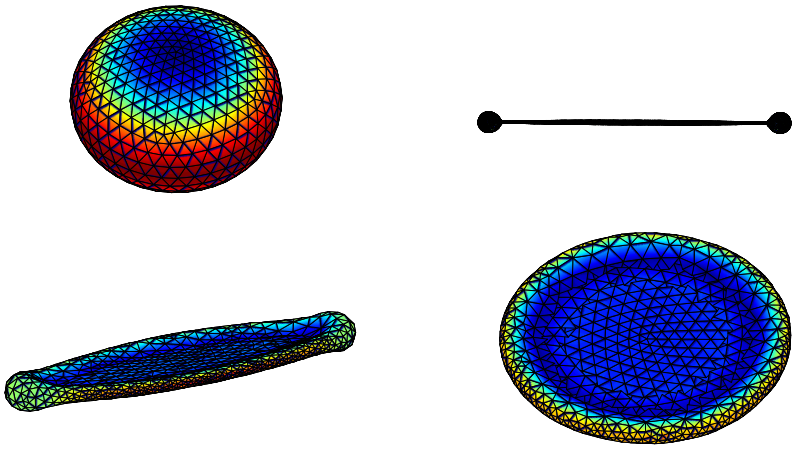

Figure 5.10: Shapes resulting from the evolution of the rotating drop at constant Ω: $\Omega < \Omega_2$ (top left), $\Omega_2 < \Omega < \Omega_{ap}$ (top right), $\Omega_{ap} < \Omega < \Omega_{sp}$ (bottom left) and $\Omega > \Omega_{sp}$ (bottom right). They are not at the same scale. The values of Ω_2, Ω_{ap} and Ω_{sp} have been obtained numerically.

5.2.2. Rotating drops at constant L

When a drop rotates at constant angular momentum, as is the case when it is mechanically isolated, and axial symmetry is imposed, the system always converges to an equilibrium shape, implying that all equilibrium solutions appear to be stable:

- If $0 < L < L^* = 2.3755\ldots$ the drop tends to an spheroidal-like equilibrium solution. The critical value L^* was determined numerically by taking into acount that its angular speed pairing in the $L - \Omega$ bifurcation diagram 5.2 is analytically known [64].
- For any other value $L > L^*$ a subfamily of equilibrium solutions appear, that we denoted as toroidal type II (see figures 5.2 and 5.11), consisting of a zero thickness film that connects a toroidal rim. A natural question that arises is whether this zero thickness film develops a hole in finite or infinite time, and if the hole develops in finite time, how the transition to toroidal type I solutions with the same angular momentum takes place. Our numerical evidence is that the convergence to solutions with a

zero thickness film occurs at infinite time, indicating that the transition to toroidal type I solutions is impossible. It is interesting to note that the film thickness follows the asymptotic law:

$$h_{\min}(t) = h(0,t) \sim \frac{C}{\sqrt{t}}, \tag{5.17}$$

and the interface profiles near the point where the film and toroidal rim meet satisfy a similarity law:

$$\frac{h(r,t)}{h_{\min}(t)} = f\left(\frac{r - r_0(t)}{\sqrt{h_{\min}(t)}}\right), \tag{5.18}$$

where $f(\xi)$ is a similarity profile such that $f(\xi) \to 1$ as $\xi \to -\infty$ and $f(\xi) \sim A\xi^2$ as $\xi \to +\infty$. The radius $r_0(t)$ is such that $r_0(t) \to a$ as $t \to \infty$, where a is the radius of the film.

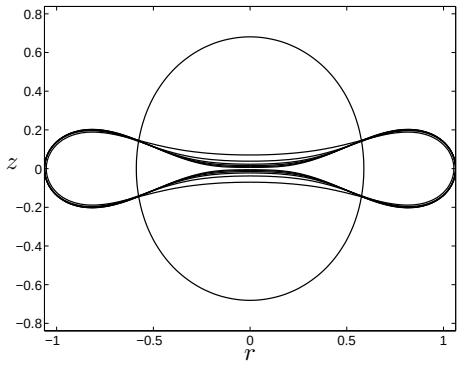

Figure 5.11: Evolution of a drop at constant $L = 2.54558$ for times $t = 0, 1, \ldots, 6$ and $\lambda = 0.1$.

The evolution of the inner film can be easily described by means of an explicit solution of Stokes system in polar coordinates [44]. To do so, and for the sake of simplicity, we will restrict ourselves to the situation where there is no outer fluid present. One can seek for solutions in the form:

$$\begin{cases} u_z = \alpha z r^2 + \beta z^3 \\ u_r = \gamma r z^2 + \delta r^3 \end{cases}. \tag{5.19}$$

where the condition $\nabla \cdot \mathbf{u} = 0$ yields the relations:

$$\begin{cases} 2\gamma + 3\beta = 0 \\ 4\delta + \alpha = 0 \end{cases},$$

so that:

$$\begin{cases} p_r = (2\gamma - 2\alpha) r \\ p_z = (4\alpha - 4\gamma) z \end{cases},$$

and therefore:

$$p = (\gamma - \alpha)\left(r^2 - 2z^2\right). \tag{5.20}$$

The balance between capillary and centrifugal forces for a planar interface $z = h(r,t) = h_{\min}(t)$ are:

$$\begin{aligned} -p + 2\mu_1 \frac{\partial u_z}{\partial z} &= -\frac{\Omega^2}{2} r^2 \\ \frac{\partial u_z}{\partial r} + \frac{\partial u_r}{\partial z} &= 0 \end{aligned},$$

so that plugging in (5.19) and (5.20) we obtain:

$$\begin{aligned} -(\gamma - \alpha)\left(r^2 - 2h^2\right) + 2\left(\alpha r^2 - 2\gamma h^2\right) &= -\frac{\Omega^2}{2} r^2 \\ 2\alpha z r + 2\gamma r z &= 0 \end{aligned},$$

giving:

$$\frac{3}{2}\beta = \alpha = -\gamma = -\frac{\Omega^2}{8} \ .$$

Since the center of the drop, at $r = 0$, moves in the vertical direction, it will follow the law:

$$\frac{dh_{\min}}{dt} = u_z(r=0,t) = \beta h_{\min}^3 = -\frac{\Omega^2}{12} h_{\min}^3 \ ,$$

yielding:

$$h_{\min}(t) \sim \frac{\sqrt{6}}{\Omega} t^{-\frac{1}{2}} \quad , \quad \text{for } t \gg 1 \ . \tag{5.21}$$

In figure 5.12 we represent the evolution of $h_{\min}^{-2}$ and compare it with a linear law for the last stages to confirm the asymptotic law (5.21). Moreover, figure 5.13 depicts numerical profiles for $t \gg 1$ and the same profiles rescaled according to (5.18) to show the convergence towards the similarity function $f(\xi)$.

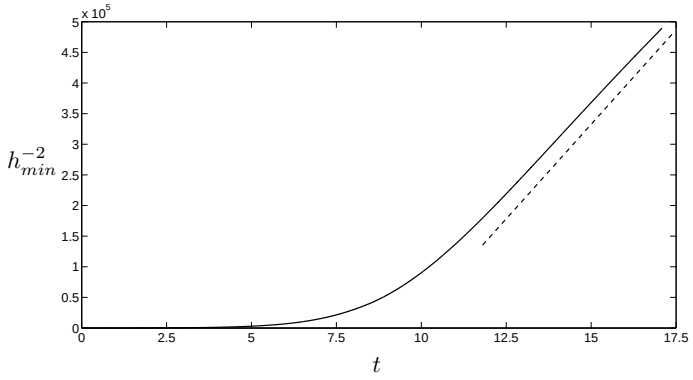

Figure 5.12: Evolution of the inverse square of the film thickness at constant $L = 2.54558$ and comparison with a straight line for $t \gg 1$.

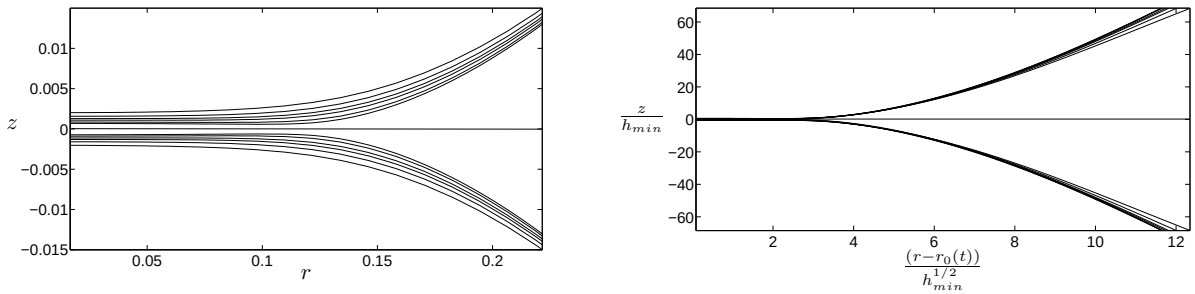

(a) Profiles without rescaling.

(b) Rescaled profiles.

Figure 5.13: Profiles near the region where the thin film and the rim meet for $t \gg 1$. In 5.13(a) profiles are depicted without scaling and in 5.13(b) the same profiles are represented after rescaling with the similarity law. Note that self-similarity behavior for constant $L > L^*$ shows convergence to toroidal type II solutions.

It is well known since the works of Brown and Scriven [11] that bifurcations breaking axial symmetry may take place for different values of L, leading to n-fold symmetries [11, 35]. We have used our 3D code to validate and extend these results when rotation takes place at constant L:

- For $0 < L < L_2 \in (0.641, 0.642)$ drops evolve towards a stable spheroidal-like equilibrium shape.
- When $L_2 < L < L_2^* \in (1.06, 1.10)$ axial symmetry breaks and drops tend to equilibrium shapes with a 2-fold symmetry, i.e. ellipsoids and *peanut* shapes.

- If $L > L_2^*$ interesting phenomena takes place as can be seen in figure 5.14. First, an initially spherical drop deforms into an axisymmetric shape. Since these shapes are also unstable under non-axisymmetric perturbations, after some time they destabilize and evolve very quickly towards a *peanut* shape, which is also unstable since $L > L_2^*$, and consequently the drop breaks up into smaller droplets. It is important to remark that centrifugal forces near the breakup point are subdominant with respect to viscous and capillary forces so that breakup occurs as theoretically described in [45] and [16]. Our numerical simulations were able to follow the evolution very close to the breakup point, allowing us to see the formation of two generations of necks (see figure 5.15).

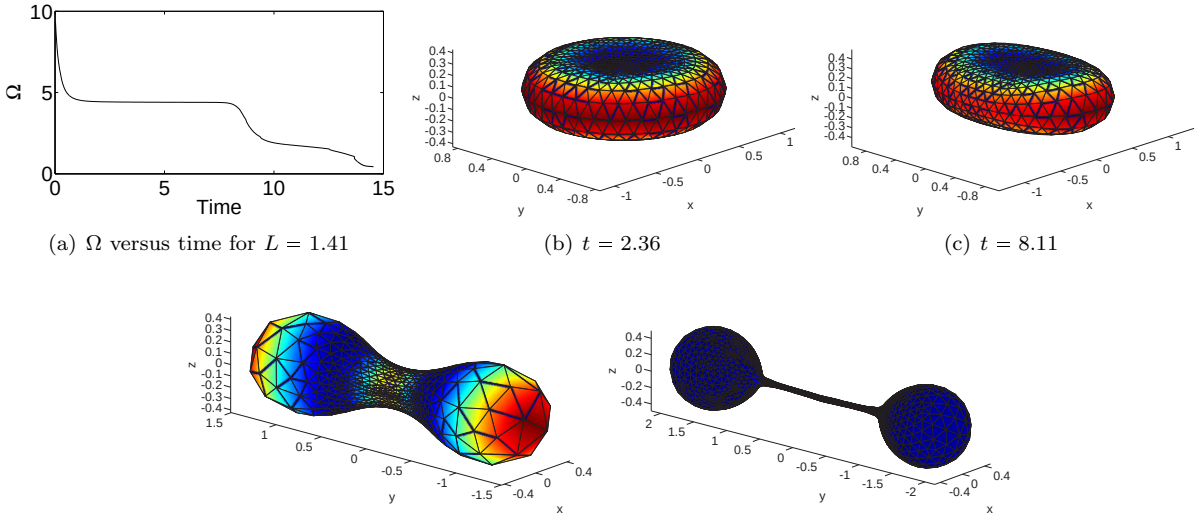

(a) Ω versus time for $L = 1.41$ (b) $t = 2.36$ (c) $t = 8.11$

(d) $t = 12.36$ (e) $t = 14.16$

Figure 5.14: Evolution of a rotating drop at constant L for $L = 1.41$ and viscosity ratio $\lambda = 0.1$.

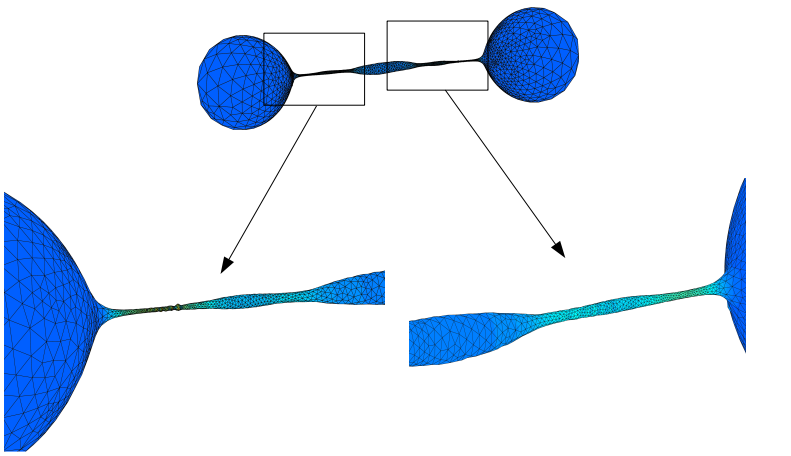

Figure 5.15: Top pictures: shape of the rotating drop at constant L near the breakup point ($t = 14.55$) for $L = 1.41$ and $\lambda = 0.1$. The original drop has transformed into two big drops with a cascade of necks between them. Bottom pictures: detail of the necks. Observe the formation of small droplets in the smaller neck at the left.

- Finally, we have estimated numerically that for $L > L_3^* \in (1.74, 1.78)$ the dominant mode driving the symmetry-breaking instability is 3-fold and, therefore, evolution leads to the formation of three necks emerging from the center of the drop, breaking up into smaller drops at a finite distance from the center (see figure 5.16).

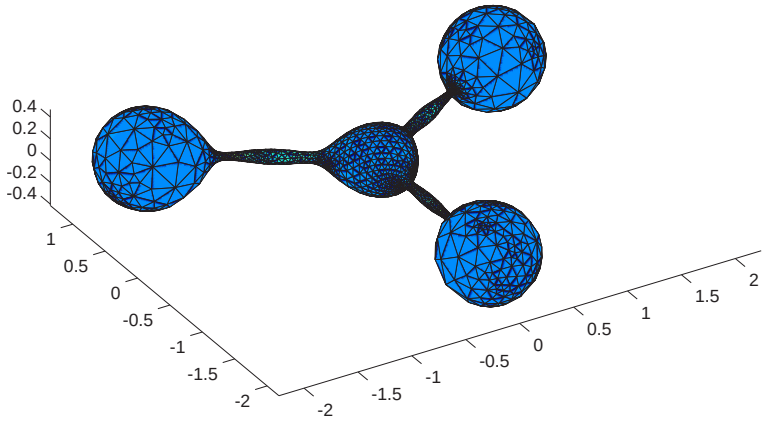

Figure 5.16: Shape of a rotating drop at constant L near the breakup point for $L = 3.54$ and $\lambda = 1$.

It is important to remark that with our analysis we could not find solutions developing into a n-fold symmetry with $n > 3$. As a curiosity, if we start the system with a torus as initial data, then for $L < L_2^*$ there is a clear tendency to close the hole so that the drop tends to an equilibrium shape with the same topology as the sphere. On the contrary, for $L > L_2^*$ the toroidal rim develops Rayleigh instabilities that lead to a breakup into a sequence of drops (see figure 5.17).

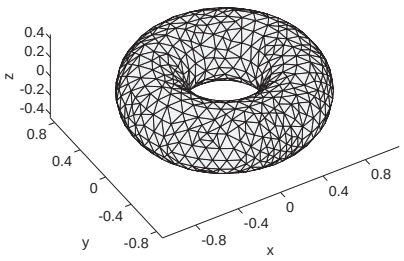

(a) Toroidal initial configuration.

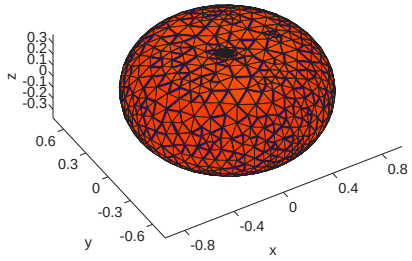

(b) Equilibrium shape for $L = 0.85$.

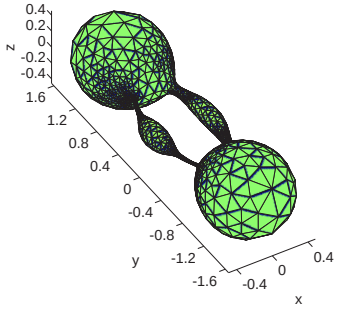

(c) Near the break-up point for $L = 1.7$.

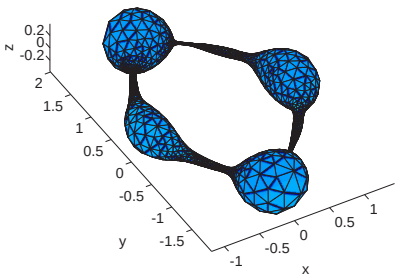

(d) Near the break-up point for $L = 2.83$.

Figure 5.17: Different equilibrium or breakup configurations starting from a torus. In all cases $\lambda = 1$.

Chapter 6

Rotational effects on conducting drops

The aim of this chapter is to study the effects that rotation has on conducting and viscous drops when they are charged or subject to an external electric field parallel to the rotation axis. In each section, we start first by introducing the main theoretical results known in the literature, and then, we present a numerical analysis of the evolution problem using our BEM codes. We also develop theoretical models to approximate equilibrium solutions and validate them with numerical simulations. The last section of this chapter tries to give an answer to how rotation modifies the opening semiangle of Taylor cones, which are structures that a droplet develops whenever it holds a very large amount of charge or a strong electric field is applied to it. All results related to rotation at constant angular momentum will be published shortly in [28] because of their physical relevance.

6.1. The effects of rotation on charged drops

To study the role that rotation plays on a conducting charged drop, one needs to understand first the effect that charge has on the system. In this direction, Rayleigh showed in 1882 using a linear stability analysis [58] that a spherical and conducting droplet with charge $Q > Q_c$ on its surface becomes unstable, evolving into a prolate spheroid that eventually ends up developing cone tips at the poles (known in the literature as Taylor cones [68]). From these tips, thin jets of microdroplets are ejected, carrying about 30% of the total charge from the mother drop but only 1% of its mass [20]. This phenomenon is applied nowadays to design industrial processes such as electrospinning, electrospraying and mass spectrometry techniques.

We will show next a back-of-the-envelope calculation of this critical charge value. Consider a spherical drop of radius R with charge Q on its surface. When the pressure jump $\delta\Pi$ at the interface between the droplet and the surrounding fluid vanishes, the drop becomes unstable and electrostatic forces balance capillary forces. In this case, Young-Laplace equation (2.41) reduces to:

$$2\gamma\mathcal{H} = \frac{\sigma^2}{2\varepsilon_0} \tag{6.1}$$

For a sphere of radius R, volume V_0 and unit normal $\mathbf{n} = \mathbf{e_r}$ we get:

$$\nabla \cdot \mathbf{e_r} = \frac{1}{r^2}\frac{\partial}{\partial r}\left(r^2\right) = \frac{2}{r} \quad \Rightarrow \quad \mathcal{H} = \frac{1}{R}\,.$$

We also know that the surface charge density for a sphere is:

$$\sigma = \frac{Q}{4\pi R^2}\,.$$

Substituting these values into (6.1), the charge that makes the droplet unstable is:

$$Q_c = \sqrt{64\pi^2\gamma\varepsilon_0 R^3} = \sqrt{48\pi\gamma\varepsilon_0 V_0}\,, \tag{6.2}$$

which corresponds in dimensionless units (2.38) to $\chi = 1$.

Rayleigh's analysis revealed not only $\chi = 1$, but a complete sequence of values for the charge at which families of n-lobed shapes bifurcate from the main branch of spherical solutions (see figure 1.7):

$$Q_n = \sqrt{12\pi\gamma\varepsilon_0 V_0\,(n+2)} \quad \Leftrightarrow \quad \chi_n = \frac{n}{4} + \frac{1}{2} \quad , \quad n \geqslant 2\,. \tag{6.3}$$

In particular, when $n = 2$, one obtains a spheroidal family branching at $\chi_2 = 1$:

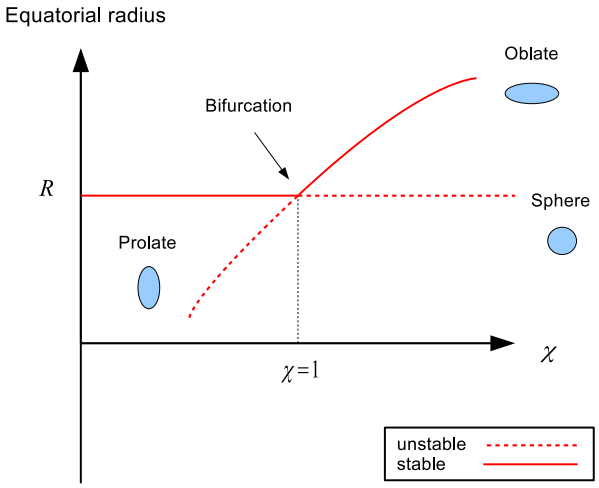

Figure 6.1: First bifurcation point for charged conducting drops.

The main question that we will answer in this section is how the critical charge that a droplet can sustain before becoming unstable varies with rotation. Another goal is to determine what happens with the bifurcation point χ_2 when rotation is considered.

6.1.1. Equilibrium shapes for rotating charged drops

In this subsection we propose two methods to approximate axisymmetric equiibrium configurations for rotating charged drops. The first one is based on asymptotic expansions and the second deals with the minimization of the energy functional associated to the system.

We start by deriving an analytical second-order approximation to (2.41) and (2.42) in the small parameters $\mathcal{L}^2$ and ω^2 similarly to the work in [63], where the ratio of the deformation amplitude to the radius of the initial spherical shape is used as the small parameter. When the drop is not rotating, i.e. $\mathcal{L} = \omega = 0$, the sphere is a solution to (2.41) and (2.42) for all values of the charge Q. Indeed, we have in this case that:

$$\delta\Pi = \frac{2\gamma}{R} - \frac{\varepsilon_0}{2}\left(\frac{Q}{4\pi\varepsilon_0 R^2}\right)^2 \quad \Leftrightarrow \quad \delta P = 1 - \chi \quad , \quad \delta\Pi = \frac{2\gamma}{R}\delta P \, ,$$

suggesting that one could search for solutions to (2.41) and (2.42) as expansions in powers of $\mathcal{L}^2 \ll 1$ or $\omega^2 \ll 1$ about the sphere. To do so, one has to solve the modified Young-Laplace equation:

$$\delta\Pi = 2\gamma\mathcal{H} - \Delta\varrho\frac{\mathcal{L}^2}{2\mathcal{I}^2}r_{axis}^2 - \frac{\varepsilon_0}{2}\left(\frac{\partial\mathcal{V}}{\partial\mathbf{n}}\right)^2 \quad , \quad \text{on } \partial\mathcal{D} \, , \tag{6.4}$$

or in terms of the angular speed:

$$\delta\Pi = 2\gamma\mathcal{H} - \Delta\varrho\frac{\omega^2}{2}r_{axis}^2 - \frac{\varepsilon_0}{2}\left(\frac{\partial\mathcal{V}}{\partial\mathbf{n}}\right)^2 \quad , \quad \text{on } \partial\mathcal{D} \, . \tag{6.5}$$

Before giving any further details, we need to introduce some basic definitions and important results [24]:

Definition 6.1. *The spherical harmonics $Y_{l,m}$ are functions on the unit sphere defined as follows:*

$$Y_{l,m}(\theta,\varphi) = \sqrt{\frac{2l+1}{4\pi}\frac{(l-m)!}{(l+m)!}}P_l^m(\cos\theta)\,e^{im\varphi} \quad , \quad \theta \in [0,\pi] \quad , \quad \varphi \in [0,2\pi] \, ,$$

with P_l^m the associated Legendre polynomials:

$$P_l^m(x) = \frac{(-1)^m}{2^l l!}\left(1-x^2\right)^{\frac{m}{2}}\frac{d^{l+m}}{dx^{l+m}}\left[\left(x^2-1\right)^l\right] \quad , \quad P_l^{-m}(x) = (-1)^m\frac{(l-m)!}{(l+m)!}P_l^m(x) \quad , \quad |m| \leqslant l \, .$$

Theorem 6.1. *Given a perturbation of the sphere:*

$$\mathcal{P}_\varepsilon \,:\, r = R + h\left(\theta,\varphi\right)\varepsilon \quad , \quad \varepsilon \ll 1 \,,$$

the mean curvature and the normal derivative of the potential can be written as:

$$\mathcal{H}\left(\mathcal{P}_\varepsilon\right) = \frac{1}{R} + \mathcal{L}_\mathcal{H}\left(h\right)\varepsilon + \frac{1}{2}\mathcal{Q}_\mathcal{H}\left(h,h\right)\varepsilon^2 + O\left(\varepsilon^3\right) \,,$$
$$\left(\frac{\partial \mathcal{V}}{\partial \mathbf{n}}\left(\mathcal{P}_\varepsilon\right)\right)^2 = \left(\frac{Q}{4\pi\varepsilon_0 R^2}\right)^2 + \mathcal{L}_\mathcal{V}\left(h\right)\varepsilon + \frac{1}{2}\mathcal{Q}_\mathcal{V}\left(h,h\right)\varepsilon^2 + O\left(\varepsilon^3\right) \,,$$

with $\mathcal{L}_\mathcal{H}$, $\mathcal{L}_\mathcal{V}$ linear operators and $\mathcal{Q}_\mathcal{H}$, $\mathcal{Q}_\mathcal{V}$ quadratic operators acting on:

$$h\left(\theta,\varphi\right) = \sum_{l=0}^{\infty}\sum_{m=-l}^{l} h_{l,m} Y_{l,m}\left(\theta,\varphi\right) \quad , \quad \theta \in \left[0,\pi\right] \quad , \quad \varphi \in \left[0,2\pi\right] .$$

These linear operators have an explicit representation in the form:

$$\mathcal{L}_\mathcal{H}\left(h\right) = -\frac{1}{R^2}\left(h + \frac{1}{2}\Delta_\omega h\right) \,,$$
$$\mathcal{L}_\mathcal{V}\left(h\right) = -\frac{2}{R}\left(\frac{Q}{4\pi\varepsilon_0 R^2}\right)^2\left(2h - \sum_{l=0}^{\infty}\sum_{m=-l}^{l}\left(l+1\right)h_{l,m}Y_{l,m}\right) \,,$$

where Δ_ω is the spherical laplacian operator:

$$\Delta_\omega h = \frac{1}{\sin\theta}\frac{\partial}{\partial\theta}\left(\sin\theta\frac{\partial h}{\partial\theta}\right) + \frac{1}{\sin^2\theta}\frac{\partial^2 h}{\partial\varphi^2} \,,$$

Proposition 6.1. *The spherical harmonics are eigenfunctions of the spherical laplacian operator:*

$$\Delta_\omega Y_{l,m} = -l\left(l+1\right)Y_{l,m} \,. \tag{6.6}$$

Theorem 6.2. *There exists a second-order approximation to (6.4) about the sphere of radius R in the form:*

$$r\left(\theta\right) = R + f_2 Y_{2,0}\left(\theta\right)\mathcal{L}^2 + \left(g_0 Y_{0,0}\left(\theta\right) + g_2 Y_{2,0}\left(\theta\right) + g_4 Y_{4,0}\left(\theta\right)\right)\mathcal{L}^4 + O\left(\mathcal{L}^6\right) \quad , \quad \mathcal{L}^2 \ll 1 \,, \tag{6.7}$$

where the coefficients are given by:

$$f_2 = -\frac{15\psi\sqrt{5}}{128\varrho_1\gamma\pi^{\frac{3}{2}}R^6\left(1-\chi\right)} \quad , \quad g_0 = -\frac{1}{2\sqrt{\pi}R}f_2^2 \,, \tag{6.8}$$

$$g_2 = \frac{5\sqrt{5}f_2^2\left(1+\chi\right)}{14\sqrt{\pi}R\left(1-\chi\right)} - \frac{15\psi f_2}{448\varrho_1\gamma\pi^2R^7\left(1-\chi\right)} \quad , \quad g_4 = \frac{5f_2^2\left(1-\chi\right)}{7\sqrt{\pi}R\left(3-2\chi\right)} - \frac{15\psi\sqrt{5}f_2}{224\varrho_1\gamma\pi^2R^7\left(3-2\chi\right)} \,, \tag{6.9}$$

and the solution behaves to first-order like an oblate spheroid for $\chi < 1$ or a prolate spheroid otherwise.

Proof. Imposing axial symmetry, one can use spherical coordinates to write the solution as:

$$\mathcal{S} \,:\, r\left(\theta\right) = R + f\left(\theta\right)\mathcal{L}^2 + g\left(\theta\right)\mathcal{L}^4 + O\left(\mathcal{L}^6\right) \quad , \quad \theta \in \left[0,\pi\right] \,,$$

where R is the radius of the sphere. Both functions f and g can be expressed in terms of spherical harmonics:

$$f\left(\theta\right) = \sum_{l=0}^{\infty} f_{2l} Y_{2l,0}\left(\theta\right) \quad , \quad g\left(\theta\right) = \sum_{l=0}^{\infty} g_{2l} Y_{2l,0}\left(\theta\right) \quad , \quad Y_{l,m}\left(\theta\right) \equiv Y_{l,m}\left(\theta,0\right) \,, \tag{6.10}$$

imposing equatorial symmetry. Now, the volume of $\mathcal{S}$ must remain constant and equal to that of the sphere:

$$V_\mathcal{S} = \int_0^{2\pi}\int_0^{\pi}\int_0^{r(\theta)} \rho^2\sin\theta \; d\rho \; d\theta \; d\varphi = \frac{4\pi}{3}R^3 + R^2\mathcal{L}^2\int_0^{2\pi}\int_0^{\pi} f\left(\theta\right)\sin\theta \; d\theta \; d\varphi +$$
$$+ R\mathcal{L}^4\int_0^{2\pi}\int_0^{\pi}\left(f^2\left(\theta\right) + Rg\left(\theta\right)\right)\sin\theta \; d\theta \; d\varphi + O\left(\mathcal{L}^6\right) \,,$$

so the first and second-order contributions to the volume are:

$$R^2\int_0^{2\pi}\int_0^{\pi} f\left(\theta\right)\sin\theta\;d\theta\;d\varphi \quad , \quad R\int_0^{2\pi}\int_0^{\pi}\left(f^2\left(\theta\right)+Rg\left(\theta\right)\right)\sin\theta\;d\theta\;d\varphi\;. \tag{6.11}$$

Substituting (6.10) into (6.11) we get:

$$R^2\sum_{l=0}^{\infty} f_{2l}\int_0^{2\pi}\int_0^{\pi} Y_{2l,0}\left(\theta\right)\sin\theta\;d\theta\;d\varphi = 2\sqrt{\pi}R^2\sum_{l=0}^{\infty} f_{2l}\int_0^{2\pi}\int_0^{\pi} Y_{2l,0}\left(\theta\right)Y_{0,0}\left(\theta\right)\sin\theta\;d\theta\;d\varphi = 2\sqrt{\pi}R^2 f_0\;,$$

$$R\sum_{l=0}^{\infty}\left(f_{2l}^2\int_0^{2\pi}\int_0^{\pi} Y_{2l,0}^2\left(\theta\right)\sin\theta\;d\theta\;d\varphi + g_{2l}R\int_0^{2\pi}\int_0^{\pi} Y_{2l,0}\left(\theta\right)\sin\theta\;d\theta\;d\varphi\right) = R\sum_{l=0}^{\infty} f_{2l}^2 + 2\sqrt{\pi}R^2 g_0\;,$$

and since the volume has to remain constant we need:

$$f_0 = 0 \quad , \quad g_0 = -\frac{1}{2\sqrt{\pi}R}\sum_{l=0}^{\infty} f_{2l}^2\;. \tag{6.12}$$

For the moment of inertia:

$$\begin{aligned}\mathcal{I}_{\mathcal{S}} = \varrho_1\int_0^{2\pi}\int_0^{\pi}\int_0^{r(\theta)}\rho^4\sin^3\theta\;d\rho\;d\theta\;d\varphi = \frac{8\pi\varrho_1 R^5}{15} + \varrho_1 R^4\mathcal{L}^2\int_0^{2\pi}\int_0^{\pi} f\left(\theta\right)\sin^3\theta\;d\theta\;d\phi + \\ + \varrho_1 R^3\mathcal{L}^4\int_0^{2\pi}\int_0^{\pi}\left(2f^2\left(\theta\right)+Rg\left(\theta\right)\right)\sin^3\theta\;d\theta\;d\phi + O\left(\mathcal{L}^6\right)\;.\end{aligned}$$

Now, considering that:

$$\sin^2\theta = \frac{4\sqrt{\pi}}{3}\left(Y_{0,0} - \frac{\sqrt{5}}{5}Y_{2,0}\right)\;, \tag{6.13}$$

and using (6.12), the contributions to first and second-order yield:

$$\varrho_1 R^4\int_0^{2\pi}\int_0^{\pi} f\left(\theta\right)\sin^3\theta\;d\theta\;d\phi = -\frac{4\varrho_1 R^4}{3}\sqrt{\frac{\pi}{5}}f_2\;,$$

$$\varrho_1 R^3\int_0^{2\pi}\int_0^{\pi}\left(2f^2\left(\theta\right)+Rg\left(\theta\right)\right)\sin^3\theta\;d\theta\;d\phi = \frac{4\varrho_1 R^3}{3}\left(\sum_{l,k=1}^{\infty} f_{2l}f_{2k}\mathcal{A}_{2l,2k} - \sqrt{\frac{\pi}{5}}Rg_2\right)\;,$$

with:

$$\mathcal{A}_{l,k} = \sqrt{\left(2l+1\right)\left(2k+1\right)}\left(\left(C_{0,0,0}^{l,k,0}\right)^2 - \frac{1}{5}\left(C_{0,0,0}^{l,k,2}\right)^2\right) - \frac{\delta_{lk}}{2}\;,$$

where $C_{m_1,m_2,m}^{j_1,j_2,j}$ are the Clebsch-Gordan coefficients [1]. The equilibrium condition (6.4) requires the inverse square of the moment of inertia multiplied by $\mathcal{L}^2$, so we will expand only to first-order. Using asymptotics:

$$\frac{1}{\left(a+bx\right)^2} \approx \frac{1}{a^2}\left(1-\frac{2b}{a}x\right) \quad , \quad x \ll 1\;,$$

gives:

$$\frac{1}{\mathcal{I}_{\mathcal{S}}^2} = \left(\frac{15}{8\pi\varrho_1 R^5}\right)^2\left(1+\frac{1}{R}\sqrt{\frac{5}{\pi}}f_2\mathcal{L}^2\right) + O\left(\mathcal{L}^4\right)\;.$$

The distance to the axis of rotation has the form:

$$r_{axis}^2 = r^2\left(\theta\right)\sin^2\theta = R^2\sin^2\theta + 2R\mathcal{L}^2 f\left(\theta\right)\sin^2\theta + O\left(\mathcal{L}^4\right)\;,$$

and thus:

$$\Delta\varrho\frac{\mathcal{L}^2}{2\mathcal{I}^2}r_{axis}^2 = \psi\left(\frac{15}{8\pi\sqrt{2\varrho_1}R^5}\right)^2\left(R^2\mathcal{L}^2 + \left(2Rf\left(\theta\right)+R\sqrt{\frac{5}{\pi}}f_2\right)\mathcal{L}^4\right)\sin^2\theta + O\left(\mathcal{L}^6\right)\;.$$

Following theorem 6.1, take $\varepsilon = \mathcal{L}^2$ and $h = f + g\mathcal{L}^2$, and since the operators are linear:

$$\mathcal{H}(\mathcal{S}) = \frac{1}{R} + \mathcal{L}_{\mathcal{H}}(f)\mathcal{L}^2 + \left(\mathcal{L}_{\mathcal{H}}(g) + \frac{1}{2}\mathcal{Q}_{\mathcal{H}}(f,f)\right)\mathcal{L}^4 + O\left(\mathcal{L}^6\right) ,$$
$$\left(\frac{\partial \mathcal{V}}{\partial \mathbf{n}}(\mathcal{S})\right)^2 = \left(\frac{Q}{4\pi\varepsilon_0 R^2}\right)^2 + \mathcal{L}_{\mathcal{V}}(f)\mathcal{L}^2 + \left(\mathcal{L}_{\mathcal{V}}(g) + \frac{1}{2}\mathcal{Q}_{\mathcal{V}}(f,f)\right)\mathcal{L}^4 + O\left(\mathcal{L}^6\right) .$$

Expanding the pressure in powers of $\mathcal{L}^2$ one gets:

$$\delta P = \frac{R}{2\gamma}\delta\Pi \quad , \quad \delta P = \delta P_0 + \delta P_1 \mathcal{L}^2 + \delta P_2 \mathcal{L}^4 + O\left(\mathcal{L}^6\right) .$$

Comparing terms in (6.4), to zeroth-order we have:

$$\delta P_0 = 1 - \chi .$$

For the first-order contribution, collect all terms with $\mathcal{L}^2$ and use the property (6.6) to yield:

$$\begin{aligned}
\delta P_1 &= R\mathcal{L}_{\mathcal{H}}(f) - \frac{\varepsilon_0 R}{4\gamma}\mathcal{L}_{\mathcal{V}}(f) - \psi\left(\frac{15}{8\pi\sqrt{2\varrho_1}R^5}\right)^2 \frac{R^3\sin^2\theta}{2\gamma} = \\
&= -\frac{1}{R}\left(f + \frac{1}{2}\Delta_\omega f\right) + \frac{2\chi}{R}\left(2f - \sum_{l=1}^{\infty}(2l+1) f_{2l} Y_{2l,0}\right) - \psi\left(\frac{15}{16\pi\sqrt{\gamma\varrho_1}R^{\frac{7}{2}}}\right)^2 \sin^2\theta = \\
&= \frac{1}{R}\sum_{l=1}^{\infty} a(\chi, l) f_{2l} Y_{2l,0} - \psi\left(\frac{15}{16\pi\sqrt{\gamma\varrho_1}R^{\frac{7}{2}}}\right)^2 \sin^2\theta ,
\end{aligned} \tag{6.14}$$

where the coefficients:

$$a(\chi, l) = 2\chi - 1 + (1 - 4\chi + 2l)\, l , \tag{6.15}$$

are eigenvalues of the operator:

$$\mathcal{K} = R^2\mathcal{L}_{\mathcal{H}} - \frac{\varepsilon_0 R^2}{4\gamma}\mathcal{L}_{\mathcal{V}} . \tag{6.16}$$

Using (6.13) and equating the $Y_{0,0}$ component of (6.14) with the pressure:

$$\delta P_1 = -\frac{75\psi}{128\varrho_1\gamma\pi^2 R^7} \quad , \quad 0 = \frac{1}{R}\sum_{l=1}^{\infty} a(\chi, l) f_{2l} Y_{2l,0} + \frac{3\psi\sqrt{125}}{64\varrho_1\gamma\pi^{\frac{3}{2}}R^7} Y_{2,0} .$$

We conclude that:

$$f(\theta) = f_2 Y_{2,0}(\theta) \quad , \quad f_2 = -\frac{15\psi\sqrt{5}}{128\varrho_1\gamma\pi^{\frac{3}{2}}R^6(1-\chi)} \quad , \quad g_0 = -\frac{1}{2\sqrt{\pi}R} f_2^2 ,$$

To complete our analysis we balance second-order terms:

$$\begin{aligned}
\delta P_2 = R\mathcal{L}_{\mathcal{H}}(g) - \frac{\varepsilon_0 R}{4\gamma}\mathcal{L}_{\mathcal{V}}(g) + \frac{R}{2}\mathcal{Q}_{\mathcal{H}}(f,f) - \frac{\varepsilon_0 R}{8\gamma}\mathcal{Q}_{\mathcal{V}}(f,f) - \\
- \psi\left(\frac{15}{16\pi\sqrt{\gamma\varrho_1}R^4}\right)^2 \left(2f + \sqrt{\frac{5}{\pi}} f_2\right)\sin^2\theta .
\end{aligned} \tag{6.17}$$

Now, the quadratic operators $\mathcal{Q}_{\mathcal{H}}$ and $\mathcal{Q}_{\mathcal{V}}$ verify, as shown in [24], that:

$$\frac{R}{2}\mathcal{Q}_{\mathcal{H}}(f,f) = \frac{Rf_2^2}{2}\mathcal{Q}_{\mathcal{H}}(Y_{2,0}, Y_{2,0}) = -\frac{5f_2^2}{2\sqrt{\pi}R^2}\left(Y_{0,0} + \frac{2\sqrt{5}}{7}Y_{2,0} + \frac{6}{7}Y_{4,0}\right) ,$$
$$\frac{\varepsilon_0 R}{8\gamma}\mathcal{Q}_{\mathcal{V}}(f,f) = \frac{\varepsilon_0 R f_2^2}{8\gamma}\mathcal{Q}_{\mathcal{V}}(Y_{2,0}, Y_{2,0}) = \frac{\chi f_2^2}{\sqrt{\pi}R^2}\left(-\frac{1}{2}Y_{0,0} + \frac{5\sqrt{5}}{7}Y_{2,0} - \frac{15}{7}Y_{4,0}\right) ,$$

and using:

$$\sqrt{\frac{5}{\pi}} f_2 \sin^2\theta = f_2\left(\frac{4\sqrt{5}}{3}Y_{0,0} - \frac{4}{3}Y_{2,0}\right) \quad , \quad Y_{2,0}^2 = \frac{1}{\sqrt{\pi}}\left(\frac{3}{7}Y_{4,0} + \frac{1}{7\sqrt{5}}Y_{2,0} + \frac{1}{2}Y_{0,0}\right) ,$$

then:

$$2f\sin^2\theta = \frac{8\sqrt{\pi}f_2}{3}\left(Y_{0,0}Y_{2,0} - \frac{\sqrt{5}}{5}Y_{2,0}^2\right) = \frac{8\sqrt{\pi}f_2}{3}\left(\frac{1}{2\sqrt{\pi}}Y_{2,0} - \frac{1}{\sqrt{5\pi}}\left(\frac{3}{7}Y_{4,0} + \frac{1}{7\sqrt{5}}Y_{2,0} + \frac{1}{2}Y_{0,0}\right)\right) =$$
$$= \frac{8f_2}{3}\left(\frac{33}{70}Y_{2,0} - \frac{\sqrt{5}}{5}\left(\frac{3}{7}Y_{4,0} + \frac{1}{2}Y_{0,0}\right)\right) = f_2\left(\frac{44}{35}Y_{2,0} - \frac{8\sqrt{5}}{35}Y_{4,0} - \frac{4}{3\sqrt{5}}Y_{0,0}\right) ,$$

$$\left(2f + \sqrt{\frac{5}{\pi}}f_2\right)\sin^2\theta = \frac{16}{15}f_2\left(-\frac{3}{42}Y_{2,0} - \frac{3\sqrt{5}}{14}Y_{4,0} + \sqrt{5}Y_{0,0}\right) .$$

These linear combinations of $Y_{0,0}$, $Y_{2,0}$ and $Y_{4,0}$ indicate that to satisfy (6.17) we need:

$$g(\theta) = g_0 Y_{0,0}(\theta) + g_2 Y_{2,0}(\theta) + g_4 Y_{4,0}(\theta) .$$

Under this assumption we have:

$$\frac{1}{R}\mathcal{K}(g) = \frac{1}{R}\sum_{l=0}^{\infty} a(\chi, l)\, g_{2l} Y_{2l,0} = \frac{1}{R}\left((2\chi-1)\, g_0 Y_{0,0} + 2(1-\chi)\, g_2 Y_{2,0} + 3(3-2\chi)\, g_4 Y_{4,0}\right) =$$
$$= \frac{(1-2\chi)\, f_2^2}{2\sqrt{\pi}R^2}Y_{0,0} + \frac{2(1-\chi)\, g_2}{R}Y_{2,0} + \frac{3(3-2\chi)\, g_4}{R}Y_{4,0} .$$

Equating the pressure with the terms involving $Y_{0,0}$ as before we get:

$$\delta P_2 = -\left(\frac{(\chi+4)\, f_2^2}{2\sqrt{\pi}R^2} + \frac{15\psi\sqrt{5}f_2}{16\varrho_1\gamma\pi^2R^8}\right)Y_{0,0} .$$

Then, the coefficients multiplying $Y_{2,0}$ and $Y_{4,0}$ must be zero:

$$g_2 = \frac{5\sqrt{5}f_2^2(1+\chi)}{14\sqrt{\pi}R(1-\chi)} - \frac{15\psi f_2}{448\varrho_1\gamma\pi^2R^7(1-\chi)} \quad , \quad g_4 = \frac{5f_2^2(1-\chi)}{7\sqrt{\pi}R(3-2\chi)} - \frac{15\psi\sqrt{5}f_2}{224\varrho_1\gamma\pi^2R^7(3-2\chi)} .$$

■

Theorem 6.3. *There exists a second-order approximation to (6.5) about the sphere of radius R in the form:*

$$r(\theta) = R + f_2 Y_{2,0}(\theta)\,\omega^2 + \left(g_0 Y_{0,0}(\theta) + g_2 Y_{2,0}(\theta) + g_4 Y_{4,0}(\theta)\right)\omega^4 + O\left(\omega^6\right) \quad , \quad \omega^2 \ll 1 . \tag{6.18}$$

where the coefficients are given by:

$$f_2 = -\sqrt{\frac{\pi}{5}}\frac{\Delta\varrho R^4}{6\gamma(1-\chi)} \quad , \quad g_0 = -\frac{\sqrt{\pi}(\Delta\varrho)^2 R^7}{360\gamma^2(1-\chi)^2} \tag{6.19}$$

$$g_2 = \frac{5\sqrt{5}f_2^2(1+\chi)}{14\sqrt{\pi}R(1-\chi)} + \frac{11\Delta\varrho R^3 f_2}{70\gamma(1-\chi)} \quad , \quad g_4 = \frac{5f_2^2(1-\chi)}{7\sqrt{\pi}R(3-2\chi)} + \frac{2\Delta\varrho R^3 f_2}{21\sqrt{5}\gamma(2\chi-3)} , \tag{6.20}$$

and the solution behaves to first-order like an oblate spheroid for $\chi < 1$ or a prolate spheroid otherwise.

Proof. Given the expansion about the sphere:

$$\mathcal{S} \,:\, r(\theta) = R + f(\theta)\,\omega^2 + g(\theta)\,\omega^4 + O\left(\omega^6\right) \quad , \quad \theta \in [0,\pi] ,$$

one obtains using the volume constraint:

$$f_0 = 0 \quad , \quad g_0 = -\frac{1}{2\sqrt{\pi}R}\sum_{l=0}^{\infty} f_{2l}^2 .$$

so that the volume does not change at first and second-order. Taking $\varepsilon = \omega^2$ and $h = f + g\omega^2$ we get:

$$\mathcal{H}(\mathcal{S}) = \frac{1}{R} + \mathcal{L}_{\mathcal{H}}(f)\,\omega^2 + \left(\mathcal{L}_{\mathcal{H}}(g) + \frac{1}{2}\mathcal{Q}_{\mathcal{H}}(f,f)\right)\omega^4 + O\left(\omega^6\right) ,$$
$$\left(\frac{\partial\mathcal{V}}{\partial\mathbf{n}}(\mathcal{S})\right)^2 = \left(\frac{Q}{4\pi\varepsilon_0 R^2}\right)^2 + \mathcal{L}_{\mathcal{V}}(f)\,\omega^2 + \left(\mathcal{L}_{\mathcal{V}}(g) + \frac{1}{2}\mathcal{Q}_{\mathcal{V}}(f,f)\right)\omega^4 + O\left(\omega^6\right) .$$

Defining a new pressure and expanding it in powers of ω^2:

$$\delta P = \frac{R}{2\gamma}\delta\Pi \quad , \quad \delta P = \delta P_0 + \delta P_1\omega^2 + \delta P_2\omega^4 + O\left(\omega^6\right) \ ,$$

we can start to compare terms in (6.5). To zeroth-order we have:

$$\delta P_0 = 1 - \chi \ .$$

For the first-order contribution we collect all terms with ω^2 and use the property (6.6) to yield:

$$\delta P_1 = \frac{1}{R}\sum_{l=1}^{\infty} a\left(\chi, l\right) f_{2l} Y_{2l,0} - \frac{\Delta\varrho R^3}{4\gamma}\sin^2\theta \ .$$

Our strategy is to equate the $Y_{0,0}$ component with the pressure to yield:

$$\delta P_1 = -\frac{\Delta\varrho R^3}{6\gamma} \quad , \quad f_2 = -\sqrt{\frac{\pi}{5}}\frac{\Delta\varrho R^4}{6\gamma\left(1-\chi\right)} \quad , \quad g_0 = -\frac{\sqrt{\pi}\left(\Delta\varrho\right)^2 R^7}{360\gamma^2\left(1-\chi\right)^2} \ ,$$

with:

$$f\left(\theta\right) = f_2 Y_{2,0}\left(\theta\right) \ ,$$

proving that our equilibrium shape behaves like an oblate or prolate spheroid to first-order approximation depending on whether $\chi < 1$ or $\chi > 1$ respectively. To complete our analysis we balance second-order terms:

$$\delta P_2 = R\mathcal{L}_{\mathcal{H}}\left(g\right) - \frac{\varepsilon_0 R}{4\gamma}\mathcal{L}_{\mathcal{V}}\left(g\right) + \frac{R}{2}\mathcal{Q}_{\mathcal{H}}\left(f,f\right) - \frac{\varepsilon_0 R}{8\gamma}\mathcal{Q}_{\mathcal{V}}\left(f,f\right) - \frac{\Delta\varrho R^2}{2\gamma}f\sin^2\theta \ .$$

Equating the pressure with the terms involving $Y_{0,0}$ as before we get:

$$\delta P_2 = \frac{f_2^2\left(\chi-5\right)}{4\pi R^2} + \frac{\Delta\varrho R^2 f_2}{6\sqrt{5\pi}\gamma} - \frac{\left(2\chi-1\right)\left(\Delta\varrho\right)^2 R^6}{720\gamma^2\left(1-\chi\right)^2} \ .$$

Then, the coefficients multiplying $Y_{2,0}$ and $Y_{4,0}$ must be zero, from where we obtain:

$$g_2 = \frac{5\sqrt{5}f_2^2\left(1+\chi\right)}{14\sqrt{\pi}R\left(1-\chi\right)} + \frac{11\Delta\varrho R^3 f_2}{70\gamma\left(1-\chi\right)} \quad , \quad g_4 = \frac{5f_2^2\left(1-\chi\right)}{7\sqrt{\pi}R\left(3-2\chi\right)} + \frac{2\Delta\varrho R^3 f_2}{21\sqrt{5}\gamma\left(2\chi-3\right)} \ ,$$

and our approximate solution to second-order is: ■

Observe that the asymptotic solutions described by (6.7) and (6.18) present singularities at the eigenvalues $a\left(\chi,l\right)$ of $\mathcal{K}$, which are some of the bifurcation points for non-rotating charged drops (6.3). Indeed, $\mathcal{K}$ has a non-null kernel when:

$$a\left(\chi,l\right) = 0 \quad \Leftrightarrow \quad \chi_{2l} = \frac{l+1}{2} \quad \Leftrightarrow \quad Q_{2l} = \sqrt{32\pi^2\varepsilon_0\gamma R^3\left(l+1\right)} \quad , \quad l \geqslant 1 \ ,$$

corresponding to the bifurcation values for $Y_{2l,m}$ as calculated by Rayleigh in [58]. Even though these second-order expansions provide us with explicit formulas for the approximate solutions, their singularity issue encourages us to look for approximate equilibrium configurations using an alternative approach.

Consider now the problem of finding the spheroids that minimize the total energy of the system. When rotation takes place at constant angular momentum, the energy functional is defined as follows:

$$E_{total} = \gamma\mathcal{A}_d + \psi\frac{\mathcal{L}^2}{2\mathcal{I}} + \frac{\varepsilon_0}{2}\int_{\mathbb{R}^3\setminus\mathcal{D}}\left\|\mathbf{E}\right\|^2 d\mathbf{x} - \delta\Pi\left(V - V_0\right) \ , \tag{6.21}$$

where $\delta\Pi\left(V-V_0\right)$ is the constraint, and $\delta\Pi$ plays the role of a Lagrange multiplier so that the volume of the drop is V_0. On the contrary, if rotation occurs at constant angular speed:

$$E_{total} = \gamma\mathcal{A}_d - \psi\frac{\omega^2}{2}\mathcal{I} + \frac{\varepsilon_0}{2}\int_{\mathbb{R}^3\setminus\mathcal{D}}\left\|\mathbf{E}\right\|^2 d\mathbf{x} - \delta\Pi\left(V - V_0\right) \ . \tag{6.22}$$

Given a spheroid with semiaxes a and c:

$$\frac{\left(x^2+y^2\right)}{a^2}+\frac{z^2}{c^2}=1 \quad \rightarrow \quad \begin{cases} a>c & , \text{ oblate spheroid} \\ a<c & , \text{ prolate spheroid} \end{cases},$$

the moment of inertia about the z-axis of this spheroid is:

$$\mathcal{I}_{oblate}=\mathcal{I}_{prolate}=\frac{2}{5}\varrho_1 a^2 \,,$$

and we also have exact formulas to calculate the surface area and the capacitance [55, 54, 26]:

$$A_{prolate}=2\pi a^2\left(1+\frac{\arcsin e}{e\sqrt{1-e^2}}\right) \quad , \quad \mathcal{C}_{prolate}=8\pi\varepsilon_0 c\frac{e}{\log\left(\frac{1+e}{1-e}\right)} \quad , \quad e^2=1-\frac{a^2}{c^2}\,,$$

$$A_{oblate}=2\pi a^2\left(1+\frac{1-e^2}{e}\operatorname{arctanh} e\right) \quad , \quad \mathcal{C}_{oblate}=4\pi\varepsilon_0 a\frac{e}{\arcsin e} \quad , \quad e^2=1-\frac{c^2}{a^2}\,.$$

Notice that using the volume condition $V_0=\frac{4\pi}{3}a^2c$ one can write a in terms of c, reducing the energy to a single variable function. Therefore, for rotation at constant angular momentum, the energy for oblate spheroids is:

$$E_{total}\,(a)=2\pi a^2\gamma\left(1+\frac{1-e^2}{e}\operatorname{arctanh} e\right)-\Delta\varrho\frac{\omega^2}{5}a^2+\frac{Q^2}{8\pi\varepsilon_0 ae}\arcsin e\,, \tag{6.23}$$

and for prolate spheroids:

$$E_{total}\,(a)=2\pi a^2\gamma\left(1+\frac{\arcsin e}{e\sqrt{1-e^2}}\right)-\Delta\varrho\frac{\omega^2}{5}a^2+\frac{a^2Q^2}{12\varepsilon_0 V_0 e}\log\left(\frac{1+e}{1-e}\right)\,. \tag{6.24}$$

Conversely, the energy function for oblate spheroids when rotation is at constant angular speed is:

$$E_{total}\,(a)=2\pi a^2\gamma\left(1+\frac{1-e^2}{e}\operatorname{arctanh} e\right)+\frac{5\psi\mathcal{L}^2}{4\varrho_1 a^2}+\frac{Q^2}{8\pi\varepsilon_0 ae}\arcsin e\,, \tag{6.25}$$

and for prolate spheroids:

$$E_{total}\,(a)=2\pi a^2\gamma\left(1+\frac{\arcsin e}{e\sqrt{1-e^2}}\right)+\frac{5\psi\mathcal{L}^2}{4\varrho_1 a^2}+\frac{a^2Q^2}{12\varepsilon_0 V_0 e}\log\left(\frac{1+e}{1-e}\right)\,. \tag{6.26}$$

Notice that the total energy as well as the eccentricity depend on the semiaxis a, which makes it very lengthy to deal with the minimization problem analytically. Consequently, to compute the critical points of these energy functionals we proceed numerically using the symbolic calculation software *Maple*©.

6.1.2. Comparison of equilibrium shapes with numerical simulations

In order to validate the models derived above to approximate equilibrium solutions, we have compared them with numerical results obtained by simulating the evolution problem. To do so, we have used the axisymmetric version of the code, taking as initial configuration a small oblate perturbation of the sphere with unit volume. All simulations use $\lambda=0.1$ as the viscosity ratio, surface tension $\gamma=1$ and were run until a stationary profile for the drop's interface is reached. The data reveals that spheroids provide better approximations (even for large values of Rayleigh's fissibility ratio) to numerical equilibriums than the solutions given by asymptotic expansions (see figures 6.2, 6.3, 6.4 and 6.5). However, observe the good agreement achieved by asymptotic expansions, provided that the angular momentum and angular speed are small, which is less than 1% for $0\leqslant\chi\leqslant 0.485$, and less than 5% when $0.485\leqslant\chi\leqslant 0.6765$. Numerical evidence demonstrates also that rotation leads to an imperfect bifurcation [38], rupturing the bifurcation point attained by charged non-rotating drops at $\chi=1$ (see figures 6.1, 6.2 and 6.3). Finally, it is important to remark that prolate solutions never show up in our numerical experiments, indicating that the family of prolate-like solutions should be of unstable nature. Indeed, if one numerically evolves the system from an initial prolate perturbation of the sphere, an oblate solution is attained or, if the charge is large enough, the drop develops dynamic Taylor cones or a pinch-off in finite time.

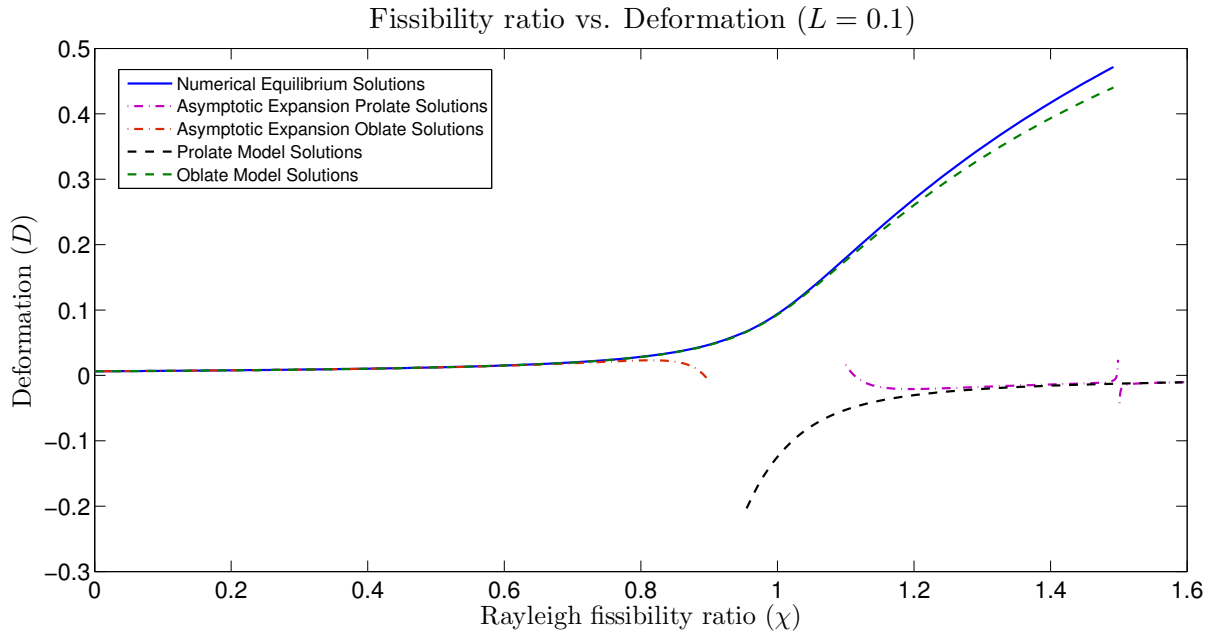

Figure 6.2: Equilibriums at constant L for different methods. Deformation is defined as $D = \frac{r_{equat} - r_{polar}}{r_{equat} + r_{polar}}$.

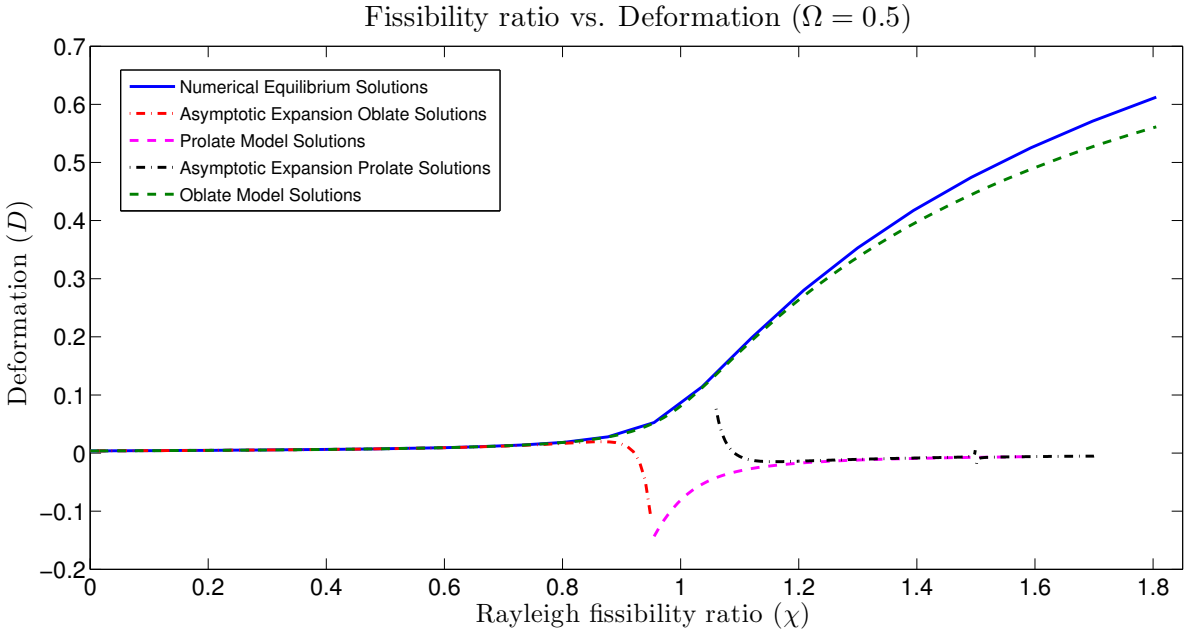

Figure 6.3: Equilibriums at constant Ω for different methods. Deformation is defined as $D = \frac{r_{equat} - r_{polar}}{r_{equat} + r_{polar}}$.

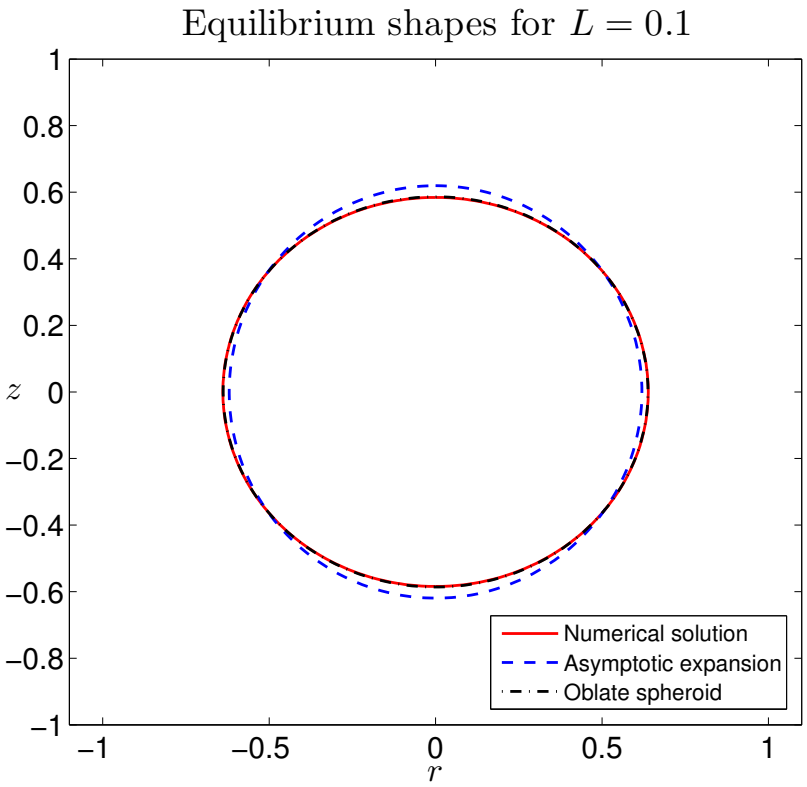

Figure 6.4: Equilibrium shapes for a rotating drop at constant L and charge $\chi = 0.892$.

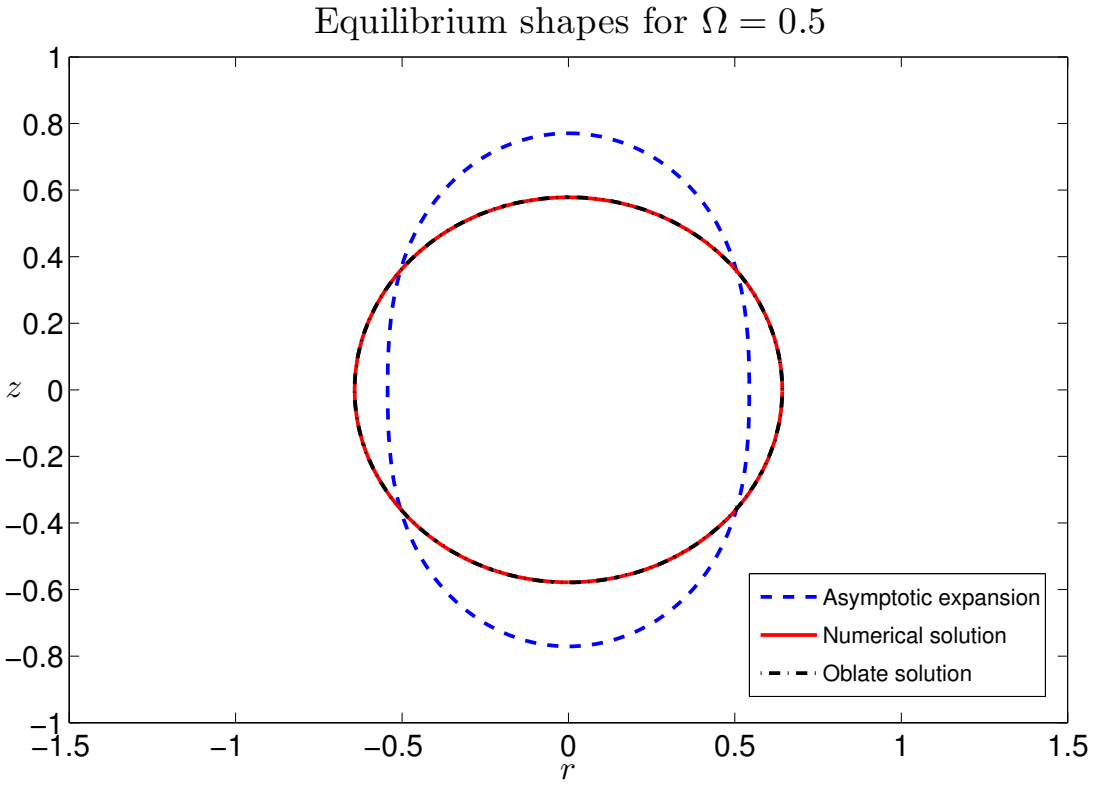

Figure 6.5: Equilibrium shapes for a rotating drop at constant Ω and charge $\chi = 0.9772$.

6.1.3. Evolution and stability in 3D

After studying the equilibrium behaviour of axisymmetric drops, we focus now on their stability when one considers 3D evolution and rotation takes place at constant angular momentum. For this analysis we start from an axisymmetric equilibrium configuration of a charged rotating droplet, $\mathbf{r}_{axi}$, and perturb it with a combination of spherical harmonics:

$$\mathbf{r} = \mathbf{r}_{axi} + \varepsilon_1 Y_{2,0} + \varepsilon_2 Y_{2,1} \quad , \quad \varepsilon_1 = \varepsilon_2 = 0.05 \ ,$$

to find that the droplet returns to its axisymmetric configuration if $\chi \in [0, \chi_{axi}(L)]$, where the upper limit of this interval has been established using an energy argument and confirmed numerically with simulations (see figure 6.6). The theoretical derivation of this limit goes as follows: suppose that there exists an ellipsoidal family of equilibrium configurations to our problem that is energetically more favorable than the oblate spheroidal family (later we show numerically that this ellipsoidal family indeed exists). The energy of the system for oblate spheroidal solutions is given by:

$$E_{oblate}(a, Q, \mathcal{L}) = \gamma A_{oblate}(a) + \psi \frac{\mathcal{L}^2}{2\mathcal{I}_{oblate}(a)} + \frac{Q^2}{2\mathcal{C}_{oblate}(a)} \ , \tag{6.27}$$

where a is the semimajor axis. The semiminor axis c is related to a by the volume condition $V_0 = \frac{4\pi}{3}a^2 c$. We find then $a^* \equiv a^*(Q, \mathcal{L})$ such that (6.27) attains a minimum and consider the energy functional for a general ellipsoid with semiaxes a, b, c:

$$E_{ellip}(a, b) = \gamma A_{ellip}(a, b) + \psi \frac{\mathcal{L}^2}{2\mathcal{I}_{ellip}(a, b)} + \frac{Q^2}{2\mathcal{C}_{ellip}(a, b)} \ , \tag{6.28}$$

where c satisfies $V_0 = \frac{4\pi}{3}abc$. For the surface area, moment of inertia and capacitance of an ellipsoid we use the formulas in [55, 54, 41, 42]:

$$I_{ellip}(a, b) = \varrho_1 \left(\frac{a^2 + b^2}{5} \right) \quad , \quad A_{ellip}(a, b, c) \approx 4\pi \left(\frac{(ab)^p + (ac)^p + (bc)^p}{3} \right)^{\frac{1}{p}} \ ,$$

$$\mathcal{C}_{ellip}(a, b, c) \approx \frac{4\pi\varepsilon_0}{45} \left(11(a + b + c) + 4\left(\sqrt{ab} + \sqrt{ac} + \sqrt{bc} \right) \right) \ ,$$

where the capacitance approximation gives a maximum relative error of 0.073% and $p \approx 1.6075$ yields a relative error of at most 1.061% for the surface area. The idea is, given a value for $\mathcal{L}$, find the value of $Q^* \equiv Q_{axi}(\mathcal{L})$ that gives a saddle-point for (6.28), where the ellipsoidal family becomes energetically favorable. Thus, we look for:

$$Hess\left(E_{ellip}(a, b)\right)\Big|_{a=b=a^*(Q^*;\mathcal{L})} = 0 \quad \Leftrightarrow \quad F\left(a^*(Q^*; \mathcal{L}), Q^*\right) = 0 \ , \tag{6.29}$$

that we solve numerically with a bisection method using *Maple*©. It is important to notice that when rotation takes place at constant angular speed, a similar analysis can be carried out with the energies:

$$E_{oblate}(a, Q, \omega) = \gamma A_{oblate}(a) - \psi \frac{\omega^2}{2} \mathcal{I}_{oblate}(a) + \frac{Q^2}{2\mathcal{C}_{oblate}(a)} \ , \tag{6.30}$$

$$E_{ellip}(a, b) = \gamma A_{ellip}(a, b) - \psi \frac{\omega^2}{2} \mathcal{I}_{ellip}(a, b) + \frac{Q^2}{2\mathcal{C}_{ellip}(a, b)} \ , \tag{6.31}$$

In order to validate the spheroid/ellipsoid transition, we have carried out numerical experiments with the 3D version of the code for values of $L \in [0, 0.5]$ at intervals of 0.1 and values of $\chi \in [0, 1.1]$ at intervals of 0.1. Similarly, if rotation occurs at constant angular speed, we take $\Omega \in [0, 3.3]$. The simulations reveal that:

- When the system is not rotating, we reproduce the results in [27], i.e. we obtain a bifurcation point at $\chi \approx 0.9935$ and, for $\chi > 0.9935$, the drop becomes unstable and develops Taylor cones at the poles.
- If the drop is rotating, a different behaviour can be observed: the oblate-like solution becomes an ellipsoid as predicted above by the energy argument and the corresponding transition value for χ decreases as L increases (see figure 6.6). Observe that this stability curve separating axisymmetric and

ellipsoidal configurations meets the vertical axis at a point L_2 which is very close to the value obtained in chapter 5. Increasing χ further, and depending on the value of L, we arrive to two different types of unstable configurations: a drop developing dynamic Taylor cones in the equatorial plane or a drop forming a neck between two smaller droplets that pinches-off in finite time. All attainable configurations for the evolution problem are summarized in figure 6.8, from which a significant result can be extracted: in the presence of rotation, the amount of charge that a drop can hold before becoming unstable is lower than Rayleigh's limit for a non-rotating drop, getting smaller as the angular momentum increases. It is also important to remark that, when dynamic Taylor cones develop, the local form of the tip remains circularly symmetric as in the case for axisymmetric droplets, provided that rotation is small.

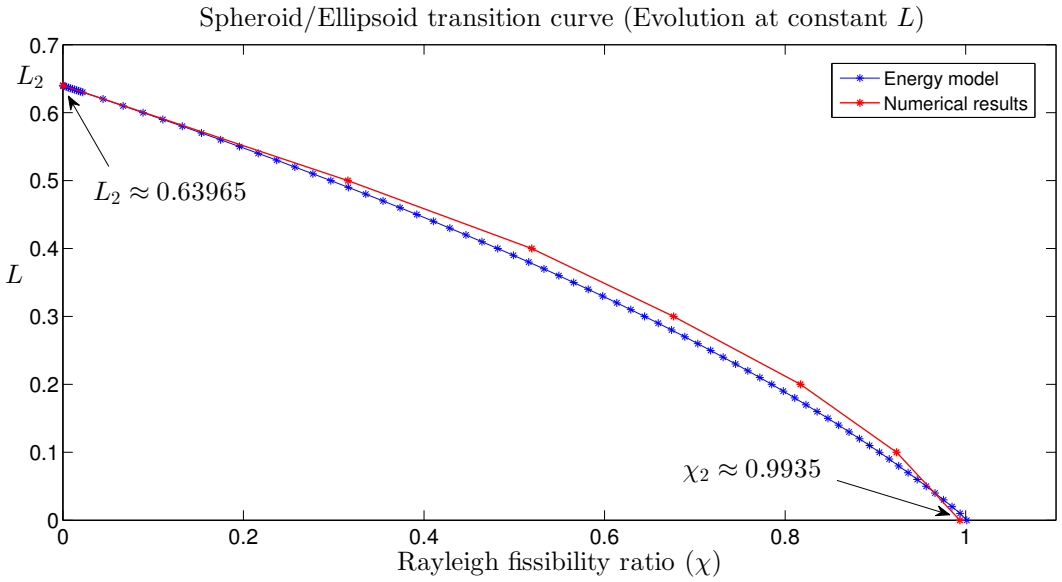

Figure 6.6: Comparison of numerical results with the spheroid/ellipsoid transition curve at constant L.

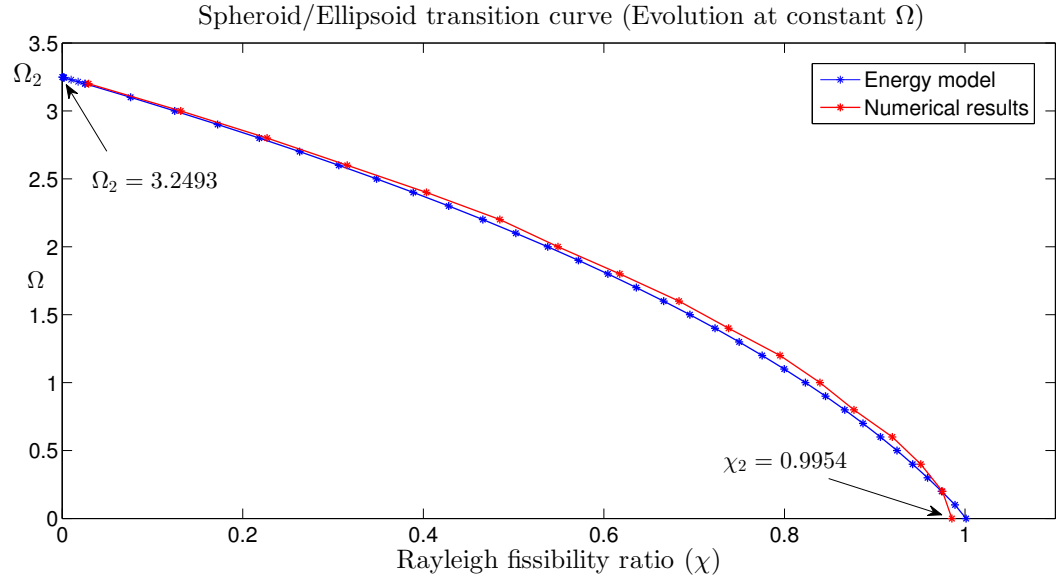

Figure 6.7: Comparison of numerical results with the spheroid/ellipsoid transition curve at constant Ω.

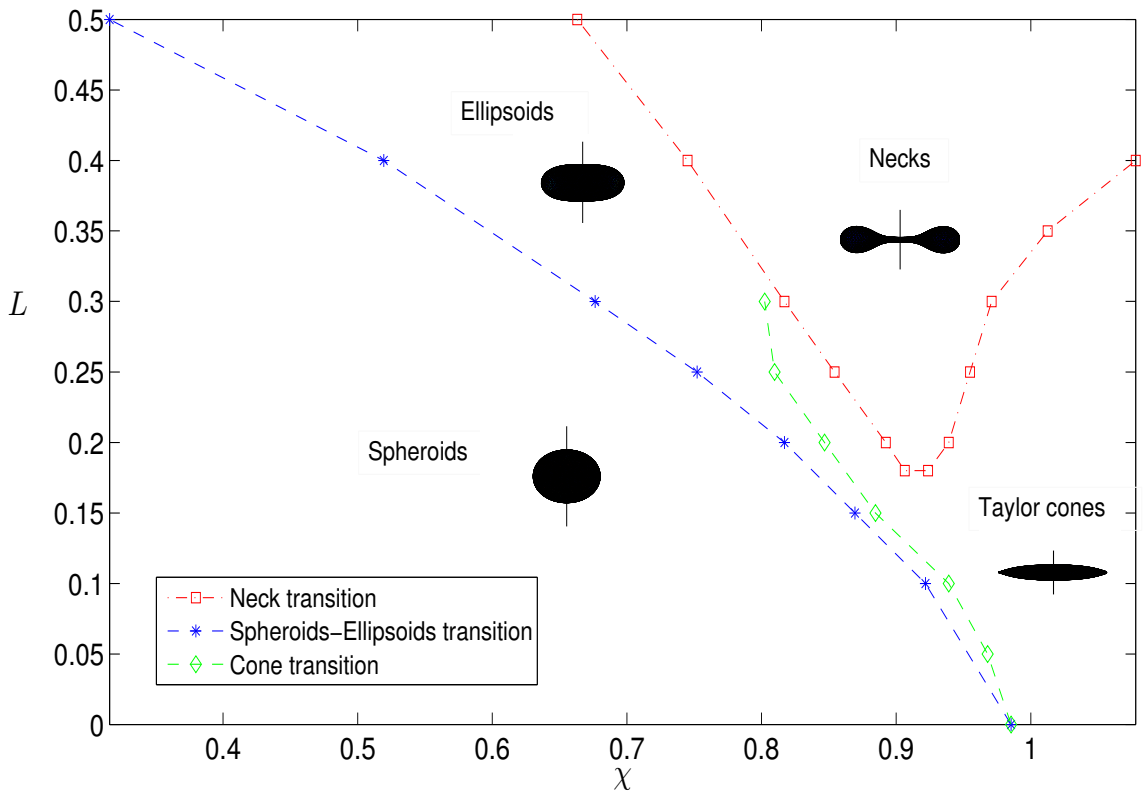

Figure 6.8: Bifurcation diagram for charged drops rotating at constant angular momentum.

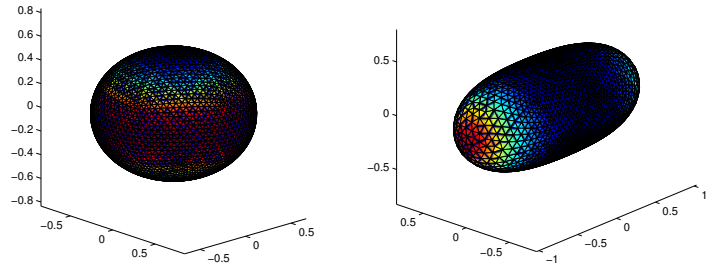

(a) Spheroidal shape

(b) Ellipsoidal shape

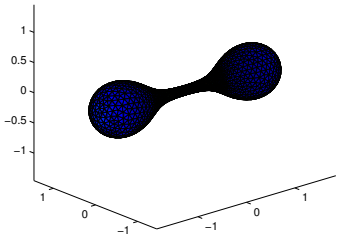

(c) Neck formation

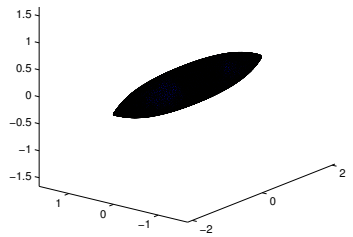

(d) Dynamic Taylor cones

Figure 6.9: Evolution of a charged rotating drop at $L = 0.3$ for different values of the Rayleigh parameter. Picture 6.9(a) corresponds to $\chi = 0.7981$: the initial axisymmetric configuration remains stable. In 6.9(b), $\chi = 0.8795$: the drop has evolved to a stable ellipsoid configuration. In 6.9(c), $\chi = 0.9528$: the drop becomes unstable, developing a neck between two smaller droplets and eventually breaks. Finally, for 6.9(d) $\chi = 1.0179$: the drop is also unstable, it develops dynamic Taylor cones in the equatorial plane. Color gradation represents mean curvature and the axis of rotation lies along the vertical z axis.

6.2. Rotating drops subject to electric fields

In this section we will study the effects that rotation has on neutral drops subject to an electric field applied in the direction of the rotation axis. The influence of electric fields on droplets was first investigated around 1964 by Taylor [68]. In his works, he showed that prolate spheroids are good approximations to equilibrium solutions and that, if the field is strong enough, droplets become unstable and develop a singular and self-similar structure known as Taylor cones, which are characterized by an opening semiangle of about 49.3°. The problem with the angle predicted by Taylor is that it turns out to be very different from results obtained with experiments (both numerical [27] and those conducted in the laboratory [20]). This disagreement will motivate the last section of this chapter, where we describe the effects that rotation has on the formation of Taylor cones.

When an electric field with magnitude $\mathcal{E}_\infty$ is applied to a droplet, forces tend to deform it in the direction of the field, attaining a prolate-like shape. For this prolate equilibrium with semiaxes a and c, given that its larger semiaxis, c, is in the direction of the field, Taylor proved the following relation between the dimensionless electric field E_∞ and the aspect ratio α:

$$E_\infty = \sqrt[6]{\frac{32\pi}{3}}\alpha^{-\frac{4}{3}}\sqrt{2-\alpha^{-3}-\alpha^{-1}}\left(\frac{1}{2\left(1-\alpha^{-2}\right)^{\frac{3}{2}}}\log\left(\frac{1+\sqrt{1-\alpha^{-2}}}{1-\sqrt{1-\alpha^{-2}}}\right)-\frac{1}{1-\alpha^{-2}}\right), \tag{6.32}$$

where:

$$E_\infty = \sqrt{\frac{\varepsilon_0 V_0^{\frac{1}{3}}}{\gamma}}\mathcal{E}_\infty \quad , \quad \alpha = \frac{c}{a},$$

and V_0 is the drop's volume. The critical value for which the drop becomes unstable and develops Taylor cones at the poles corresponds to the point where (6.32) reaches a maximum, which occurs for $\alpha_c \approx 1.859$ and $E_\infty^c \approx 0.582$. Our numerical simulations with BEM show that drops become unstable at $E_\infty^c \approx 0.575$, that is within 1% of error from the value predicted by Taylor (see Figure 6.10).

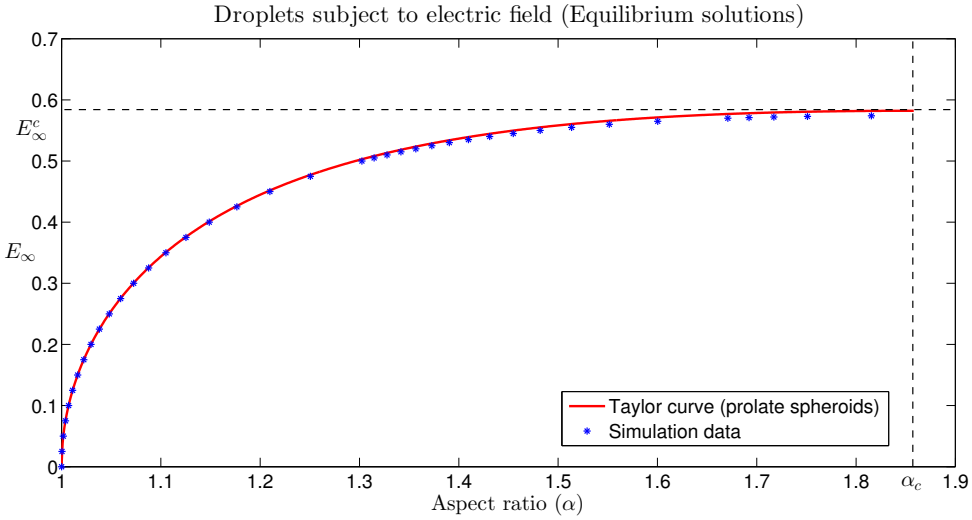

Figure 6.10: Comparison between numerical experiments and Taylor theoretical curve.

6.2.1. Equilibrium shapes for rotating drops subject to an electric field

When a drop starts to rotate about an axis in the direction of the applied electric field, the resulting centrifugal forces tend to flatten the droplet, balancing electrostatic forces and generating two different families of solutions: oblate- and prolate-like. In fact, there exists a linear combination between the angular momentum L (or angular speed Ω) and the electric field E_∞ that yields spherical equilibrium configurations as shown in [65] (see Figure 6.11 for a comparison with numerical experiments). We start this subsection proving that spheres are no longer solutions when they also hold an amount of charge Q on its surface:

Theorem 6.4. *Rotating drops subject to an electric field attain spherical solutions if and only if $Q = 0$. The linear relation between the electric field and the angular momentum (or angular speed) that yields these configurations is:*

$$E_\infty = \frac{5}{6}\sqrt[3]{\frac{4\pi}{3}}L = \frac{\Omega}{\sqrt[3]{36\pi}} \,. \tag{6.33}$$

Proof. Consider a conducting sphere of radius R rotating with angular speed ω about the z-axis and subject to an electric field with strength $\mathcal{E}_\infty$ in the direction of the rotation axis. Suppose also that the drop holds an amount of charge Q on its surface. In this situation, the electric potential satisfies:

$$\begin{cases} \Delta\mathcal{V} = 0 & , \quad \text{in } \mathbb{R}^3 - \mathcal{B}_R(\mathbf{0}) \\ \mathcal{V} = \mathcal{V}_0 & , \quad \text{on } \partial\mathcal{B}_R(\mathbf{0}) \\ \mathcal{V} \to -\mathcal{E}_\infty z + O(\|\mathbf{x}\|^{-1}) & , \quad \text{when } \|\mathbf{x}\| \to \infty \end{cases} .$$

Define the auxiliary potential $\widetilde{\mathcal{V}} = \mathcal{V} + \mathcal{E}_\infty z$ that solves:

$$\begin{cases} \Delta\widetilde{\mathcal{V}} = 0 & , \quad \text{in } \mathbb{R}^3 - \mathcal{B}_R(\mathbf{0}) \\ \widetilde{\mathcal{V}} = \mathcal{V}_0 + \mathcal{E}_\infty R\cos\theta & , \quad \theta \in [0,\pi] \\ \widetilde{\mathcal{V}} \to 0 & , \quad \text{when } \|\mathbf{x}\| \to \infty \end{cases} ,$$

where we have used spherical coordinates. All bounded solutions for Laplace equation are in the form:

$$\widetilde{\mathcal{V}}(r,\theta,\varphi) = \sum_{l=0}^{\infty}\sum_{m=-l}^{l} C_{l,m}\frac{Y_{l,m}(\theta,\varphi)}{r^{l+1}} \,,$$

and since the boundary condition is independent of φ, so is our electric potential:

$$\widetilde{\mathcal{V}}(r,\theta) = \sum_{l=0}^{\infty} C_{l,0}\frac{Y_{l,0}(\theta)}{r^{l+1}} \,.$$

Imposing the boundary condition:

$$\widetilde{\mathcal{V}}(R,\theta) = \mathcal{V}_0 + \mathcal{E}_\infty R\cos\theta = \sum_{l=0}^{\infty} C_{l,0}\frac{Y_{l,0}(\theta)}{R^{l+1}} \,,$$

and using that:

$$Y_{0,0}(\theta) = \frac{1}{2\sqrt{\pi}} \quad , \quad Y_{1,0}(\theta) = \frac{1}{2}\sqrt{\frac{3}{\pi}}\cos\theta \,,$$

we have:

$$C_{0,0} = 2R\sqrt{\pi}\mathcal{V}_0 \quad , \quad C_{1,0} = 2\mathcal{E}_\infty R^3\sqrt{\frac{\pi}{3}} \quad , \quad C_{l,0} = 0 \quad , \quad \text{when} \quad l \geqslant 2 \,.$$

This gives:

$$\widetilde{\mathcal{V}}(r,\theta) = \frac{R}{r}\mathcal{V}_0 + \frac{R^3}{r^2}\mathcal{E}_\infty\cos\theta \quad \Leftrightarrow \quad \mathcal{V}(r,\theta) = \frac{R}{r}\mathcal{V}_0 + \frac{R^3}{r^2}\mathcal{E}_\infty\cos\theta - \mathcal{E}_\infty r\cos\theta \quad , \quad r \geqslant R \,,$$

from which we can compute the normal derivative of the potential on the surface of the sphere:

$$\frac{\partial\mathcal{V}}{\partial\mathbf{n}} = \frac{\partial\mathcal{V}}{\partial r}\Big|_{r=R} = -\frac{\mathcal{V}_0}{R} - 3\mathcal{E}_\infty\cos\theta \quad , \quad \mathbf{n} = \mathbf{e}_r \,.$$

To calculate $\mathcal{V}_0$ we have to impose the condition:

$$Q = \int_{\partial\mathcal{B}_R(\mathbf{0})} \sigma \, dS \,,$$

where $\sigma = -\varepsilon_0\dfrac{\partial\mathcal{V}}{\partial\mathbf{n}}$ is the surface charge density. This results in:

$$-\frac{Q}{\varepsilon_0} = \int_{\partial\mathcal{B}_R(\mathbf{0})}\frac{\partial\mathcal{V}}{\partial\mathbf{n}}\,dS = -\int_0^\pi\int_0^{2\pi}\left(\frac{\mathcal{V}_0}{R} + 3\mathcal{E}_\infty\cos\theta\right)R^2\sin\theta\,d\varphi\,d\theta \quad \Leftrightarrow \quad \mathcal{V}_0 = \frac{Q}{4\pi\varepsilon_0 R} \,,$$

and consequently:

$$\frac{\partial \mathcal{V}}{\partial r}\Big|_{r=R} = -\frac{Q}{4\pi\varepsilon_0 R^2} - 3\mathcal{E}_\infty \cos\theta \ .$$

Now, the mean curvature and the electrostatic pressure for a sphere of radius R are:

$$\mathcal{H} = \frac{1}{R} \quad , \quad p_e = \frac{\varepsilon_0}{2} E_n^2 = \frac{\varepsilon_0}{2}\left(\frac{\partial \mathcal{V}}{\partial \mathbf{n}}\Big|_{r=R}\right)^2 \ ,$$

where $E_n = \mathbf{E}\cdot\mathbf{n}$ is the normal component of the electric field. The modified Young-Laplace equation gives:

$$\begin{aligned}\delta\Pi &= 2\gamma\mathcal{H} - \frac{1}{2}\Delta\varrho R^2\omega^2\sin^2\theta - \frac{\varepsilon_0}{2}\left(\frac{\partial \mathcal{V}}{\partial \mathbf{n}}\Big|_{r=R}\right)^2 = \\ &= \frac{2\gamma}{R} - \frac{1}{2}\Delta\varrho R^2\omega^2\sin^2\theta - \frac{\varepsilon_0}{2}\left(\frac{Q^2}{16\pi^2\varepsilon_0^2 R^4} + 9\mathcal{E}_\infty^2\cos^2\theta + \frac{3Q\mathcal{E}_\infty}{2\pi\varepsilon_0 R^2}\cos\theta\right) \ .\end{aligned}$$

Introducing Rayleigh fissibility ratio χ and rearranging:

$$\delta\Pi + \frac{2\gamma}{R}(\chi - 1) + \frac{9\varepsilon_0\mathcal{E}_\infty^2}{2} = \left(\frac{9\varepsilon_0\mathcal{E}_\infty^2}{2} - \frac{1}{2}\Delta\varrho\omega^2 R^2\right)\sin^2\theta - \frac{3Q\mathcal{E}_\infty}{4\pi R^2}\cos\theta \ ,$$

whose solution is a sphere only when $Q = 0$ and the following identity holds:

$$9\varepsilon_0\mathcal{E}_\infty^2 = \Delta\varrho\omega^2 R^2 \ .$$

Using the dimensionless electric field and applying that the volume is $V_0 = \frac{4\pi}{3}R^3$:

$$\frac{9\gamma}{\sqrt[3]{V_0}} E_\infty^2 = \Delta\varrho\omega^2 R^2 \ .$$

Now, since the angular momentum satisfies $\mathcal{L} = \mathcal{I}\omega$ and the moment of inertia of a solid sphere is:

$$\mathcal{I}_{sphere} = \frac{8\pi}{15}\varrho_1 R^5 \ ,$$

we get:

$$\frac{9\gamma}{\sqrt[3]{V_0}} E_\infty^2 = \frac{225\psi\mathcal{L}^2}{64\pi^2\varrho_1 R^8} \quad \Leftrightarrow \quad E_\infty = \frac{5\sqrt[6]{V_0}}{8\pi R^4}\sqrt{\frac{\psi}{\gamma\varrho_1}}\mathcal{L} = \frac{5}{6}\sqrt[3]{\frac{4\pi}{3}}L = \frac{\Omega}{\sqrt[3]{36\pi}} \ , \tag{6.34}$$

which is the linear relation sought. ■

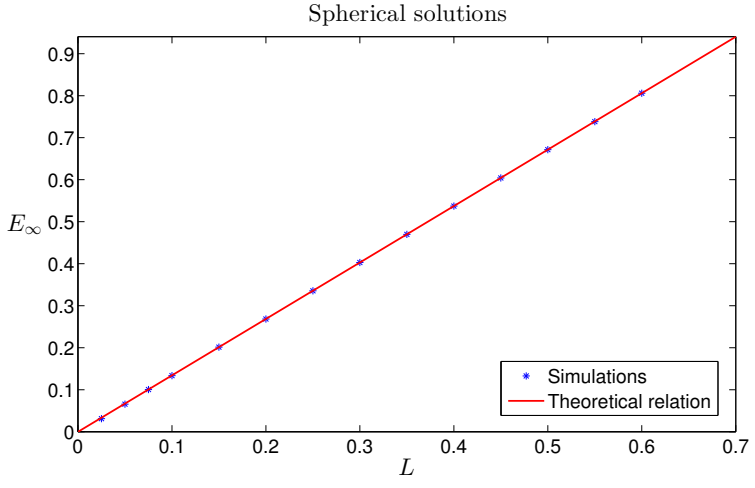

Figure 6.11: Comparison between simulations and the linear relation for spherical solutions.

The theoretical study of equilibrium solutions for rotating drops subject to electric fields began in 1974 with the works by Rosenkilde & Randall [61]. Using the tensor virial method developed by Chandrasekhar, they discussed spheroidal equilibriums together with their stability and obtained a linear relation between L^2 (or Ω^2) and E_∞^2 satisfied by the solutions with the same aspect ratio. Before comparing our numerical simulations with this theory, we will briefly introduce here the approximation formulas derived by Rosenkilde *et al.*, and for this purpose, we need some results from [14], [71], [13] and [60].

Given an spheroid with semiaxes a and c, in order to make them dimensionless consider:

$$a_1 = a_2 = \frac{a}{R} \quad , \quad a_3 = \frac{c}{R} \, ,$$

where R is the radius of the sphere with the same volume V_0 as the spheroid. The formula that gives the relation between the angular momentum and the electric field derived by Rosenkilde is:

$$2y = a_1^2 \left(\mathcal{A}_3 - \mathcal{A}_1\right) - \frac{2a_1^2}{A_3}\left(a_1^2 A_{13} - 3a_3^2 A_{33}\right) x \, , \tag{6.35}$$

where the coefficients A_i, A_{ij} and $\mathcal{A}_i$ are defined as:

$$\begin{aligned}
A_i &= \int_0^\infty \frac{dt}{\sqrt{\left(a_1^2+t\right)\left(a_2^2+t\right)\left(a_3^2+t\right)}\left(a_i^2+t\right)} \quad , \quad i \in \{1,2,3\} \, , \\
A_{ij} &= \int_0^\infty \frac{dt}{\sqrt{\left(a_1^2+t\right)\left(a_2^2+t\right)\left(a_3^2+t\right)}\left(a_i^2+t\right)\left(a_j^2+t\right)} \quad , \quad i,j \in \{1,2,3\} \, , \\
\mathcal{A}_i &= \int_0^\infty \frac{dt}{\sqrt{\left(a_1^2+t^2\right)\left(a_2^2+t^2\right)\left(a_3^2+t^2\right)}\left(a_i^2+t^2\right)} \quad , \quad i \in \{1,2,3\} \, ,
\end{aligned}$$

and satisfy the properties:

$$\sum_{i=1}^{3} A_i = \frac{2}{a_1 a_2 a_3} \quad , \quad 3A_{ii} + \sum_{j \neq i} A_{ij} = \frac{2}{a_1 a_2 a_3 a_i^2} \quad , \quad A_{ij} = -\frac{A_i - A_j}{a_i^2 - a_j^2} \quad \text{when } j \neq i \, ,$$

$$\sum_{i=1}^{3} a_i^2 \mathcal{A}_i = 2g \quad , \quad g = \int_0^\infty \frac{dt}{\sqrt{\left(a_1^2+t^2\right)\left(a_2^2+t^2\right)\left(a_3^2+t^2\right)}} \, .$$

For spheroids with semiaxes $a_1 = a_2 \neq a_3$ we have explicit formulas [13, 60] in terms of the eccentricity:

$$\begin{aligned}
A_1^{oblate} &= \frac{1}{a_1^3 e^3}\left(\arcsin e - e\sqrt{1-e^2}\right) \quad , \quad A_3^{oblate} = \frac{2}{a_1^3 e^3}\left(\frac{e}{\sqrt{1-e^2}} - \arcsin e\right) \, , \\
\mathcal{A}_1^{oblate} &= \frac{1}{2a_1^4 e^2}\left(\left(1+e^2\right)\frac{\operatorname{arctanh} e}{e} - 1\right) \quad , \quad \mathcal{A}_3^{oblate} = \frac{1}{a_1^4 e^2}\left(\frac{1}{1-e^2} - \frac{\operatorname{arctanh} e}{e}\right) \, , \\
A_1^{prolate} &= \frac{1}{a_3^3 e^3}\left(\frac{e}{1-e^2} - \frac{1}{2}\log\left(\frac{1+e}{1-e}\right)\right) \quad , \quad A_3^{prolate} = \frac{1}{a_3^3 e^3}\left(\log\left(\frac{1+e}{1-e}\right) - 2e\right) \, , \\
\mathcal{A}_1^{prolate} &= \frac{\sqrt{1-e^2}}{2a_1^4 e^2}\left(\sqrt{1-e^2} - \left(1-2e^2\right)\frac{\arcsin e}{e}\right) \quad , \quad \mathcal{A}_3^{prolate} = \frac{1}{a_3^4 e^2 \sqrt{1-e^2}}\left(\frac{\arcsin e}{e} - \sqrt{1-e^2}\right) \, ,
\end{aligned}$$

where for an oblate spheroid:

$$a_1 = a_2 > a_3 \quad , \quad e = \sqrt{1 - \frac{a_3^2}{a_1^2}} \, ,$$

and for a prolate one:

$$a_1 = a_2 < a_3 \quad , \quad e = \sqrt{1 - \frac{a_1^2}{a_3^2}} \, .$$

Now, x and y are defined as follows:

$$x = \frac{E_c}{E_s^0} = \frac{\varepsilon_0 \mathcal{E}_\infty^2 R}{3\gamma A_3} = \frac{E_\infty^2 R}{3A_3 \sqrt[3]{V_0}} \quad , \quad y = \frac{\psi \mathcal{L}^2}{2\mathcal{I}_0 E_s^0} = \frac{15\psi\mathcal{L}^2}{64\gamma\varrho_1\pi^2 R^7} \, ,$$

where $\mathcal{I}_0$ is the sphere's moment of inertia, E_s^0 its surface area energy and E_c is related to the electric field:

$$\mathcal{I}_0 = \frac{8\pi}{15}\varrho_1 R^5 \quad , \quad E_s^0 = 4\pi R^2\gamma \quad , \quad E_c = \frac{4\pi\varepsilon_0\mathcal{E}_\infty^2 R^3}{3A_3} \, .$$

We have then:

$$\frac{15\psi}{32\gamma\varrho_1\pi^2 R^7}\mathcal{L}^2 = a_1^2\left(\mathcal{A}_3 - \mathcal{A}_1\right) - \frac{2a_1^2 R}{3A_3^2\sqrt[3]{V_0}}\left(a_1^2 A_{13} - 3a_3^2 A_{33}\right)E_\infty^2 \, .$$

or equivalently, using the dimensionless angular momentum L and the fact that $V_0 = \dfrac{4\pi}{3}R^3$:

$$\frac{5}{6}\sqrt[3]{\frac{4\pi}{3}}L^2 = a_1^2\left(\mathcal{A}_3 - \mathcal{A}_1\right) - \frac{2a_1^2}{3A_3^2}\sqrt[3]{\frac{3}{4\pi}}\left(a_1^2 A_{13} - 3a_3^2 A_{33}\right)E_\infty^2 \, . \tag{6.36}$$

In particular, if we take a sphere of radius R:

$$a_1 = a_2 = a_3 = 1 \quad , \quad A_1 = A_2 = A_3 = \mathcal{A}_1 = \mathcal{A}_2 = \mathcal{A}_3 = \frac{2}{3} \quad , \quad A_{13} = A_{23} = A_{33} = \frac{2}{5} \, ,$$

equation (6.36) reduces to (6.34). For an spheroid with semiaxes $a_1 = a_2 \neq a_3$, use above properties to yield:

$$a_1^2 A_{13} - 3a_3^2 A_{33} = \frac{2a_3^2 + a_1^2}{a_1^2 - a_3^2}\left(A_3 - A_1\right) - \frac{2}{a_1^2 a_3} \, ,$$

so that (6.36) gives:

$$\frac{5}{6}\sqrt[3]{\frac{4\pi}{3}}L^2 = a_1^2\left(\mathcal{A}_3 - \mathcal{A}_1\right) - \frac{2a_1^2}{3A_3^2}\sqrt[3]{\frac{3}{4\pi}}\left(\frac{2a_3^2 + a_1^2}{a_1^2 - a_3^2}\left(A_3 - A_1\right) - \frac{2}{a_1^2 a_3}\right)E_\infty^2 \, .$$

If one defines the aspect ratio $\alpha = \dfrac{a_3}{a_1}$ and considers the volume property:

$$V_0 = \frac{4\pi}{3}abc = \frac{4\pi}{3}a_1^2 a_3 R^3 = a_1^2 a_3 V_0 \quad \Leftrightarrow \quad 1 = a_1^2 a_3 \, ,$$

then (6.36) can be rewritten in the form:

$$\frac{5}{6}\sqrt[3]{\frac{4\pi}{3}}L^2 = \frac{1}{\sqrt[3]{\alpha^2}}\left(\mathcal{A}_3 - \mathcal{A}_1\right) - \frac{2}{3A_3^2}\sqrt[3]{\frac{3}{4\pi\alpha^2}}\left(\frac{2\alpha^2 + 1}{1 - \alpha^2}\left(A_3 - A_1\right) - 2\right)E_\infty^2 \, , \tag{6.37}$$

or in terms of the dimensionless angular speed:

$$\frac{\Omega^2}{10\pi} = \sqrt[3]{\alpha^2}\left(\mathcal{A}_3 - \mathcal{A}_1\right) - \frac{2}{3A_3^2}\sqrt[3]{\frac{3\alpha^2}{4\pi}}\left(\frac{2\alpha^2 + 1}{1 - \alpha^2}\left(A_3 - A_1\right) - 2\right)E_\infty^2 \, , \tag{6.38}$$

Equivalently:

$$E_\infty^2 = h_{_L}\left(\alpha\right) + g_{_L}\left(\alpha\right)L^2 \quad , \quad E_\infty^2 = h_{_\Omega}\left(\alpha\right) + g_{_\Omega}\left(\alpha\right)\Omega^2 \, , \tag{6.39}$$

that for each α is the equation of a line.

6.2.2. Comparison of equilibrium shapes with numerical simulations

Although Rosenkilde's results are only valid for isolated, conducting, incompressible, inviscid and rotating drops at constant angular speed, we have compared them with numerical simulations where rotation takes place at constant angular momentum or constant angular speed. We have found that the theory is in close agreement with simulations as depicted in figures 6.12 and 6.13), provided that L (or Ω) and E_∞ are small. Evolution experiments were run with the axisymmetric version of the code, taking as an initial configuration an oblately perturbed spherical drop with unit volume. The ratio of viscosities was set to $\lambda = 0.1$ and the surface tension is $\gamma = 1$. The values for the angular momentum L range between 0 and 1.05 at intervals of 0.05 (for Ω we took values ranging from 0 to 4.3 at intervals of 0.1) and for E_∞ between 0 and 1 at intervals of 0.025 respectively. Even though Rosenkilde's theoretical solutions do not match numerical results for large

values of the parameters, the data shows that simulations are also linearly related in the $\left(L^2, E_\infty^2\right)$-space (or $\left(\Omega^2, E_\infty^2\right)$-space). We can thus obtain representations for the functions $h_{_L}$, $g_{_L}$, $h_{_\Omega}$ and $g_{_\Omega}$ in (6.39) which are more accurate than those found by Rosenkilde. Using standard interpolation one can easily calculate that:

$$\begin{aligned} h_{_L}(\alpha) &= 4.9586\alpha^3 - 18.135\alpha^2 + 22.835\alpha - 9.6572 \\ g_{_L}(\alpha) &= -2.2864\alpha^3 + 8.3977\alpha^2 - 11.369\alpha + 7.0616 \\ h_{_\Omega}(\alpha) &= 4.526\alpha^3 - 16.668\alpha^2 + 21.175\alpha - 9.0309 \\ g_{_\Omega}(\alpha) &= -0.23397\alpha^3 + 0.84134\alpha^2 - 1.0653\alpha + 0.50056 \end{aligned} \quad , \tag{6.40}$$

describe the aspect ratio isolines satisfied by numerical solutions. These expressions provide us with an easy and accurate way to compute approximate spheroidal-like solutions for droplets rotating at constant angular momentum or constant angular speed are subject to a uniform external electric field in the direction of the rotation axis.

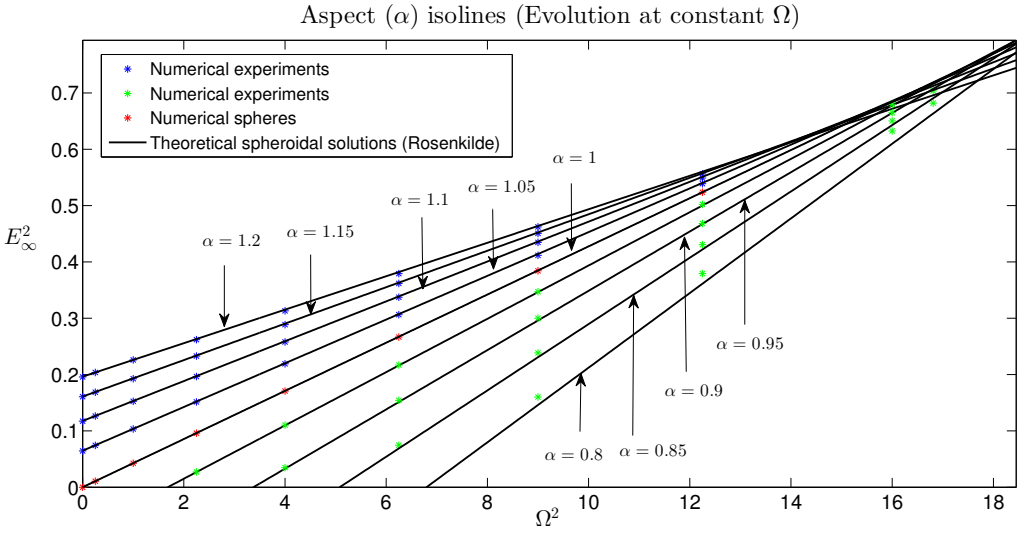

Figure 6.12: Comparison of Rosenkilde's solutions with simulations at constant Ω.

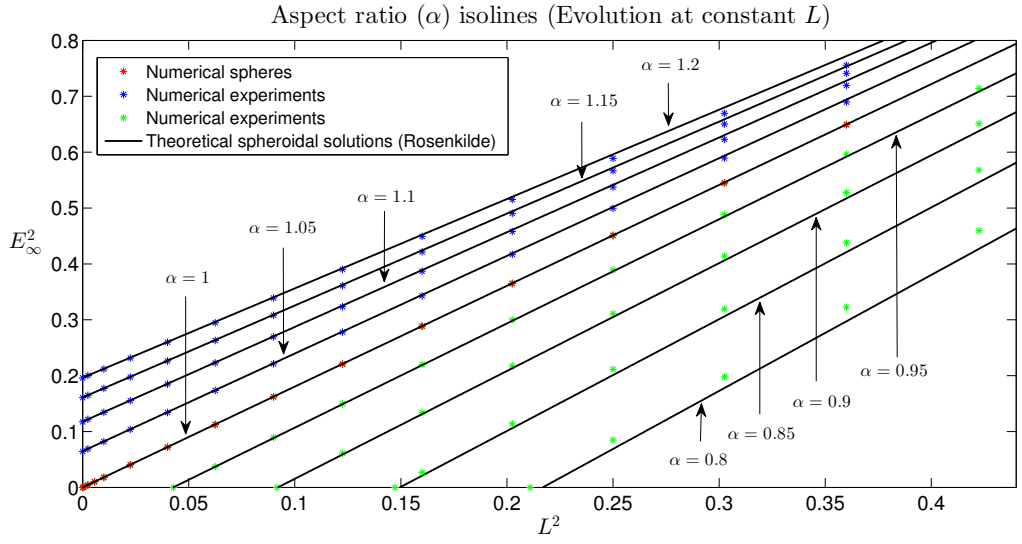

Figure 6.13: Comparison of Rosenkilde's solutions with simulations at constant L.

We focus now on the stability of axisymmetric equilibrium configurations. Suppose that we start from a situation where no electric field is present and we set a value for the angular momentum $L > 0$ (or angular speed $\Omega > 0$) for which the corresponding equilibrium solution is oblate-like. As the magnitude of the electric field increases, electrostatic pressure counterbalances the flattening effect of rotation, which tends to thicken the equatorial region, by stretching the droplet in the direction of the applied field and, consequently, a smooth transition from oblate- to prolate-like solutions takes place. In this process, and since the variation of the parameters is continuous, a spherical solution is attained, marking the point where oblate configurations meet prolate ones. If one keeps increasing the electric field, prolate spheroids eventually become unstable and develop dynamic Taylor cones at the poles. From simulations, the values where this change in stability takes place shows a cubic relation between L (or Ω) and E_∞ as shown below:

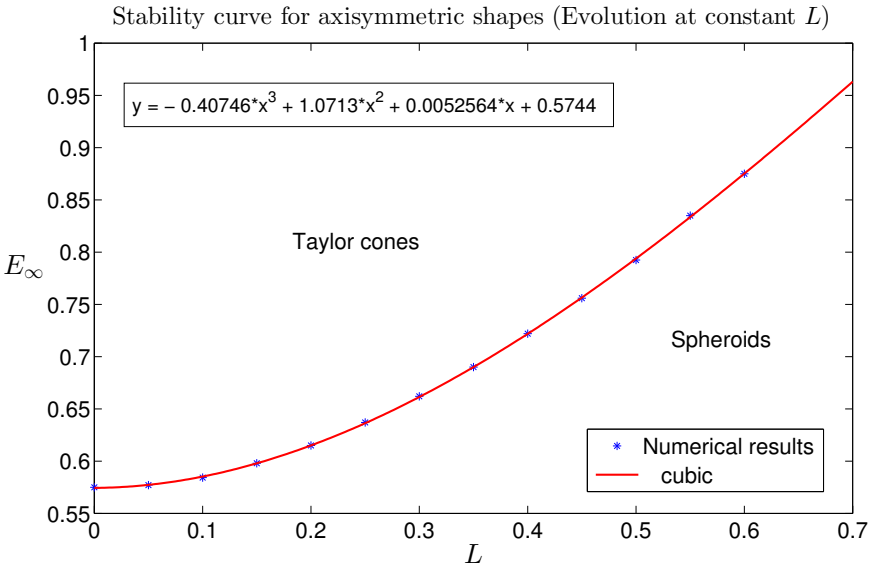

Figure 6.14: Stability curve where spheroids at constant L become unstable and develop Taylor cones.

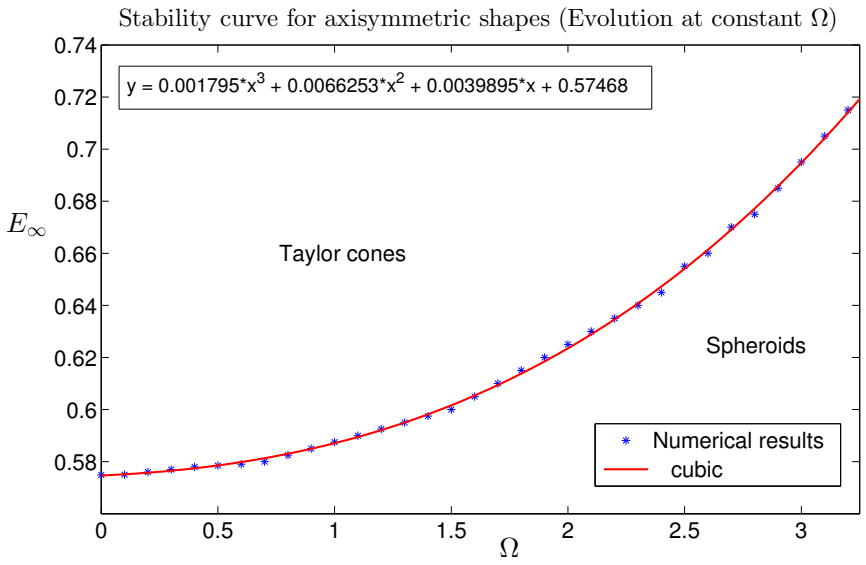

Figure 6.15: Stability curve where spheroids at constant Ω become unstable and develop Taylor cones.

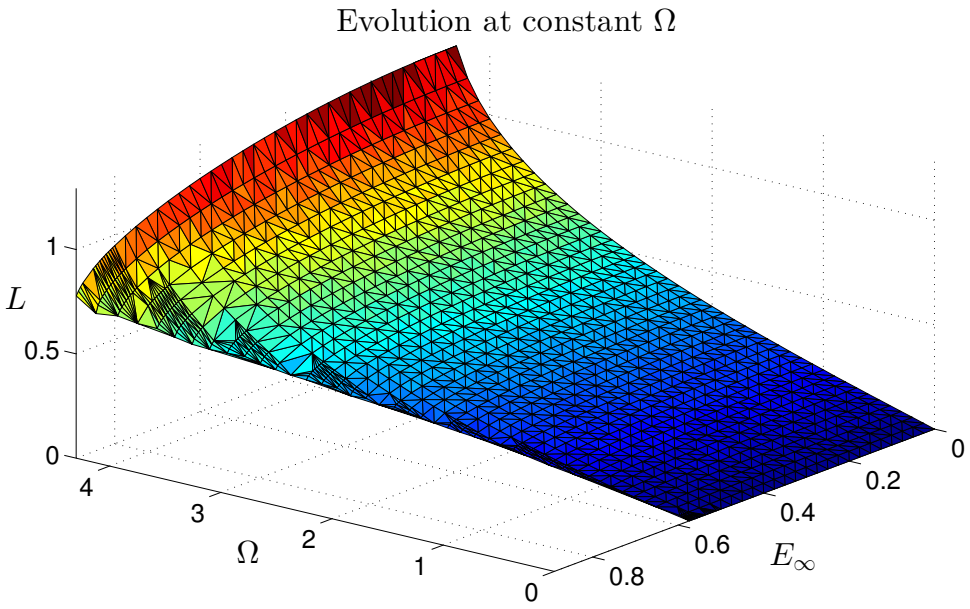

Figure 6.16: Evolution diagram I for rotating drops at constant Ω subject to an electric field.

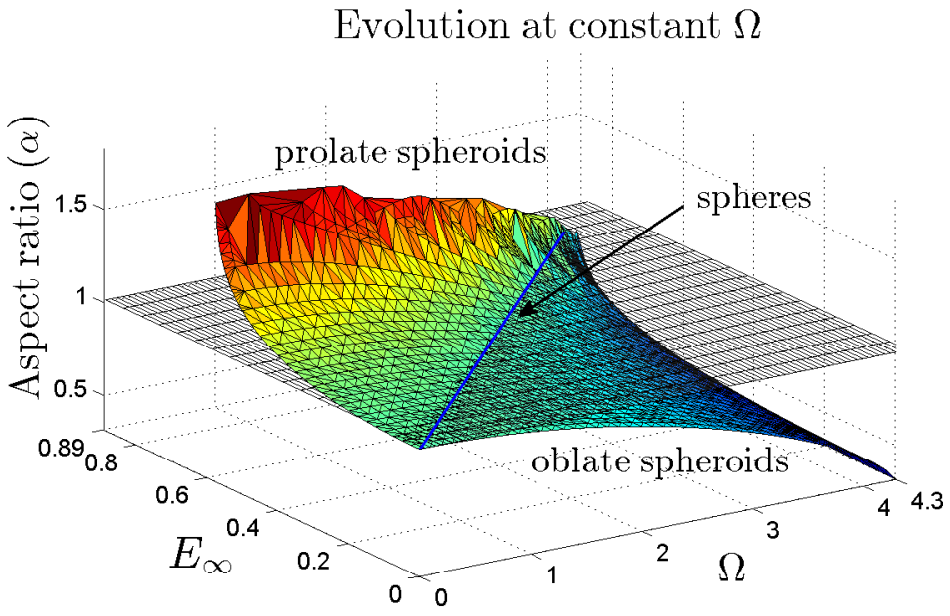

Figure 6.17: Evolution diagram II for rotating drops at constant Ω subject to an electric field.

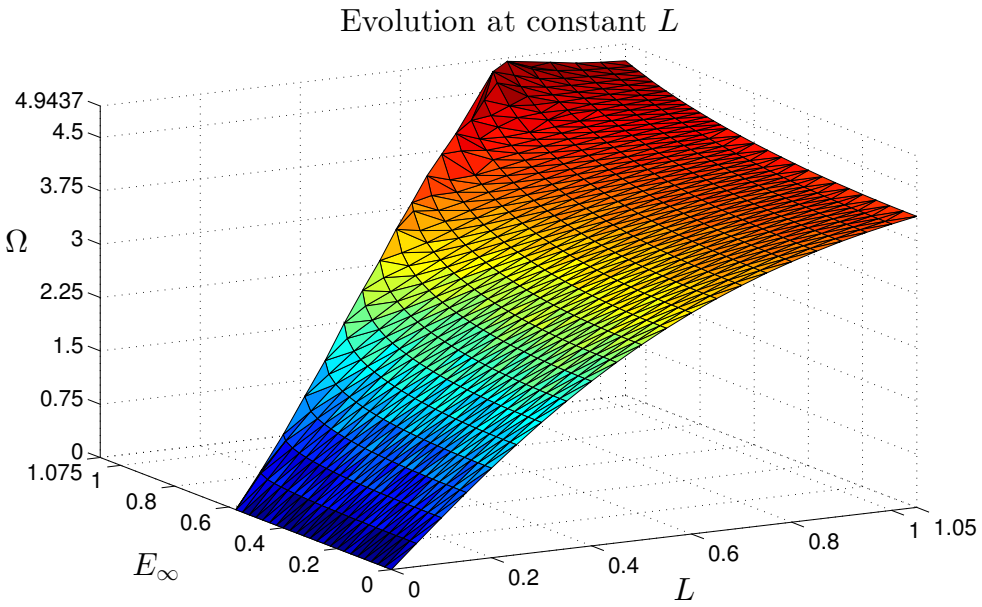

Figure 6.18: Evolution diagram I for rotating drops at constant L subject to an electric field.

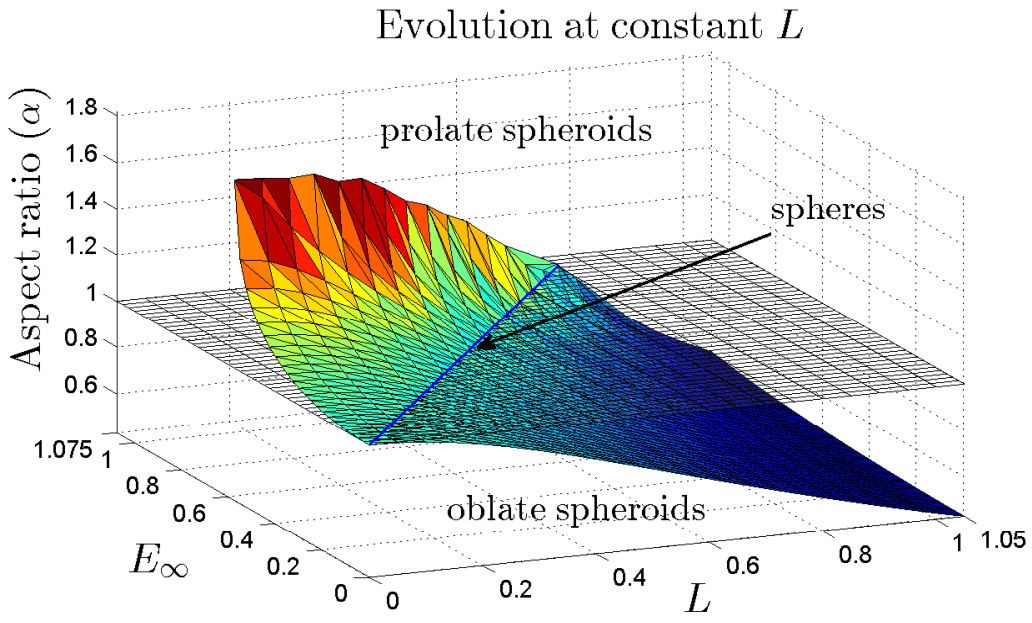

Figure 6.19: Evolution diagram II for rotating drops at constant L subject to an electric field.

6.2.3. Evolution and stability in 3D

To finish this section, we perform a 3D stability analysis for rotating drops at constant angular momentum immersed in an uniform electric field parallel to the rotation axis. This is done by evolving an initially spherical drop with the 3D version of the code and studying all different configurations attained during this process. The values for the angular momentum L and the electric field E_∞ range from 0 to 0.95 at 0.05 intervals, the surface tension is taken as $\gamma = 1$ and the ratio of viscosities is set to $\lambda = 0.1$. Our simulations show oblate- and prolate-like solutions (the same ones obtained with the axisymmetric model) together with spherical equilibrium shapes according to [65]. A transition curve between spheroidal and ellipsoidal-like equilibrium shapes is determined together with a stability limit curve separating equilibrium solutions from singularity formation. Results show that this stability curve increases at first, proving that rotating drops are more stable to higher electric field values, but eventually turns back on itself, implying that too much rotation penalizes the stability instead of contributing to it. Above the spheroid-ellipsoid transtition curve, ellipsoidal-like solutions and peanut shapes [11] appear, and for large values of the electric field, a two-lobed structure forms for which time scales play a key role in determining wether a pinch-off occurs or cone tips develop in finite time.

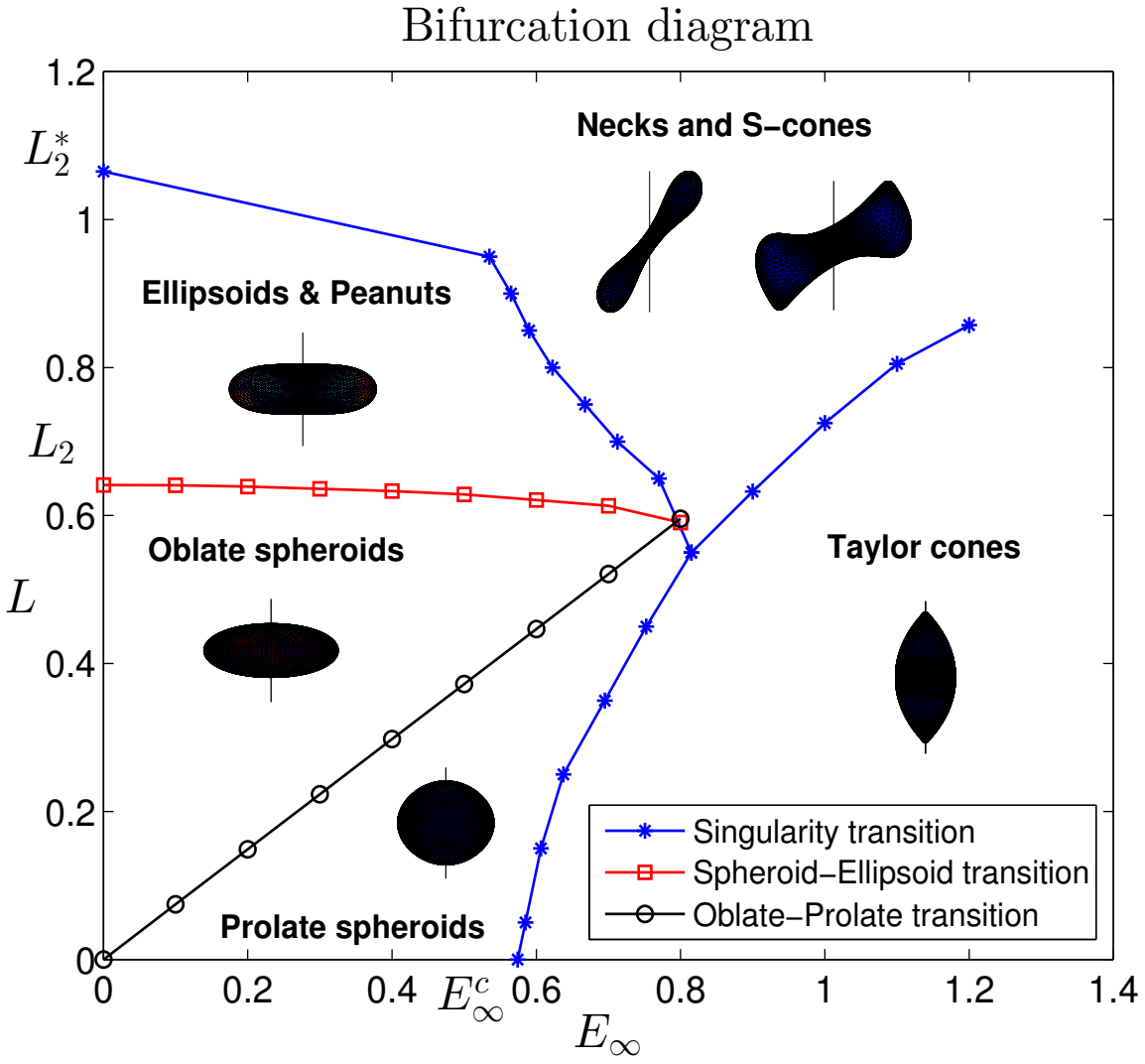

Figure 6.20: Sketch of the bifurcation diagram summarizing numerical results (symbols) determining the transition curves between different regimes.

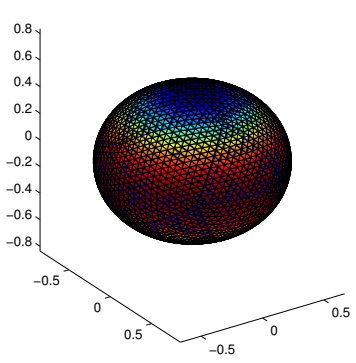

(a) Oblate spheroid

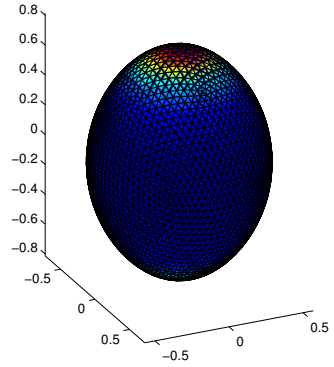

(b) Prolate spheroid

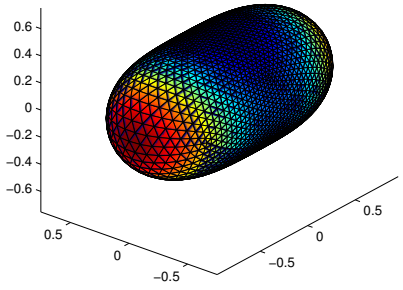

(c) Ellipsoid

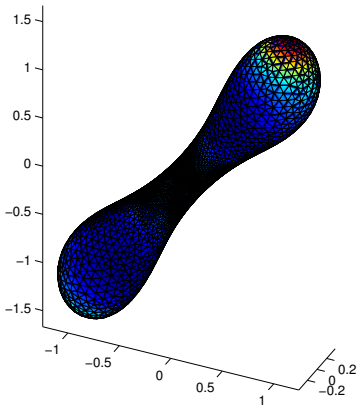

(d) Neck formation

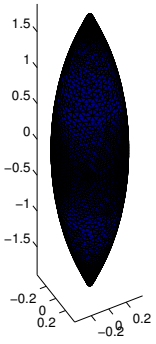

(e) Dynamic Taylor cone

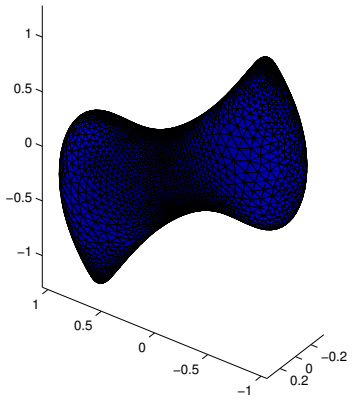

(f) S-shaped Taylor cone

Figure 6.21: Evolution of a neutral rotating drop subject to an electric field in the direction of the rotation axis. Picture 6.21(a) corresponds to $L = 0.55$ and $E_\infty = 0.4$. In 6.21(b) the parameters are $L = 0.45$ and $E_\infty = 0.75$. Figure 6.21(c) is obtained when $L = 0.75$ and $E_\infty = 0.3$. For $L = 0.95$ and $E_\infty = 0.55$ a two-lobed structure forms leading to a pinch-off in finite time. For 6.21(e) we have $L = 0.05$ and $E_\infty = 0.6$. Finally, the structure in 6.21(f), where an s-shaped Taylor cone develops in finite time, is obtained for $L = 1$ and $E_\infty = 1$. Color gradation represents mean curvature and the axis of rotation and applied electric field are both aligned with the vertical z axis.

6.3. Analysis of dynamic Taylor cones

The destabilizing effect that a conducting fluid droplet undergoes when it bears an amount of charge above Rayleigh's limit or is immersed in a strong electric field gives rise to cone-like singularities known in the literature as dynamic Taylor cones. This phenomenon was first discovered by Taylor [68] in 1964 and takes place in very short time scales. In his works, Taylor predicted theoretically an opening semiangle for these cones of 49.3°, which has turned out to be very different from the average value of about 30° obtained from simulations [27] and laboratory experiments [20]. Moreover, this angle seems to depend slightly on the viscosity ratio for the two fluids involved and interestingly it develops in a self-similar way [27].

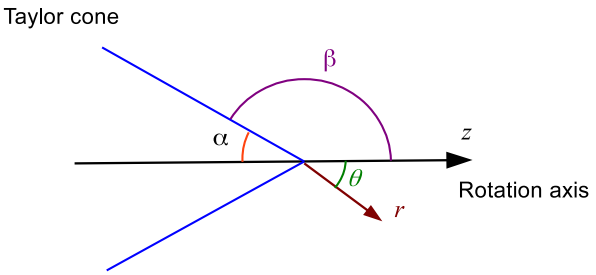

Figure 6.22: Taylor cone with semiangle α.

The theoretical derivation of the opening semiangle for Taylor cones goes as follows: under axial symmetry and imposing spherical coordinates at the tip of the cone, one has to solve Laplace equation for the electrostatic potetial $\mathcal{V}$. To do so, one can look for a self-similar solution in the form:

$$\mathcal{V}(r,\theta) = r^{\lambda} f(\theta) \ ,$$

yielding:

$$\Delta\mathcal{V} = 0 \quad \Leftrightarrow \quad 0 = \lambda(\lambda+1) f(\theta) + f''(\theta) + f'(\theta)\cot\theta \ .$$

Changing variables, $x = \cos\theta$, above equation becomes Legendre differential equation, which has solutions:

$$f(\theta) = AP_{\lambda}(\cos\theta) + BQ_{\lambda}(\cos\theta) \ ,$$

where P_λ and Q_λ are Legendre polynomials of the first and second kind respectively. Since Q_λ contains logarithmic singularities that would make $\|\mathbf{E}\|^2$ non-integrable, the solution sought must satisfy:

$$f(\theta) = AP_{\lambda}(\cos\theta) \ ,$$

and consequently:

$$\mathcal{V}(r,\theta) = Ar^{\lambda}P_{\lambda}(\cos\theta) \sim O\left(r^{\lambda}\right) \ .$$

Supposing that the potential at the surface of the cone is zero, the boundary condition reads:

$$f(\beta) = 0 \quad , \quad \text{with} \quad \beta = \pi - \alpha \ ,$$

giving a relation between λ and the semiangle α in the form:

$$P_{\lambda}(\cos(\pi-\alpha)) = 0 \ , \tag{6.41}$$

From differential geometry we know that the mean curvature of a cone with semiangle α is:

$$\mathcal{H} = -\frac{1}{2r\tan\beta} \sim O\left(r^{-1}\right) \ ,$$

and since the normal derivative of the electric potential at the interface of the cone is:

$$\frac{\partial\mathcal{V}}{\partial\mathbf{n}} = Ar^{\lambda-1}P'_{\lambda}(\cos\beta)\sin\beta \sim O\left(r^{\lambda-1}\right) \ ,$$

and rotational forces have the form:

$$\frac{1}{2}\Delta\varrho\,\omega^2 r^2\sin^2\beta \sim O\left(r^2\right)\ ,$$

then Young-Laplace equation becomes:

$$\delta\Pi = -\frac{\gamma}{r\tan\beta} - \frac{1}{2}\Delta\varrho\,\omega^2 r^2\sin^2\beta - \frac{1}{2}\varepsilon_0 A^2 r^{2\lambda-2}\left(P'_\lambda\left(\cos\beta\right)\right)^2\sin^2\beta\ .$$

Now, imposing that capillary forces balance electrostatic forces at the cone tips (observe that near the tip, rotational forces are clearly negligible compared to surface tension), one gets:

$$2\lambda - 2 = -1 \quad \Leftrightarrow \quad \lambda = \frac{1}{2}\ , \tag{6.42}$$

and the corresponding value for λ results from the boundary condition:

$$P_{\frac{1}{2}}\left(\cos\beta\right) = 0 \quad \Leftrightarrow \quad \beta \approx 130.71^\circ \quad \Leftrightarrow \quad \alpha \approx 49.29^\circ\ ,$$

To understand the role that rotation at constant angular momentum L or constant angular speed Ω plays in the formation of Taylor cones, we have studied its contribution to charged conducting drops and separately to neutral conducting droplets under the influence of electric fields. Comparing the centrifugal and surface tension stresses near the region where the tips develop, we have found that the effects of rotation are negligible and, therefore, the cone formation mechanism behaves as if there was no rotation. This implies in particular that we still get self-similar evolution in the form:

$$\mathcal{H}_{tip} \sim O\left((t_0-t)^{-\frac{1}{2}}\right) \quad , \quad \sigma_{tip} \sim O\left((t_0-t)^{-\frac{1}{2}}\right) \quad , \quad u_{z,tip} \sim O\left((t_0-t)^{-\frac{1}{2}}\right) \tag{6.43}$$

where $\mathcal{H}_{tip}$, σ_{tip} and $u_{z,tip}$ are respectively the mean curvature, the surface charge density and the z component of velocity field at the tip, and t_0 is the time at which the singularity occurs. This asymptotic behaviour was proved in [7] numerically and from dimensional considerations. In figure 6.23 we show some evolution profiles for the drop near the tip together with the same profiles scaled according to (6.43). Then, in figure 6.24 drop profiles for several values of the angular momentum are superimposed to justify that the cone semiangle does not vary significantly with angular momentum. The reason for this is that centrifugal forces become subdominant at the tips with respect to surface tension as demonstrated in diagrams 6.25 and 6.26. Following the evolution of the tangent to the interface as a function of r as t tends to t_0, we found a clear tendency to form a conical tip which is roughly independent of L (see figure 6.27). The opening semiangle of the cones, β, is measured by considering the angle at which the line that best fits the node located at the rotation axis and its neighbours intersects the vertical z axis.

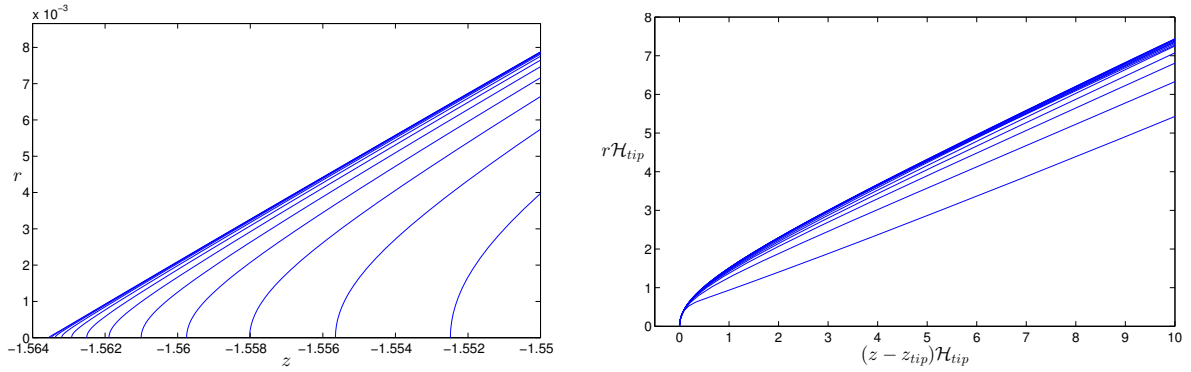

(a) Profiles without rescaling.

(b) Rescaled profiles.

Figure 6.23: Profiles near the formation of the tip for $t \gg 1$. In 6.23(a) the profiles are drawn without any scaling applied to them, and 6.23(b) depicts the same profiles after rescaling to show self-similar behaviour. For this simulation, parameteres take the values $L = 0.2$ and $E_{\mathscr{C}} = 0.9$.

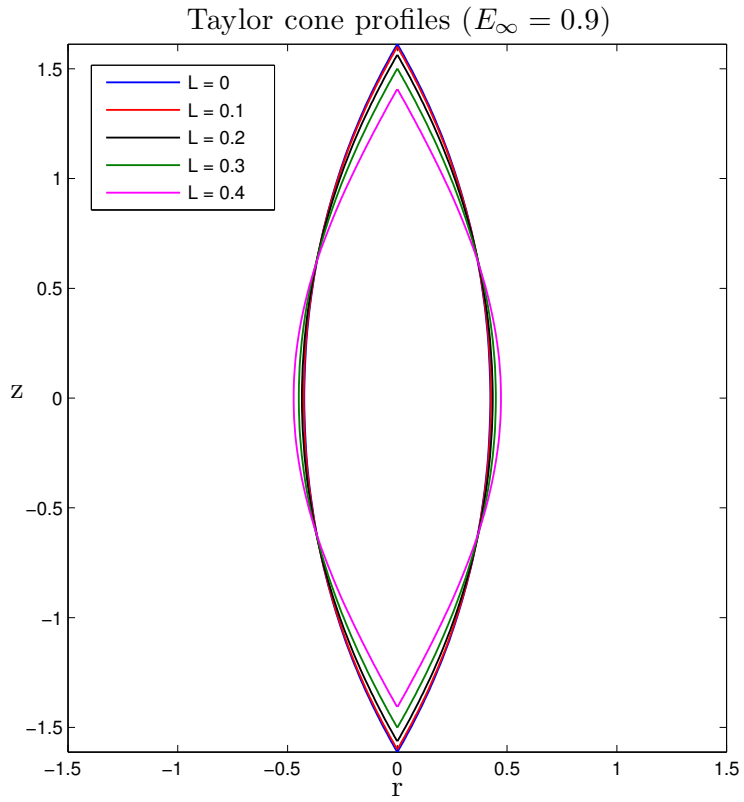

Figure 6.24: Taylor cones for different values of angular momentum. Note that they all have the same angle.

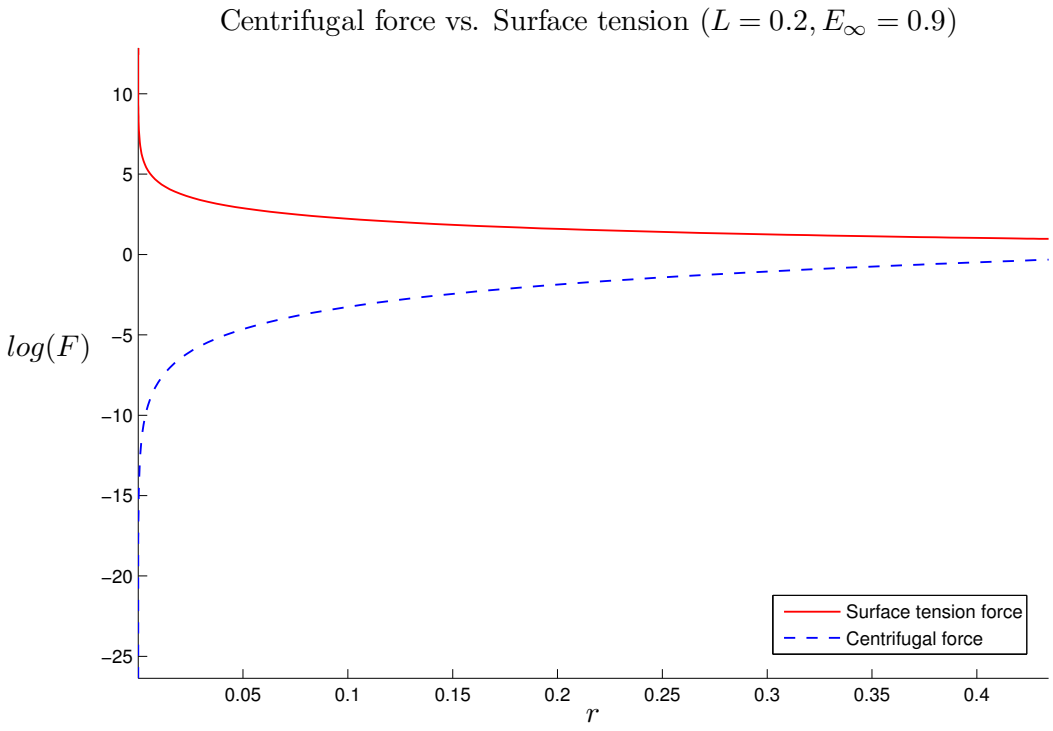

Figure 6.25: Comparison of the magnitude of forces near the tip.

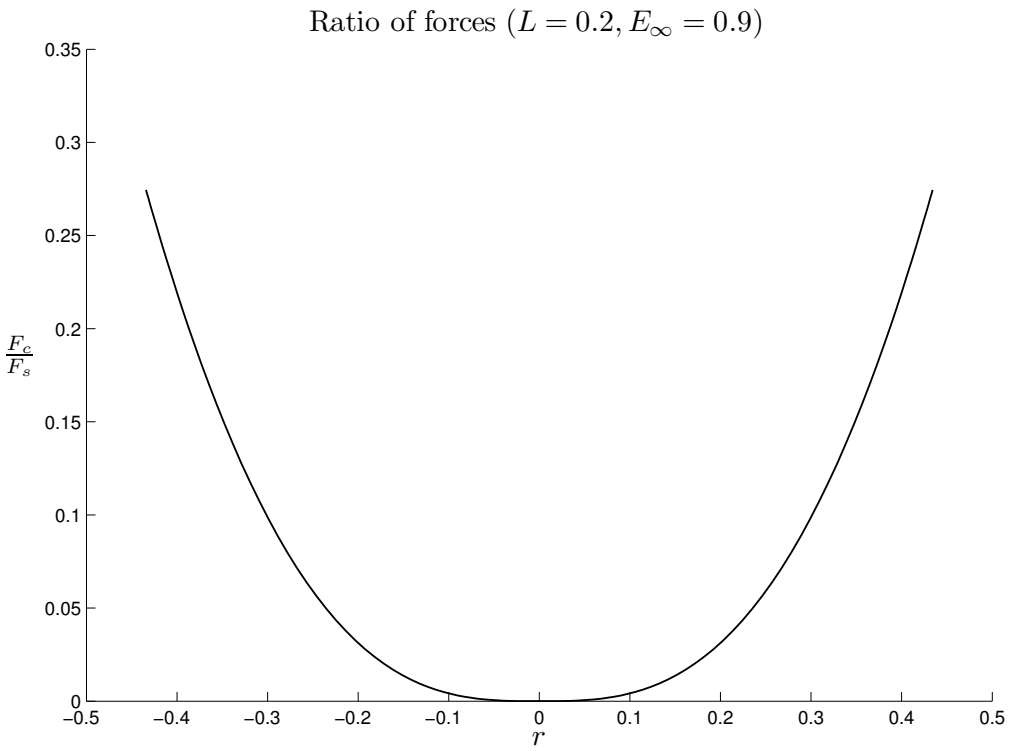

Figure 6.26: Ratio of forces near the tip. F_s represents surface tension and F_c is the centrifugal force.

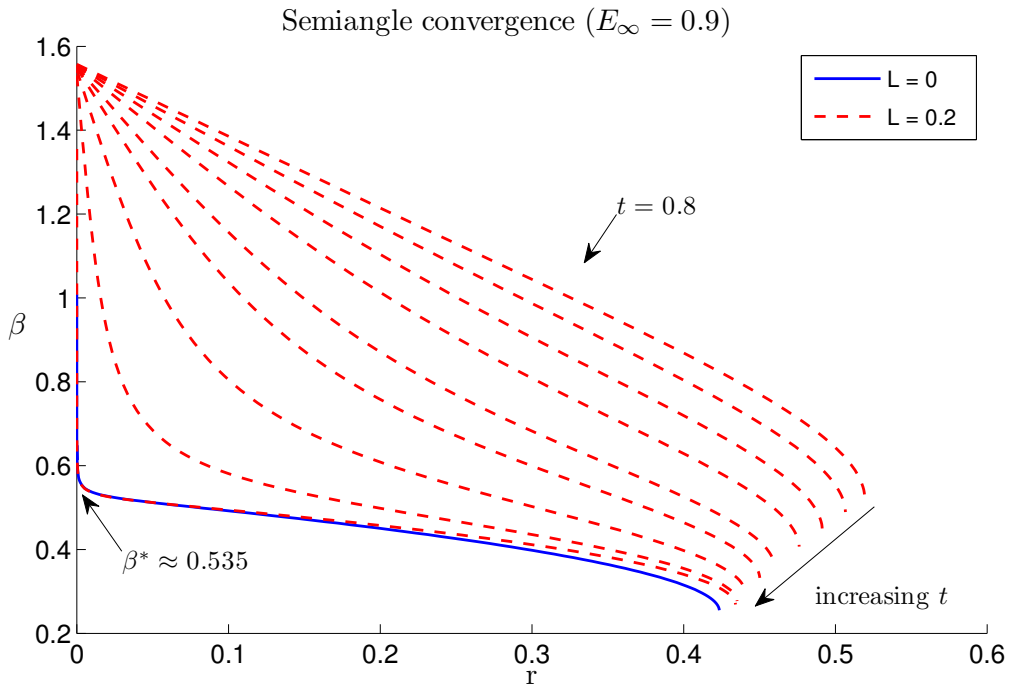

Figure 6.27: Evolution of the angle formed by the tangent line to the drop's interface with the z axis as a function of r. Notice the convergence towards a tip semiangle of $\beta^* \approx 0.535\ rad\ (= 30.6°)$. Discontinuous curves correspond to times $t = 0.8, 0.9, 1, 1.1, 1.2, 1.25, 1.3, 1.325, 1.33$.

Chapter 7

A FEM code for rotating drops

This chapter is devoted to introducing a FEM code developed by Prof. Jie Li at Cambridge University to simulate axisymmetric multiphase flows, which has been used to validate the results for rotating drops obtained in chapter 5. The reason for choosing this method is that, with it, one can study the effects that the nonlinear terms appearing in Navier-Stokes equations have on the evolution and stability of rotating drops (this problem is currently under research). We will start by deriving the weak formulation associated to Navier-Stokes equations followed by a detailed explanation on how to discretize it in order to solve the free-surface problem. Then, we will give some details on Uzawa's algorithm, which solves the sparse linear system resulting from this numerical approximation, and also on the adaption techniques implemented to enhance the quality of the moving triangle mesh. We conclude this chapter comparing some numerical simulations that were performed using FEM with those corresponding to BEM.

Given a drop of density ϱ_1 and viscosity μ_1 surrounded by another fluid of density ϱ_2 and viscosity μ_2, suppose that the system rotates about the z axis with angular speed $\boldsymbol{\omega}(t)$ and occupies a region $\mathcal{D} \subset \mathbb{R}^3$. We describe this system by working in the rotating (non-inertial) reference frame, where ficticious forces must be included into the equations of motion. In this way, considering that Coriolis and Euler forces are negligible and that the fluid is incompressible, Navier-Stokes equations have the form:

$$\begin{cases} \varrho \, \dfrac{D\mathbf{u}}{Dt} = \nabla \cdot \widetilde{T} - \varrho \, \boldsymbol{\omega} \times (\boldsymbol{\omega} \times \mathbf{x}) + \mathbf{F}_b \quad , \quad \text{in } \mathcal{D} \\ \nabla \cdot \mathbf{u} = 0 \quad , \quad \text{in } \mathcal{D} \end{cases} , \tag{7.1}$$

where $\mathbf{F}_b$ are the body forces acting on the droplet and $\widetilde{T}$ is the newtonian stress tensor:

$$\widetilde{T} = -p\,\mathbb{I} + 2\mu\mathbb{D}(\mathbf{u}) \quad , \quad \mathbb{D}(\mathbf{u}) = \frac{1}{2}\left(\nabla\mathbf{u} + (\nabla\mathbf{u})^T\right) , \tag{7.2}$$

with p the fluid pressure and $\mathbb{D}(\mathbf{u})$ the rate-of-strain tensor. Observe that by taking the divergence of the stress tensor and considering that the viscosity is constant one gets:

$$\nabla \cdot \widetilde{T} = -\nabla p + 2\mu \nabla \cdot \mathbb{D}(\mathbf{u}) \ .$$

Suppose that the drop is axisymmetric about the rotation axis and that no body forces (gravity, electromagnetic fields, ...) act on it, i.e. $F_b \equiv \mathbf{0}$. Under these assumptions, and working in cylindrical coordinates, the velocity field and pressure satisfy:

$$u_\varphi = \frac{\partial p}{\partial \varphi} = 0 \quad , \quad \frac{\partial \mathbf{u}}{\partial \varphi} = \mathbf{0} \, ,$$

with $\mathbf{u} = u_r\widehat{\mathbf{r}} + u_\varphi\widehat{\boldsymbol{\varphi}} + u_z\widehat{\mathbf{k}}$. The material derivative components are:

$$\left(\frac{D\mathbf{u}}{Dt}\right)_r = \frac{Du_r}{Dt} \quad , \quad \left(\frac{D\mathbf{u}}{Dt}\right)_\varphi = 0 \quad , \quad \left(\frac{D\mathbf{u}}{Dt}\right)_z = \frac{Du_z}{Dt} \, ,$$

where the material derivative operator is given by:

$$\frac{Df}{Dt} = \frac{\partial f}{\partial t} + u_r\frac{\partial f}{\partial r} + u_z\frac{\partial f}{\partial z} \ .$$

Similarly, the gradient of the velocity field is:

$$\nabla \mathbf{u} \equiv \nabla \otimes \mathbf{u} \equiv \left\{ \frac{\partial u_j}{\partial x_i} \right\}_{i,j} = \begin{pmatrix} \dfrac{\partial u_r}{\partial r} & 0 & \dfrac{\partial u_r}{\partial z} \\ 0 & \dfrac{u_r}{r} & 0 \\ \dfrac{\partial u_z}{\partial r} & 0 & \dfrac{\partial u_z}{\partial z} \end{pmatrix} ,$$

and the stress tensor components result:

$$\tilde{T}_{rr} = -p + 2\mu \frac{\partial u_r}{\partial r} \quad , \quad \tilde{T}_{\varphi\varphi} = -p + 2\mu \frac{u_r}{r} \quad , \quad \tilde{T}_{zz} = -p + 2\mu \frac{\partial u_z}{\partial z} ,$$

$$\tilde{T}_{r\varphi} = \tilde{T}_{\varphi r} = \tilde{T}_{z\varphi} = \tilde{T}_{\varphi z} = 0 \quad , \quad \tilde{T}_{rz} = \tilde{T}_{zr} = \mu \left(\frac{\partial u_r}{\partial z} + \frac{\partial u_z}{\partial r} \right) .$$

Now, the incompressibility condition yields:

$$\nabla \cdot \mathbf{u} = \frac{1}{r} \frac{\partial}{\partial r} (r u_r) + \frac{\partial u_z}{\partial z} ,$$

and the divergence of the stress tensor:

$$\nabla \cdot \tilde{T} = \tilde{T}_r \hat{\mathbf{r}} + \tilde{T}_z \hat{\mathbf{k}} ,$$

where:

$$\tilde{T}_r = \frac{1}{r} \frac{\partial}{\partial r} (r T_{rr}) + \frac{\partial T_{rz}}{\partial z} - \frac{T_{\varphi\varphi}}{r} \quad , \quad \tilde{T}_z = \frac{1}{r} \frac{\partial}{\partial r} (r T_{zr}) + \frac{\partial T_{zz}}{\partial z} .$$

Taking z as the rotation axis, $\boldsymbol{\omega}(t) = \omega(t) \hat{\mathbf{k}}$, the centrifugal force results:

$$\mathbf{F}_{Centrifugal} \equiv \mathbf{F}_c = \varrho \, \boldsymbol{\omega} \times (\boldsymbol{\omega} \times \mathbf{x}) = \varrho \, \omega \hat{\mathbf{k}} \times \left(\omega \hat{\mathbf{k}} \times \left(r \hat{\mathbf{r}} + z \hat{\mathbf{k}} \right) \right) = -\varrho \, r \, \omega^2 \hat{\mathbf{r}} .$$

Finally, and to complete the formulation of the problem, we need to set boundary conditions on the system. Since the problem is axially symmetric, it suffices to consider the solution of Navier-Stokes equations over a plane that contains the profile curve, so one can decompose the domain as:

$$\mathcal{D} = \mathcal{D}_{axi} \times [0, 2\pi) \quad , \quad \mathcal{D}_{axi} \subset \mathbb{R}^2 , \tag{7.3}$$

and consequently, the boundary of the domain $\mathcal{D}_{axis} = D_1 \cup D_2$ can be written as follows:

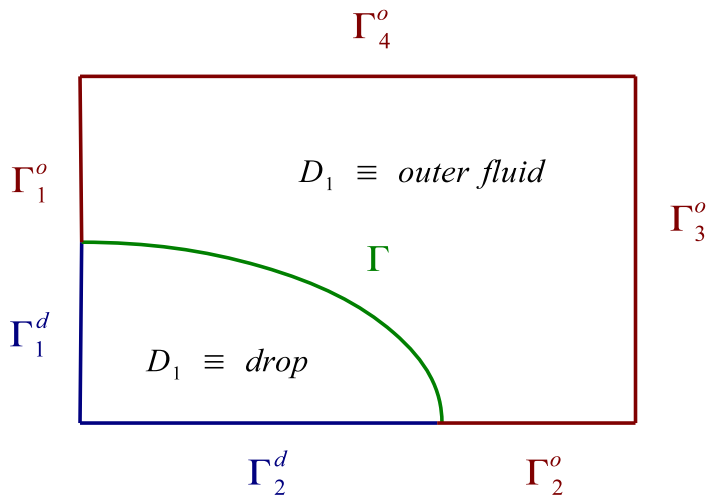

Figure 7.1: FEM domain.

where:

$$\partial\mathcal{D}_{axi} = \Gamma \cup \Gamma_b \quad , \quad \Gamma_b = \Gamma_1^d \cup \Gamma_2^d \cup \Gamma_1^o \cup \Gamma_2^o \cup \Gamma_3^o \cup \Gamma_4^o \, . \tag{7.4}$$

Over each section of the boundary we have to impose:

$$\begin{aligned} [\widetilde{T}]\,\mathbf{n} = 2\gamma\mathcal{H}\,\mathbf{n} \quad &, \quad \text{on } \Gamma \, , \\ u_r = 0 \quad &, \quad \text{on } \Gamma_1^o \cup \Gamma_3^o \cup \Gamma_1^d \, , \\ u_z = 0 \quad &, \quad \text{on } \Gamma_2^o \cup \Gamma_4^o \cup \Gamma_2^d \, , \end{aligned}$$

where $\mathbf{n}$ is the outward unit normal to the drop and $[\widetilde{T}] = \widetilde{T}^{(2)} - \widetilde{T}^{(1)}$ is the stress jump across the interface.

7.1. A review on functional spaces

Before deriving the weak formulation associated to Navier-Stokes, it is necessary to remember some basic definitions related to Sobolev spaces that we will use later for that purpose. A simple introduction to the theory of functional spaces is available in [59] and for a deeper insight see [9]. For the rest of this section, $\Omega \subset \mathbb{R}^m$ represents a bounded domain with a regular boundary $\partial\Omega$ (i.e. Lipshitz continuous).

Definition 7.1. *The space $P_k(\Omega)$ with $k \in \mathbb{N}$ is the set of polynomials $p : \Omega \to \mathbb{R}$ of degree less or equal to k.*

Definition 7.2. *The space $L^p(\Omega)$ with $1 \leqslant p \leqslant \infty$ is the set of measurable functions $f : \Omega \to \mathbb{R}$ satisfying:*

$$\|f\|_{L^p(\Omega)} = \begin{cases} \left(\displaystyle\int_\Omega |f|^p \, dx \right)^{\frac{1}{p}} < +\infty & , \quad 1 \leqslant p < \infty \\ ess \sup\limits_{\Omega} |f| < +\infty & , \quad p = \infty \end{cases} .$$

Definition 7.3. *The space $\mathbf{L}^p(\Omega)$ with $1 \leqslant p \leqslant \infty$ is formed by the vector functions $\mathbf{f} : \Omega \to \mathbb{R}^N$ whose components belong to $L^p(\Omega)$. Its norm is defined as follows:*

$$\|\mathbf{f}\|_{\mathbf{L}^p(\Omega)} = \begin{cases} \left(\displaystyle\sum_{i=1}^N \|f_i\|_{L^p(\Omega)}^p \right)^{\frac{1}{p}} & , \quad 1 \leqslant p < \infty \\ \max\limits_{i=1,\ldots,n} \{ \, ess \sup\limits_{\Omega} |f_i| \, \} & , \quad p = \infty \end{cases} .$$

Definition 7.4. *Given a multiindex $\alpha = (\alpha_1, \ldots, \alpha_n) \in \mathbb{N}^n$, its order is k when:*

$$|\alpha| = \sum_{i=1}^n \alpha_i = k \, .$$

For any function $f : \Omega \to \mathbb{R}$ one can define:

$$D^\alpha u = \frac{\partial^{|\alpha|} u}{\partial x_1^{\alpha_1} \cdots \partial x_n^{\alpha_n}} \, ,$$

and the set of all partial derivatives of order $k \in \mathbb{N}$ has the form:

$$D^k u = \{ D^\alpha u \mid \, |\alpha| = k \} \, ,$$

which can be seen as a point in $\mathbb{R}^{n^k}$, whose norm is:

$$\left\| D^k u \right\| = \left(\sum_{|\alpha|=k} |D^\alpha u|^2 \right)^{\frac{1}{2}} .$$

Definition 7.5. *Given $u, v \in L^1_{loc}(\Omega)$ and a multiindex α, we say that v is the α^{th}-weak partial derivative of u, i.e. $D^\alpha u = v$, provided that:*

$$\int_\Omega u \, D^\alpha \varphi \, d\mathbf{x} = (-1)^{|\alpha|} \int_\Omega v\varphi \, d\mathbf{x} \quad , \quad \forall \varphi \in C_c^\infty(\Omega) \, .$$

Definition 7.6. *The Sobolev space $W^{k,p}(\Omega)$ consists of all locally summable functions $f:\Omega\to\mathbb{R}$ such that for each multiindex α with order k, the α^{th}-weak partial derivative of u exists and belongs to $L^p(\Omega)$. The norm in this space is defined as follows:*

$$\|f\|_{W^{k,p}(\Omega)} = \begin{cases} \left(\sum_{|\alpha|\leqslant k}\int_\Omega |D^\alpha f|^p \, d\mathbf{x}\right)^{\frac{1}{p}} & , \quad 1\leqslant p<\infty \\ \sum_{|\alpha|\leqslant k} ess\ \sup_\Omega |D^\alpha f| & , \quad p=\infty \end{cases} .$$

In particular, when $p=2$ the standard notation is $W^{k,2}\equiv H^k$ because H^k is a Hilbert space (notice that $H^0\equiv L^2$). The inner product defined in these spaces is given by the following formula:

$$(f,g)_{H^k(\Omega)} = \sum_{|\alpha|\leqslant k}\int_\Omega D^\alpha f\cdot D^\alpha g\, d\mathbf{x} \quad , \quad f,g\in H^k(\Omega) .$$

Definition 7.7. *The space $\mathbf{H}^k(\Omega)$ with $k\in\mathbb{N}$ is comprised of the vector functions $\mathbf{f}:\Omega\to\mathbb{R}^N$ whose components belong to $H^k(\Omega)$. Its norm is defined as follows:*

$$\|\mathbf{f}\|_{\mathbf{H}^k(\Omega)} = \left(\sum_{i=1}^N \|f_i\|^2_{H^k(\Omega)}\right)^{\frac{1}{2}} .$$

7.2. Weak formulation

Any problem written in terms of PDEs has a weak formulation associated to it, which is the cornerstone of FEM. To derive the variational representation of Navier-Stokes equations, consider two functional spaces, $\mathbf{V}$ and Q, and multiply the first equation in (7.1) by the test function $\boldsymbol{\phi}\in\mathbf{V}$ and the second one by $\psi\in Q$ and integrate over the whole domain:

$$\int_{\mathcal{D}} \varrho\frac{D\mathbf{u}}{Dt}\cdot\boldsymbol{\phi}\, d\mathbf{x} = \int_{\mathcal{D}} (-\mathbf{F}_c - \nabla p + 2\mu\nabla\cdot\mathbb{D}(u))\cdot\boldsymbol{\phi}\, d\mathbf{x} , \tag{7.5}$$

$$\int_{\mathcal{D}} \psi\nabla\cdot\mathbf{u}\, d\mathbf{x} = 0 . \tag{7.6}$$

Now, to change the derivatives from the unknowns to the test functions, apply the divergence theorem:

$$\int_{\mathcal{D}}\nabla p\cdot\boldsymbol{\phi}\, d\mathbf{x} = \int_{\partial\mathcal{D}} p\boldsymbol{\phi}\cdot\mathbf{n}\, dS - \int_{\mathcal{D}} p\nabla\cdot\boldsymbol{\phi}\, d\mathbf{x} = \int_{\partial\mathcal{D}} p\mathbf{n}\cdot\boldsymbol{\phi}\, dS - \int_{\mathcal{D}} p\nabla\cdot\boldsymbol{\phi}\, d\mathbf{x} ,$$

and take into account the following result:

Proposition 7.1. *Given a symmetric matrix A, the following identity holds:*

$$\nabla\cdot(A\mathbf{b}) = (\nabla\cdot A)\cdot\mathbf{b} + A:\mathbb{D}(\mathbf{b}) \quad , \quad \forall\ \mathbf{b}\in\mathbb{R}^n .$$

Proof. Using the product rule for derivatives:

$$\nabla\cdot(A\mathbf{b}) = \frac{\partial}{\partial x_i}(A_{ij}b_j) = \frac{\partial A_{ij}}{\partial x_i}b_j + A_{ij}\frac{\partial b_j}{\partial x_i} = (\nabla\cdot A)\cdot\mathbf{b} + A:\nabla\mathbf{b} = (\nabla\cdot A)\cdot\mathbf{b} + A:\mathbb{D}(\mathbf{b}) ,$$

where the colon symbol represents the dot product between matrices. ∎

If we apply previous proposition with $A=\mathbb{D}(\mathbf{u})$ and use the divergence theorem:

$$\int_{\mathcal{D}}\nabla\cdot(\mathbb{D}(u))\cdot\boldsymbol{\phi}\, d\mathbf{x} = \int_{\partial\mathcal{D}}\mathbf{n}\cdot\mathbb{D}(\mathbf{u})\,\mathbf{b}\, d\mathbf{x} - \int_{\mathcal{D}}\mathbb{D}(\mathbf{u}):\mathbb{D}(\mathbf{b})\, d\mathbf{x} .$$

At this point, one can rearrange (7.5) to place the source terms on the RHS:

$$\int_{\mathcal{D}}\varrho\frac{D\mathbf{u}}{Dt}\cdot\boldsymbol{\phi} + 2\mu\mathbb{D}(\mathbf{u}):\mathbb{D}(\boldsymbol{\phi}) - p\nabla\cdot\boldsymbol{\phi}\, d\mathbf{x} = -\int_{\mathcal{D}}\mathbf{F}_c\cdot\boldsymbol{\phi}\, d\mathbf{x} + \int_{\partial\mathcal{D}}\mathbf{n}\cdot\widetilde{T}\boldsymbol{\phi}\, dS .$$

Consequently, the weak formulation of Navier-Stokes is:

$$\int_{\mathcal{D}} \varrho \frac{D\mathbf{u}}{Dt} \cdot \boldsymbol{\phi} + 2\mu \mathbb{D}(\mathbf{u}) : \mathbb{D}(\boldsymbol{\phi}) - p\nabla \cdot \boldsymbol{\phi} \, d\mathbf{x} = -\int_{\mathcal{D}} \mathbf{F}_c \cdot \boldsymbol{\phi} \, d\mathbf{x} + \int_{\partial\mathcal{D}} \mathbf{n} \cdot \widetilde{T}\boldsymbol{\phi} \, dS \tag{7.7}$$

$$\int_{\mathcal{D}} \psi \nabla \cdot \mathbf{u} \, d\mathbf{x} = 0 \tag{7.8}$$

Notice that we have reduced Navier-Stokes momentum equation (7.7) to a scalar version that involves the test function $\boldsymbol{\phi}$. By choosing this test function appropriately, one can recover the weak formulation for each component of the velocity field in cylindrical coordinates:

$$\boldsymbol{\phi} = \phi \, \hat{\mathbf{r}} \quad , \quad \phi \in V \quad \rightarrow \quad \text{weak NS for } u_r \, , \tag{7.9}$$

$$\boldsymbol{\phi} = \phi \, \hat{\mathbf{k}} \quad , \quad \phi \in V \quad \rightarrow \quad \text{weak NS for } u_z \, , \tag{7.10}$$

Imposing axial symmetry about the rotation axis (7.3), equations (7.7) and (7.8) become:

$$\int_{\mathcal{D}_{axi}} \left(\varrho \frac{D\mathbf{u}}{Dt} \cdot \boldsymbol{\phi} + 2\mu \mathbb{D}(\mathbf{u}) : \mathbb{D}(\boldsymbol{\phi}) - p\nabla \cdot \boldsymbol{\phi} \right) r \, drdz = -\int_{\mathcal{D}_{axi}} \mathbf{F}_c \cdot \boldsymbol{\phi} \, r \, drdz + \int_{\partial\mathcal{D}_{axi}} \mathbf{n} \cdot \widetilde{T}\boldsymbol{\phi} \, r \, dl \, ,$$

$$\int_{\mathcal{D}_{axi}} \psi \left(\frac{\partial u_r}{\partial r} + \frac{u_r}{r} + \frac{\partial u_z}{\partial z} \right) r \, drdz = 0 \, .$$

Observe now that the decomposition (7.4) gives:

$$\int_{\partial\mathcal{D}_{axi}} \mathbf{n} \cdot \widetilde{T}\boldsymbol{\phi} \, r \, dl = -\int_{\Gamma} \mathbf{n} \cdot [\widetilde{T}] \, \boldsymbol{\phi} \, r \, dl + \int_{\Gamma_b} \mathbf{n} \cdot \widetilde{T} \, \boldsymbol{\phi} \, r \, dl \, ,$$

and from this structure, one can easily determine what function spaces are necessary so that the weak formulation is consistent. In this case, we take $p, \psi \in Q$, the velocity satisfying $\mathbf{u} \in \mathbf{V}_b$ and $\boldsymbol{\phi} \in \mathbf{V}$, where:

$$\mathbf{V} = \{ \mathbf{v} \in \mathbf{H}^1(\mathcal{D}_{axi}) \mid \mathbf{v}|_{\Gamma_b} = 0 \} \quad , \quad Q = L^2(\mathcal{D}_{axi}) \, ,$$

$$\mathbf{V}_d = \{ \mathbf{u} \in \mathbf{H}^1(\mathcal{D}_{axi}) \mid \begin{cases} u_r = 0 & , \quad \text{on } \Gamma_1^o \cup \Gamma_3^o \cup \Gamma_1^d \\ u_z = 0 & , \quad \text{on } \Gamma_2^o \cup \Gamma_4^o \cup \Gamma_2^d \end{cases} \} \, .$$

This results in:

$$\int_{\mathcal{D}_{axi}} \left(\varrho \frac{D\mathbf{u}}{Dt} \cdot \boldsymbol{\phi} + 2\mu \mathbb{D}(\mathbf{u}) : \mathbb{D}(\boldsymbol{\phi}) - p\nabla \cdot \boldsymbol{\phi} \right) r \, drdz = -\int_{\mathcal{D}_{axi}} \mathbf{F}_c \cdot \boldsymbol{\phi} \, r \, drdz - \int_{\Gamma} \mathbf{n} \cdot [\widetilde{T}] \, \boldsymbol{\phi} \, r \, dl \, , \tag{7.11}$$

$$\int_{\mathcal{D}_{axi}} r\psi \left(\frac{\partial u_r}{\partial r} + \frac{u_r}{r} + \frac{\partial u_z}{\partial z} \right) \, drdz = 0 \, , \tag{7.12}$$

from which we obtain the weak formulation for the radial component u_r by taking $\boldsymbol{\phi}$ as in (7.9) to yield:

$$\nabla \cdot \boldsymbol{\phi} = \frac{1}{r} \frac{\partial}{\partial r}(r\phi) \quad , \quad \mathbb{D}(\boldsymbol{\phi}) = \begin{pmatrix} \dfrac{\partial \phi}{\partial r} & 0 & \dfrac{1}{2}\dfrac{\partial \phi}{\partial z} \\ 0 & \dfrac{\phi}{r} & 0 \\ \dfrac{1}{2}\dfrac{\partial \phi}{\partial z} & 0 & 0 \end{pmatrix} ,$$

and (7.11) results:

$$\begin{aligned} \int_{\mathcal{D}_{axi}} \varrho \, \phi \, \frac{Du_r}{Dt} r \, drdz = & \int_{\mathcal{D}_{axi}} p \, \frac{\partial}{\partial r}(r\phi) \, drdz + \int_{\mathcal{D}_{axi}} \varrho \, \omega^2 \phi \, r^2 \, drdz - \int_{\mathcal{D}_{axi}} 2\mu \frac{\partial u_r}{\partial r} \frac{\partial \phi}{\partial r} r \, drdz - \\ & - \int_{\mathcal{D}_{axi}} \mu \frac{\partial \phi}{\partial z} \left(\frac{\partial u_r}{\partial z} + \frac{\partial u_z}{\partial r} \right) r \, drdz - \int_{\mathcal{D}_{axi}} 2\mu \frac{\phi \, u_r}{r} \, drdz - \int_{\Gamma} 2\gamma \mathcal{H} \, \phi \, r \, dl \, . \end{aligned} \tag{7.13}$$

Similarly, for the vertical component of velocity u_z, we choose $\boldsymbol{\phi}$ as in (7.10) to yield:

$$\nabla \cdot \boldsymbol{\phi} = \frac{\partial \phi}{\partial z} \quad , \quad \mathbb{D}(\boldsymbol{\phi}) = \begin{pmatrix} 0 & 0 & \frac{1}{2}\frac{\partial \phi}{\partial r} \\ 0 & 0 & 0 \\ \frac{1}{2}\frac{\partial \phi}{\partial r} & 0 & \frac{\partial \phi}{\partial z} \end{pmatrix},$$

and (7.11) transforms into:

$$\begin{aligned} \int_{\mathcal{D}_{axi}} \varrho\, \phi\, \frac{Du_z}{Dt} r\, drdz = \int_{\mathcal{D}_{axi}} p\, \frac{\partial \phi}{\partial z}\, r\, drdz - \int_{\mathcal{D}_{axi}} 2\mu \frac{\partial u_z}{\partial z}\frac{\partial \phi}{\partial z}\, r\, drdz - \\ - \int_{\mathcal{D}_{axi}} \mu \frac{\partial \phi}{\partial r}\left(\frac{\partial u_r}{\partial z} + \frac{\partial u_z}{\partial r}\right) r\, drdz - \int_{\Gamma} 2\gamma \mathcal{H}\, \phi\, r\, dl\,. \end{aligned} \tag{7.14}$$

7.3. Galerkin approximation

Now that the weak formulation has been established, and since our problem is formulated in the plane, we have to discretize the domain with a triangle mesh such that the interface of the droplet is described by some of the triangle edges defining the mesh:

$$\mathcal{D}_{axi} \approx \bigcup_{i=1}^{N_t} T_i \quad , \quad \Gamma \approx \bigcup_{i=1}^{N_b} E_i\,,$$

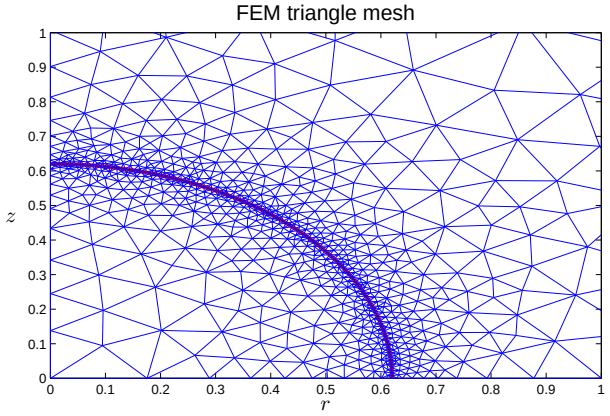

Figure 7.2: Example of a triangle mesh used to simulate drop evolution with FEM. Observe that the method approximates the drop's interface (solid red curve) with some of the triangle edges defining the mesh, making it easier to track the free-surface.

where T_i are the triangles that define the mesh, N_t the number of triangles, E_i the interface edges and N_b the number of interface edges. We also need to substitute the function spaces with finite vector spaces. In this case, the right choice is to approximate the velocity over each triangle T as a quadratic function in $P_2(T)$ and the pressure as a linear function in $P_1(T)$. This setting, called in the literature $P_2 - P_1$, is necessary to comply with the LBB (Ladyzhenskaya-Babuska-Brezzi) condition [43, 3, 10], which has to hold in order to avoid severe spatial oscillations in the pressure. These polynomial spaces give rise to the so-called Taylor-Hood triangle element, which is characterized by:

- six nodes for the radial velocity u_r, located at the vertices and the edge midpoints of the triangle.
- six nodes for the vertical velocity u_z, located at the vertices and the edge midpoints of the triangle.
- three nodes for the pressure, located at the vertices of the triangle.

For the whole triangle mesh, this configuration yields a total number of degrees of freedom of $N_{P_2} = N_v + N_e$ for each component of the velocity, where N_v is the number of mesh vertices and N_e the number of edges, and a total of $N_{P_1} = N_v$ for the pressure field. Using this node distribution, one can approximate the velocity and pressure by the expressions:

$$u_r \approx \sum_{i=1}^{N_{P_2}} \phi_i u_i \quad , \quad u_z \approx \sum_{i=1}^{N_{P_2}} \phi_i v_i \quad , \quad p \approx \sum_{i=1}^{N_{P_1}} \psi_i p_i \tag{7.15}$$

where $\{\phi_i\}_{i=1}^{N_{P_2}}$ and $\{\psi_i\}_{i=1}^{N_{P_1}}$ are families of basis functions such that:

- $\phi_i(\mathbf{x}_j) = \delta_{ij} \quad , \quad \psi_k(\mathbf{y}_l) = \delta_{kl} \quad , \quad i,j \in \{1,\dots,N_{P_2}\} \quad , \quad k,l \in \{1,\dots,N_{P_1}\}$,
- ϕ_j is quadratic over each triangle containing node $\mathbf{x}_j$ and vanishes elsewhere,
- ψ_l is linear over each triangle containing node $\mathbf{y}_l$ and vanishes elsewhere,

with $\{\mathbf{x}_j\}_{j=1}^{N_{P_2}}$ the mesh nodes for each component of the velocity and $\{\mathbf{y}_l\}_{l=1}^{N_{P_1}}$ those for the pressure. If we take as test functions $\phi = \phi_j$ and $\psi = \psi_j$ and substitute (7.15) into (7.13), (7.14) and (7.12) one gets:

$$\sum_{i=1}^{N_{P_2}}\sum_{k=1}^{N_t} u_i \int_{T_k} \psi_j \left(r\frac{\partial \phi_i}{\partial r} + \phi_i \right) \, drdz + \sum_{i=1}^{N_{P_2}}\sum_{k=1}^{N_t} v_i \int_{T_k} \frac{\partial \phi_i}{\partial z} r \, drdz = 0 \, ,$$

$$\begin{aligned}
\sum_{i=1}^{N_{P_2}}\sum_{k=1}^{N_t} \frac{Du_i}{Dt} \int_{T_k} \varrho \, \phi_i\phi_j \, r \, drdz = {} & \sum_{i=1}^{N_{P_1}}\sum_{k=1}^{N_t} p_i \int_{T_k} \psi_i \left(\phi_j + r\frac{\partial \phi_j}{\partial r} \right) \, drdz + \sum_{k=1}^{N_t} \int_{T_k} \varrho \, \omega^2 r^2 \phi_j \, drdz - \\
& - \sum_{i=1}^{N_{P_2}}\sum_{k=1}^{N_t} u_i \int_{T_k} \mu \left(2\frac{\partial \phi_i}{\partial r}\frac{\partial \phi_j}{\partial r} r + \frac{\partial \phi_i}{\partial z}\frac{\partial \phi_j}{\partial z} r + 2\frac{\phi_i\phi_j}{r} \right) \, drdz - \\
& - \sum_{i=1}^{N_{P_2}}\sum_{k=1}^{N_t} v_i \int_{T_k} \mu \frac{\partial \phi_j}{\partial z}\frac{\partial \phi_i}{\partial r} \, r \, drdz - \sum_{k=1}^{N_b} \int_{E_k} 2\gamma\mathcal{H} \, \phi_j \, r \, dl \, ,
\end{aligned}$$

$$\begin{aligned}
\sum_{i=1}^{N_{P_2}}\sum_{k=1}^{N_t} \frac{Dv_i}{Dt} \int_{T_k} \varrho \, \phi_i\phi_j \, r \, drdz = {} & \sum_{i=1}^{N_{P_1}}\sum_{k=1}^{N_t} p_i \int_{T_k} \psi_i \frac{\partial \phi_j}{\partial z} \, r \, drdz - \sum_{i=1}^{N_{P_2}}\sum_{k=1}^{N_t} u_i \int_{T_k} \mu \frac{\partial \phi_j}{\partial r}\frac{\partial \phi_i}{\partial z} r \, drdz - \\
& - \sum_{i=1}^{N_{P_2}}\sum_{k=1}^{N_t} v_i \int_{T_k} \mu \left(2\frac{\partial \phi_i}{\partial z}\frac{\partial \phi_j}{\partial z} + \frac{\partial \phi_i}{\partial r}\frac{\partial \phi_j}{\partial r} \right) r \, drdz - \sum_{k=1}^{N_b} \int_{E_k} 2\gamma\mathcal{H} \, \phi_j \, r \, dl \, ,
\end{aligned}$$

Rearranging, we can write it in matrix form:

$$\begin{aligned}
B_r^T\mathbf{u} + B_z^T\mathbf{v} &= 0 \, , \\
M_r\frac{D\mathbf{u}}{Dt} + K_{ru}\mathbf{u} + K_{rv}\mathbf{v} + B_r\mathbf{p} &= \mathbf{f} + \mathbf{g} \, , \\
M_r\frac{D\mathbf{v}}{Dt} + K_{rv}^T\mathbf{u} + K_{zv}\mathbf{v} + B_z\mathbf{p} &= \mathbf{g} \, ,
\end{aligned}$$

where:

$$(M_r)_{ji} = \sum_{k=1}^{N_t} \int_{T_k} \varrho \, \phi_i\phi_j \, r \, drdz \quad , \quad f_j = \sum_{k=1}^{N_t} \int_{T_k} \varrho \, \omega^2 r^2 \phi_j \, drdz \quad , \quad g_j = -\sum_{k=1}^{N_b} \int_{E_k} 2\gamma\mathcal{H} \, \phi_j \, r \, dl \, ,$$

$$(B_r)_{ji} = -\sum_{k=1}^{N_t} \int_{T_k} \psi_i \left(\phi_j + r\frac{\partial \phi_j}{\partial r} \right) \, drdz \quad , \quad (B_z)_{ji} = -\sum_{k=1}^{N_t} \int_{T_k} \psi_i \frac{\partial \phi_j}{\partial z} \, r \, drdz$$

$$(K_{ru})_{ji} = \sum_{k=1}^{N_t} \int_{T_k} \mu \left(2\frac{\partial \phi_i}{\partial r}\frac{\partial \phi_j}{\partial r} r + \frac{\partial \phi_i}{\partial z}\frac{\partial \phi_j}{\partial z} r + 2\frac{\phi_i\phi_j}{r} \right) \, drdz \quad , \quad (K_{rv})_{ji} = \sum_{k=1}^{N_t} \int_{T_k} \mu \frac{\partial \phi_j}{\partial z}\frac{\partial \phi_i}{\partial r} \, r \, drdz \, ,$$

$$(K_{zv})_{ji} = \sum_{k=1}^{N_t} \int_{T_k} \mu \left(2 \frac{\partial \phi_i}{\partial z} \frac{\partial \phi_j}{\partial z} + \frac{\partial \phi_i}{\partial r} \frac{\partial \phi_j}{\partial r} \right) r \, dr dz \, .$$

In general matrix form:

$$\begin{cases} M \frac{D\mathbf{w}}{Dt} + K\mathbf{w} + B\mathbf{p} = \mathbf{b} \\ B^T \mathbf{w} = 0 \end{cases} , \tag{7.16}$$

with:

$$\mathbf{w} = \begin{pmatrix} \mathbf{u} \\ \mathbf{v} \end{pmatrix} \quad , \quad M = \begin{pmatrix} M_r & 0 \\ 0 & M_r \end{pmatrix} \quad , \quad K = \begin{pmatrix} K_{ru} & K_{rv} \\ K_{rv}^T & K_{zv} \end{pmatrix} \quad , \quad \mathbf{b} = \begin{pmatrix} \mathbf{f} + \mathbf{g} \\ \mathbf{g} \end{pmatrix} \quad , \quad B = \begin{pmatrix} B_r \\ B_z \end{pmatrix} .$$

7.4. Reference triangle transformation

Since every matrix coefficient appearing in (7.16) involves the computation of an integral over a triangle, it is useful to find a tranformation that takes any triangle into the reference triangle T_R with vertices $(0,0)$, $(1,0)$ and $(0,1)$. To do so, given a triangle T with vertices at points $\mathbf{x}_1$, $\mathbf{x}_2$ and $\mathbf{x}_3$, define the mapping:

$$\Psi^{-1}(\xi, \eta) = \mathbf{x}_1 + \xi (\mathbf{x}_2 - \mathbf{x}_1) + \eta (\mathbf{x}_3 - \mathbf{x}_1) \quad , \quad \xi, \eta \in [0,1] \, .$$

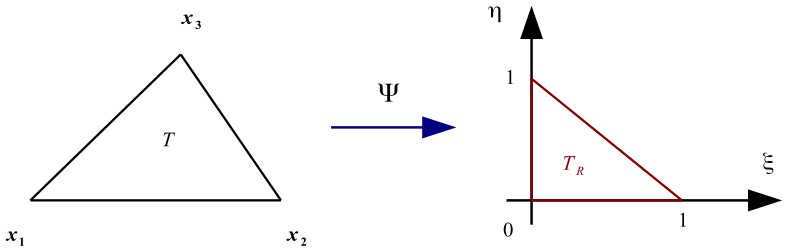

Figure 7.3: Transformation of a flat triangle T into the reference triangle T_R.

This transformation satisfies $\Psi^{-1}(T_R) = T$, and surprisingly, has a very simple jacobian:

$$J\left(\Psi^{-1}\right) = 2A_T \, ,$$

where A_T is the area of triangle T. Using this result, the integral over T of any function f has the form:

$$\int_T f(\mathbf{x}) \, dS = 2A_T \int_{T_R} F(\xi, \eta) \, d\xi d\eta \quad , \quad F = f \circ \Psi^{-1} \, .$$

We will now explain how to approximate a function over a triangle using a family of basis functions. This is motivated by the approximations considered in the previous section for the velocity field (quadratic) and the pressure (linear). First, consider a linear function $f \in P_1(T_R)$ given by:

$$f(\xi, \eta) = a\,\xi + b\,\eta + c \, .$$

Since we have three degrees of freedom, i.e. a, b and c, we have to look for a basis $\{\varphi_i\}_{i=1}^3$ satisfying:

$$\varphi_i \in P_1(T_R) \quad , \quad \forall i \in \{1,2,3\} \quad \text{and} \quad \varphi_i(\boldsymbol{\tau}_j) = \delta_{ij} \, ,$$

such that:

$$f = \sum_{i=1}^{3} f_i \varphi_i \, ,$$

where $\{\boldsymbol{\tau_i}\}_{i=1}^3$ are the three vertices of T_R, and f_i are the values of f at the three triangle vertices. From these assumptions, it is straightforward to show that the basis functions are:

$$\varphi_1 = \xi \quad , \quad \varphi_2 = \eta \quad , \quad \varphi_3 = 1 - \xi - \eta \, .$$

For the case of a quadratic function $g \in P_2(T_R)$ in the form:

$$g(\xi,\eta) = a\,\xi^2 + b\,\xi\eta + c\,\eta^2 + d\,\xi + e\,\eta + h\ ,$$

we have now six degrees of freedom, so one has find a basis $\{\varphi_i\}_{i=1}^6$ satisfying:

$$\varphi_i \in P_2(T_R) \quad , \quad \forall i \in \{1,\ldots,6\} \quad \text{and} \quad \varphi_i(\boldsymbol{\tau}_j) = \delta_{ij}\ ,$$

such that:

$$g = \sum_{i=1}^{6} g_i \varphi_i\ ,$$

where $\{\boldsymbol{\tau_i}\}_{i=1}^6$ are the vertices and edge midpoints of T_R, and g_i the values of g at those points. Using basic algebra, one finds that:

$$\varphi_1 = \xi(2\xi-1) \quad , \quad \varphi_2 = \eta(2\eta-1) \quad , \quad \varphi_3 = \zeta(2\zeta-1)\ ,$$

$$\varphi_4 = 4\xi\zeta \quad , \quad \varphi_5 = 4\xi\eta \quad , \quad \varphi_6 = 4\eta\zeta\ ,$$

where $\zeta = 1-\xi-\eta$.

7.5. Uzawa's algorithm

Before solving the linear system (7.16), we need to discretize the material derivative. This is done by creating a time-marching scheme and, in order to model the convective acceleration, the previous values of velocity $\tilde{\mathbf{w}}^n$ are found by following characteristics backwards through the flow for one time step:

$$\frac{D\mathbf{w}}{Dt} \approx \frac{\mathbf{w}^{n+1} - \tilde{\mathbf{w}}^n}{\Delta t}\ .$$

In this way, at time step $n+1$ we have:

$$\begin{cases} A\mathbf{w}^{n+1} + B\mathbf{p}^{n+1} = \mathbf{b} + M\tilde{\mathbf{w}}^n \\ B^T\mathbf{w}^{n+1} = 0 \end{cases} \quad , \quad A = M_t + K \quad , \quad M_t = \frac{M}{\Delta t}\ . \tag{7.17}$$

To solve (7.17, the code makes use of Uzawa's algorithm, where the pressure is found by iteration, adding an amount α of the divergence to the pressure value at each point. Consequently, an area in which flow sinks has its pressure increased to remove the sink and enforce continuity and, similarly, an area acting as a source has it's pressure reduced:

$$\mathbf{p}^{n+1} = \mathbf{p}^n + \alpha B^T\mathbf{w}^{n+1}\ . \tag{7.18}$$

This gives the system:

$$\left(A + \alpha BB^T\right)\mathbf{w}^{n+1} = \mathbf{b} + M\tilde{\mathbf{w}}^n - B\mathbf{p}^n\ , \tag{7.19}$$

from which $\mathbf{w}^{n+1}$ is obtained, and once solved, the pressure is calculated with (7.18).

7.6. Adaptive mesh

One of the most relevant challenges when simulating a free-surface problem is to achieve a good-qualty mesh which can adapt itself to the evolving boundary, describing with precision the domain under study. When performing mesh adaption, one has two main strategies, local re-arrangement of the mesh at each time step, or occasional complete remeshing. The FEM code that we have used adopts the first approach, and the algorithms it implements to adapt the mesh are:

- Once the velocity field is known at some time step, the interface is evolved with a Lagrangian method:

  $$\mathbf{x}^{n+1} = \mathbf{x}^n + \Delta t\ \mathbf{w}^n(\mathbf{x}^n)\ ,$$

  where $\mathbf{x}$ is the position of a vertex located at the interface and $\mathbf{w}$ is the velocity field at that point. The rest of the nodes in the mesh that do not belong to the interface are relocated using a Laplacian smoothing operator.

- The edges which are not on the interface are swapped whenever they fail Delaunay condition.
- The spatial variation of the mesh size is controlled using a length scale l_s, which specifies the intended grid size at each node. Starting with the interface vertices, the value of l_s at a point $\mathbf{q}$ on the interface is inversely proportional to the curvature value at that point:

$$l_s(\mathbf{q}) = \frac{C}{\kappa(\mathbf{q})} .$$

  For a vertex $\mathbf{q}$ outside the interface, we need to impose:

$$l_s(\mathbf{q}) \leqslant l_s(\mathbf{p}) + G\|\mathbf{q}-\mathbf{p}\| ,$$

  where G is a constant controlling the rate of change of the mesh size, and $\mathbf{p}$ represents all neighbouring points of $\mathbf{q}$. The above condition allows the mesh size to grow exponentially far from high curvature interface regions, and is thus essential to reduce the total number of vertices in the mesh, enhancing computation efficiency.
- Edge splitting/contraction to refine or coarsen the mesh. The length scale l_s^e of an edge is defined as the average of the length scales of its two vertices. The code requires that the real length l of an edge satisfies the condition:

$$r_{min} \leqslant \frac{l}{l_s^e} \leqslant r_{max} .$$

  When the ratio of lengths is below r_{min} the edge is contracted, whereas if the ratio is larger than r_{max} the edge is split. Note that splitting always produces valid meshes. If an edge on the interface is split, the code uses a local cubic spline algorithm to compute the position of the newly added vertex. For the case of edge contraction resulting in an invalid mesh, the operation is abandoned.

7.7. Numerical results

Finally, in this section we present some results to validate the FEM code explained in this chapter. To do so, we have compared a simulation using FEM with its BEM counterpart. For this, we have simulated the evolution of a rotating drop at contant angular momentum using as viscosity ratio $\lambda = 0.1$ and taking $\gamma = 1$ for the surface tension. The excellent agreement of results obtained under Stokes regime is shown below and encourages our future research, relying on the application of this method to study the effects that the nonlinear terms appearing in Navier-Stokes equations have on the evolution and stability of rotating drops.

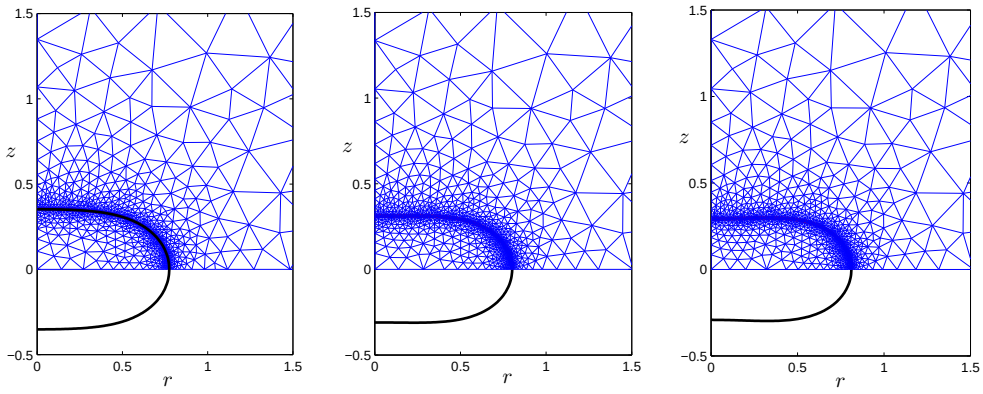

(a) $t = 0.56$. (b) $t = 1.05$. (c) $t = 2.19$.

Figure 7.4: Pictures showing the evolution of the drop's interface for three different times when rotation is at constant $L = 1.2$. The solid black curve represents the solution calculated with BEM and the triangle mesh is the solution using FEM. Observe that there is an excellent agreement of results.

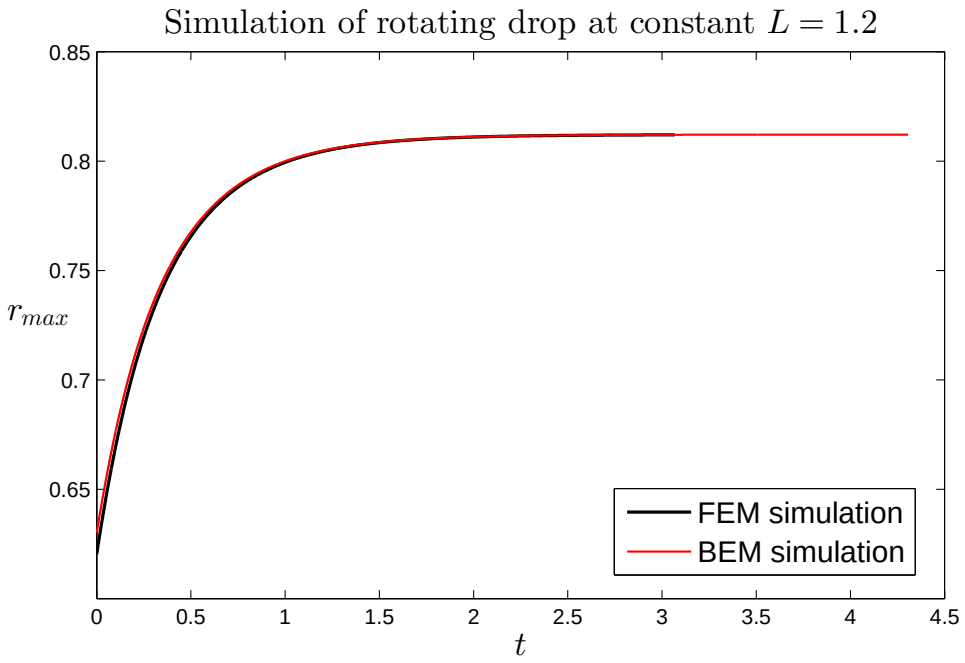

Figure 7.5: Comparison between BEM and BEM for a rotating drop at constant $L = 1.2$. In this plot we represent the time evolution of the drop's equatorial radius to show that both methods converge to the same equilibrium solution.

Chapter 8

Conclusions and future research

In this thesis we have studied the effects of rotation on the evolution of a charged drop or a neutral droplet immersed in an electric field applied in the direction of the rotation axis. For that purpose, we have developed a numerical algorithm based on the boundary integral formulation of Stokes system which is adaptive and automatically introduces local refinement in critical regions of the interface such as necks, where the drop could break up, and tips when dynamic Taylor cones develop. Based on numerical results and the analysis of the equations, we describe the effects of rotation both at constant angular speed Ω and constant angular momentum L.

First, we have studied the rotating droplet problem with no electrostatic forces, and all different regimes observed are summarized in the tables below:

Table 8.1: Evolution of axisymmetric rotating drops

Constant Ω	**C**onstant L
$\Omega < \Omega^*$ Axisymmetric equilibrium	$L < L^*$ Axisymmetric equilibrium
$\Omega > \Omega^*$ Expanding *pizza* shape	$L > L^*$ Toroidal Type II

Table 8.2: Evolution of 3D rotating drops

Constant Ω	**C**onstant L
$\Omega < \Omega_2$ Axisymmetric equilibrium	$L < L_2$ Axisymmetric equilibrium
$\Omega_2 < \Omega < \Omega_{ap}$ Elongating filament	$L_2 < L < L_2^*$ stable *peanut* shape
$\Omega_{ap} < \Omega < \Omega_{sp}$ Asymmetric expanding *pizza* shape	$L_2^* < L < L_3^*$ Breakup (2-fold)
$\Omega > \Omega_{sp}$ Axisymmetric expanding *pizza* shape	$L > L_3^*$ Breakup (3-fold)

These transition values, which appear in chapters 5 and 6, were determined numerically and, in particular, those related to 3D evolution were obtained when the drop and the surrounding fluid have the same viscosity. When rotation is at constant angular momentum and axial symmetry is imposed, the approach to toroidal type II solutions for $L > L^*$ occurs at a $O(t^{-1/2})$ rate and the interface profiles present self-similar behaviour. Breakup for 3D evolution is via an axisymmetric similarity profile of the type described by Lister and Stone [45] and Cohen et al. [16]. For rotation at constant angular speed, when elongating filaments develop, they reach an infinite length in finite time and their length blows up like $O((t_0 - t)^{-1/2})$ with the interface profile approaching an explicit self-similar solution. Finally, we find that the radius of axisymmetric expanding *pizza* shapes grows like $O((t_0 - t)^{-1/2})$ as shown by Howell et al. [37].

After describing the evolution of rotating drops, we have studied the effects of rotation on the evolution and equilibrium shapes of a conducting and viscous droplet immersed in another viscous and insulating fluid. For charged rotating drops at constant angular momentum, two theoretical methods are presented to calculate stationary solutions, one based on asymptotic expansions and the other on spheroidal approximations that minimize the energy. Numerical data combined with these models shows that when rotation is present, a rupture of the bifurcation point attained by the family of charged non-rotating drops occurs. Concerning the stability of charged rotating drops, for each value of the angular momentum there exists a range of values for the charge for which solutions are stable to non-symmetric perturbations. Over this critical value for the

charge, a family of ellipsoidal solutions branches and extends until a second critical value is reached, where singularity behaviours such as dynamic Taylor cones or two-lobed drop breakup appear. An important consequence that can be drawn from simulations is that rotating drops can hold less charge (below Rayleigh's limit) than non-rotating ones before becoming unstable. When we consider conducting neutral drops rotating with constant angular momentum and subject to a uniform electric field parallel to the rotation axis, oblate and prolate-like spheroidal solutions are obtained. In this case, numerical experiments indicate that equilibrium solutions with the same aspect ratio are linearly related in the $\left(L^2, E_\infty^2\right)$ diagram. These simulations determine a curve in the (L, E_∞) plane defining the stability limit for equilibrium configurations which eventually turns back on itself. Our analysis concludes from this curve that rotating drops show more stability to higher values of the electric field strength, unless the angular momentum becomes very high and penalizes stability instead of contributing to it. Additionally, a transition curve between spheroidal and ellipsoildal-like solutions is computed numerically. Finally, we have measured the opening semiangle obtained when dynamic Taylor cones develop to find that it remains the same as the ones corresponding to the system without rotation, provided that the angular momentum is small.

Many questions arise for further research concerning charged and rotating droplets under the influence of an electric field. Among them, our interest focuses on the description of the (χ, E_∞) diagram under the pressence of the drop's angular momentum and the role that rotation plays in the overall stability of this complex system.

Another important point concerns the contribution of inertial terms from Navier-Stokes equations when the Reynolds and Ekman numbers take any possible value and the way they influence evolution and stability. These issues will be the aim of future work to come with the FEM code introduced in this thesis.

Chapter 9

Conclusiones y trabajo futuro

En esta tesis hemos estudiado los efectos de la rotación sobre la evolución de una gota cargada ó de una gota neutra inmersa en un campo eléctrico externo aplicado en la dirección del eje de giro. Con este propósito, hemos desarrollado un algoritmo numérico basado en la formulación integral de contorno de la ecuación de Stokes, que es adaptativo e introduce de manera automática refinamiento local en las regiones críticas de la interfase como son los cuellos, donde la gota puede romperse, y las puntas cuando se desarrollan conos dinámicos de Taylor. Basándonos en resultados numéricos y en el análisis de las ecuaciones, describimos los efectos de la rotación tanto a velocidad angular constante Ω como a momento angular constante L.

Primero, hemos estudiado el problema de una gota sometida a rotación sin fuerzas electrostáticas, y todos los regímenes encontrados están resumidos en las tablas abajo presentadas:

Table 9.1: Evolución de gotas rotantes axialmente simétricas

Ω **c**onstante	L **c**onstante
$\Omega < \Omega^*$ Axisymmetric equilibrium	$L < L^*$ Axisymmetric equilibrium
$\Omega > \Omega^*$ Expanding *pizza* shape	$L > L^*$ Toroidal Type II

Table 9.2: Evolución de gotas rotantes en 3D

Ω **c**onstante	L **c**onstante
$\Omega < \Omega_2$ Axisymmetric equilibrium	$L < L_2$ Axisymmetric equilibrium
$\Omega_2 < \Omega < \Omega_{ap}$ Elongating filament	$L_2 < L < L_2^*$ stable *peanut* shape
$\Omega_{ap} < \Omega < \Omega_{sp}$ Asymmetric expanding *pizza* shape	$L_2^* < L < L_3^*$ Breakup (2-fold)
$\Omega > \Omega_{sp}$ Axisymmetric expanding *pizza* shape	$L > L_3^*$ Breakup (3-fold)

Los valores de transición presentados, que aparecen en los capítulos 5 y 6, han sido determinados numéricamente y, en particular, aquellos relacionados a la evolución en 3D, se han obtenido considerando que la gota y el fluido que la envuelve tienen la misma viscosidad. Cuando la rotación tiene lugar a momento angular constante e imponemos simetría axial al problema, la formación de soluciones toroidales de tipo II para $L > L^*$ ocurre a un ritmo $O(t^{-1/2})$ y los perfiles de la interfase presentan comportamiento autosimilar. La ruptura que sucede para evoluciones en 3D es vía un perfil axisimétrico autosimilar del tipo descrito por Lister y Stone [45] y Cohen et al. [16]. Por otro lado, si la rotación es a velocidad angular constante, en el caso de que se desarrollen filamentos que se elongan, éstos alcanzan una longitud infinita en tiempo finito que explota como $O((t_0 - t)^{-1/2})$ con el perfil de la interfase aproximándose a una solución explícita autosimilar. Finalmente, encontramos que el radio de las formas de equilibrio axisimétricas de tipo *pizza* crece como $O((t_0 - t)^{-1/2})$, en acuerdo con lo mostrado por Howell et al. [37].

Después de describir la evolución de gotas en rotación, hemos estudiado los efectos que tiene la rotación sobre la evolución y las formas de equilibrio de una gota viscosa y conductora contenida en otro fluido viscoso y aislante. Para gotas cargdas rotando a momento angular constante, dos métodos teóricos han sido presentados para calcular soluciones estacionarias, uno basado en expansiones asintóticas y el otro en aproximar las soluciones por esferoides que minimizan la energía. Los datos numéricos combinados con estos métodos muestran que cuando el sistema está girando, se produce una ruptura del punto de bifurcación alcanzado por

la familia de gotas cargadas sin rotación. En relación a la estabilidad de gotas cargadas en rotación, para cada valor del momento angular existe un rango de valores para la carga para el cual las soluciones son estables ante perturbaciones asimétricas. Por encima de este valor de la carga, una familia de soluciones elipsoidales se ramifica y extiende hasta alcanzar un segundo valor crítico de la carga, donde aparecen comportamientos singulares como la formación de conos dinámicos de Taylor ó tiene lugar la formación de dos lóbulos (un cuello) con su posterior ruptura. Una consecuencia importante que puede deducirse de las simulaciones es que una gota rotando puede almacenar menos carga antes de volverse inestables (por debajo del límite de Rayleigh) que gotas no sometidas a rotación. Cuando consideramos una gota neutra rotando a momento angular constante y sometida a un campo eléctrico paralelo al eje de giro, obtenemos soluciones de equilibrio aproximadamente esferoidales de tipo oblato y prolato. En este caso, los experimentos numéricos muestran que las soluciones de equilibrio con el mismo ratio de semiejes están linealmente relacionadas en el diagrama $\left(L^2, E_\infty^2\right)$. Estas soluciones también nos determinan una curva en el plano (L, E_∞) que define el límite de estabilidad para configuraciones de equilirio y que, eventualmente, alcanza un punto de inflexión donde vuelve sobre sí misma. Nuestro análisis concluye de esta curva que una gota rotando muestra más estabilidad para valores mayores de la intensidad del campo eléctrico, a menos de que el momento angular sea suficientemente grande, pasando a penalizar la estabilidad en lugar de contribuir a ella. Además, una curva de transición entre las soluciones esferoidales y elipsoidales es determinada numéricamente. Finalmente, hemos analizado el semiángulo de apertura obtenido para los conos de Taylor dinámicos y mostramos que, siempre que el momento angular sea pequeño, éste permanece igual que en el caso en el que el sistema no está rotando.

Muchas preguntas surgen para trabajos futuros en relación a gotas cargadas en rotación bajo la influencia de campos eléctricos. Entre ellas, nuestro interés se centra en la descripción del diagrama (χ, E_∞) bajo la influencia del momento angular de la gota y el papel que la rotación juega en la estabilidad global de este sistema complejo.

Otro punto importante involucra la contribución de los términos inerciales de las ecuaciones de Navier-Stokes cuando los números de Reynolds y Ekman toman cualquier posible valor, y la forma en la que éstos influyen en la evolución y la estabilidad. Estas cuestiones serán el objeto de futuras investigaciones con el código de elementos finitos presentado en esta tesis.

Appendix A

Fourier transforms

When one deals with a problem formulated in terms of linear PDEs, the Fourier transform is a powerful mathematical tool that can transform systems of PDEs into a linear system of algebraic equations. In this appendix we will describe some of its properties, which are important in this thesis to obtain the fundamental solutions for Stokes equation. Throughout this work we make use of *Einstein's summation convention* to abbreviate formulas. This notation states that, if a subscript appears twice in an expression involving products, then summation over that subscript is implied in its range.

Definition A.1. *Given a function $f : \mathbb{R}^n \to \mathbb{C}$, the Fourier transform of f is:*

$$\mathcal{F}(f)(\boldsymbol{\xi}) \equiv \widehat{f}(\boldsymbol{\xi}) = \frac{1}{(2\pi)^{\frac{n}{2}}} \int_{\mathbb{R}^n} f(\mathbf{x})\, e^{-i\,\boldsymbol{\xi}\cdot\mathbf{x}}\, d\mathbf{x} \;\;,\;\; \boldsymbol{\xi} \in \mathbb{R}^n \;,$$

whenever this integral converges.

Observe that this definition is subject to convergence issues. These difficulties can be tackled by considering the largest family of functions which ensures convergence, namely *rapidly decreasing functions*, or more accurately, *Schwartz test functions*. In what follows, we will suppose that the integral is always convengent. Notice also that by linearity of the integral, the Fourier transform is a linear operator. Together with the Fourier transform of a function we have the inverse operation:

Definition A.2. *Given a function $g : \mathbb{R}^n \to \mathbb{C}$, the inverse Fourier transform of g is:*

$$\mathcal{F}^{-1}(g)(\mathbf{x}) \equiv \breve{g}(\mathbf{x}) = \frac{1}{(2\pi)^{\frac{n}{2}}} \int_{\mathbb{R}^n} g(\boldsymbol{\xi})\, e^{\,i\,\boldsymbol{\xi}\cdot\mathbf{x}}\, d\boldsymbol{\xi} \;\;,\;\; \mathbf{x} \in \mathbb{R}^n \;,$$

whenever this integral converges.

It is clear that the inverse transform is also a linear operator. The numerical factors $(2\pi)^{-\frac{n}{2}}$ introduced in the expressions for the Fourier transform and its inverse are chosen so that the *Inversion Theorem* holds:

Theorem A.1 (Inversion Theorem)**.** *Given a function $f : \mathbb{R}^n \to \mathbb{C}$, it satisfies:*

$$\mathcal{F}^{-1}(\mathcal{F}(f)) = \mathcal{F}\left(\mathcal{F}^{-1}(f)\right) = f \;.$$

From the structure of the Fourier transform operator one can derive a very useful property:

Proposition A.1. *Given a function $f : \mathbb{R}^n \to \mathbb{R}$, we have:*

$$\mathcal{F}\left(\frac{\partial f}{\partial x_j}\right)(\boldsymbol{\xi}) = i\xi_j \mathcal{F}(f)(\boldsymbol{\xi}) \;.$$

Proof. Applying integration by parts we get:

$$\begin{aligned}\mathcal{F}\left(\frac{\partial f}{\partial x_j}\right)(\boldsymbol{\xi}) &= \frac{1}{(2\pi)^{\frac{n}{2}}} \int_{\mathbb{R}^n} \frac{\partial f}{\partial x_j}(\mathbf{x})\, e^{-i\,\boldsymbol{\xi}\cdot\mathbf{x}}\, d\mathbf{x} = -\frac{1}{(2\pi)^{\frac{n}{2}}} \int_{\mathbb{R}^n} f(\mathbf{x})\, \frac{\partial}{\partial x_j}\left(e^{-i\,\boldsymbol{\xi}\cdot\mathbf{x}}\right)\, d\mathbf{x} = \\ &= \frac{i\xi_j}{(2\pi)^{\frac{n}{2}}} \int_{\mathbb{R}^n} f(\mathbf{x})\, e^{-i\,\boldsymbol{\xi}\cdot\mathbf{x}}\, d\mathbf{x} = i\xi_j \mathcal{F}(f)(\boldsymbol{\xi}) \;.\end{aligned}$$

■

Using above proposition and the linearity of the Fourier transform one can easily prove:

Proposition A.2. *Given a function* $\mathbf{f} : \mathbb{R}^n \to \mathbb{R}^m$*, the following are true:*

1. $\mathcal{F}(\Delta \mathbf{f})(\boldsymbol{\xi}) = -\|\boldsymbol{\xi}\|^2 \mathcal{F}(\mathbf{f})(\boldsymbol{\xi})$,
2. $\mathcal{F}\left(\Delta^2 \mathbf{f}\right)(\boldsymbol{\xi}) = \|\boldsymbol{\xi}\|^4 \mathcal{F}(\mathbf{f})(\boldsymbol{\xi})$,
3. $\mathcal{F}(\nabla \cdot \mathbf{f})(\boldsymbol{\xi}) = i\boldsymbol{\xi} \cdot \mathcal{F}(\mathbf{f})(\boldsymbol{\xi})$,

where $\mathcal{F}(\mathbf{f}) = \mathcal{F}(f_k)\,\mathbf{e}_k$*,* Δ^2 *is the biharmonic operator and* $\boldsymbol{\xi} = \xi_j \mathbf{e}_j$*.*

Proof. To prove 1 apply Proposition A.1 twice:

$$\mathcal{F}(\Delta \mathbf{f})(\boldsymbol{\xi}) = \mathcal{F}\left(\frac{\partial^2 f_k}{\partial x_j^2}\right)(\boldsymbol{\xi})\,\mathbf{e}_k = i\xi_j \mathcal{F}\left(\frac{\partial f_k}{\partial x_j}\right)(\boldsymbol{\xi})\,\mathbf{e}_k = -\xi_j^2 \mathcal{F}(f_k)(\boldsymbol{\xi})\,\mathbf{e}_k = -\|\boldsymbol{\xi}\|^2 \mathcal{F}(\mathbf{f})(\boldsymbol{\xi}) \ .$$

For property 2 it suffices to apply property 1 twice. Finally, for 3 we have:

$$\mathcal{F}(\nabla \cdot \mathbf{f})(\boldsymbol{\xi}) = \mathcal{F}\left(\frac{\partial f_j}{\partial x_j}\right)(\boldsymbol{\xi}) = i\xi_j \mathcal{F}(f_j)(\boldsymbol{\xi}) = i\boldsymbol{\xi} \cdot \mathcal{F}(\mathbf{f})(\boldsymbol{\xi}) \ .$$

■

Appendix B

Fundamental solutions

In this appendix we will calculate the fundamental solutions (or Green's functions) for the Laplace and biharmonic equations using Fourier transforms. Alternatively, we will calculate these solutions by imposing radial symmetry and solving the equation in spherical coordinates by standard integration.

B.1. Laplace problem

We want to solve Laplace equation:

$$(\mathcal{P}_{\mathcal{L}}) \quad -\Delta u = f \ , \ \text{in } \mathbb{R}^n \ , \tag{B.1}$$

where $u : \mathbb{R}^n \to \mathbb{R}$ is a scalar function that can represent a stationary distribution of temperatures and f is a source term. To calculate the fundamental solutions we will suppose that we have a point force acting on $\mathbf{x}_0 \in \mathbb{R}^n$, that can be modeled by a Dirac's delta at that point:

$$\left(\mathcal{P}_{\mathcal{L}}^{\mathcal{F}}\right) \quad -\Delta u = \delta_{\mathbf{x}_0} \ , \ \text{in } \mathbb{R}^n \ , \tag{B.2}$$

Taking transforms on both sides:

$$\|\boldsymbol{\xi}\|^2 \mathcal{F}(u)(\boldsymbol{\xi}) = \frac{e^{-i\,\boldsymbol{\xi}\cdot\mathbf{x}_0}}{(2\pi)^{\frac{n}{2}}} \ , \ \boldsymbol{\xi} \in \mathbb{R}^n \ ,$$

obtaining:

$$\mathcal{F}(u)(\boldsymbol{\xi}) = \frac{e^{-i\,\boldsymbol{\xi}\cdot\mathbf{x}_0}}{(2\pi)^{\frac{n}{2}}\|\boldsymbol{\xi}\|^2} \ .$$

Now, taking the inverse transform:

$$u(\mathbf{x}) = \frac{1}{(2\pi)^n}\int_{\mathbb{R}^n} \frac{e^{i\,\boldsymbol{\xi}\cdot\hat{\mathbf{x}}}}{\|\boldsymbol{\xi}\|^2}\, d\boldsymbol{\xi} \quad , \quad \hat{\mathbf{x}} = \mathbf{x} - \mathbf{x}_0 \ , \tag{B.3}$$

which is a formula for the solution. In particular, when $n = 3$ the fundamental solution has the form:

$$u(\mathbf{x}) = \frac{1}{(2\pi)^3}\int_{\mathbb{R}^3} \frac{e^{i\,\boldsymbol{\xi}\cdot(\mathbf{x}-\mathbf{x}_0)}}{\|\boldsymbol{\xi}\|^2}\, d\boldsymbol{\xi} \ ,$$

To solve this integral we change to spherical coordinates and suppose that our reference frame is chosen so that $\hat{\mathbf{x}}$ coincides with the z axis (this is possible because the laplacian operator is invariant under rotations). We have then:

$$\boldsymbol{\xi} = \begin{cases} \xi_x = r\sin\theta\cos\phi \\ \xi_y = r\sin\theta\sin\phi \\ \xi_z = r\cos\theta \end{cases} \quad , \quad \hat{\mathbf{x}} = \begin{cases} \hat{x} = 0 \\ \hat{y} = 0 \\ \hat{z} = \|\hat{\mathbf{x}}\| \end{cases} \ .$$

giving:

$$u(\mathbf{x}) = \frac{1}{(2\pi)^3}\int_{\mathbb{R}^3}\frac{e^{\,i\,\boldsymbol{\xi}\cdot\hat{\mathbf{x}}}}{\|\boldsymbol{\xi}\|^2}\,d\boldsymbol{\xi} = \frac{1}{(2\pi)^2}\int_0^\pi\int_0^\infty e^{\,i\,r\cos\theta\|\hat{\mathbf{x}}\|}\sin\theta\;dr\;d\theta = \frac{1}{(2\pi)^2\|\hat{\mathbf{x}}\|}\int_0^\pi\int_0^\infty e^{\,i\,v\cos\theta}\sin\theta\;dv\;d\theta$$
$$= \frac{1}{(2\pi)^2\|\hat{\mathbf{x}}\|}\int_0^\infty\int_{-1}^1 e^{\,ivw}\,dw\,dv = \frac{1}{(2\pi)^2\|\hat{\mathbf{x}}\|}\int_0^\infty\left(\frac{e^{iv}-e^{-iv}}{iv}\right)dv = \frac{1}{2\pi^2\|\hat{\mathbf{x}}\|}\int_0^\infty\frac{\sin v}{v}\,dv = \frac{1}{4\pi\|\hat{\mathbf{x}}\|}\,,$$

which is the fundamental solution for (B.1) in $\mathbb{R}^3$.

An alternative way to compute the fundamental solutions for Laplace equation is writing the laplacian and Dirac's delta in spherical coordinates and integrate the resulting differential equation. For $\mathbb{R}^3$ we have:

$$\Delta u = \frac{1}{r^2}\frac{\partial}{\partial r}\left(r^2\frac{\partial u}{\partial r}\right) + \frac{1}{r^2\sin\theta}\frac{\partial}{\partial\theta}\left(\sin\theta\frac{\partial u}{\partial\theta}\right) + \frac{1}{r^2\sin^2\theta}\frac{\partial^2 u}{\partial\varphi^2} \quad , \quad \delta_{\mathbf{x}_0}(\mathbf{x}) = \frac{\delta(r)}{4\pi r^2}\,,$$

with $r = \|\hat{\mathbf{x}}\|$. Imposing that u is radially symmetric, $\dfrac{\partial u}{\partial\varphi} = \dfrac{\partial u}{\partial\theta} = 0$, one gets:

$$\Delta u = \frac{1}{r^2}\frac{\partial}{\partial r}\left(r^2\frac{\partial u}{\partial r}\right)\,,$$

and thus (B.2) yields:

$$-\frac{1}{r^2}\frac{\partial}{\partial r}\left(r^2\frac{\partial u}{\partial r}\right) = \frac{\delta(r)}{4\pi r^2} \quad \Leftrightarrow \quad \frac{\partial}{\partial r}\left(r^2\frac{\partial u}{\partial r}\right) = -\frac{\delta(r)}{4\pi}\,.$$

Integrating:

$$r^2\frac{\partial u}{\partial r} = -\frac{1}{4\pi}\int\delta(r)\;dr + C_1 = -\frac{1}{4\pi} + C_1 \quad \Leftrightarrow \quad \frac{\partial u}{\partial r} = -\frac{1}{4\pi r^2} + \frac{C_1}{r^2} \quad \Leftrightarrow \quad u = \frac{1}{4\pi r} + \frac{C_2}{r} + C_3\,.$$

To finish, we show that $C_1 = 0$. Integrating (B.2) in $\Omega = B_\varepsilon(\mathbf{x}_0)$ we obtain:

$$\int_\Omega \Delta u\;d\mathbf{x} = -\int_\Omega \delta_{\mathbf{x}_0}\;d\mathbf{x} = -1$$

and by applying the divergence theorem:

$$\int_\Omega \Delta u\;d\mathbf{x} = \int_{\partial\Omega}\nabla u\cdot\mathbf{n}\;dS \underset{\substack{\underline{\text{Spherical coordinates:}}\\ \nabla u = \dfrac{\partial u}{\partial r}\hat{\mathbf{r}}\;,\;\mathbf{n}=\hat{\mathbf{r}}}}{=} \int_{\partial\Omega}\frac{\partial u}{\partial r}\;dS = \frac{\partial u}{\partial r}\Big|_{r=\varepsilon}\int_{\partial\Omega}\;dS = 4\pi\varepsilon^2\frac{\partial u}{\partial r}\Big|_{r=\varepsilon}\,.$$

Now:

$$\frac{\partial u}{\partial r}\Big|_{r=\varepsilon} = -\frac{1}{4\pi\varepsilon^2} + \frac{C_1}{\varepsilon^2}\,,$$

and then:

$$-1 = -1 + 4\pi C_1 \quad \Rightarrow \quad C_1 = 0\,.$$

Consequently, if we take $C_3 = 0$, the fundamental solution for (B.1) in $\mathbb{R}^3$ is:

$$u(\mathbf{x}) = \frac{1}{4\pi\|\hat{\mathbf{x}}\|}\,.$$

B.2. The biharmonic equation

Now we move to deriving the fundamental solution for the biharmonic equation:

$$(\mathcal{P}_{\mathcal{H}}) \quad -\Delta^2 u = f \quad , \quad \text{in } \mathbb{R}^3\,,$$

which can be done by considering the singularly forced problem:

$$\left(\mathcal{P}_{\mathcal{H}}^{\mathcal{F}}\right) \quad -\Delta^2 u = \delta_{\mathbf{x}_0} \quad , \quad \text{in } \mathbb{R}^3\,. \tag{B.4}$$

The biharmonic operator is defined as:

$$\Delta^2 u = \Delta\left(\Delta u\right) = \frac{\partial^4 u}{\partial x_j^2 \partial x_k^2} \ ,$$

and in spherical coordinates, for a radially symmetric function, it has the form:

$$\Delta^2 u = \frac{1}{r^2}\frac{\partial}{\partial r}\left(r^2 \frac{\partial}{\partial r}\left(\frac{1}{r^2}\frac{\partial}{\partial r}\left(r^2 \frac{\partial u}{\partial r}\right)\right)\right) \quad , \quad r = \|\hat{\mathbf{x}}\| \ .$$

Integrating this expression one gets:

$$u = \frac{A}{2}r + \frac{B}{6}r^2 + \frac{C}{r} + D \ .$$

Now, integrating (B.4) over a ball of radius a centered at the singularity $\mathbf{x}_0$ we obtain:

$$\int_{B_a(\mathbf{x}_0)} \Delta^2 u \ d\mathbf{x} = -\int_{B_a(\mathbf{x}_0)} \delta_{\mathbf{x}_0} \ d\mathbf{x} = -1 \ .$$

Since:

$$\Delta^2 u = \nabla \cdot \left(\nabla \Delta u\right) \ ,$$

then by applying the divergence theorem:

$$\int_{B_a(\mathbf{x}_0)} \Delta^2 u \ d\mathbf{x} = \int_{\partial B_a(\mathbf{x}_0)} \nabla \Delta u \cdot \mathbf{n} \ dS \underset{\mathbf{n}\,=\,\hat{\mathbf{r}}}{=} \int_{\partial B_a(\mathbf{x}_0)} \frac{\partial}{\partial r}\left(\Delta u\right) \ dS = -1 \ .$$

But:

$$\Delta u = \frac{1}{r^2}\frac{\partial}{\partial r}\left(r^2 \frac{\partial u}{\partial r}\right) \quad , \quad \Delta r = \frac{2}{r} \quad , \quad \Delta\left(r^2\right) = 6 \quad , \quad \Delta\left(\frac{1}{r}\right) = 0 \ ,$$

and so:

$$\int_{\partial B_a(\mathbf{x}_0)} \frac{\partial}{\partial r}\left(\Delta u\right) \ dS = -\int_{\partial B_a(\mathbf{x}_0)} \frac{A}{r^2} dS = -4\pi A = -1 \ ,$$

which gives:

$$A = \frac{1}{4\pi} \ .$$

By setting $B = C = D = 0$, the fundamental solution to (B.4) is:

$$u\left(\mathbf{x}\right) = \frac{\|\hat{\mathbf{x}}\|}{8\pi} \ .$$

Appendix C

Maxwell stress tensor

This part of the appendix is dedicated to deriving Maxwell stress tensor, which measures the force per unit area (pressure) experienced by a charged object subject to an electromagnetic field. In particular, we will obtain at the end of this section its expression for a perfectly conducting material. We know that Maxwell's equations are:

$$\begin{cases} \nabla \cdot \mathbf{E} = \dfrac{\rho}{\varepsilon_0} \\ \nabla \cdot \mathbf{B} = 0 \\ \nabla \times \mathbf{E} = -\dfrac{\partial \mathbf{B}}{\partial t} \\ \nabla \times \mathbf{B} = \mu_0 \mathbf{j} + \mu_0 \varepsilon_0 \dfrac{\partial \mathbf{E}}{\partial t} \end{cases} , \tag{C.1}$$

where $\mathbf{E}$ amd $\mathbf{B}$ are respectively the electric and magnetic fields, ρ is the volume charge density, $\mathbf{j}$ is the volume current density, ε_0 is the permittivity of free space and μ_0 the permeability of free space. We also know that the Lorentz force acting on a test charge q moving with velocity $\mathbf{v}$ is given by:

$$\mathbf{F} = q\left(\mathbf{E} + \mathbf{v} \times \mathbf{B}\right) ,$$

so introducing the definitions of $q = \rho\, dV$ and $\mathbf{j} = \rho \mathbf{v}$ for an infinitesimal volume of charge we have:

$$\mathbf{F}_{lorentz} = \left(\rho \mathbf{E} + \mathbf{j} \times \mathbf{B}\right) dV \quad , \quad \mathbf{f} = \frac{\mathbf{F}_{lorentz}}{dV} ,$$

with $\mathbf{f}$ the Lorentz force per unit volume. Now, expanding this force using (C.1) one gets:

$$\begin{aligned} \mathbf{f} = \rho \mathbf{E} + \mathbf{j} \times \mathbf{B} = \varepsilon_0 \left(\nabla \cdot \mathbf{E}\right) \mathbf{E} + \left(\frac{\nabla \times \mathbf{B}}{\mu_0} - \varepsilon_0 \frac{\partial \mathbf{E}}{\partial t}\right) \times \mathbf{B} = \\ = \varepsilon_0 \left(\nabla \cdot \mathbf{E}\right) \mathbf{E} + \frac{1}{\mu_0} \left(\nabla \times \mathbf{B}\right) \times \mathbf{B} - \varepsilon_0 \frac{\partial \mathbf{E}}{\partial t} \times \mathbf{B} . \end{aligned}$$

Using that $\mathbf{B}$ is solenoidal ($\nabla \cdot \mathbf{B} = 0$) and the vector calculus identity:

$$\left(\nabla \times \mathbf{B}\right) \times \mathbf{B} = \left(\mathbf{B} \cdot \nabla\right) \mathbf{B} - \frac{1}{2} \nabla \left\|\mathbf{B}\right\|^2 , \tag{C.2}$$

then:

$$\begin{aligned} \mathbf{f} = \varepsilon_0 \left(\nabla \cdot \mathbf{E}\right) \mathbf{E} + \frac{1}{\mu_0} \left(\left(\mathbf{B} \cdot \nabla\right) \mathbf{B} + \left(\nabla \cdot \mathbf{B}\right) \mathbf{B}\right) - \frac{1}{2\mu_0} \nabla \left\|\mathbf{B}\right\|^2 - \varepsilon_0 \frac{\partial \mathbf{E}}{\partial t} \times \mathbf{B} = \\ = \varepsilon_0 \left(\nabla \cdot \mathbf{E}\right) \mathbf{E} + \frac{1}{\mu_0} \left(\left(\mathbf{B} \cdot \nabla\right) \mathbf{B} + \left(\nabla \cdot \mathbf{B}\right) \mathbf{B}\right) - \frac{1}{2\mu_0} \nabla \left\|\mathbf{B}\right\|^2 - \varepsilon_0 \frac{\partial}{\partial t} \left(\mathbf{E} \times \mathbf{B}\right) + \varepsilon_0 \mathbf{E} \times \frac{\partial \mathbf{B}}{\partial t} . \end{aligned}$$

Using the definition of the Poynting vector:

$$\mathbf{S} = \frac{\mathbf{E} \times \mathbf{B}}{\mu_0} , \tag{C.3}$$

and Maxwell's equations:

$$\mathbf{f} = \varepsilon_0 \left(\nabla \cdot \mathbf{E}\right) \mathbf{E} + \frac{1}{\mu_0} \left(\left(\mathbf{B} \cdot \nabla\right) \mathbf{B} + \left(\nabla \cdot \mathbf{B}\right) \mathbf{B} - \frac{1}{2} \nabla \left\|\mathbf{B}\right\|^2 \right) - \varepsilon_0 \mu_0 \frac{\partial \mathbf{S}}{\partial t} - \varepsilon_0 \mathbf{E} \times \left(\nabla \times \mathbf{E}\right) \ .$$

Applying (C.2) we have:

$$\mathbf{f} = \varepsilon_0 \left(\left(\mathbf{E} \cdot \nabla\right) \mathbf{E} + \left(\nabla \cdot \mathbf{E}\right) \mathbf{E} - \frac{1}{2} \nabla \left\|\mathbf{E}\right\|^2 \right) + \frac{1}{\mu_0} \left(\left(\mathbf{B} \cdot \nabla\right) \mathbf{B} + \left(\nabla \cdot \mathbf{B}\right) \mathbf{B} - \frac{1}{2} \nabla \left\|\mathbf{B}\right\|^2 \right) - \varepsilon_0 \mu_0 \frac{\partial \mathbf{S}}{\partial t} \ .$$

Now, an arbitrary vector field $\mathbf{A}$ satisfies:

$$\left(\nabla \cdot \mathbf{A}\right) \mathbf{A} + \left(\mathbf{A} \cdot \nabla\right) \mathbf{A} = A_i \frac{\partial A_j}{\partial x_j} + A_j \frac{\partial A_i}{\partial x_j} = \frac{\partial}{\partial x_j} \left(A_i A_j\right) = \nabla \cdot \left(\mathbf{A} \otimes \mathbf{A}\right) \ ,$$

so:

$$\mathbf{f} = \varepsilon_0 \left(\nabla \cdot \left(\mathbf{E} \otimes \mathbf{E}\right) - \frac{1}{2} \nabla \left\|\mathbf{E}\right\|^2 \right) + \frac{1}{\mu_0} \left(\nabla \cdot \left(\mathbf{B} \otimes \mathbf{B}\right) - \frac{1}{2} \nabla \left\|\mathbf{B}\right\|^2 \right) - \varepsilon_0 \mu_0 \frac{\partial \mathbf{S}}{\partial t} \ .$$

Finally, we can write for a given vector field that:

$$\nabla \left(\left\|\mathbf{E}\right\|^2 \right) = \nabla \cdot \left(\left\|\mathbf{E}\right\|^2 \mathbb{I} \right) \ ,$$

where $\mathbb{I}$ is the identity tensor, resulting in:

$$\mathbf{f} = \varepsilon_0 \nabla \cdot \left(\mathbf{E} \otimes \mathbf{E} - \frac{1}{2} \left\|\mathbf{E}\right\|^2 \mathbb{I} \right) + \frac{1}{\mu_0} \nabla \cdot \left(\mathbf{B} \otimes \mathbf{B} - \frac{1}{2} \left\|\mathbf{B}\right\|^2 \mathbb{I} \right) - \varepsilon_0 \mu_0 \frac{\partial \mathbf{S}}{\partial t} \ .$$

Defining Maxwell stress tensor as:

$$\mathbb{T}_M = \varepsilon_0 \left(\mathbf{E} \otimes \mathbf{E} - \frac{1}{2} \left\|\mathbf{E}\right\|^2 \mathbb{I} \right) + \frac{1}{\mu_0} \left(\mathbf{B} \otimes \mathbf{B} - \frac{1}{2} \left\|\mathbf{B}\right\|^2 \mathbb{I} \right) \ , \tag{C.4}$$

then the force per unit volume is:

$$\mathbf{f} = \nabla \cdot \mathbb{T}_M - \frac{1}{c^2} \frac{\partial \mathbf{S}}{\partial t} \quad , \quad c^2 = \frac{1}{\varepsilon_0 \mu_0} \ ,$$

with c the speed of light. In particular, in the absence of a magnetic field, the normal pressure on a perfectly conducting object is given by the expression:

$$\mathbb{T}_M^C \, \mathbf{n} = \varepsilon_0 \left(\mathbf{E} \otimes \mathbf{E} - \frac{1}{2} \left\|\mathbf{E}\right\|^2 \mathbb{I} \right) \mathbf{n} = \frac{\sigma^2}{\varepsilon_0} \left(\mathbf{n} \otimes \mathbf{n} - \frac{1}{2} \mathbb{I} \right) \mathbf{n} = \frac{\sigma^2}{2\varepsilon_0} \mathbf{n} \ , \tag{C.5}$$

where $\mathbf{E} = \dfrac{\sigma}{\varepsilon_0} \mathbf{n}$ is the electric field on the surface of a conductor.

Appendix D

Spheroids & Ellipsoids

In this appendix we will describe in detail some useful geometric and electrostatic properties concerning spheroids and ellipsoids that are important for the contents of this thesis. First, classical properties such as volume, surface area, outward unit nomal, moment of inertia and mean curvature are presented, and then, we introduce capacitance and surface charge density for ellipsoidal conductors.

D.1. Geometric properties of spheroids

Given an spheroid with semiaxes a and c, density ϱ and mass M defined by:

$$\frac{x^2}{a^2}+\frac{y^2}{a^2}+\frac{z^2}{c^2}=1 \quad , \quad \begin{cases} a>c & , \text{ oblate spheroid} \\ a<c & , \text{ prolate spheroid} \end{cases} , \tag{D.1}$$

the volume and moment of inertia with respect to the z axis are:

$$V \equiv V_{prolate}=V_{oblate}=\frac{4\pi}{3}a^2c \quad , \quad \mathcal{I}_{prolate}=\mathcal{I}_{oblate}=\frac{2M}{5}a^2=\frac{8\pi}{15}\varrho a^4 c \, . \tag{D.2}$$

Now, the surface area is:

$$A_{prolate}=2\pi a^2\left(1+\frac{\arcsin e}{e\sqrt{1-e^2}}\right) \quad , \quad e^2=1-\frac{a^2}{c^2} \, , \tag{D.3}$$

$$A_{oblate}=2\pi a^2\left(1+\frac{1-e^2}{e}\operatorname{arctanh} e\right)=2\pi a^2\left(1+\frac{1-e^2}{2e}\log\left(\frac{1+e}{1-e}\right)\right) \quad , \quad e^2=1-\frac{c^2}{a^2} \, , \tag{D.4}$$

and in the limit case $a=b=c$ we obtain the surface area of the sphere:

$$A_{sphere}=4\pi a^2 \, . \tag{D.5}$$

If we write (D.1) in spherical coordinates:

$$\begin{cases} x=a\cos\varphi\sin\theta \\ y=a\sin\varphi\sin\theta \\ z=c\cos\theta \end{cases} \quad , \quad \varphi\in[0,2\pi) \quad , \quad \theta\in[0,\pi] \, ,$$

the outward unit normal vector is:

$$\mathbf{n}\left(\varphi,\theta\right)=\frac{\left(c\cos\varphi\sin\theta,c\sin\varphi\sin\theta,a\cos\theta\right)}{\sqrt{c^2\sin^2\theta+a^2\cos^2\theta}} \quad , \quad \mathbf{n}\left(x,y,z\right)=\frac{\left(c^2x,c^2y,a^2z\right)}{\sqrt{c^4\left(x^2+y^2\right)+a^4z^2}} \, . \tag{D.6}$$

and the mean curvature:

$$\mathcal{H}\left(\theta\right)=\frac{c\left(3a^2+c^2+\left(a^2-c^2\right)\cos\left(2\theta\right)\right)}{\sqrt{2}a\left(a^2+c^2+\left(a^2-c^2\right)\cos\left(2\theta\right)\right)^{\frac{3}{2}}} \, . \tag{D.7}$$

Observe that the mean curvature can be written in terms of the aspect ratio, $\alpha=\frac{c}{a}$, as:

$$\mathcal{H}\left(\theta\right)=\sqrt[3]{\frac{\sqrt{2}\pi\alpha}{3V}}\frac{\left(3\alpha+\alpha^3+\left(\alpha-\alpha^3\right)\cos\left(2\theta\right)\right)}{\left(1+\alpha^2+\left(1-\alpha^2\right)\cos\left(2\theta\right)\right)^{\frac{3}{2}}} \, .$$

D.2. Geometric properties of ellipsoids

Consider now an ellipsoid of density ϱ and mass M with semiaxes s_x, s_y and s_z in the form:

$$\frac{x^2}{s_x^2}+\frac{y^2}{s_y^2}+\frac{z^2}{s_z^2}=1\,. \tag{D.8}$$

The volume and moment of inertia with respect to the z axis are given by:

$$V_{ellip}=\frac{4\pi}{3}s_x s_y s_z \quad , \quad \mathcal{I}_{ellip}=\frac{M}{5}\left(s_x^2+s_y^2\right)=\frac{4\pi}{15}\varrho\left(s_x^2+s_y^2\right)s_x s_y s_z\,. \tag{D.9}$$

The surface area for an ellipsoid with semiaxes a, b and c is:

$$A_{ellip}=2\pi c^2+\frac{2\pi ab}{\sin\phi}\left(E\left(\phi,k\right)\sin^2\phi+F\left(\phi,k\right)\cos^2\phi\right) \quad , \quad a\geqslant b\geqslant c \quad , \quad a\neq c\,, \tag{D.10}$$

where:

$$\cos\phi=\frac{c}{a} \quad , \quad k=\frac{a}{b}\sqrt{\frac{b^2-c^2}{a^2-c^2}}\,,$$

and the functions F and E are the incomplete elliptic integrals of the first and second kind respectively:

$$F\left(\phi,k\right)=\int_0^\phi\frac{d\theta}{\sqrt{1-k^2\sin^2\theta}} \quad , \quad E\left(\phi,k\right)=\int_0^\phi\sqrt{1-k^2\sin^2\theta}\,d\theta\,.$$

Setting $a=b>c$ in (D.10) we get (D.4), and with $a>b=c$, (D.3). Surface area can be approximated as:

$$A_{ellip}\approx 4\pi\sqrt[p]{\frac{(ab)^p+(ac)^p+(bc)^p}{3}} \quad , \quad p\approx 1.6075\,, \tag{D.11}$$

yielding a maximum relative error of 1.061×10^{-2} (see [41, 42]). Writing (D.8) in spherical coordinates:

$$\begin{cases} x=s_x\cos\varphi\sin\theta \\ y=s_y\sin\varphi\sin\theta \\ z=s_z\cos\theta \end{cases} \quad , \quad \varphi\in[0,2\pi) \quad , \quad \theta\in[0,\pi]\,,$$

the mean curvature is given by:

$$\mathcal{H}\left(\varphi,\theta\right)=\frac{s_x s_y s_z\left(3\left(s_x^2+s_y^2\right)+2s_z^2+\left(s_x^2+s_y^2-2s_z^2\right)\cos\left(2\theta\right)-2\left(s_x^2-s_y^2\right)\cos\left(2\varphi\right)\sin^2\theta\right)}{8\left(s_x^2s_y^2\cos^2\theta+s_z^2\left(s_y^2\cos^2\varphi+s_x^2\sin^2\varphi\right)\sin^2\theta\right)^{\frac{3}{2}}}\,, \tag{D.12}$$

and the outward unit normal:

$$\mathbf{n}\left(\varphi,\theta\right)=\frac{\left(s_z s_y\cos\varphi\sin\theta,s_x s_z\sin\varphi\sin\theta,s_x s_y\cos\theta\right)}{\sqrt{s_z^2\sin^2\theta\left(s_y^2\cos^2\varphi+s_x^2\sin^2\varphi\right)+s_x^2s_y^2\cos^2\theta}}\,, \tag{D.13}$$

which in cartesian coordinates is:

$$\mathbf{n}\left(x,y,z\right)=\frac{\left(s_y^2s_z^2x,s_x^2s_z^2y,s_x^2s_y^2z\right)}{\sqrt{s_y^4s_z^4x^2+s_x^4s_z^4y^2+s_x^4s_y^4z^2}}\,.$$

D.3. Ellipsoidal conductors

Consider an ellipsoidal conductor which has an amount of charge Q on its surface and defined by three semiaxes a, b and c with the equation:

$$\frac{x^2}{a^2}+\frac{y^2}{b^2}+\frac{z^2}{c^2}=1\,. \tag{D.14}$$

The surface charge density of this ellipsoid has the form [47]:

$$\sigma_{ellipsoid} = \frac{Q}{4\pi abc\sqrt{\dfrac{x^2}{a^4}+\dfrac{y^2}{b^4}+\dfrac{z^2}{c^4}}} \; . \tag{D.15}$$

First, to compute the capacitance of an spheroid we will the property that the projection of the surface charge density of an ellipsoid over the symmetry plane $z = 0$ is independent of the semiaxis c, and is given by:

$$\sigma_{xy} = \frac{Q}{2\pi ab\sqrt{1-\dfrac{x^2}{a^2}-\dfrac{y^2}{b^2}}} \; .$$

For spheroids we have $(a = b)$ and thus:

$$\sigma^s_{xy} = \frac{Q}{2\pi a\sqrt{a^2-r^2}} \quad , \quad r^2 = x^2+y^2 \; ,$$

The electrostatic potential $\mathcal{V}$ at the origin for an spheroid is:

$$4\pi\varepsilon_0\mathcal{V} = \int \frac{\sigma^s_{xy}}{\sqrt{x^2+y^2+z^2}}\,dx\,dy = \frac{Q}{a}\int_0^a \frac{r}{\sqrt{a^2-r^2}\sqrt{r^2+z^2}}\,dr = \frac{Q}{a}\int_0^a \frac{r}{\sqrt{a^2-r^2}\sqrt{\left(1-\dfrac{c^2}{a^2}\right)r^2+c^2}}\,dr \; .$$

Changing variables, $r^2 = s$, one gets:

$$4\pi\varepsilon_0\mathcal{V} = \frac{Q}{2a}\int_0^{a^2} \frac{ds}{\sqrt{\left(\dfrac{c^2}{a^2}-1\right)s^2+(a^2-2c^2)\,s+a^2c^2}} \; .$$

Now, this integral can be calculated using formula 380.001 from [21] to yield:

$$\int \frac{dx}{\sqrt{\mathcal{X}}} = \begin{cases} \dfrac{1}{\sqrt{A}}\log\left|2\sqrt{A\mathcal{X}}+2Ax+B\right| & , \quad A>0 \\ \dfrac{1}{\sqrt{A}}\operatorname{arcsinh}\left(\dfrac{2Ax+B}{\sqrt{-\Delta}}\right) & , \quad A>0 \quad , \quad \Delta<0 \\ \dfrac{1}{\sqrt{A}}\log|2Ax+B| & , \quad A>0 \quad , \quad \Delta=0 \\ -\dfrac{1}{\sqrt{-A}}\arcsin\left(\dfrac{2Ax+B}{\sqrt{\Delta}}\right) & , \quad A<0 \quad , \quad \Delta>0 \quad , \quad |2Ax+B|<\sqrt{\Delta} \end{cases} ,$$

where:

$$\mathcal{X} = Ax^2+Bx+C \quad , \quad \Delta = B^2-4AC \; .$$

For oblate spheroids, $c < a$, and consequently $A < 0$, $\Delta > 0$ and $|2Ax + B| < \sqrt{\Delta}$, so:

$$\mathcal{V}_{oblate} = \frac{Q}{4\pi\varepsilon_0 ae}\arcsin e \quad , \quad e = \sqrt{1-\frac{c^2}{a^2}} \; . \tag{D.16}$$

In the case of prolate spheroids, $a < c$, and since $A > 0$, $\Delta > 0$, we obtain:

$$\mathcal{V}_{prolate} = \frac{Q}{8\pi\varepsilon_0 ce}\log\left(\frac{1+e}{1-e}\right) \quad , \quad e = \sqrt{1-\frac{a^2}{c^2}} \; . \tag{D.17}$$

The capacitance of a conductor is defined by:

$$\mathcal{C} = \frac{Q}{\mathcal{V}} \; , \tag{D.18}$$

then:

$$\mathcal{C}_{oblate} = 4\pi\varepsilon_0 a \frac{e}{\arcsin e} \quad , \quad e = \sqrt{1 - \frac{c^2}{a^2}} \, , \tag{D.19}$$

$$\mathcal{C}_{prolate} = 8\pi\varepsilon_0 c \frac{e}{\log\left(\frac{1+e}{1-e}\right)} \quad , \quad e = \sqrt{1 - \frac{a^2}{c^2}} \, . \tag{D.20}$$

In the limit case $a = b = c$ we obtain the electrostatic potential and capacitance of a conducting sphere:

$$\mathcal{V}_{sphere} = \frac{Q}{4\pi\varepsilon_0 a} \quad , \quad \mathcal{C}_{sphere} = 4\pi\varepsilon_0 a \, . \tag{D.21}$$

To finish this appendix we present the general formula for the capacitance of an ellipsoid with semiaxes a_1, a_2 and a_3, where $a_1 \geqslant a_2 \geqslant a_3$ and $a_1 \neq a_3$, which is given by:

$$\mathcal{C}_{ellip} = \frac{8\pi\varepsilon_0 \lambda}{F(\phi, k)} \, , \tag{D.22}$$

where:

$$\lambda = \frac{1}{2}\sqrt{a_1^2 - a_3^2} \quad , \quad \cos\phi = \frac{a_3}{a_1} \quad , \quad k = \sqrt{\frac{a_1^2 - a_2^2}{a_1^2 - a_3^2}} \, .$$

We can approximate the capacitance of an ellipsoid with the formula:

$$\mathcal{C}_{ellip} \approx \frac{4\pi\varepsilon_0}{45} \left(11\,(a_1 + a_2 + a_3) + 4\,(\sqrt{a_1 a_2} + \sqrt{a_1 a_3} + \sqrt{a_2 a_3})\right) \, ,$$

taken from [55]. Finally, observe that if $a_1 = a_2 > a_3$ one obtains (D.19) and for $a_1 > a_2 = a_3$ we get (D.20).

Appendix E

Barycentric coordinates

Take a triangle in the plane with area A, defined by the vertices P_1, P_2 and P_3, and a point P inside it:

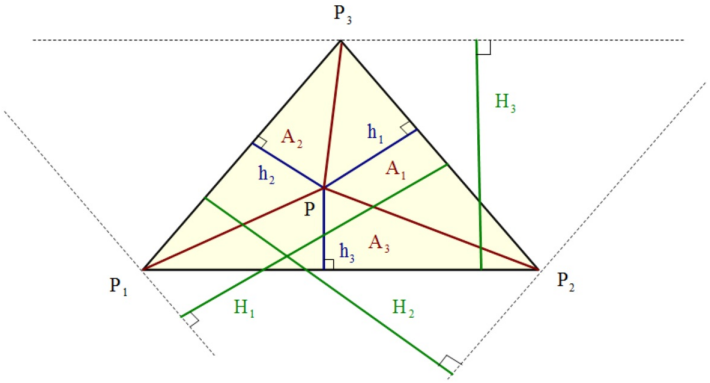

Figure E.1: Barycentric coordinates of a point P.

If the triangles PP_2P_3, PP_3P_1 and PP_1P_2 have areas A_1, A_2 and A_3 respectively, $\mathbf{r}_i = (x_i, y_i)$ are the coordinates of P_i and $\mathbf{r} = (x, y)$ the ones for P, the barycentric coordinates of P are defined as:

$$\lambda_i^P = \frac{h_i}{H_i} = \frac{A_i}{A} \quad , \quad A_i = \frac{1}{2}\begin{vmatrix} 1 & x & y \\ 1 & x_j & y_j \\ 1 & x_k & y_k \end{vmatrix} \quad , \quad A = \frac{1}{2}\begin{vmatrix} 1 & x_1 & y_1 \\ 1 & x_2 & y_2 \\ 1 & x_3 & y_3 \end{vmatrix} , \tag{E.1}$$

where $i, j, k \in \{1, 2, 3\}$ with $i \neq j \neq k$ and (i, j, k) an even permutation. Equvalently:

$$\lambda_i^P = \frac{a_i + b_i x + c_i y}{2A} \quad \text{with} \quad \begin{cases} a_i = x_j y_k - x_k y_j \\ b_i = y_j - y_k \\ c_i = x_k - x_j \end{cases} . \tag{E.2}$$

Any point P inside the triangle can be expressed as a linear combination of the three vertices:

$$\mathbf{r} = \lambda_i^P \mathbf{r}_i \quad , \quad \sum_{i=1}^{3} \lambda_i^P = 1 , \tag{E.3}$$

where the barycentric coordinates of the triangle vertices satisfy:

$$\lambda_i^{P_j} = \delta_{ij} .$$

The notation that is most common in the literature for barycentric coordinates is:

$$\lambda_1^P = \xi_P \quad , \quad \lambda_2^P = \eta_P \quad , \quad \lambda_3^P = \zeta_P .$$

In matrix form, the identities in (E.3) give:

$$\begin{cases} x = x_1\xi_P + x_2\eta_P + x_3\zeta_P \\ y = y_1\xi_P + y_2\eta_P + y_3\zeta_P \\ 1 = \xi_P + \eta_P + \zeta_P \end{cases} \quad \Leftrightarrow \quad \begin{pmatrix} x \\ y \\ 1 \end{pmatrix} = \begin{pmatrix} x_1 & x_2 & x_3 \\ y_1 & y_2 & y_3 \\ 1 & 1 & 1 \end{pmatrix} \begin{pmatrix} \xi_P \\ \eta_P \\ \zeta_P \end{pmatrix} , \tag{E.4}$$

and, since $\zeta_P = 1 - \xi_P - \eta_P$, these matrix expression yields:

$$\begin{pmatrix} x - x_3 \\ y - y_3 \end{pmatrix} = \begin{pmatrix} x_1 - x_3 & x_2 - x_3 \\ y_1 - y_3 & y_2 - y_3 \end{pmatrix} \begin{pmatrix} \xi_P \\ \eta_P \end{pmatrix} . \tag{E.5}$$

The solution to this system is trivial:

$$\xi_P = \frac{(x - x_3)(y_2 - y_3) - (x_2 - x_3)(y - y_3)}{(x_1 - x_3)(y_2 - y_3) - (x_2 - x_3)(y_1 - y_3)} \quad , \quad \eta_P = \frac{(x_1 - x_3)(y - y_3) - (x - x_3)(y_1 - y_3)}{(x_1 - x_3)(y_2 - y_3) - (x_2 - x_3)(y_1 - y_3)} ,$$

$$\zeta_P = 1 - \xi_P - \eta_P ,$$

One important aspect about barycentric coordinates is that one can easily check if a point lies inside a triangle, on one of the triangle edges or coincides with a triangle vertex. We have that a point is:

- inside the triangle, if $0 < \xi_P, \eta_P, \zeta_P < 1$.
- on a triangle edge, if one of the barycentric coordinates is zero and the other two are between 0 and 1.
- a triangle vertex, if two of the barycentric coordinates are zero and the third is 1.

In any other case, the point is located outside the triangle. Barycentric coordinates are also very useful when linearly interpolating a function f over a triangle, as we can immediately compute the value of the function at any point $\mathbf{r}$ inside the triangle just by knowing the barycentric coordinates of that point and the values taken by the function at the vertices of the triangle:

$$\mathbf{r} = \lambda_i^P \mathbf{r}_i \quad \Leftrightarrow \quad f(\mathbf{r}) = \lambda_i^P f(\mathbf{r}_i) . \tag{E.6}$$

Bibliography

[1] M. Abramowitz and I. A. Stegun. *Handbook of Mathematical Functions: With Formulas, Graphs, and Mathematical Tables*. Applied mathematics series. Dover Publications, 1964.

[2] P. Aussillous and D. Quéré. Shapes of rolling liquid drops. *Journal of Fluid Mechanics*, 512:133–151, 2004.

[3] I. Babuska. The finite element method with lagrangian multipliers. *Numerische Mathematik*, 20:179–192, 1972/73.

[4] O. A. Basaran and L. E. Scriven. Axisymmetric shapes and stability of charged drops in an external electric field. *Phys. Fluids A*, 1(5):799–809, 1989.

[5] O. A. Basaran and L. E. Scriven. Axisymmetric shapes and stability of isolated charged drops. *Phys. Fluids A*, 1(5):795–798, 1989.

[6] A. Beer. *Einleitung in die mathematische Theorie der Elasticität und Capillarität*. Teubner, 1869.

[7] S. I. Betelu, M. A. Fontelos, U. Kindelan, and O. Vantzos. Singularities on charged viscous droplets. *Physics of Fluids*, 18(5):051706, 2006.

[8] N. Bohr and J. A. Wheeler. The Mechanism of Nuclear Fission. *Phys. Rev.*, 56(5):426–450, 1939.

[9] H. Brezis. *Analyse functionnelle*. Masson, Paris, 1983.

[10] F. Brezzi and M. Fortin. *Mixed and hybrid finite element methods*. Springer-Verlag New York, Inc., New York, NY, USA, 1991.

[11] R. A. Brown and L. E. Scriven. The shape and stability of rotating liquid drops. *Proc. R. Soc. Lond. A*, 371:331–357, 1980.

[12] S. Chandrasekhar. The stability of a rotating liquid drop. *Proc. R. Soc. Lond. A*, 286:1–26, 1965.

[13] S. Chandrasekhar. *Ellipsoidal figures of equilibrium*. Dover Books on Mathematics. Dover, 1987.

[14] S. Chandrasekhar and N. R. Lebovitz. The potentials and superpotentials of homogeneous ellipsoids. *Astrophysical Journal*, 136, 1962.

[15] S. K. Cho, H. J. Moon, and C. J. Kim. Creating, transporting, cutting, and merging liquid droplets by electrowetting-based actuation for digital microfluidic circuits. *Journal of Microelectromechanical Systems*, 12(1):70–80, 2003.

[16] I. Cohen, M. P. Brenner, J. Eggers, and S. R. Nagel. Two Fluid Drop Snap-Off Problem: Experiments and Theory. *Phys. Rev. Lett.*, 83(6):1147–1150, 1999.

[17] V. Cristini, J. Blawzdziewicz, and M. Loewenberg. An Adaptive Mesh Algorithm for Evolving Surfaces: Simulations of Drop Breakup and Coalescence. *Journal of Computational Physics*, 168(2):445–463, 2001.

[18] H.T. Davis. *Introduction to Nonlinear Differential and Integral Equations*. Dover Science Books, S971. Dover Publications, 1962.

[19] M. P. do Carmo. *Differential geometry of curves and surfaces*. Prentice-Hall, 1976.

[20] D. Duft, T. Achtzehn, R. Müller, B. A. Huber, and T. Leisner. Rayleigh jets from levitated microdroplets. *Nature*, 421, 2003.

[21] H. B. Dwight. *Tables of integrals and other mathematical data.* Macmillan, 1961.

[22] J. Eggers and M. A. Fontelos. The role of self-similarity in singularities of partial differential equations. *Nonlinearity*, 22(1):R1–R44, 2009.

[23] J. Eggers and E. Villermaux. Physics of liquid jets. *Reports on Progress in Physics*, 71(3):036601, 2008.

[24] M. A. Fontelos and A. Friedman. Symmetry-breaking bifurcations of charged drops. *Archive for Rational Mechanics and Analysis*, 172:267–294, 2004.

[25] M. A. Fontelos, V. J. García-Garrido, and U. Kindelán. Evolution and breakup of viscous rotating drops. *SIAM J. Appl. Math.*, 71:1941–1964, 2011.

[26] M. A. Fontelos and U. Kindelán. The shape of charged drops over a solid surface and symmetry-breaking instabilities. *SIAM J. Appl. Math.*, 69:126–148, 2008.

[27] M. A. Fontelos, U. Kindelan, and O. Vantzos. Evolution of neutral and charged droplets in an electric field. *Physics of Fluids*, 20(9):092110, 2008.

[28] V. J. García-Garrido, M. A. Fontelos, and U. Kindelán. Evolution, stability and equilibrium shapes of rotating drops which are charged or subject to electric fields. *Q. J. Mechanics Appl. Math.*, To appear.

[29] H. Goldstein. *Classical Mechanics.* Addison-Wesley Publishing Company, Reading, MA, 2nd edition, 1980.

[30] I. S. Gradshteyn, I. M. Ryzhik, A. Jeffrey, and D. Zwillinger. *Table of integrals, series and products.* Academic Press. Academic, 2007.

[31] H.P. Greenspan. *The theory of rotating fluids.* Cambridge monographs on mechanics and applied mathematics. Cambridge University Press, 1990.

[32] R. Grimm and J. Beauchamp. Dynamics of field-induced droplet ionization: time-resolved studies of distortion, jetting, and progeny formation from charged and neutral methanol droplets exposed to strong electric fields. *J. Phys. Chem. B*, 109(16):8244–50, 2005.

[33] R. Gulliver. Tori of prescribed mean curvature and the rotating drop. *Soc. Math. de France, Astérisque*, 118:167–179, 1984.

[34] R. A. Hayes and B. J. Feenstra. Video speed electronic paper based on electrowetting. *Nature*, 425:383–385, 2003.

[35] C. J. Heine. Computations of form and stability of rotating drops with finite elements. *IMA Journal of Numerical Analysis*, 26(4):723–751, 2006.

[36] R. Hill and L. Eaves. Nonaxisymmetric shapes of a magnetically levitated and spinning water droplet. *Physical Review Letters*, 101, 2008.

[37] P. D. Howell, B. Scheid, and H. A. Stone. Newtonian pizza: spinning a viscous sheet. *Journal of Fluid Mechanics*, 659:1–23, 2010.

[38] G. Iooss and D. D. Joseph. *Elementary stability and bifurcation theory.* Undergraduate texts in mathematics. Springer-Verlag, New York, 1980.

[39] C. G. J. Jacobi. Über die Figur des Gleichgewichts. *Annln. Phys.*, 33:229–238, 1834.

[40] M. Kallay. Computing the Moment of Inertia of a Solid Defined by a Triangle Mesh. *Journal of Graphics, GPU, & Game Tools*, 11(2):51–57, 2006.

[41] M. S. Klamkin. Elementary approximations to the area of n-dimensional ellipsoids. *American Mathematical Monthly*, 78:280–283, 1971.

[42] M. S. Klamkin. Corrections to "elementary approximations to the area of n-dimensional ellipsoids". *American Mathematical Monthly*, 83:478, 1976.

[43] O. A. Ladyzhenskaya. *The Mathematical Theory of Viscous Incompressible Flow*. Gordon and Breach, 1963.

[44] L. D. Landau and E. M. Lifshitz. *Fluid Mechanics*. Pergamon Press, 1987.

[45] J. R. Lister and H. A. Stone. Capillary breakup of a viscous thread surrounded by another viscous fluid. *Physics of Fluids*, 10(11):2758–2764, 1998.

[46] C. Maclaurin. *A treatise on fluxions*. T. W. & T. Ruddimans, 1742.

[47] K. T. McDonald. Conducting ellipsoid and circular disk. (Oct. 19, 2002).

[48] F. Morgan. *Riemannian geometry: a beginner's guide*. Ak Peters Series. A.K. Peters, 1998.

[49] A. D. Myshkis, V. G. Babskii, N. D. Kopachevskii, L. A. Slobozhanin, and A. D. Tyuptsov. *Low-Gravity Fluid Mechanics*. Springer-Verlag, 1987.

[50] J. R. A. Pearson. *Mechanics of Polymer Processing*. Elsevier Applied Science Publishers, 1985.

[51] J. A. F. Plateau. Mémoire sur les phénomènes que présente une masse liquide libre et soustraite à l'action de la pesanteur. *Mémoires de l'Academy Bruxelles*, 16:1–35, 1843.

[52] J. A. F. Plateau. Experimental and theoretical researches on the figures of equilibrium of a liquid mass withdrawn from the action of gravity. *Annual Report of the Board of Regents of the Smithsonian Institute*, pages 270–285, 1863. Translation of Plateau's 1843 article.

[53] H. Poincaré. Sur l'équilibre d'une masse fluide animée d'un mouvement de rotation. *Acta Mathematica*, 7:259–380, 1885.

[54] G. Pólya and G. Szegő. Inequalities for the capacity of a condenser. *Amer. J. Math.*, 67:1–32, 1945.

[55] G. Pólya and G. Szegő. *Isoperimetric inequalities in mathematical physics*. Annals of mathematics studies. Princeton University Press, 1951.

[56] C. Pozrikidis. *Boundary integral and singularity methods for linearized viscous flow*. Cambridge Texts in Applied Mathematics. Cambridge University Press, 1992.

[57] H. M. Princen, I. Y. Z. Zia, and S. G. Mason. Measurement of interfacial tension from the shape of a rotating drop. *Journal of Colloid and Interface Science*, 23:99–107, 1967.

[58] Lord Rayleigh. On the equilibrium of liquid conducting masses charged with electricity. *Phil. Mag.*, 14:184–186, 1882.

[59] B.D. Reddy. *Introductory functional analysis. With applications to boundary value problems and finite elements.* Springer-Verlag, New York, 1998.

[60] C. Rosenkilde. Surface-energy tensors for ellipsoids. *Journal of Mathematical Physics*, 8(1), 1967.

[61] C. Rosenkilde and R. R. Randall. On the shape and stability of a conducting fluid drop rotating in an electric field. *Acta Mechanica*, 20:167–186, 1974.

[62] Y. Saad and M.H. Schultz. GMRES: A generalized minimal residual algorithm for solving nonsymmetric linear systems. *SIAM J. Sci. Stat. Comput.*, 7(3):856–869, 1986.

[63] S. O. Shiryaeva, A.I. Grigorév, and P.V. Moksheev. Nonlinear analysis of the equilibrium shape of a charged drop rotating around its symmetry axis. *Technical Physics*, 52(4):422–430, 2007.

[64] D. R. Smith and J. E. Ross. Universal shapes and bifurcation for rotating incompressible fluid drops. *Methods and Applications of Analysis*, 1(2):210–228, 1994.

[65] C. Sozou. A rotating spherical liquid drop in an electric field. *J. Fluid Mech.*, 56:305–312, 1972.

[66] H. A. Stone, A. D. Stroock, and A. Ajdari. Engineering flows in small devicces: Microfluidics toward a lab-on-a-chip. *Annual Review of Fluid Mechanics*, 36:381–411, 2004.

[67] T. Surazhsky, E. Magid, O. Soldea, G. Elber, and E. Rivlin. A comparison of gaussian and mean curvatures estimation methods on triangular meshes. In *ICRA*, pages 1021–1026, 2003.

[68] G. I. Taylor. Disintegration of water drops in an electric field. *Proc. R. Soc. London, Ser. A*, 280(1382):383–397, 1964.

[69] A. VanderWyst, A. Christlieb, M. Sussman, and I. D. Boyd. Level set simulations of charged droplets using a boundary element method. In *IEPC-2005-019*. Princeton University, November 2005. Presented at the 29th International Electric Propulsion Conference.

[70] O. Vantzos. *Mathematical modeling of charged liquid droplets: Numerical simulation and stability analysis*. PhD thesis, University of North Texas, Denton TX, 2006.

[71] S. Velick and M. Gorin. The electrical conductance of suspensions of ellipsoids and its relation to the study of avian erythrocytes. *J. Gen. Physiol.*, 23(6):753–771, 1940.

[72] T. G. Wang, A. V. Anilkumar, C. P. Lee, and K. C. Lin. Bifurcation of rotating liquid drops: results from USML-1 experiments in Space. *Journal of Fluid Mechanics*, 276:389–403, 1994.

[73] T. G. Wang, E. H. Trinh, A. P. Croonquist, and D. D. Elleman. Shapes of rotating free drops: Spacelab experimental results. *Phys. Rev. Lett.*, 56(5):452–455, Feb 1986.

[74] E. W. Weisstein. Rotation Formula. `http://mathworld.wolfram.com/RotationFormula.html`. Online: From MathWorld - A Wolfram Web Resource.

[75] A. Z. Zinchenko, M. A. Rother, and R. H. Davis. A novel boundary-integral algorithm for viscous interaction of deformable drops. *Physics of Fluids*, 9(6):1493–1511, 1997.